WOODHEAD PUBLISHING IN MATERIALS

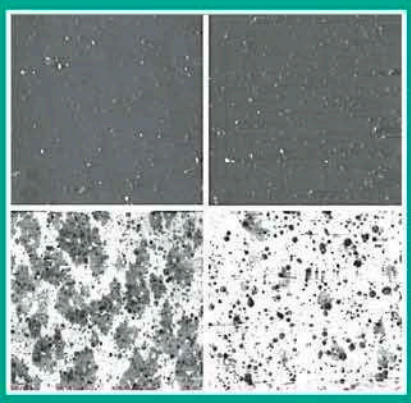

European Federation of
Corrosion Publications
Number 45

Local probe techniques for corrosion research

Edited by R. Oltra, V. Maurice,
R. Akid and P. Marcus

CRC

WP

ISSN 1354-5116

Local probe techniques for corrosion research

European Federation of Corrosion Publications
NUMBER 45

Local probe techniques for corrosion research

Edited by
R. Oltra, V. Maurice, R. Akid and P. Marcus

**Published for the European Federation of Corrosion
by Woodhead Publishing and Maney Publishing
on behalf of
The Institute of Materials, Minerals & Mining**

**CRC Press
Boca Raton Boston New York Washington, DC**

WOODHEAD PUBLISHING LIMITED
Cambridge England

Woodhead Publishing Limited and Maney Publishing Limited on behalf of
The Institute of Materials, Minerals & Mining

Woodhead Publishing Limited, Abington Hall, Abington,
Cambridge CB21 6AH, England
www.woodheadpublishing.com

Published in North America by CRC Press LLC, 6000 Broken Sound Parkway, NW,
Suite 300, Boca Raton, FL 33487, USA

First published 2007 by Woodhead Publishing Limited and CRC Press LLC

British Library Cataloguing in Publication Data
A catalogue record for this book is available from the British Library.

Library of Congress Cataloging in Publication Data
A catalog record for this book is available from the Library of Congress.

Woodhead Publishing ISBN-13: 978-1-84569-236-0 (book)
Woodhead Publishing ISBN-10: 1-84569-236-5 (book)
Woodhead Publishing ISBN-13: 978-1-84569-259-9 (e-book)
Woodhead Publishing ISBN-10: 1-84569-259-4 (e-book)
CRC Press ISBN-13: 978-1-4200-5405-7
CRC Press ISBN-10: 1-4200-5405-8
CRC Press order number: WP5405
ISSN 1354-5116

The publishers' policy is to use permanent paper from mills that operate a sustainable forestry policy, and which has been manufactured from pulp which is processed using acid-free and elementary chlorine-free practices. Furthermore, the publishers ensure that the text paper and cover board used have met acceptable environmental accreditation standards.

Typeset by SNP Best-set Typesetter Ltd., Hong Kong
Printed by TJ International Limited, Padstow, Cornwall, England

Contents

Contributor contact details

(* = main contact)

Editor and Chapter 1

Dr Roland Oltra
Laboratoire de Recherche sur la Réactivité des Solides
UMR 5613 CNRS-Université de Bourgogne
BP 47870, 21078 Dijon
France
E-mail: roland.oltra@u-bourgogne.fr

Chapter 2

Dr Kevin Ogle*
Ecole Nationale de Chimie de Paris
Laboratoire de Physico-Chimie des Surfaces UMR 7045
11 rue Pierre et Marie Curie
75005 Paris
France
E-mail: kevin-ogle@enscp.fr

S. Morel and D. Jacquet
Arcelor R&D
Voie Romaine BP 30320
F-57283 Maizières lès Metz Cedex
France

Chapter 3

Prof. R. Akid*, P. Roffey, Dr D. Greenfield and D. Guillen
Centre for Corrosion Technology
Materials & Engineering Research Institute
Sheffield Hallam University
Howard Street
Sheffield
S1 1WB
UK
E-mail: r.akid@shu.ac.uk

Chapter 4

Dr David A. Worsley*, Dr Jonathan Elvins and Dr John A Spittle
Materials Research Centre
School of Engineering
University of Wales Swansea
Singleton Park
Swansea
SA2 8PP
UK
E-mail: D.A.Worsley@swansea.ac.uk

Chapter 5

Dr R. Basséguy*, Dr J. Idrac, Dr C. Jacques, Dr A. Bergel, Dr M. L Délia, and Dr L. Etcheverry
Laboratoire de Génie Chimique
CNRS UMR 5503
Site Basso Cambo
5 rue Paulin Talabot
31106 Toulouse
Cedex 01
France
E-mail: Regine.Basseguy@ensiacet.fr

Chapter 6

Jean-Baptiste Jorcin and Dr Nadine Pébère*
Centre Inter Universitaire de Recherche et d'Ingénierie des Matériaux
CNRS UMR 5085
ENSIACET
118 Route de Narbonne
31077 Toulouse Cedex 04
France
E-mail: Nadine.Pebere@ensiacet.fr

Dr Emmanuel Aragon and Dr Céline Merlatti
UPRES 1356 Matériaux à Finalités Spécifiques
Université du Sud Toulon Var
ISITV
BP 56, Avenue Georges Pompidou
83162 La Valette du Var Cedex
France

Chapter 7

Dr V. Maurice*, Dr T. Nakamura, Dr L. H. Klein and Dr P. Marcus
Laboratoire de Physico-Chimie des Surfaces
ENSCP – CNRS (UMR 7045)
Ecole Nationale Supérieure de Chimie de Paris,
11 rue Pierre et Marie Curie
75231 Paris Cedex 05
France
E-mail: vincent-maurice@enscp.fr

Chapter 8

Dr F. A. Martin, Dr J. Cousty*, Dr J.-L. Masson and Dr C. Bataillon
CEA de Saclay DRECAM/SPCSI
District du Plateau de Saclay
Val Courcelle
91196 Gif-sur-Yvette Cedex
France
E-mail: jacques.cousty@cea.fr

Chapter 9

Prof. Junji Inukai*
New Industry Creation Hatchery Centre
Tohoku University
Aoba-yama 10
Sendai 980-8579
Japan
E-mail: jinukai@atom.che.tohoku.ac.jp

Prof. Kingo Itaya
Department of Applied Chemistry
Graduate School of Engineering
Tohoku University
Aoba-yama 04
Sendai 980-8579
Japan

Chapter 10

Dr B. S. Tanem*, Dr O. Lunder and Dr O. Ø. Knudsen
SINTEF Materials and Chemistry
Høgskoleringen 5
N-7465 Trondheim
Norway
E-mail: Bjorn.S.Tanem@sintef.no

Chapter 11

Martin Jönsson*
Swedish Corrosion Institute
Kräfriket 23A
104 05 Stockholm
Sweden
E-mail: martin.jonsson@kimab.com

Dr Dominique Thierry and Dr Nathalie LeBozec
Institut de la Corrosion
220 Rue Rivoalon
29200 Brest
France

Chapter 12

Dr F. Andreatta
University of Udine, Department of Chemical Science and Technologies
Via del Cotoniçico 108
33100 Udine
Italy
E-mail: francesco.andreatta@uniud.it

Dr H. Terryn and Dr S. H. W. de Wit
Netherlands Institute for Metals Research (NIMR)
Corrosion Technology and Electrochemistry
Rotterdamseweg 137
2600GA Delft
The Netherlands

Dr M. M. Lohrengel
Heinrich Heine University
Institute for Physical Chemistry and Electrochemistry
Universitätsstr. 1
40225 Düsseldorf
Germany

Chapter 13

Dr H. Masuda
Corrosion Analysis Group
MEL NIMS
1-2-1 Sengen
Tsukuba
Ibaraki 305-0047
Japan
E-mail: MASUDA.Hiroyuki@nims.go.jp

Chapter 14

Dr V. Vignal* and Dr R. Oltra
Laboratoire de Recherche sur la Réactivité des Solides
UMR 5613
CNRS–Université de Bourgogne
BP 47870
21078 Dijon Cedex
France
E-mail: vincent.vignal@u-bourgogne.fr

Chapter 15

Dr B. J. Connolly
School of Engineering, Metallurgy and Materials
The University of Birmingham
Edgbaston
Birmingham
B15 2TT
UK
E-mail: B.J.Connolly@bham.ac.uk

Chapter 16

Dr Halina Krawiec*
Department of Foundry Engineering
AGH University of Science and Technology
Krakow
Poland
E-mail: Krawiec@agh.edu.pl

Dr Roland Oltra and Dr Vincent Vignal
Laboratoire de Recherches sur la Réactivité des Soldes
UMR 5613
CNRS – Université de Bourgogne
Dijon
France

Chapter 17

Prof. Y. Wouters*, L. Marchetti, Prof. A. Galerie, Dr P. Bouvier and Prof. J.-P. Petit
Laboratoire de Thermodynamique et de Physicochimie Métallurgiques UMR CNRS/INPG/UJF 5614
Institut National Polytechnique de Grenoble
Ecole Nationale Supérieure d'Electrochimie et d'Electrométallurgie de Grenoble
BP 75 Domaine Universitaire
F – 38402 Saint-Martin-d'Hères Cedex
France
E-mail: Yves.Wouters@ltpcm.inpg.fr

European Federation of Corrosion (EFC) publications: Series introduction

The EFC, incorporated in Belgium, was founded in 1955 with the purpose of promoting European co-operation in the fields of research into corrosion and corrosion prevention.

Membership of the EFC is based upon participation by corrosion societies and committees in technical Working Parties. Member societies appoint delegates to Working Parties, whose membership is expanded by personal corresponding membership.

The activities of the Working Parties cover corrosion topics associated with inhibition, education, reinforcement in concrete, microbial effects, hot gases and combustion products, environment sensitive fracture, marine environments, refineries, surface science, physico-chemical methods of measurement, the nuclear industry, the automotive industry, computer-based informative systems, coatings, tribo-corrosion and the oil and gas industry. Working Parties and Task Forces on other topics are established as required.

The Working Parties function in various ways, e.g. by preparing reports, organising symposia, conducting intensive courses and producing instructional material, including films. The activities of the Working Parties are coordinated, through a Science and Technology Advisory Committee, by the Scientific Secretary. The administration of the EFC is handled by three Secretariats: DECHEMA e.V. in Germany, the Société de Chimie Industrielle in France, and The Institute of Materials, Minerals and Mining in the United Kingdom. These three Secretariats meet at the Board of Administrators of the EFC. There is an annual General Assembly at which delegates from all member societies meet to determine and approve EFC policy. News of EFC activities, forthcoming conferences, courses, etc. is published in a range of accredited corrosion and certain other journals throughout Europe. More detailed descriptions of activities are given in a Newsletter prepared by the Scientific Secretary.

The output of the EFC takes various forms. Papers on particular topics, for example, reviews or results of experimental work, may be published in

scientific and technical journals in one or more countries in Europe. Conference proceedings are often published by the organisation responsible for the conference.

In 1987 the, then, Institute of Metals was appointed as the official EFC publisher. Although the arrangement is non-exclusive and other routes for publication are still available, it is expected that the Working Parties of the EFC will use The Institute of Materials, Minerals and Mining for publication of reports, proceedings, etc. wherever possible.

The name of The Institute of Metals was changed to The Institute of Materials on 1 January 1992 and to The Institute of Materials, Minerals and Mining with effect from 26 June 2002. The series is now published by Woodhead Publishing and Maney Publishing on behalf of The Institute of Materials, Minerals and Mining.

P. McIntyre
EFC Series Editor, The Institute of Materials, Minerals and Mining, London, UK

EFC Secretariats are located at:

Dr B. A. Rickinson
European Federation of Corrosion, The Institute of Materials, Minerals and Mining, 1 Carlton House Terrace, London SW1Y 5DB, UK

Dr J. P. Berge
Fédération Européenne de la Corrosion, Société de Chimie Industrielle, 28 rue Saint-Dominique, F-75007 Paris, FRANCE

Professor Dr G. Kreysa
Europäische Föderation Korrosion, DECHEMA e.V., Theodor-Heuss-Allee 25, D-60486 Frankfurt, GERMANY

Volumes in the EFC series

1 **Corrosion in the nuclear industry**
Prepared by the Working Party on Nuclear Corrosion

2 **Practical corrosion principles**
Prepared by the Working Party on Corrosion Education
(Out of print)

3 **General guidelines for corrosion testing of materials for marine applications**
Prepared by the Working Party on Marine Corrosion

4 **Guidelines on electrochemical corrosion measurements**
Prepared by the Working Party on Physico-chemical Methods of Corrosion Testing

5 **Illustrated case histories of marine corrosion**
Prepared by the Working Party on Marine Corrosion

6 **Corrosion education manual**
Prepared by the Working Party on Corrosion Education

7 **Corrosion problems related to nuclear waste disposal**
Prepared by the Working Party on Nuclear Corrosion

8 **Microbial corrosion**
Prepared by the Working Party on Microbial Corrosion

9 **Microbiological degradation of materials – and methods of protection**
Prepared by the Working Party on Microbial Corrosion

10 **Marine corrosion of stainless steels: chlorination and microbial effects**
Prepared by the Working Party on Marine Corrosion

11 **Corrosion inhibitors**
Prepared by the Working Party on Inhibitors (Out of print)

12 **Modifications of passive films**
Prepared by the Working Party on Surface Science and Mechanisms of Corrosion and Protection

13 **Predicting CO_2 corrosion in the oil and gas industry**
Prepared by the Working Party on Corrosion in Oil and Gas Production (Out of Print)

14 **Guidelines for methods of testing and research in high temperature corrosion**
Prepared by the Working Party on Corrosion by Hot Gases and Combustion Products

15 **Microbial corrosion (Proc. 3rd Int. EFC Workshop)**
Prepared by the Working Party on Microbial Corrosion

16 **Guidelines on materials requirements for carbon and low alloy steels for H_2S-containing environments in oil and gas production**
Prepared by the Working Party on Corrosion in Oil and Gas Production

17 **Corrosion resistant alloys for oil and gas production: guidance on general requirements and test methods for H_2S Service**
Prepared by the Working Party on Corrosion in Oil and Gas Production

18 **Stainless steel in concrete: state of the art report**
Prepared by the Working Party on Corrosion of Reinforcement in Concrete

19 **Sea water corrosion of stainless steels – mechanisms and experiences**
Prepared by the Working Parties on Marine Corrosion and Microbial Corrosion

20 **Organic and inorganic coatings for corrosion prevention – research and experiences**
Papers from EUROCORR '96

21 **Corrosion – deformation interactions**
CDI '96 in conjunction with EUROCORR '96

22 **Aspects on microbially induced corrosion**
Papers from EUROCORR '96 and the EFC Working Party on Microbial Corrosion

23 **CO_2 corrosion control in oil and gas production – design considerations**
Prepared by the Working Party on Corrosion in Oil and Gas

24 **Electrochemical rehabilitation methods for reinforced concrete structures – a state of the art report**
Prepared by the Working Party on Corrosion of Reinforced Concrete

25 **Corrosion of reinforcement in concrete – monitoring, prevention and rehabilitation**
Papers from EUROCORR '97

26 **Advances in corrosion control and materials in oil and gas production**
Papers from EUROCORR '97 and EUROCORR '98

27 **Cyclic oxidation of high temperature materials**
Proceedings of an EFC Workshop, Frankfurt/Main, 1999

28 **Electrochemical approach to selected corrosion and corrosion control studies**
Papers from 50th ISE Meeting, Pavia, 1999

29 **Microbial Corrosion (proceedings of the 4th international EFC workshop)**
Prepared by the Working Party on Microbial Corrosion

30 **Survey of literature on crevice corrosion (1979–1998): mechanisms, test methods and results, practical experience, protective measures and monitoring**
Prepared by F. P. Ijsseling and the Working Party on Marine Corrosion

31 **Corrosion of reinforcement in concrete: corrosion mechanisms and corrosion protection**
Papers from EUROCORR '99 and the Working Party on Corrosion of Reinforcement in Concrete

32 **Guidelines for the compilation of corrosion cost data and for the calculation of the life cycle cost of corrosion – a working party report**
Prepared by the Working Party on Corrosion in Oil and Gas Production

33 **Marine corrosion of stainless steels: testing, selection, experience, protection and monitoring**
Edited by D. Féron

34 **Lifetime modelling of high temperature corrosion processes**
Proceedings of an EFC Workshop 2001. Edited by M. Schütze, W. J. Quadakkers and J. R. Nicholls

35 **Corrosion inhibitors for steel in concrete**
Prepared by B. Elsener with support from a Task Group of Working Party 11 on Corrosion of Reinforcement in Concrete

36 **Prediction of long term corrosion behaviour in nuclear waste systems**
Edited by D. Féron of Working Party 4 on nuclear corrosion

37 **Test methods for assessing the susceptibility of prestressing steels to hydrogen induced stress corrosion cracking**
Prepared by B. Isecke on behalf of Working Party 11 on Corrosion of Reinforcement in Concrete

38 **Corrosion of reinforcement in concrete: mechanisms, monitoring, inhibitors and rehabilitation techniques**
Edited by M. Raupach, B. Elsener, R. Polder and J. Mietz on behalf of Working Party 11 on Corrosion of Steel in Concrete

39 **The use of corrosion inhibitors in oil and gas production**
Edited by J. W. Palmer, W. Hedges and J. L. Dawson

40 **Control of corrosion in cooling waters**
Edited by J. D. Harston and F. Ropital

41 **Metal dusting, carburisation and nitridation**
Edited by M. Schütze and H. Grabke

42 **Corrosion in refineries**
Edited by J. Harston

43 **The electrochemistry and characteristics of embeddable reference electrodes for concrete**
Prepared by R. Myrdal on behalf of Working Party 11 on Corrosion of Steel in Concrete

44 **The use of electrochemical scanning tunnelling microscopy (EC-STM) in corrosion analysis: reference material and procedural guidelines**
Prepared by R. Lindström, V. Maurice, L. Klein and P. Marcus on behalf of Working Party 6 on Surface Science

45 **Local probe techniques for corrosion research**
Edited by R. Oltra (on behalf of Working Party 8 on Physico-Chemical Methods of Corrosion Testing)

46 **Amine unit corrosion survey**
Edited by F. Ropital (on behalf of Working Party 15 on Corrosion in the Refinery Industry)

47 **Novel approaches to the improvement of high temperature corrosion resistance**
Edited by M. Schütze and W. Quadakkers (on behalf of Working Party 3 on Corrosion in Hot Gases and Combustion Products)

48 **Corrosion of metallic heritage artefacts: investigation, conservation and prediction of longterm behaviour**
Edited by P. Dillmann, G. Béranger, P. Piccardo, H. Matthiessen and D. Féron (on behalf of Working Party 4 on Nuclear Corrosion)

49 **Electrochemistry in light water reactors: focus on reference electrodes, measurements, corrosion and tribocorrosion issues**
Edited by R. W. Bosch, D. Féron and J. P. Célis

50 **Corrosion behaviour and protection of copper and aluminium alloys in seawater**
Edited by D. Féron

51 **Corrosion issues in light water reactors: stress corrosion cracking**
Edited by D. Féron and J-M. Olive

Preface

The investigation of corrosion at the nano and micro-scales requires the use of appropriate instrumentation and methods that have high spatial resolution to probe material surfaces down to the level of atoms or molecules and that can be used *in situ*, i.e. in a liquid (usually aqueous) environment.

At the nanoscale, scanning probe microscopies, i.e. EC-STM and EC-AFM (electrochemical scanning tunnelling microscopy and atomic force microscopy) are largely used in corrosion research. Functionalisation of the AFM tips may also be one approach to investigate the interactions between atoms, molecules (organic molecules and biomolecules) and the surface.

On the other hand, local electrochemical techniques, SECM (scanning electrochemical microscope), SVET (scanning vibrating electrode techniques), scanning droplet, SKFM (scanning Kelvin probe) allow nano- and micro-scale characterisations to be related. These *in situ* electrochemical microprobes are essential to investigate mesoscopic aspects which remain absolutely necessary as a first control of the nanomaterials and the materials with functionalised surfaces. To complement potential and current characterisations generated by these probes, micro Raman spectroscopy and photoelectrochemical imaging are also useful in identifying the adsorbed species or micro-inclusions on the materials. To date, all these probes operate at or above the **micrometre level scale**. In this book, it has been shown that some attempts are being made to improve the resolution capability of these local techniques to that of the **submicron scale**.

This volume contains a peer reviewed selection of the 25 communications presented during the Workshop '**Local Probe Techniques for Corrosion Research**' which was a part of **EUROCORR 2004, Nice (F), 12–16 September 2004**. This workshop was co-organized by the WP 6 'Surface Science and Mechanisms of Corrosion and Protection' and the WP 8 'Physico-chemical Methods of Corrosion Testing'.

The organizers, R. Oltra, R. Akid (WP8), V. Maurice and P. Marcus (WP6), would like to thank all the authors for their contributions.

1

Local electrochemical methods in corrosion research

R. OLTRA,
CNRS-Université de Bourgogne, France

1.1 Introduction

The phenomenology of localised corrosion, i.e. mainly pitting and stress corrosion cracking, which affects mainly highly resistant materials, has been widely discussed. The basic driving force of localised corrosion is the galvanic coupling of which the dimensional aspect is fixed by a combination of scales which can be described at the electrolyte–metal interface, taking into account the microstructure (including all real-time modification induced for example by applied stresses), the possible chemical changes at the surface of the material, and the electrolyte conductivity contribution, among others factors.

Conventional electrochemical methods have major limitations in measuring the kinetics of a heterogeneous electrochemical process such as localised corrosion because traditional electrochemical kinetic methods are based on the fundamental Butler–Volmer equation which only describes the kinetics of a uniform electrode process and does not permit measurement of the kinetics of heterogeneous electrochemical processes.

For reasons due to either the metallic material, the corrosive medium or the industrial process, the anodic and cathodic zones may take on individual characteristics at the metal–electrolyte solution interface and thus localised corrosion is initiated. The nature of the galvanic coupling in the case of localised corrosion of passive metals takes on properties that differ depending on whether initiation (transient) or propagation (stationary) is under consideration. In the case of stationary conditions, localised corrosion phenomena cause anodes to coexist on the metal surface with the unaffected part behaving like a cathode.

Localised description of the distribution of these reactions has been largely described in the literature in the framework of mixed electrode behaviour. More recently, localised probes have been developed to predict the spatial distribution of these reactions and to quantify the corrosion rate.

1.2 The process of localised corrosion

Firstly, localised corrosion starts mainly in small areas such as precipitates, inclusions and cracks that can be micrometre or submicrometre in scale.[1] The localization of corrosion for example in the presence of inclusions can be induced by applied stresses. Recently this point has been illustrated by Vignal.[2]

Secondly, local electrochemical or chemical process can be induced by metallurgical treatments or even during the early stages of local attack by aggressive solutions. This can be illustrated by local depletion of noble elements like chromium (the well known case of intergranular corrosion of stainless steels) or by more speculative results found recently to explain pitting of stainless steels.[3,4] On the other hand dynamic local change in surface composition due to precipitation of dissolved species coming for example from inclusion dissolution has been demonstrated.[5]

Thirdly, the localised distribution of electrochemical reactions (anodic and cathodic) induces a current circulation in the electrolyte coupled with a local potential gradient; a basic study of all these phenomena has been proposed by Wagner.[6] The dimensional aspects of the electrochemical polarisation in this situation of localised corrosion can be summarised as follows. The effect of the ohmic drop stabilises processes of localised corrosion. In terms of electrochemical kinetics, this means that the ohmic drop becomes part of the electrochemical polarisation of the system. The analysis of this situation described in Fig. 1.1 was performed taking into account:

(i) the Laplace equation: $\Delta^2\Phi = 0$.
(ii) the relation between the current density (j) and potential (E) on each electrode (cathode and anode).

The current density (j) is related to the potential:

(i) by Ohm's law: $J = \frac{1}{\rho}\nabla\phi$ where ρ is the electrolyte resistivity, valid in all electrochemical cells.
(ii) by the electrochemical polarisation: $j = f(E_{\text{surf}})$.

C. Wagner has introduced a parameter L, which takes into account the fact that a knowledge of the two reactions (anodic and cathode) is not sufficient for determining the coupling current of the two electrodes. There is an effect of the electrode size, reflected by the length:

$$L = \kappa\left|\frac{\partial\Delta E}{\partial j}\right|$$

As illustrated in Fig. 1.1, it is then possible to define the characteristic length of the coupling (λ) between anodic and cathodic zones: the nature

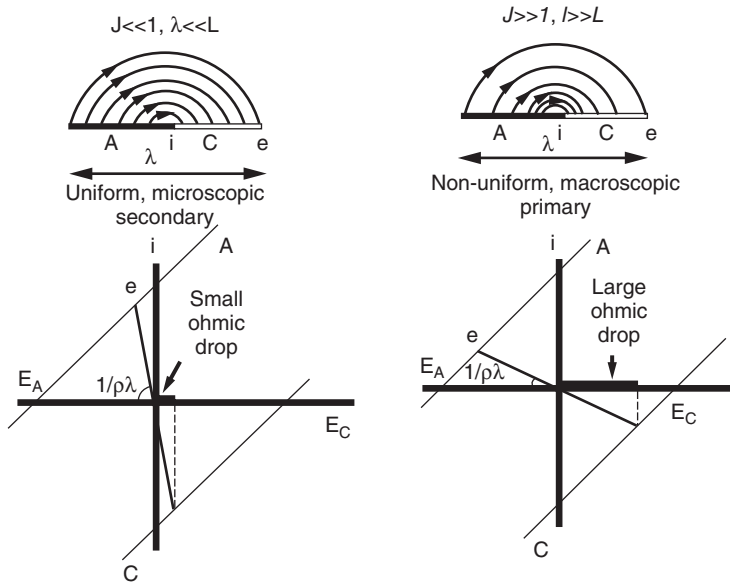

1.1 Concept formulated by the Wagner parameter.

of the coupling will change as a function of the ratio between λ and *L* and therefore will depend on a scale factor. This theoretical approach is both stationary and coplanar and does not take into account changes in e.g. chemistry or the time evolution of the geometry of the corroding site.

The chemical gradient is the fourth parameter which can be also at the origin of the characteristic length of the time evolution of the localised corrosion kinetics. It has been clearly illustrated for example by Smyrl on aluminium alloys[7] showing that the critical length for galvanic coupling is controlled by pH evolution around non-metallic precipitates.

These parameters are not simply metallurgical parameters and clearly demonstrate the need to develop or to apply local probes to reach an *in situ* and a real-time monitoring of the dimensional aspect of the localised corrosion (Fig. 1.2). On the other hand, very close to the surface, changes in solution chemistry can be significant so that the conductivity may be unknown (it depends on supporting electrolyte concentration) and also some of the current is carried by diffusion (assuming no convection here). Thus, as indicated, there will be limitations/uncertainties in the use of Laplace's equation. Consequently, local probing such as the scanning vibrating electrode (SVET) must be applied carefully.

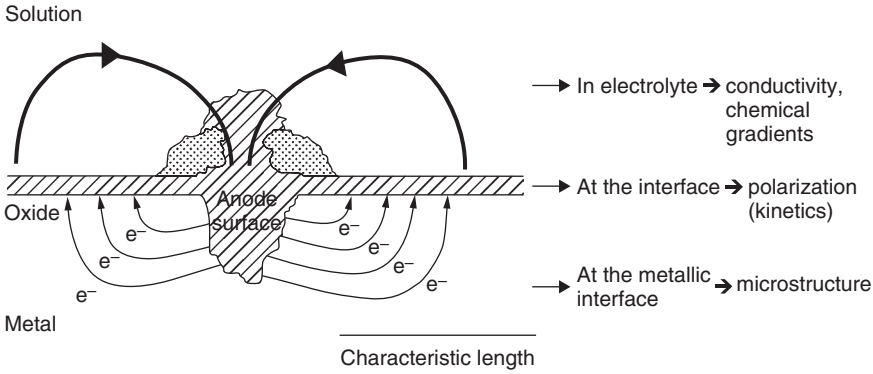

1.2 Parameters affecting the characteristic length controlling galvanic coupling at the metal–electrolyte interface.

1.3 Recent developments in electrochemical probes

Through various examples, the combination of local probes in the case of localised corrosion analysis will be illustrated. Local probes are based on electrochemical, physical or chemical measurements at the metal or metal–electrolyte interface in the case of *in situ* analysis.

Three main groups of techniques can be defined:

(i) *in-situ* probing: the probe is immersed in the bulk electrolyte and a local electrochemical measurement based on conventional electrochemical kinetics is performed. This group includes scanning reference electrode technique (SRET), scanning vibrating electrode technique (SVET) and localised impedance spectroscopy (LEIS).

(ii) the probe is also immersed in the bulk volume but local electroanalytical measurements are performed. It is the case of scanning electrochemical microscopy (SECM) which allows the local chemical evolution of the electrolyte to be defined around a localised corrosion site.

(iii) the probe permits selection of a reduced volume of electrolyte: the microcells techniques.

The most interesting scanning probe in terms of corrosion kinetics is the **SVET** which measures the local current density. This technique initially developed in the biological domain for extracellular current measurement was transferred to corrosion studies by the pioneering work of H. Isaacs in the 1970s.[8] This technique is based on ohmic measurement in the electrolyte between two virtual points defined by the vibration of Pt–Ir microelectrodes (Micro Probe Inc.) which are black platinised. In Isaacs work, the

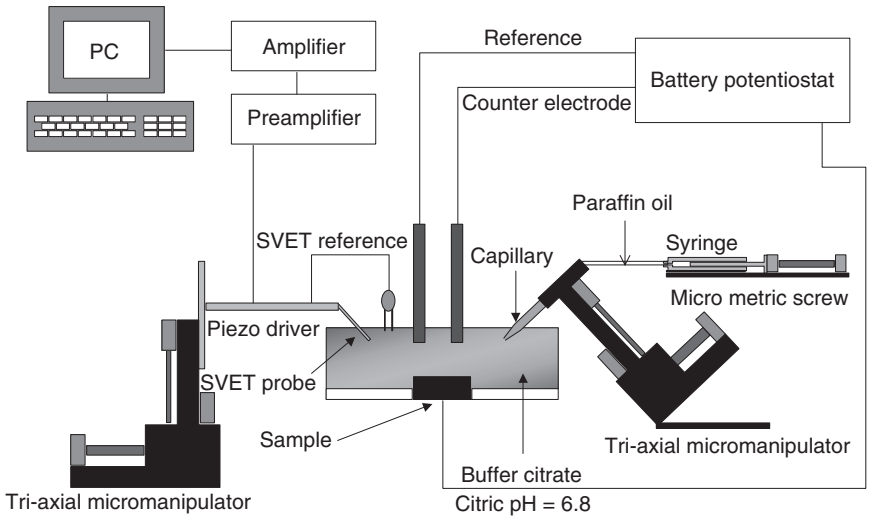

1.3 Experimental setup used for local activation and SVET.

diameter of the sphere of the black platinum deposit was 15 µm, corresponding to a capacitance of about 10 nF. The amplitude of vibration was typically 20 µm, with a frequency around 600 and 200 Hz, respectively, parallel and normal to the sample surface. The potential drop measured by the microelectrode is converted with Ohm's law into a current density value after amplification. The displacement of the microelectrode is performed using a motorised and computer controlled XYZ micromanipulator allowing 0.5 µm steps. Recently,[5] this set-up was combined with a capillary technique in order to be able to follow a well defined site of corrosion which is generated by a local injection of aggressive solution in a buffered solution (Fig. 1.3)

The **scanning electrochemical microscope (SECM)** is a scanned probe microscope (SPM) that has proven to be a powerful instrument for the quantitative investigation of a wide range of processes that occur at interfaces. The probe tip in SECM is an ultramicroelectrode (UME), which typically has a characteristic dimension in the 0.1–10 µm range. The amperometric or potentiometric response of the tip of the UME is recorded as the probe is scanned either normal to the interface of interest (tip approach measurements) or over the interface typically at some fixed height (for imaging purposes) or when held in a fixed position with respect to the substrate (for time-dependent measurements). SECM is mainly used in two modes: feedback or generation collection using a redox mediator in solution in order to characterise the species to be analyzed; this is an analytical technique.

SECM applications have been reported for localised corrosion studies. Still and Wipf[9] investigated the localised corrosion of a passivated iron sample using SECM in generation and collection modes of SECM separately, firstly to induce local generation of aggressive ion and secondly to collect, after initiation, the dissolution current issuing from the dissolving pit. They described experiments in which an iron sample was immersed in a solution of 30 mM trichloroacetic acid solution in phosphate/citrate buffer at pH 6, and passivated at fixed potential for a given period of time. A gold microdisc electrode initially at a potential of 0 V (*versus* a mercurous sulphate electrode (MSE) was positioned close to the surface (within 1 tip radius). The potential of the tip of the electrode was then adjusted to –1.6 V to generate chloride ions by the reduction of the trichloroacetic acid. The equation given for this reaction is

$$Cl_3CCOO^- + H_2O + 2e^- \leftrightarrow Cl_2CHCOO^- + OH^- + Cl^-$$

Current fluctuations at the substrate were observed within a few seconds, indicating pitting corrosion. In addition, the tip current also fluctuated, and correlated well with the sharp changes in current observed at the substrate. This behaviour was attributed to the release of iron species by the sample during the corrosion process, which were then reduced at the tip.

The **micro-electrochemical** setup, proposed by Suter and Böhni,[10] consists of a microcapillary fixed like an objective to the revolving nosepiece of an optical microscope, as shown in Fig. 1.4. The capillary, containing a counter and a reference electrode to perform electrochemical measurements, is filled with the appropriate electrolyte. The ground tip of the micro-

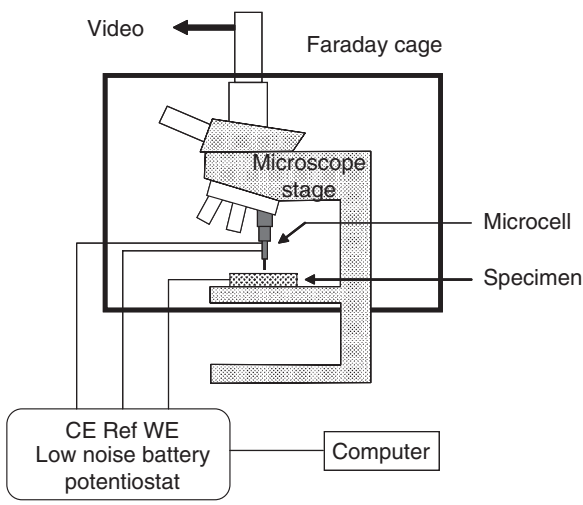

1.4 Schematic setup of the microcell technique.

capillary can be varied from 1 to 1000 μm in diameter. Additionally a sealing layer of silicon rubber is applied to the tip of the capillary to prevent leaking of the electrolyte. This experimental technique not only allows an easy alignment of the micro-electrode to the desired spot of the working electrode, but also limits the electrolytic contact to a small area to obtain current resolutions in the picoampere to femtoampere range. Furthermore, measurements can be performed on metals with a wide range of surface roughness.

1.4 Recent developments in physical and chemical probes

1.4.1 Physical probes

In the field of corrosion, various probes have been derived from basic near field microscopy, AFM and STM, in order to give *in situ* quantitative evaluation of the local corrosion damage. We can mention mainly the EC-STM (STM performed in electrolyte) and the SKPFM (scanning Kelvin probe force microscopy). These techniques will not be described in this chapter.

1.4.2 Chemical probes

Various approaches that have been proposed in the literature are described as a function of local chemical changes. Local surface segregations connected to the microstructure have been mapped by scanning auger microscopy[11] or FIB-SIMS (focused ion beam-secondary ion mass spectroscopy).[3] These techniques can provide characterisation of the material chemistry as a function of the proximity to the precipitates, inclusions, etc. In the case of *in situ* chemical changes at the surface of the material, SECM has been used to define the nature of species involved in local depassivation for example.[12]

Finally, to characterise the chemical gradient in an electrolyte, few studies have been conducted as conventional amperometric sensors are relatively fragile (made of glass and unable to support any kind of contact with a solid surface). One can mention the pioneering work of Park *et al.*[13] trying to apply to corrosion the well-known practice developed in neurobiology.[14] Nevertheless, optical techniques have been proposed to image the chemical change, especially the pH changes, around local corrosion sites.[7,15]

1.5 Combining probes to assess localised corrosion

Schematic drawings ('cartoons') are frequently proposed in the conclusions of various papers which are based on assumptions defined through limited

analysis, e.g. only metallurgical, only electrochemical, only chemical in more reduced cases.

To our knowledge, no complete study has been undertaken of the use of combined microprobe techniques to characterise the changes at the metal–solution interface associated with localised corrosion in corrosion-resistant alloys. To highlight the interest in combination of local probes in elucidating localised corrosion mechanisms some examples can be given in order to illustrate the trends of future works in this domain.

1.5.1 pH and local current density measurements

pH maps have been obtained using liquid membrane glass capillary pH electrodes, fabricated by pulling single-barrelled glass capillaries used to prepare a conventional glass electrode containing ionophore. These pH microelectrodes can be mounted on the SVET system to perform separate chemical measurements assuming the localised corrosion is reproducible or sufficiently stable. To our knowledge, this combination has been applied only to spatially defined galvanic corrosion such as corrosion at the cut-edge of galvanized steel.[16] This combination permits characterisation of the chemical and electrochemical phenomena which occur on the cut edge of galvanized steel. pH variations between 7 and 11 were observed, primarily due to the formation of hydroxyl ions by the cathodic reaction.

More refined work was performed using capillary cells by the Böhni and Suter group. They proposed a combination of capillaries, pH microsensor and microelectrochemical cell to investigate current transients and local pH changes in both non-chloride and chloride solutions. In this work a pH microsensor ($d = 10\,\mu m$) was fixed at the centre of the microcapillary opening ($d = 100\,\mu m$) under a microscope, and the microcapillary cell was placed on any desired location of the metal sample. The tip of the microsensor was positioned 50 mm away from the surface of the samples. With this multifunctional probe, they measured simultaneously the pH and the polarisation curves of local corrosion sites on reduced surfaces containing or not containing MnS inclusions.[17]

Figure 1.5 shows the potential sweep of AISI 304 SS in 0.1 M NaCl solution in which a stable pit growth was obtained at the end of the experiment. This combination of pH and current probes shows that the current (dark line) and pH (dotted line) decreases started about 1 s after the sharp increases in the currents. During the pit growth, the pH of the electrolyte at 50 μm above the pit varied between 2.3 and 2.5.

1.5.2 Microelectrochemical cell and SECM

The objective of the work performed by Paik and Alkire,[18] was to demonstrate the role of adsorbed sulfur species near sulfide inclusions as a driving force for the pitting of nickel.

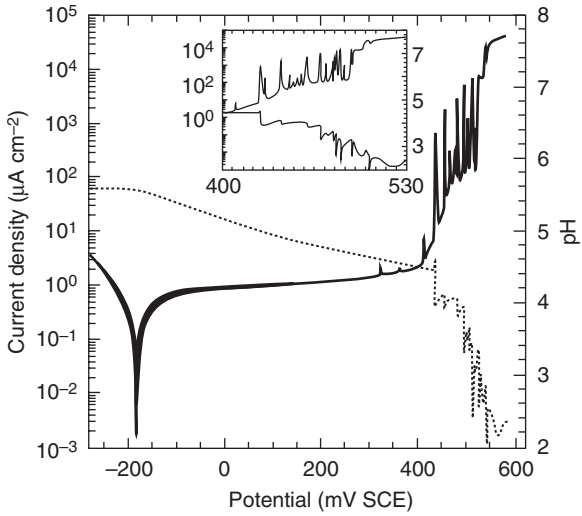

1.5 Stable pitting at a large MnS inclusion on AISI 304, potential sweep from –300 to 600 mV SCE (0.5 mV s^{-1}), 0.1 M NaCl, current (dark line) and pH (dotted line) responses.[17]

From an experimental point of view, electrochemical current–voltage measurements on microarea electrodes were carried out with capillaries of 20–100 microns manipulated so as to cover specific sulfide inclusions, previously characterised by SEM/EDX measurements. On the other hand, the active part of the scanning electrochemical microscopy apparatus, consisted of a carbon fibre tip. The solution used for SECM measurements was 10 mM KI + 0.1 M NaCl. The Ni and C fibre electrodes were independently controlled by two separate potentiostatic circuits. The SECM tip potential (E_{tip}) was held at 0.6 V to reduce I_2 to triiodide.

1.5.3 SVET, AFM and SAM combination

Recently,[5] a combination of SVET, AFM and SAM (scanning auger microscopy) was proposed to study pitting corrosion on a MnS inclusion on 316 L stainless steel. The main originality consists in modifying locally the chemistry in its vicinity by injecting with a microcapillary an aggressive solution of NaCl, H_2SO_4 or HCl (Fig. 1.3). Once a pit appears, the scanning vibrating electrode technique (SVET) is used to follow the current fluctuations in potentiostatic mode (non-conventional use of SVET) over and around the pit when the metal is polarised at a passive potential. In parallel, the activation of a MnS inclusion was studied *ex situ* using Auger electron spectroscopy (AES) and atomic force microscopy (AFM).

It was observed that a single pit can be initiated only when hydrochloric acid is injected, whereas sulfuric acid only partially dissolved the inclusion. A significant enrichment in sulfur is detected around the inclusion by AES, and micropits are observed in the metal at the edge of the inclusion after HCl activation. Anodic zones are detected by SVET around the inclusion, whereas a cathodic current flows from the inclusion. The anodic current was clearly ascribed to the breakdown of passivity induced by adsorbed sulfur species coming from local dissolution of MnS sulfides.

1.6 Conclusions

All these examples have demonstrated that combinations of local probes give deeper understanding of local mechanisms and, in some cases, quantitative measurement of the local corrosion rates. Nevertheless, local probing is mainly performed consecutively, especially in the case of *in situ* analysis. The future trend will be to develop specific multifunctional probes allowing simultaneous measurement of electrochemical, chemical and topographical changes. Recent results obtained in other fields could then be transferred.[19]

Such local probing, to monitor the generation and repassivation of localised corrosion sites on various lateral length scales ranging from nanometers up to tens of microns would be very useful to support the modelling effort to correlate environmental conditions with surface morphological characteristics associated with the onset and stabilisation of localised corrosion.

1.7 References

1 R. C. Alkire and M. Verhoff, *Electrochim. Acta*, 1998, **43**, 2733–2741.
2 V. Vignal and R. Oltra, this volume, ch. 14.
3 M. P. Ryan, D. E. Williams, R. J. Chater, B. M. Hutton and D. S. McPhall, *Nature*, 2002, **145**, 770–774.
4 B. Baroux, D. Gorse and R. Oltra, *Proc. – Electrochem. Soc.*, 2003, 2002–24 (Critical Factors in Localized Corrosion IV), 335–346.
5 B. Vuillemin, X. Philippe, R. Oltra, V. Vignal, L. Coudreuse, L. C. Dufour and E. Finot, *Corros. Sci.*, 2003, **45**, 1143–1159.
6 C. Wagner, *J. Electrochem. Soc.*, 1951, **98**, 116–128.
7 M. A. Alodan and W. H. Smyrl, *J. Electrochem. Soc.*, 1997, **144**, L282–284.
8 H. S. Isaacs, *J. Electrochem. Soc.*, 1988, **135**, 2180–2183.
9 J. W. Still and D. O. Wipf, *J. Electrochem. Soc.*, 1997, **144**, 2657.
10 T. Suter and H. Böhni, *Electrochim. Acta*, 1997, **42**, 3275–3280.
11 M. A. Baker and J. E. Castle, *Corros. Sci.*, 1993, **34**, 667–682.
12 C. H. Paik, H. S. White and R. C. Alkire, *J. Electrochem. Soc.*, 2000, **147**, 4120–4124.

13 J. O. Park, C.-H. Paik and R. C. Alkire, *J. Electrochem. Soc.*, 1996, **143**, L174–L176.
14 R. Wen and B. Oakley, *J. Neurosci. Methods*, 1990, **31**, 207–213.
15 H. S. Isaacs, *Corrosion*, 2000, **56**, 971–982.
16 K. Ogle, V. Baudu, L. Garrigues and X. Philippe, *J. Electrochem. Soc.*, 2000, **147**, 3654–3660.
17 J. O. Park and H. Böhni, *Electrochem. Solid-State Lett.*, 2000, **3**, 416–417.
18 C. H. Paik and R. C. Alkire, *J. Electrochem. Soc.*, 2001, **148**, B276–B281.
19 C. Krantz, G. Friedbacher, B. Mizaikoff, A. Lungstein, J. Smoliner and E. Bertagnolli, *Anal. Chem.*, 2001, **73**, 2491–2500.

2

Observation of self healing functions on the cut edge of galvanised steel using scanning vibrating electrode technique (SVET) and pH microscopy

K. OGLE, Ecole Nationale de Chimie de Paris, France,
S. MOREL and D. JACQUET, Arcelor R&D, France

2.1 Introduction

'Self-healing' properties are important for the anticorrosion performance of galvanised steel. This is especially important at the cut edge of galvanised steel where the steel substrate is exposed directly to the atmosphere. If the face of the sample is painted, the ratio of anode to cathode surface area is equal to the ratio of the thickness of the zinc coating to that of the steel substrate. For many galvanised steel products, this can be on the order of 1/100 and is insufficient to assure galvanic protection for an extended length of time. The good anti-cut edge corrosion properties of state-of-the-art galvanic coatings is due in part to the formation of the inhibiting films of zinc-based corrosion products on the exposed steel surface. The inhibiting nature of these films may be enhanced by the addition of water-soluble inhibiting pigments. We refer to this precipitation/passivation phenomenon as a 'self-healing' mechanism.

The formation of inhibiting films depends upon the local chemical and electrochemical environment. This environment is, in turn, determined by the geometry of the defect, the composition of the coatings and the chemistry of the electrolyte. The geometry of the defect is important as changes in the thickness of the steel substrate or zinc coating will have important consequences on the distribution of current and, therefore, the precipitation of corrosion products.

The nature of the electrolyte phase and the composition of the metallic coating will determine the nature of the species present in solution and the composition and solubility of the solid phases that might precipitate on the cathodic surface. The majority of corrosion tests use NaCl solutions, but other species such as ammonium and sulfate may also be important factors in atmospheric corrosion in some environments and are included in the electrolyte phase of certain corrosion tests. One such test is the Prohesion™ test (ASTM G 85) that has an electrolyte containing 0.05% NaCl and 0.35% $(NH_4)_2SO_4$ at 35°C and is operated in cycles of one hour wet, one hour dry.

The test is generally considered to be a less severe form of the more common salt spray test because of the more dilute electrolyte and the fact that the sample is not continuously wet; but anecdotal evidence has suggested that cut edge corrosion of galvanized steel may be more severe in this test than in similar NaCl-only based tests.

The goal of this work was to apply localised electrochemical methods to characterise the behaviour of galvanised steel in NaCl and NaCl + 0.35% $(NH_4)_2SO_4$ solutions. For this work, scanning pH microscopy[1] and the scanning vibrating electrode technique (SVET) were used. Both of these techniques have been successfully applied to cut edge corrosion in previous studies.[1–7] The SVET and pH microscopy are well suited for the characterisation of galvanic coupling reactions with a spatial resolution consistent with the form of the cut edge environment. In previous work,[1] the SVET and scanning pH microscopy were used to characterise the electrochemical and chemical environment on the cut edge of galvanised steel in a NaCl solution. The results showed that inhibiting film formation occurs at the interface between anodic and cathodic regions, probably brought about by pH variation observed under these conditions. These results have been confirmed by Tada *et al.*[8,9] who used different methods and electrode geometries and who also measured the Zn^{+2} concentration around the zinc anodes. In the present work, these results are confirmed for cut edge electrodes of different thicknesses in the NaCl solution and are extended to measurements in an ammonium sulfate containing electrolyte as used in the Prohesion™ test.

2.2 Experimental method

The scanning vibrating electrode system (SVET) and the micro-capillary ion selective electrodes have been previously described,[1] including details of fabrication, calibration, and their applicability to cut edge phenomena in general. Briefly, a commercial SVET system from Applicable Electronics was used. A Pt–Ir wire electrode, with a Pt black tip approximately 20 μm in diameter was used as the vibrating probe. Measurements were performed at 200 μm from the surface using a 0.5-s integration period. The SVET response was calibrated in the pure electrolyte using a stainless-steel point source.

The pH microelectrodes were fabricated in-house from single-barrelled glass capillaries (OD = 1.5 mm), pulled to form an approximately 5 μm tip. The ionophore was a hydrogen I cocktail B from Fluka, with a given functional pH range of 5.5 to 12 and the electrodes were calibrated using standard pH buffer solutions.

The metallic samples consisted of commercial hot dip galvanised steel. Steel thicknesses of 0.9, 1.5, 2.0 and 2.5 mm were used with a constant zinc

Table 2.1 Composition of electrolytes used in this work with conductivity and pH under aerated and non-aerated conditions

	Composition	R/Ω cm	pH / air	pH / N_2
30 mM NaCl	0.03 M NaCl	303	5.7	6.5
Prohesion™ test	0.0086 M NaCl 0.027 M $(NH_4)_2SO_4$	152	5.4	5.6

coating at 275 g m^{-2} corresponding to approximately 25 µm per side by optical microscopy. The samples were cut with a mechanical press into a 1 cm band. They were then mounted in Araldite resin and polished successively to a 1 µm diamond finish. Electrolytes were composed of reagent grade products and deionised water (>10 MΩ cm). Experiments were performed in two different electrolytes. The primary characteristics of the two electrolytes are given in Table 2.1.

2.3 Results and discussion

2.3.1 Visual observation of phenomena

As cut edge electrodes are exposed to 30 mM NaCl and Prohesion™ test electrolyte, a precipitated film very rapidly forms a wavy pattern on the surface of the steel during the first few seconds of the exposure. The corrosion products then spread out and thicken slowly with the initial pattern still visible after 2 h of exposure. After 18 h of exposure, the surface is visibly covered with a film. Different behaviour is observed for the ammonium sulfate solution. In this case, very little corrosion product precipitation is observed during the early stages of the reaction although a complete coverage is obtained after 18 h of exposure.

2.3.2 Raman analysis of corrosion products

The corrosion products formed in the NaCl solution are well known to be zinc hydroxychloride $Zn_5(OH)_8Cl_2$ and $Zn(OH)_2$.[10,11] The nature of the corrosion products in sulfate containing media has been less well studied although a database of the major products has been obtained.[12] Figure 2.1 shows the Raman spectrum obtained for the corrosion products on the cut edge in the Prohesion™ test electrolyte. This spectrum is representative of the general class of zinc hydroxy sulfate species – the broad high frequency peak is due to the elongation of OH groups in water and hydroxide ions; and the low frequency features are due to the SO_4^{2-} ion. The previously

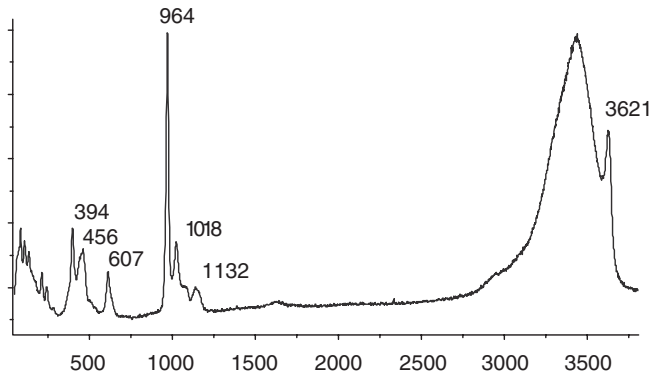

2.1 Raman spectrum of corrosion products obtained after 32 h of immersion in the Prohesion™ test electrolyte.

cited work[12] gives spectra for $ZnSO_4.3Zn(OH)_2.nH_2O$ with n variable between 1 and 5; as well as $NaZn_4Cl(OH)_6SO_4.6H_2O$ and $Zn_4Cl_2(OH)_4SO_4.5H_2O$. The spectrum in Fig. 2.1 is entirely consistent with $ZnSO_4.3Zn(OH)_2.5H_2O$ and does not show some of the major features of the zinc chlorohydroxide sulfates.

2.3.3 Galvanic corrosion rate measurement

The average value of zinc dissolution was measured in the Prohesion™ test electrolyte by exposing the sample to 4 ml for 24 h. Following this exposure, the quantity of Zn and Fe dissolved in the electrolyte was measured by ICP atomic emission spectroscopy using standard analytical techniques. The Fe content was consistently below the detection limit of this technique and no red rust was visible on the cut edges indicating that the corrosion rate of the steel was minimal. The Zn concentration was used to calculate the average rate of zinc corrosion expressed in current by use of Faraday's law for the reaction.

$$Zn \rightarrow Zn^{2+} + 2e^- \qquad [2.1]$$

The results are shown in Fig. 2.2 as a function of steel thickness for these samples. It is clear that the dissolution rate is a direct linear function of the steel thickness. This demonstrates that the reaction rate is controlled by the cathodic surface and is consistent with the rate-limiting step being the diffusion-limited reduction of dissolved oxygen on the steel surface. Localised polarisation curves on the anodic and cathodic sites of the cut edge also supported this model.[1]

$$O_2 + 2H_2O + 4e^- \rightarrow 4OH^- \qquad [2.2]$$

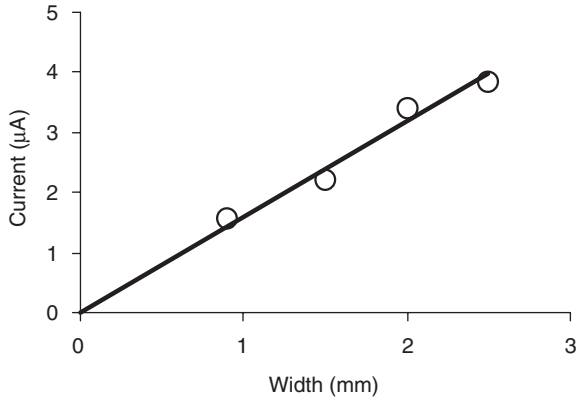

2.2 Variation of average galvanic coupling current over 24 h exposure to 4 ml of the Prohesion™ test electrolyte. The linear relationship demonstrates that the reaction is under cathodic control and most likely limited by oxygen diffusion.

2.3.4 Variations of anodic and cathodic current on cut edge

Typical current cartographies for the various electrolytes and samples were measured after 15 min of immersion in the centre of the cut edge electrode for a 3.5 mm × 4.0 mm rectangle. The current distribution was very different in the two electrolytes. In the ammonium sulfate solution, the zinc appeared to be uniformly active and the cathodic reaction was evenly distributed on the steel surface. Although the anodic current was uniform over the active zinc edge, five samples out of seven showed a situation where only one side of the galvanised steel cut edge was active despite the fact that both sides were nominally identical. We attribute this to slight differences in sample preparation although we were unable to determine a specific origin of this behaviour.

By contrast, in the NaCl electrolyte both anodic and cathodic activity showed significant non-uniformities. The anodic activity appeared to be localised in specific areas of the zinc surface on the edge of the sample. The zinc-based corrosion products appeared on the steel surface in a wavy pattern; a clear correlation was observed between the formation of corrosion products and the current distribution. The dense part of the corrosion product contours closely followed the iso-current contours between –10 and –30 μA cm^{-2}, forming rings around the anodic zones for the situation in which the cathodic current was in the centre of the cut edge sample. In a previous publication,[1] it was suggested that this was due to the interaction between Zn^{2+} formed at the anode (reaction 1) and OH^- formed at the

cathode (reaction 2) by the precipitation reaction. Zinc oxides and hydroxides show a minimum solubility between pH 9 and 10.

Several interesting trends may be established by inspection of the three profiles. It is clear that the thickness of the steel sample influences the corrosion product distribution. For the widest, 2.0-mm sample, very broad contours are observed consistent with the spreading out of the cathodic reaction on the steel surface. The 1.5-mm samples show a narrower corrosion product distribution while the 0.9-mm curve shows a very narrow wavy pattern. Under these circumstances, the corrosion products no longer circle the anodic reaction since the cathodes and anodes are no longer in the same region of the cut edge. These trends were confirmed for the seven different samples measured.

These results suggest that, in the NaCl solution, the cathodic reaction is somehow pushed away from the anodic reaction. For the wider samples, the cathodic reaction reaches its maximum in the centre of the cut edge, whereas for the 0.9-mm sample, the cathodic reaction is pushed down from the anodic zone. (The cartography shows that the entire upper zone appears anodic, but this is due to the poor spatial resolution of the SVET. In fact, the anodes are entirely localised on the zinc surfaces at the edges of the sample, as indicated by the absence of red iron oxide formation during these experiments.)

Figure 2.3 gives single line scans across the cut edge for the cartographies. Note that in the ammonium sulfate electrolyte (5A), the anodic and cathodic reactions are quite close to one another. The leading edge between the anodic and cathodic regions is very abrupt and, in many cases, drops from a maximum anodic activity to a maximum cathodic activity over a distance of only a few hundred micrometres. However, the anodic peak maximum drops off slowly to the cathodic minimum, and the anodes and cathodes are in general separated by a much larger distance than in the ammonium sulfate electrolyte. This result demonstrates the inhibiting nature of the corrosion products produced in the NaCl solution.

2.3.5 pH distributions on cut edge

A marked difference was observed between pH distributions measured over the 0.9 mm and 2.0 mm surface in both the Prohesion™ and the NaCl electrolyte after 15 min of immersion. In the ammonium sulfate electrolyte, only slight pH variation was observed despite the very significant anodic and cathodic currents detected by the SVET.

Large pH variations were obtained in the NaCl solution ranging from near neutral over the resin and in the anodic zones, to slightly above 10 in cathodic regions. The pattern of precipitated corrosion products was as observed for the SVET experiments: the corrosion products appeared in

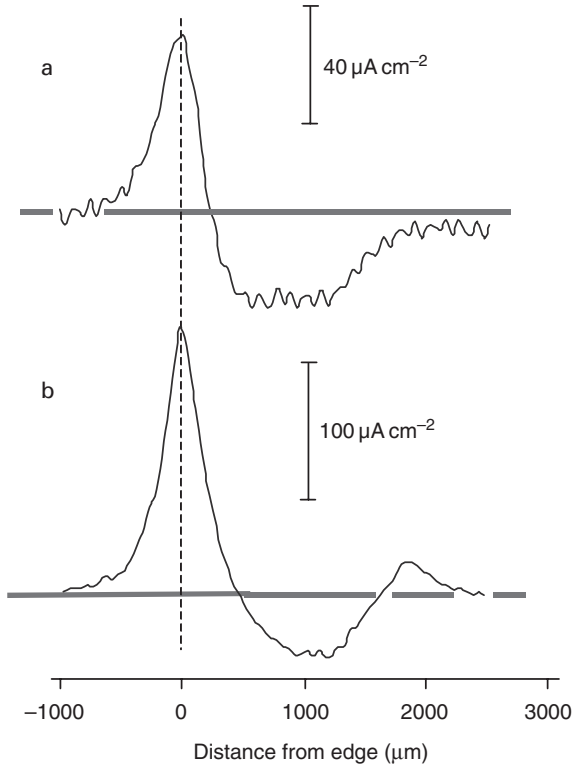

2.3 Single line scans from the current cartographies of Fig. 2.2: *a* 1.5 mm sample in Prohesion™ test electrolyte; *b* 2 mm sample in NaCl electrolyte.

contours that seem to follow closely the iso-pH lines between 8 and 9 pH units. The thickness of the contours varied with the steel thickness as previously described.

The pH changes are almost exclusively related to the production of hydroxide by equation 2.2, the hydrolysis of Zn^{2+} being minimal.[1,8,9] Since the cathodic reaction is quite intense in the Prohesion™ test electrolyte, the absence of a significant pH increase is probably due to a buffering effect associated with the ammonium ion. This effect is demonstrated by the experimental titration curves of Fig. 2.4. These experiments involved the addition of 20 μl volumes of 0.01 M NaOH to 100 ml of the Prohesion™ test electrolyte bringing the pH into the range of 8 to 10. For the Prohesion™ electrolyte, significantly larger quantities of hydroxide must be generated at the interface to give a pH increase into the 10–11 range as compared with the NaCl electrolyte.

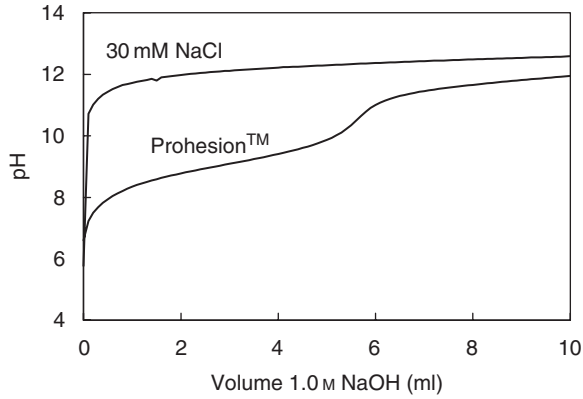

2.4 Titration curves for 100 ml of 30 mM NaCl and the Prohesion™ test electrolyte with 1.0 M NaOH.

2.3.6 Equilibrium considerations

To better interpret the results of this work in terms of the equilibrium chemistry of the two electrolytes, calculations were performed using the HYDRA-MEDUSA software and equilibrium database.[13] This database contains solubility data for zinc hydroxides, oxides, chlorides, hydroxychlorides, hydroxysulfates, and chlorohydroxysulfates as well as the sequential formation constants for ammonia and hydroxide complexes. Figure 2.5 gives the fraction of species in the two electrolytes as a function of pH for 1 mM Zn^{2+} concentration. As the pH increases, the initial precipitation reaction is $Zn_4(OH)_6SO_4$ in the Prohesion™ test electrolyte in agreement with the Raman results, and $Zn_5(OH)_8Cl_2$ in the NaCl electrolyte in agreement with previous reports. Above pH 10, $Zn(OH)_2$ is the major stable phase in both electrolytes. This diagram demonstrates that the increase in solubility in the Prohesion™ test electrolyte is due to the formation of $Zn(NH_3)_x^{2+}$, where $x = 2$ to 4, between pH 8 and 10. Above pH 10, the dominant species are the $Zn(OH)_x^{2-x}$, $x = 3$ to 4 in equilibrium with solid $Zn(OH)_2$.

Figure 2.6 shows the variation of the log-solubility of Zn^{2+} as a function of pH, determined for the two electrolytes. The solubility is calculated from the sum of the various Zn^{2+} complexes in solution. The formation of solid phases is indicated by a decrease in solubility. Several important points become evident from this data. The letters refer to the indicated points on the solubility – pH curve.

(i) The pH for the onset of precipitation is shifted to a higher value of pH. This is explained by the stability of the $ZnSO_4$ complex in solution.

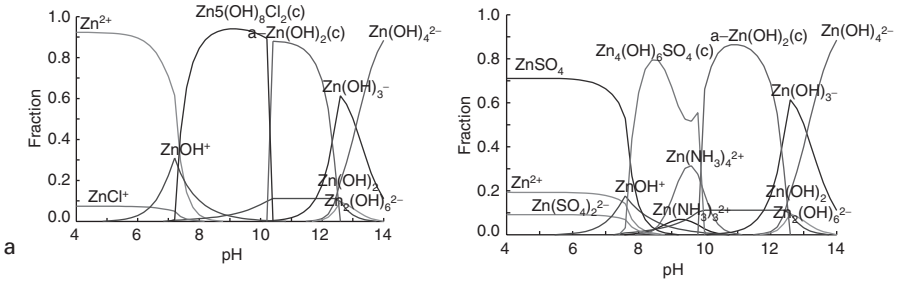

2.5 Distribution of Zn^{2+} species showing dominant solid phases at various pH values: *a* in 30 mM NaCl *b* in Prohesion™ test electrolyte.

(ii) The minimum solubility of the solid zinc hydroxysulfate phase in Prohesion™ electrolyte is still an order of magnitude larger than that of the hydroxychloride phase in 30 mM NaCl.

(iii) The hydroxysulfate phase becomes increasingly soluble between pH 8 and 10, showing a maximum around pH 9.3 due to the formation of NH_3 complexes.

(iv) Finally, above pH 10, the solid $Zn(OH)_2$ phase dominates and the solubility increases with subsequent increase in pH. Beyond point (d), the two electrolytes show identical behaviour.

These results show that the precipitation of zinc-based corrosion products occurs at a higher pH in the Prohesion™ test electrolyte than in the NaCl solution. This is indicated by the onset of the solid phase and by the fact that the solubility of Zn^{2+} is about an order of magnitude higher until a pH > 10, at which point the two electrolytes show similar behaviour (Fig. 2.6).

2.4 Conclusions

This work has demonstrated that in the NaCl solution, there is a clear correlation between the patterns of precipitated corrosion products, the presence of local anodes and cathodes, and the variations of pH on the cut edge of galvanised steel. The corrosion products precipitate in specific regions of iso-pH between 8 and 9, corresponding to a corrosion current between 0 and $-10\,\mu A\,cm^{-2}$. This observation may be attributed to the fact that $Zn(OH)_2$ has a minimum near pH 9.2 and becomes more soluble at higher pH due to the formation of $Zn(OH)_4^{-2}$. The non-uniformity of the anodic and cathodic current distributions in this electrolyte suggests an inhibiting effect of the corrosion products.

In the ammonium sulfate solution, the situation is quite different. Despite significant anodic and cathodic activity, very little pH change is detected

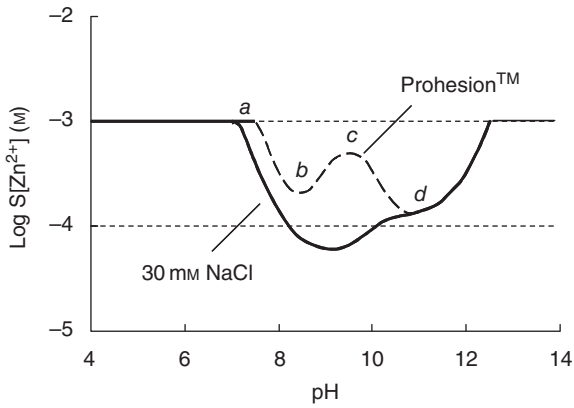

2.6 Calculated Zn^{2+} solubility for 0.001 M Zn^{2+} initial concentration in 30 mM NaCl (solid) and the Prohesion™ test electrolyte (dashed).

and no precipitation is observed at short times. These observations can be interpreted in terms of the increased solubility of Zn^{2+} ion in the Prohesion™ test electrolyte. This is due to two factors:

- A buffering effect due to the ammonium ion that leads to smaller pH changes due to the cathodic oxygen reduction.
- The increased solubility of Zn^{2+} in electrolytes containing complexing species such as ammonium and sulfate.

In more general terms, these results demonstrate that the self-healing mechanisms of galvanised steel are closely linked to the electrolyte chemistry. The presence of $(NH_4)_2SO_4$ in the Prohesion™ test electrolyte, for example, selectively turns off the self-healing mechanism. Failure to understand and account for these mechanisms when considering the results of accelerated corrosion testing may lead to erroneous conclusions.

2.5 References

1 K. Ogle, V. Baudu, L. Garrigues and X. Philippe, *J. Electrochem. Soc.*, 2000, **147**, 3654–3660.
2 K. Ogle, S. Morel and H. Meichelbeck, 5th International Conference on Zinc and Zinc Alloy Coated Steel Sheet, Brussels, Belgium, June, 2001, p. 361.
3 K. Ogle and S. Morel, 'Galvanized steel for saving environment and resources', 144th ISIJ Meeting, International Session, Osaka, Japan, November 3, 2002.
4 H. N. McMurray, S. M. Powell and D. A. Worsley, *Br. Corros. J.*, 2001, **36**, 42–48.
5 S. Bohm, M. Challis, T. Heatley and D. A. Worsley, *Trans. IMF*, 2001, **79**,16–21.
6 F. Zou, C. Barreau, R. Hellouin, D. Quantin and D. Thierry, *Proceedings of the 3rd International Converence on Zinc and Zinc Alloy Coated Steel Sheet, Galvatech'95*, Japan, 1995, p. 837.

7 D. A. Worsley, A. Belghazi and S. M. Powell, *Ironmaking Steelmaking*, 1999, **26**, 387–392.
8 E. Tada, K. Sugawara and H. Kaneko, *Electrochim. Acta*, 2004, **49**, 1019–1026.
9 E. Tada, S. Satoh and H. Kaneko, *Electrochim. Acta*, 2004, **49**, 2279–2285.
10 M. C. Bernard, A. Hugot le Goff, D. Massinon and N. Phillips, *Corros. Sci.*, 1993, **35**, 1339–1349.
11 A. Hugot le Goff, M. C. Bernard and N. Phillips, *J. Electrochem. Soc.*, 1995, **142**, 2167–2170.
12 C. Merlin, PhD Thesis, Université Henri Poincaré, Nancy I, 1999.
13 I Puigdomenech, *HYDRA MEDUSA*; *make equilibrium diagrams using sophisticated algorithms*; Royal Institute of Technology, Stockholm, Sweden, 2001.

3

Application of scanning vibrating electrode technique (SVET) and scanning droplet cell (SDC) techniques to the study of weld corrosion

R. AKID, P. ROFFEY, D. GREENFIELD and D. GUILLEN, Sheffield Hallam University, UK

3.1 Introduction

The incorporation of welded joints enabling the fabrication of structures continues to be a popular strategy used by engineers at the design stage. Such an approach is entirely acceptable subject to an understanding of the implications of the joining technique on the resulting structural and corrosion behaviour of the materials used. Conventional fusion welding causes the joint materials to experience complex heating regimes, where at the weld itself, the material cools from a molten state, through to the parent plate which experiences a thermal gradient from room temperature through to its melting point. The implication of this process is that a weld joint has a complicated microstructure ranging from an as-cast structure through to the original microstructure of the original materials making up the weld joint. In addition to this, the welding process contributes to the development of residual stresses within the joint. Residual stresses not only affect the mechanical properties of the joint but also the corrosion response.[1] Therefore welded joints can suffer from a reduction in structural integrity not only from the standpoint of their structural strength and fatigue performance, but also from the response of the heterogeneous microstructure of the joint to the effect of the environment, i.e. corrosion.

Given that major microstructural changes and changes in local residual stress state do occur during welding, this paper addresses the use of selected corrosion test methods, including the scanning vibrating electrode technique, SVET, and the scanning droplet cell technique, SDC, to evaluate the localised corrosion behaviour of welded joints.

3.1.1 Scanning vibrating electrode technique

Electrochemical scanning techniques are based broadly upon the assumption that localised corrosion, where anodic and cathodic processes take

place at separate sites, can be represented as point sources. The electric field generated by sites of localised corrosion consists of equi-potential lines which can be measured and graphically represented as a contour map. SVET techniques rely on the spatial separation of anodic and cathodic activity on a surface which lead to small variations in potential and the generation of ionic flow within the electrolyte. The potential gradient resulting from actively corroding sites may be measured using a vibrating probe system, where the vibrating probe, typically a Pt wire, oscillates between two positions above or parallel to the surface.[2] This experimental approach has now found favour over that of single- and twin-probe systems, namely the scanning reference electrode techniques (SRET), as it has the direct advantage that the signal-to-noise ratio is significantly improved.[3,4]

For an anodic site acting as a point in space (PIS) current source, the electric field, E (V), at any point (x, y, z) in solution is given by:[5]

$$E = \frac{I}{2 \cdot k \cdot \pi \cdot \sqrt{x^2 + y^2 + z^2}} \qquad [3.1]$$

where I is the current through the PIS (mA) and x, y and z are the distances to the PIS in their respective axes (cm).

The vibrating probe provides a direct measure of the electric field or, from Ohm's law, the component of current at the point in the direction in which the electrode vibrates. Only one direction is considered; that is the vibration perpendicular to the surface containing the current source.[5] The normal field strength (F) can be obtained from equation 3.1 by differentiation with respect to z, as shown in equation 3.2.

$$F = \frac{\mathrm{d}E}{\mathrm{d}z} = -\frac{I \cdot z}{2 \cdot k \cdot \pi \cdot \left(x^2 + y^2 + z^2\right)^{1.5}} \qquad [3.2]$$

The maximum field strength (F_{max}) at height z occurs directly over the current source,[5] as follows:

$$F_{max} = \frac{\mathrm{d}E_{max}}{\mathrm{d}z} = -\frac{\mathrm{I}}{2 \cdot k \cdot \pi \cdot z^2} \qquad [3.3]$$

The factors affecting the maximum output signal, sensitivity and resolution have been reported elsewhere.[6] For brevity, the operational parameters that affect the SVET signal include:

(i) Time constant (TC): the output time constant of the lock-in amplifier.
(ii) Speed (v): the probe scan speed in the x-direction.
(iii) Vibration amplitude (VA): the vibration amplitude of the measurement probe in μm, peak-to-peak value.

(iv) Probe–sample distance: operator and specimen surface dependent, being the distance of the probe above the sample surface.
(v) Scan mode, continuous sweep or step.

3.2 Materials and experimental methods

3.2.1 Materials

The following welded joints were selected for investigation.

(i) carbon steel–carbon steel,
(ii) carbon steel, laser weld
(iii) copper–stainless steel–aluminium bronze (CuSSAB)

3.2.2 Microstructural evaluation

Metallographic examination was carried out on selected samples to evaluate the microstructures associated with each of these joints. Carbon steel joints were etched in 2% Nital. Optical and scanning electron microscopy (Phillips XL40, SEM) were used to obtain images of the sectioned welds.

3.2.3 Electrochemical measurements

The corrosion tendency of the different regions of the welded joints was determined from measurements of corrosion potential (E_{corr}) at selected sites of the weld joint using a capillary electrode covering an area around 2–3 mm. Unless stated, all quoted corrosion potential measurements are based upon the use of a saturated calomel electrode (SCE).

3.2.4 Scanning droplet cell

SDC measurements were made using a Uniscan® 270 scanning droplet cell to evaluate the open circuit potential along cross sections of the welds. This technique involved scanning a continuously refreshed droplet, in both x and y directions, over the surface of the weld in a step scan mode making local measurements every 250 μm. This method generated a 2D area map of the corrosion potential (versus Ag/AgCl reference electrode) of the weld. Maps were generated in either 0.1M NaCl or an alkali solution, as described in the following section.

3.2.5 SVET measurements

SVET measurements of individual weld joints were made using a Uniscan® SVP100 system. Corrosion mapping was conducted at room temperature in

either 0.1M NaCl (samples a and b) or an alkali-based solution, pH 8.3 and conductivity of 1619 $\mu S\,cm^{-1}$ (sample c). Based upon an evaluation of the optimum parameter settings for output signal and resolution,[6] the following experimental settings were used: step scan mode, probe–sample distance 100 μm and a probe vibration amplitude of 30 μm. Colour contours on the original SVET maps (Fig. 3.1–3.4) illustrated the anodic and cathodic activity on the surface.

3.3 Experimental results

3.3.1 Carbon steel–carbon steel

Measurements of corrosion potential were made for each of the different microstructural zones of the welds, namely parent plate (PP), heat affected zone (HAZ) and weld metal (WM). The results are given in Fig. 3.1. Also shown in this figure are SVET and SDC corrosion potential maps for the two steels. Cross-section photographs are shown to illustrate the location of the measurements.

3.3.2 Carbon steel laser weld

The results of metallographic examination, electrochemical measurements and SVET mapping for the laser welded joint are given in Fig. 3.2.

3.3.3 Copper–stainless steel–aluminium bronze (CuSSAB) welded joint

The optical micrograph, individual E_{corr} values, SVET at open circuit potential and SDC maps for the CuSSAB welded joint are given in Fig. 3.3. Additional SVET scans were carried out on this joint, being conducted at anodic potentials of +50 mV and +100 mV. The results of these scans are presented in Fig. 3.4. The results of SEM examination of the sample after corrosion testing are shown in Fig. 3.5. In order to identify whether or not this welded joint was susceptible to pitting and to compliment the SVET scans conducted at anodic potentials, conventional dc polarisation curves were obtained. Fig. 3.6a presents the corrosion response at room temperature and at 40°C, while Fig. 3.6b shows the effect of increasing chloride ion concentration at room temperature.

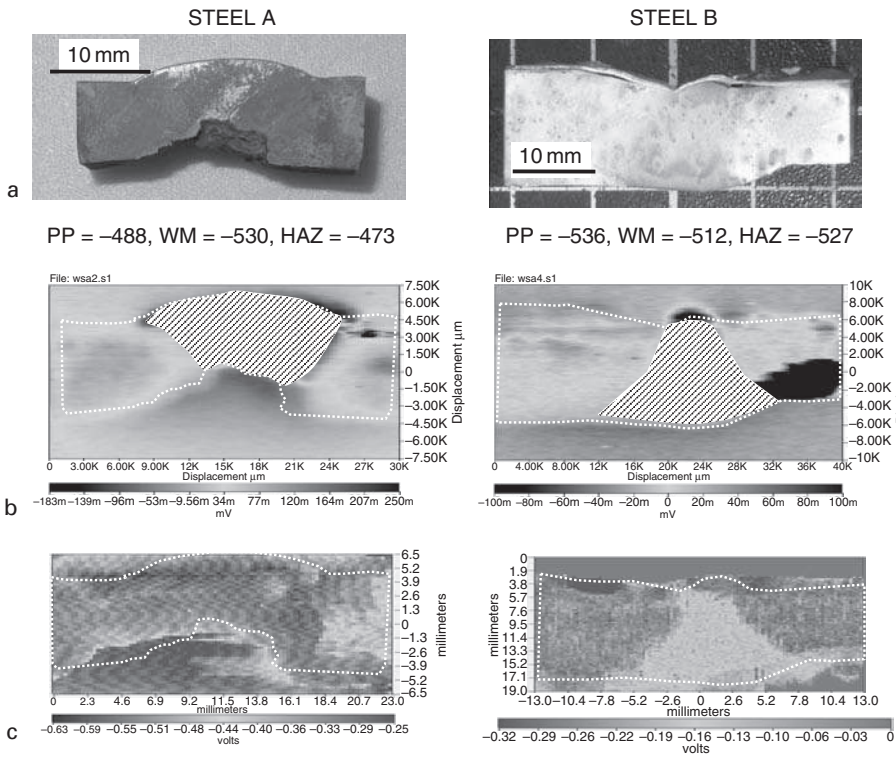

3.1 *a* Micrographs for steels A and B with individual PP, WM and HAZ E_{corr} measurements (mV vs. SCE); *b* SVET maps; *c* continuous scanning droplet E_{corr} measurements (V vs. Ag/AgCl). Note: dotted lines represent outline of samples and areas demarcated by continuous lines represent weld zone.

3.4 Discussion

3.4.1 Carbon steel–carbon steel weld

SVET mapping of the carbon steel–carbon steel joints A and B showed significant differences in response, as presented in Fig. 3.1b. Steel A showed highly localised attack of the weld metal, while steel B showed a lower degree of attack of the weld region and more general corrosion across the joint as a whole. Note in Fig. 3.1b, steel B, that the intense activity at the top of the weld is associated with corrosion products that have developed due to crevice corrosion between the steel and the delaminated coating. The intense activity at the lower right hand edge of the sample is an artefact wherein the SVET probe came into contact with the specimen during

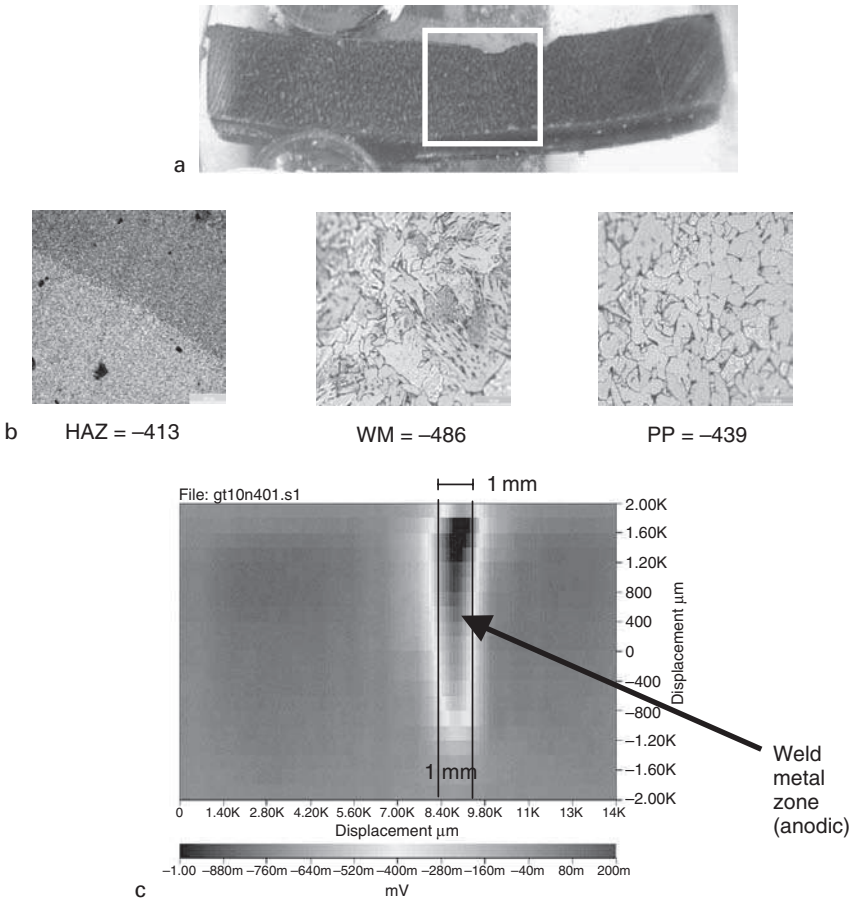

3.2 *a* Weld cross section (SVET measurements taken within boxed area); *b* micrograph with E_{corr} measurements (in mV); *c* SVET map for laser welded joint.

scanning. The localised corrosion response was somewhat unexpected given that the nominal chemical composition of the parent plates of the two steels was similar. Further analysis using the EDX elemental analysis facility of the SEM showed there to be compositional differences between the PP, HAZ and WM, see Table 3.1. For example, when the ratio of elements was compared with the PP, i.e. PP ratio equal to unity; weld A contained 70% less C and 650% more aluminium at the bottom section of the weld; note the severe localised attack in the weld zone of steel A, as shown in Fig. 3.1. The welded joint of steel B revealed much smaller compositional gradients particularly for C and Al.

SDC scans of the two welds somewhat reflected the results obtained from the SVET scans in that steel A exhibited a much more active weld zone

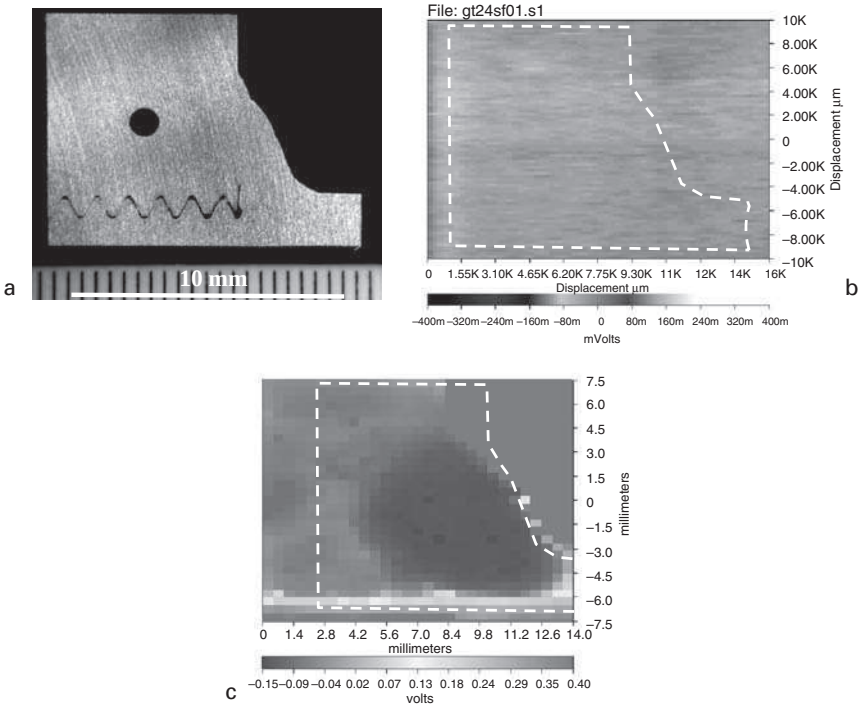

3.3 *a* Micrograph and individual E_{corr} values (in mV *vs.* SCE) AB = –15, SS = 101, Cu = –15, mixed potential CuSSAB = –40; *b* SVET area map of the CuSSAB welded joint at open circuit potential; *c* SDC E_{corr} measurements (mV *vs.* Ag/AgCl) using a scanning droplet cell.

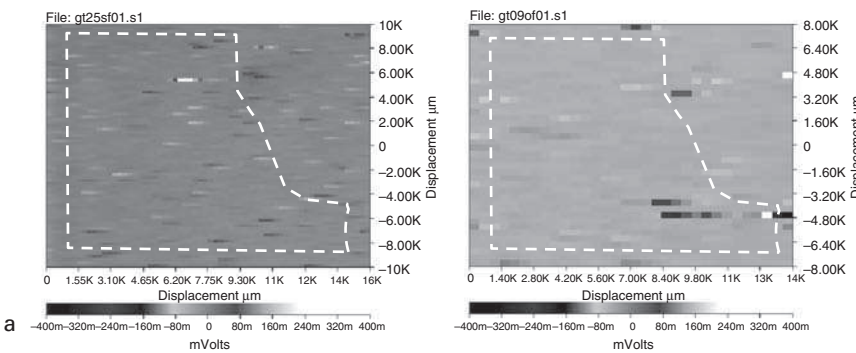

3.4 SVET maps for CuSSAB: (a) at +50 mV; (b) at +100 mV above the open circuit potential.

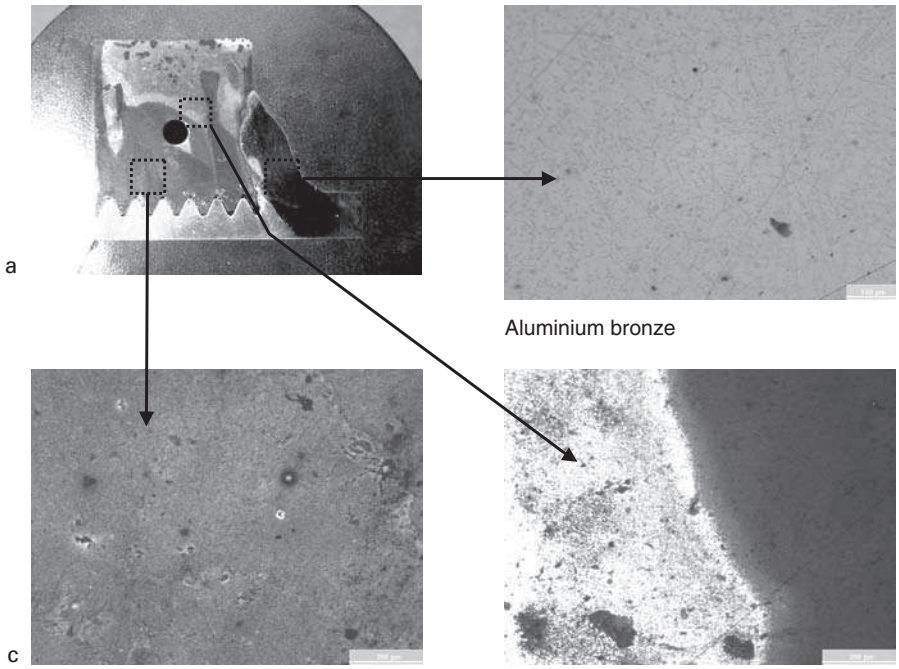

3.5 SEM images of CuSSAB following three days at +100 mV above open circuit potential. Note: all SEM marker bars are 100 μm.

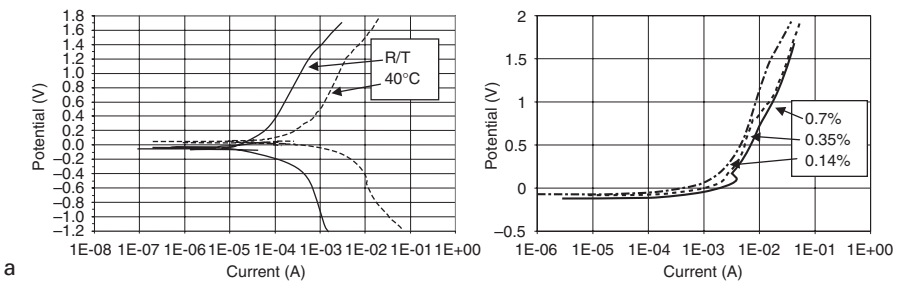

3.6 Polarisation curves of the CuSSAB joint at (a) room temperature and 40°C and (b) various chloride ion concentrations.

than that of steel B. In fact, the SDC corrosion potential measurements clearly indicated that the weld zone of steel B was cathodic to that of the parent plate. This was further validated with capillary electrode E_{corr} measurements. SDC E_{corr} measurements vary from that of the capillary electrode E_{corr} measurements in that the former involve the use of a flowing electrolyte over a small area, in this case around 300–500 μm diameter. The

Table 3.1 Chemical composition variations within the weld joint, as determined from EDX analysis

Element	Compositional analysis (ratio)			
	Parent plate	HAZ	Weld	
			Top	Bottom
Steel A				
Carbon	1	1.02	1.09	0.29
Aluminium	1	1	1	6.5
Silicon	1	1.19	1.8	2.1
Manganese	1	1	1.3	1.3
Iron	1	1	0.99	1.01
Copper	1	1	2	2
Steel B				
Carbon	1	1.34	0.69	0.54
Aluminium	1	–	0.42	1.75
Silicon	1	1	1.59	1.88
Manganese	1	1	1	1.16
Iron	1	1	1	0.99
Copper	1	1.12	3.25	3.8
Chromium	1	1	0.42	0.75

apparent benefit of this method is that it eliminates the averaging effect which arises due to mass galvanic coupling due to differences in microstructure and draws out the slight changes of corrosion potential across the weld section.

3.4.2 Carbon steel laser weld

SVET analysis of the laser welded joint showed highly localised attack of the weld metal microstructure. From Fig. 3.2 it can be seen that corrosion attack is confined to a zone 1 mm wide. This correlates with the E_{corr} values obtained from the individual microstructural zones, where again it can be seen that there is a difference in potential of more than 60 mV between the PP and WM. Note: SDC results were not available at the time of writing.

3.4.3 CuSSAB weld

SVET tests conducted on the CuSSAB joint showed there to be little observable localised corrosion activity within the alkali-based solution, Fig. 3.3b. In an attempt to assess whether or not this joint was susceptible to pitting, additional SVET maps were obtained at applied anodic potentials of +50 mV and +100 mV above the open circuit potential, see Fig. 3.4a and b, respectively. Analysis of these SVET maps showed no localised

breakdown on any of the three materials making up the joint. This was confirmed through SEM analysis, see Fig. 3.5b–d. Furthermore, increasing the temperature and chloride ion concentrations did not lead to the development of localised corrosion, but rather to an increase in overall corrosion rate activity of the whole weld joint. The effect of temperature on corrosion activity is presented in Fig. 3.6a, where it can be seen that corrosion rate increases and no observation of pitting is observed. The effect of different chloride ion concentrations on the corrosion rate at room temperature is given in Fig. 3.6b. As expected, an increase in corrosion rate occurs as the chloride ion concentration increases, but again no pitting is observed on increasing the chloride ion concentration. When compared with the original alkali solution where the chloride ion concentration is negligible, an increase in corrosion current at room temperature of between 1–2 orders of magnitude is observed, as shown Fig. 3.6a and b.

For comparison, an SDC map was also obtained for this weld joint, as shown in Fig. 3.3c. From this figure it can be seen that the AB and Cu portions of the joint are slightly more negative than the SS portion of the joint. It should be recognised that when the three metals are coupled via the conducting electrolyte a mixed potential, AB/Cu/SS, will develop. This mixed potential was measured via the SDC electrode at +40 mV, being almost the half way between that of the SS and AB/Cu values.

3.5 Conclusions

SVET has shown itself to be a useful technique for differentiating, *in situ* and in real time, corrosion activity of metals immersed in conducting electrolytes. Care must be taken when interpreting SVET data from different laboratories and from test to test as the output signal of the vibrating probe system depends upon several parameters, related to both the machine settings and solution conditions. In the present study, SVET and a novel SDC have been used to assess the local corrosion activity of a selection of welds. In all cases, the SVET results compare favourably with the SDC results and that of the corrosion response observed visually on the samples.

3.6 References

1 V. Vignal *et al.*, *Electrochem. Solid State Lett.*, 2004, **7**(4), 1–4.
2 X. Philippe, B. Vuillemin, R. Oltra and V. Vignal, 7th International Symposium on *Electrochemical Methods in Corrosion Research*, Budapest, Hungary, May 28–June 1, 2000.
3 R. C. Gesteland, B. Howland, J. Lettvin and W. H. Pitts, *Proc. IRE*, 1959, **47**, 1856.
4 L. F. Jaffe and R. Nuccitelli, *J. Cell Biol.*, 1974, **63**, 614.
5 H. S. Isaacs, *J. Electrochem. Soc.*, 1991, **138**(3), 722.
6 R. Akid and M. Garma, *Electrochem. Acta*, 2004, **49**, 2871–2879.

4

Use of scanning vibrating electrode technique (SVET) to probe mechanistic changes in corrosion resistance of zinc aluminium alloy galvanising

D. A. WORSLEY, J. ELVINS and J. A. SPITTLE,
University of Wales Swansea, UK

4.1 Introduction

The construction industry now requires galvanised organically coated steels (OCS) with exceptional durability and this has led to considerable current interest in the development and application of new zinc galvanising coatings containing *ca.* 4.5% aluminium. This coating system demonstrates superior corrosion resistance and better ductility[1] than conventional systems[2] where aluminium is only included at very low levels (*ca.* 0.15%) as a means of preventing large-scale iron/zinc intermetallic formation.[3] Painted scribed panels coated with 4.5% aluminium galvanising layers show superior corrosion resistance[4] generally displaying two to three times the performance of conventional coated galvanised steel sheet containing 0.15% Al.

The 4.5% aluminium alloy coating has a relatively complex microstructure. During solidification, the β-zinc (pro-eutectic) phase, containing about 1% aluminium, crystallises first, followed by the crystallisation of a eutectic of zinc containing about 5% aluminium.[5] In producing such coatings, it is desirable to maximise the amount of this latter, eutectic structure allowing the coating to have maximum homogeneity. The unique microstructure of the Zn/Al alloy coating is the reason for its increased corrosion resistance. The zinc/aluminium eutectic retains the cathodic protection capability seen in pure zinc coatings, but demonstrates a better intrinsic corrosion resistance, which has been attributed to the development of an adherent aluminium oxide layer over exposed areas.[6] In the absence of significant zinc dendritic phases, the coating has been shown to corrode through uniform dissolution of the sub-micron lamellae.[7] The corrosion resistance of the coating is, however, critically dependent on its overall microstructure and this can be affected by impurities such as lead and cadmium, which can congregate at grain boundaries causing non-uniform corrosion phenomena.[2] Lead and other elements (e.g. Sb and Bi) also inhibit the nucleation of the primary zinc resulting in fewer and larger crystals. A mischmetal of cerium and lanthanum (*ca.* 0.1%) is also often added to the hot dip

galvanising bath to enhance the wetting ability of the alloy on the steel surface.[8] Additional elements, such as magnesium have also been incorporated to improve the overall corrosion performance of the coating.[9] In recent work,[10,11] it has been shown that, as far as cut edge corrosion protection is concerned, this addition is not desirable since it leads to the formation of a larger amount of primary zinc in the coating, which is exposed at the cut edge on shearing the steel sheet.

One of the principal failure mechanisms in coated galvanised materials is a form of localised corrosion occurring at cut edges of the organic coated substrate, where the metallic coating is exposed.[12] The undermining of the organic coating as a result of anodic zinc dissolution, equation (4.1), with cathodic oxygen reduction, equation (4.2), localised on the steel is frequently, although not exclusively, a cause of cut edge corrosion.

$$Zn(s) \rightarrow Zn^{2+}(aq) + 2e^{-} \quad [4.1]$$

$$O_2(g) + 2H_2O(l) + 4e^{-} \rightarrow 4OH^{-}(aq) \quad [4.2]$$

In this study, the scanning vibrating electrode technique (SVET) has been used to elucidate the mechanisms of surface and cut edge corrosion occurring on a zinc aluminium alloy galvanised steel substrate in 5% aqueous sodium chloride using experimental metallic coatings comprising *ca*. 4.5% aluminium and 95.5% zinc deposited on a steel substrate in a hot dip galvanising bath and cooled at varying rates using a high powered cooler on an industrial coil coating line.

4.2 Experimental methods

4.2.1 Materials

Experimental samples of aluminium zinc alloy galvanised steel were prepared, in which the metallic composition of the hot dip galvanising bath was carefully controlled (with Al 4.5% Zn *ca*. 95.5%). Steel gauges of 0.67 mm and 0.47 mm were chosen travelling through the galvanising bath at a rate of 165 and 167 m min^{-1}, respectively. The strip entry temperature was 440°C and the pot temperature was 420°C. The thickness of the galvanising layer was controlled to *ca*. 20 µm using air knives. Solidification of the resultant coating was then achieved using a fast air cooler situated above the air knives enabling cooling rates of up to 40 deg s^{-1}. Precise measurement of the cooling rate was not possible *in situ* and as such the materials produced will be referred to in terms of the percentage power output of the cooler. They shall henceforth be referred to as 55H, 80H and 100H with the numeric prefix being the power output of the cooler in percentage terms and 'H' representing heavy gauge i.e. 0.67 mm. Samples of the light gauge 0.47 mm, consequently, are referred to as 55L, 80L and 100L.

All other materials were purchased from Aldrich in their highest purity and all solutions were prepared in distilled de-ionised water.

4.2.2 Sample preparation

For cut edge corrosion measurements, the samples were guillotined into 20 × 10 mm coupons, which were then embedded in Metset or Bakelite resin (for SVET and micrographic analysis, respectively) so as to avoid any geometrical effects that might have been introduced as a result of differential organic coating thickness.[13] Each resultant sample was then ground to reveal one metallic edge with the rest of the sample completely insulated from the exposure electrolyte for SVET testing. Before immersion in the electrolyte, the edge to be exposed was polished using increasingly fine carborundum paper (down to 1200 grade). The edge was then subject to optical microscopic investigation to ensure that sample preparation had not lead to the formation of any crevices at the metal mounting material interface and that the edge remained completely flat.

In the case of samples prepared for surface corrosion investigation, the large panels collected from the line trial were first guillotined into 50 × 50 mm coupons. The SVET scan area used was typically a 10 × 10 mm in the centre of this coupon. To avoid corrosion activity occurring anywhere outside of the scan area, the samples were sealed with an extruded self-adhesive tape (3M 5490). This tape was chosen since, in testing, it prevented any crevice corrosion occurring beneath it and also could be removed from the coupon after exposure without leaving an adherent residue. Hence, one 50 × 50 mm coupon could be used to make several measurements of corrosion activity.

4.2.3 Micrographic investigations

The samples for microscopic investigation were polished down to a 1 μm diamond slurry and then etched using chromic acid to bring out the microstructure of the different phases. In order to examine the microstructural changes as a function of depth in the coating, the samples were first indented with a Vickers Hardness Tester diamond. The depth into the coating could then be estimated following careful polishing by measuring the diameter of the indent and knowing the diamonds indentation angle (136°). Hence images could be recorded at known positions within the metallic coating. The images were then subjected to image analysis routines (using Sigma Scan version 5.0) to calculate first the area of the primary zinc phase at each level in the coating and then the overall volume fraction by averaging the values at each level in the coating.

4.2.4 The scanning vibrating electrode technique – SVET

The SVET has been shown to be an invaluable tool in the mechanistic investigation of corrosion in organic coated steels[14–17] and specifically cut edge corrosion.[18–21] This electrochemical technique operates by measurement of the vertical component of current flux in solution, at known points, above a corroding metal surface via a movable vibrating microtip electrode.[22,23] The SVET apparatus used has been assembled in our laboratories; this apparatus is fully described elsewhere.[19–21] The sample under test was held vertically with the exposed cut edge horizontal and uppermost, immersed in a tank of 5% (0.86 mol dm^{-3}) aqueous sodium chloride electrolyte, which was unstirred and open to the air. The dissolved oxygen concentration (in bulk solution) was assumed to be constant at 2.8×10^{-4} mol dm^{-3} (i.e. the equilibrium concentration for air saturated water)[24] and all measurements were carried out at 25°C.

The SVET microtip electrode (probe) was scanned at a fixed height (100 µm) above the exposed cut edge. The probe used consisted of a 125 µm diameter platinum microdisc electrode, which was vibrated normal to the scanned surface at a frequency of 140 Hz with an amplitude of *ca.* 10 µm. The vibration frequency was set by a lockin amplifier (EG & G model 7260), which also served to measure the signal detected by the probe. The probe was moved step-wise over the sample in a plane parallel to that of the surface by linear bearings driven by stepper motors.

For cut edge corrosion measurements, the area scanned was typically 20 mm along the cut edge and 2 mm perpendicular to this, across the edge. The probe made 80 measurements along the length and 20 across the width of the scan, generating a mesh of 1600 points across the surface. For surface corrosion measurements, the scan area was typically 10×10 mm with an equal point density of 40×40, again generating a mesh of 1600 points. During the 24-hour experimental period the SVET performed scans at hourly intervals.

4.3 Results and discussion

4.3.1 Effects of cooling rate and gauge on zinc aluminium alloy microstructure

Typical results of through coating imaging, described in section 4.2.3, are shown in Fig. 4.1 for the light gauge samples. In Fig. 4.1, the images are taken from near the coating surface (~2 µm in depth), the approximate centre of the coating (~10 µm in depth) and at the interface between the coating and the steel substrate (~18 µm in depth). In these images, the zinc dendrites show up as lighter areas. The remainder of the coating consists of a two-

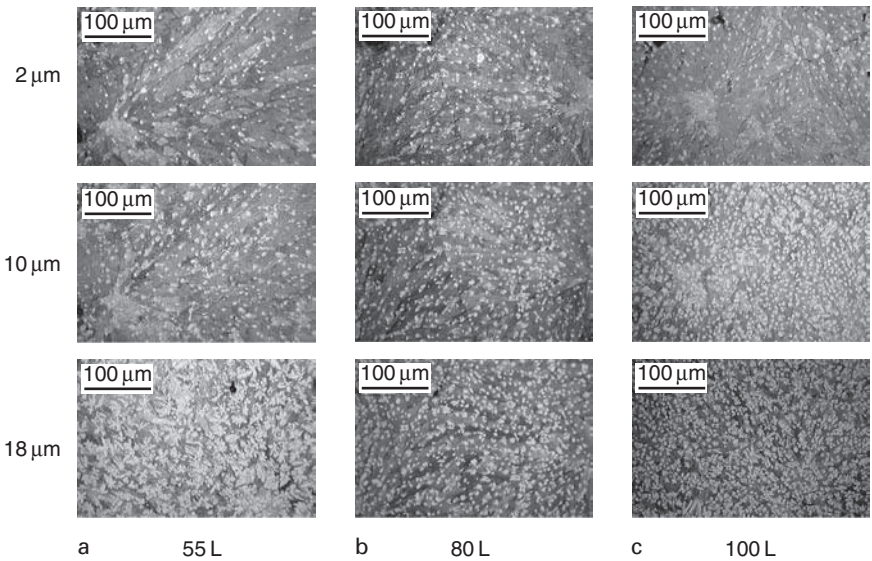

4.1 Optical micrographic images of 95.5% zinc 4.5% aluminium alloy galvanised coatings on a 0.47 mm gauge steel substrate as a function of depth into the coating for a range of cooling rates: *a* 55L, *b* 80L and *c* 100L.

phase eutectic structure (predominantly of lamella morphology). From an initial inspection of the images shown in Fig. 4.1 it appears that the primary zinc dendrites are concentrated at, or close to the steel-coating interface which reflects their nucleation from this surface. It is also clear from Fig. 4.1 that the zinc dendrites in the slowly cooled specimens are larger than those in the rapidly cooled samples and that they are significantly fewer in number.

The structure of the eutectic remains lamellar regardless of the cooling rate and does not change when the gauge of the steel is altered (at least in the limited range used here). Both samples cooled at the highest rate (100 H/L) were predominantly of lamella morphology, but contained small regions of rod eutectic. A further observation is that the inter-lamella spacing of the rapidly cooled samples was reduced when compared with the slowly cooled. This is to be expected given that the inter lamella spacing is dependent upon the speed of growth.[25]

The average percentage area of primary material at each depth was calculated from a number of micrographs taken from different depths and positions in the coating. A summary of these results is presented in Fig. 4.2, from which it can be seen that the average area of primary zinc is increasing as the coating substrate interface is approached. This again reflects the nucleation of zinc dendritic phases in the coating at the steel surface. By

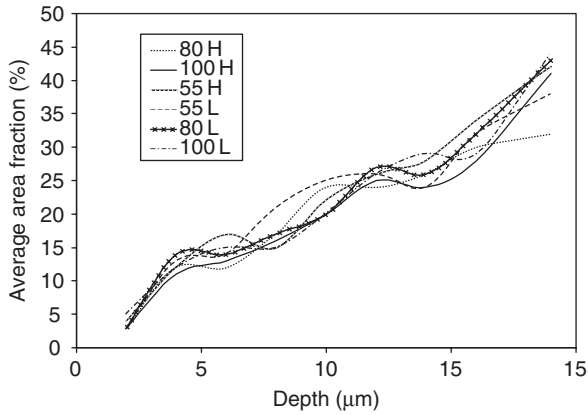

4.2 Averaged area of primary zinc as a result of the micrographic image analyses for the 95.5% zinc 4.5% aluminium alloy galvanised coatings on a 0.47(L)/0.67(H) mm gauge steel substrate as a function of depth into the coating for cooling rates of 55, 80 and 100% cooler output (55 H/L, 80 H/L and 100 H/L samples).

taking the average of these results a measurement of the total volume percentage of zinc dendrites in coating can be obtained. The overall volume fraction remains within ~20% (±2%) for all cooling rates on both gauges.

The images at different positions in the coatings were recorded and analysed to produce a full quantification of dendrite numbers in the coating. These data are also summarised in Fig. 4.3, from which it can be seen that the number of dendrites per unit area increases dramatically with the cooling rate. Since the volume fraction is constant, the overall size of the dendrites is necessarily lower in the more rapidly cooled samples. To a lesser extent, an effect of gauge is also evident with an increase in dendrite number on the heavy gauge materials for each cooling rate when compared with the lighter gauge. The difficulty in inferring any mechanistic change as a function of gauge is that there was no information on the individual strip surface characteristics. In other words, whilst gauge might be responsible for the changes observed, the effect of say surface roughness could not be ruled out. What is clear, however, is that, within each gauge, the influence of cooling rate on the microstructure of the coating both in terms of the eutectic structure and the nature and distribution of zinc dendrites is the same.

The observed microscopic changes in the coating composition are also matched by macroscopic changes in the eutectic cell sizes apparent on the surface of the galvanised material. The cells grow radially from a central nucleation point and cease growth upon impingement with neighbouring cells. Solidification shrinkage occurs at the boundaries of the cells due to

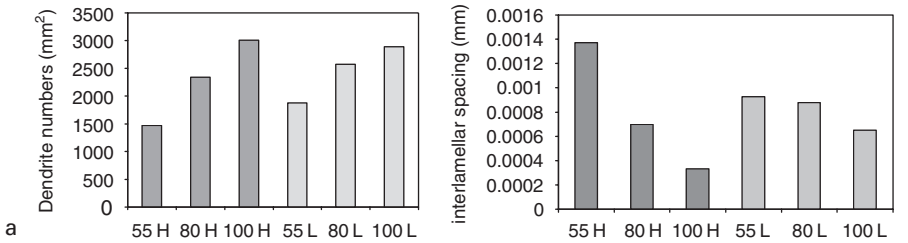

4.3 (*a*) Average size of primary dendrites and (*b*) interlamellar spacing of eutectic for the 95.5% zinc 4.5% aluminium alloy galvanised coatings on a 0.47(L)/0.67(H) mm gauge steel for cooling rates of 55, 80 and 100% cooler output (55 H/L, 80 H/L and 100 H/L samples).

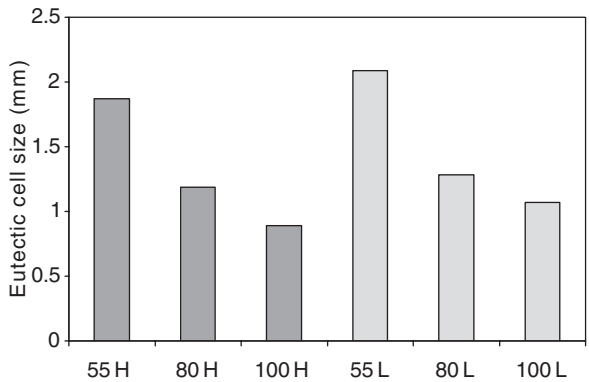

4.4 Average surface eutectic cell size for the 95.5% zinc 4.5% aluminium alloy galvanised coatings on a 0.47(L)/0.67(H) mm gauge steel for cooling rates of 55, 80 and 100% cooler output (55H/L, 80 H/L and 100 H/L samples).

massive volume changes between the liquid and solid states. The size of the eutectic cells was also measured using surface images processed through image enhancing software and the summary of this measurement is presented in Fig. 4.4. The eutectic cell sizes decrease with faster cooling rates leading to an increasing length of the depressed cell boundary on the surface of the galvanised material as cooling rate increases.

4.3.2 SVET response for a point current source

SVET measurements are carried out in aqueous electrolyte employing a vibrating microtip electrode at a small fixed distance above the corroding surface. The SVET tip registers an alternating potential at the vibration

frequency that is proportional to the electrical field strength, F, or potential gradient in the direction of vibration. It has been shown[26] for a point current source (i), the value of F at any distance x, y and z from the point source in a medium of conductivity κ is given by:

$$F = \frac{dE}{dz} = \frac{iz}{2\pi\kappa\left(x^2 + y^2 + z^2\right)^{1.5}} \quad [4.3]$$

Furthermore, the maximum field strength (F_{max}) will be obtained when the SVET electrode is directly over the point source ($x = y = 0$):

$$F_{max} = \frac{i}{2\pi\kappa z^2} \quad [4.4]$$

The SVET apparatus was calibrated using a point current source consisting of a platinum microdisc anode (25 µm diameter) set in an insulating plane and a remote, large area (2 cm^2), platinum gauze cathode. The calibration cell was immersed in 0.86 mol dm^{-3} (5%) aqueous NaCl and known currents i (0.1–10 µA) were passed through it using a galvanostat. The SVET probe was then scanned above the Pt microdisc anode at a constant height of 100 µm. The field strength distribution above the microdisc electrode exhibited the characteristic bell shape proportions reported previously[22,23] with a width at half maximum (*whm*) height of 0.22 mm. The maximum electrical field strength values, F_{max} were recorded when the SVET probe was directly above the microdisc anode and increased linearly with applied cell current, i (correlation coefficient 0.998). This produced a calibration factor of 7.82×10^5 A V^{-1} m^{-2}. This value was checked before each experiment using a point source incorporated within the sample holder.

The conductivity of 5% (0.86 mol dm^{-3}) NaCl at 20°C is 7.01 S m^{-1} (70.1×10^{-3} Ω^{-1} cm^{-1}) and substituting this value into equations (4.3) and (4.4) gives a theoretical value of the *whm* at $z = 100$ µm of 0.153 mm. This is approximately half of the experimental value of 0.22 mm. This departure from theoretical performance derives from the finite dimensionality of the SVET probe since the probe tip consists of a 125 µm microdisc electrode. As the calibration cell anode may be considered as a point current source with a *whm* value of 0.22 mm, this value is an indication of the limiting spatial resolution of our SVET.

4.3.3 Cut edge corrosion measurements using SVET

Location and intensity of anodic sites

The SVET measures the normal component of current flux in the plane of the scan. In the case of galvanised steel materials exposed to a chloride-

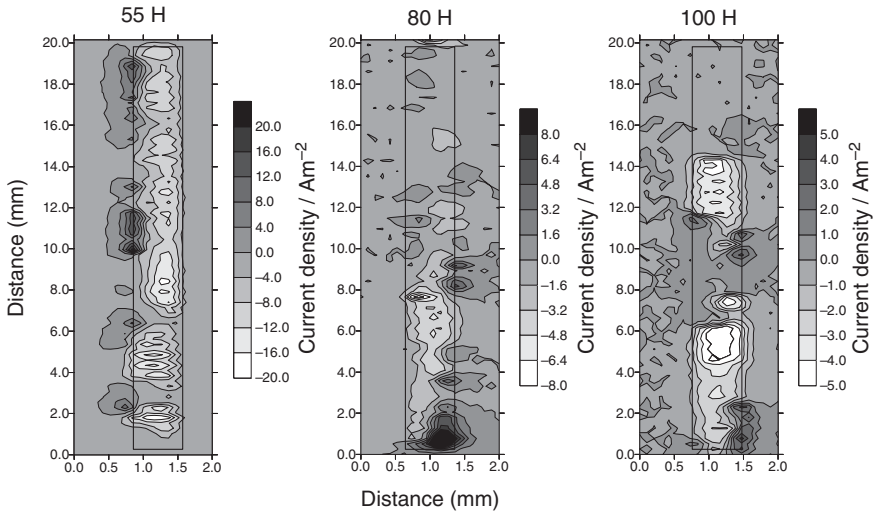

4.5 SVET iso-current contour plots showing the anodic (dark) and cathodic (light) current density distribution over 55H, 80H and 100H corroding cut edge samples embedded in a resin block after 12-h immersion in 5% aqueous NaCl. The sample position is shown.

containing electrolyte, this leads to localised corrosion and excellent SVET detection efficiency. This has been recently demonstrated using ICP mass spectrometry.[27] In 24-h immersion experiments, SVET-measured total zinc losses were found to correlate well with ICP MS measurements. In all cases the SVET measurement was found to be an overestimate of zinc loss of between 15 and 25%. This is most likely a reflection of the deposition of corrosion product onto the metal surface and a failure of ions to be dissolved in solution and detected using ICP MS rather than an indication of poor detection efficiency on the part of the SVET. Where there are issues with detection efficiency are situations where the spatial separation of anode and cathode is less than the *whm* value such that current loops do not pass through the plane of the SVET scan. Hence, in cases of general corrosion, the SVET could underestimate metal losses.

Figure 4.5 shows representative SVET iso-current contour plots obtained by scanning the cut edge of 55H, 80H and 100H samples after a 12-h immersion in 5% aqueous NaCl. The plots show anodic areas (dark) located on the galvanising layers and cathodic activity (light) located on the steel. Initial inspection of the current density scales in Figure 4.5 indicates that the rate of corrosion is influenced by the microstructural changes induced by altering the cooling rate. There are significantly higher corrosion current densities occurring upon the more slowly cooled specimen and this trend was found to be repeated for the light gauge materials.

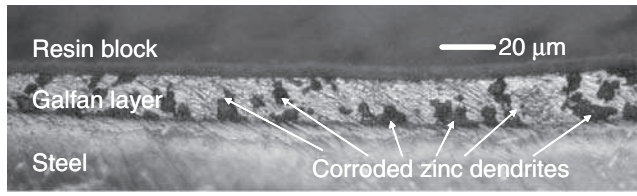

4.6 Optical micrograph of a sample of 55H following corrosion showing the selective attack at the zinc dendrites.

Previous work has shown that immersion of zinc aluminium alloy galvanising coatings led to preferential corrosion of the zinc dendritic phases.[10] Figure 4.6 shows a micrograph of a typical cut edge directly after the end of an experiment. The corrosion products have been removed using ultrasonic cleaning and the sample has not been chemically etched. This image confirms that the primary dendrites have been corroded preferentially to any other component of the coating or steel substrate.

Effects of metallic coating cooling rate on total zinc loss and anode lifetimes along the cut edge

The SVET records signals proportional to the normal component of current density in the plane of scan. The data from a single SVET iso-current contour map can be integrated over the sample area to provide a measure of the ionic current emitted for that particular scan. The simplifying assumption made has been that from scan to scan the current remains constant. By the use of Faraday's law, the current data can be converted into a zinc loss over the one-hour period. Summation of the individual hourly-scan zinc losses yields a total zinc loss (*tzl*) over the 24-h immersion period. Each of the six coating types was scanned five times and an average value of the total zinc loss recorded by the SVET is presented for each sample in Fig. 4.7. This is a reliable measurement of zinc loss as has been recently demonstrated for a wide range of galvanised steel samples immersed in 5% NaCl.[10]

By comparing the *tzl* values in Fig. 4.7, it is clear that, in both gauges of materials, the increasing cooling rate decreases the level of corrosion activity. Thus, the critical factor in determining the corrosion activity on the 4.5% Al zinc galvanising coating is not necessarily the volume fraction (which remains constant) or number (which increases) of primary zinc dendrites, but is rather their physical size. This is more clearly shown in Fig. 4.6, in which the dendrite weight is compared with the *tzl* value measured using SVET for the two gauges of material. In this plot, the weight of individual dendrites has been calculated from a knowledge of the volume fraction, the coating thickness and the number of dendrites per square mm. The plot in

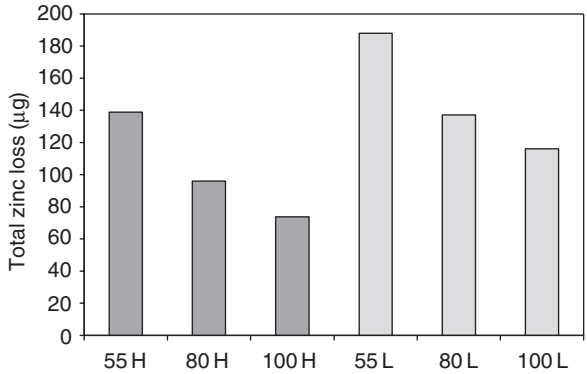

4.7 SVET-measured total zinc loss from 2 mm × 20 mm cut edges zinc aluminium alloy galvanised steel samples embedded in a resin block after 24-h immersion in 5% aerated NaCl as a function of the cooling rate (55H/L, 80H/L and 100H/L) applied to the solidifying metallic coating. Results are presented as an average of five 24-h experiments.

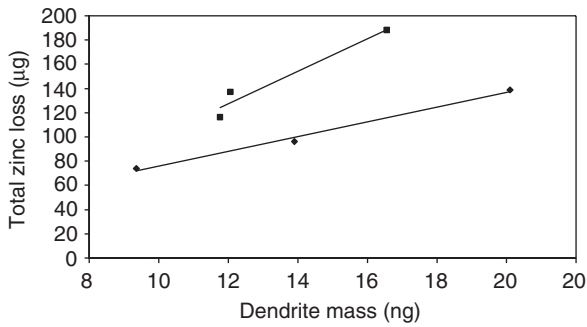

4.8 SVET-measured total zinc loss from 2 mm × 20 mm cut edges zinc aluminium alloy galvanised steel samples embedded in a resin block after 24-h immersion in 5% aerated NaCl compared with the dendrite mass in the coating for light gauge (■) and heavy gauge (◆) samples.

Fig. 4.8 illustrates the link between increasing corrosion intensity and the individual mass of the dendrites in the coating (when the volume fraction is constant at least). What is rather surprising is that the zinc loss from the light gauge material is the greatest, again suggesting that the surface condition of the heavy gauge strip may have been different, potentially leading to greater nucleation.

To determine what the nature of the anodic events is on the metallic coating we have subjected the SVET data to further scrutiny. Individual

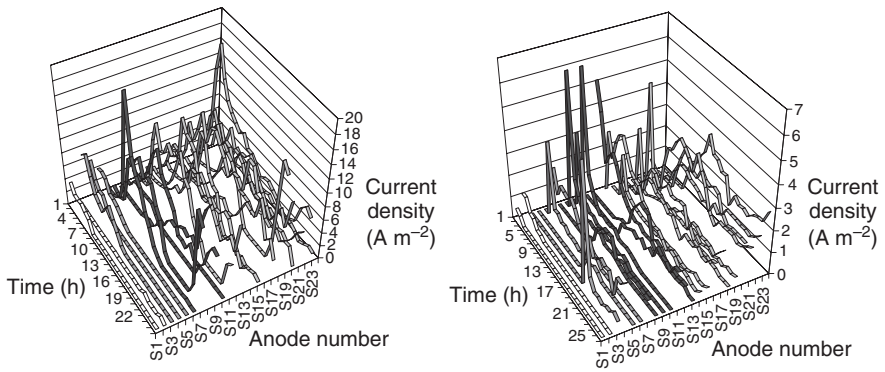

4.9 Plot of SVET-measured anodic activity against anode number for the cut edge over 24 h of immersion freely corroding in 5% aerated NaCl for *a* 55H and *b* 100H samples. Ribbon colour indicates anode lifetime: less that 6 h (white, left-hand side), 6 to 12 h (mid grey), 12 to 20 h (dark grey), 20+ h (light grey, right-hand side).

anodes were identified over the 24-h exposure period and their temporal evolution profile plotted for the 55H and 100H samples. The results for this analysis for typical scans are shown in Fig. 4.9 (a) and (b) for the 55H and 100H samples, respectively. The results shown represent the number of active anodes and their corrosion current densities as a function of time. In order to simplify the analysis, it is assumed that each of these anodes is a point current source. This is a reasonable assumption since, on this substrate, corrosion is localised and the *whm* values measured were typically <0.22 mm suggesting that the anodes resembled closely our point source calibration cell. Inspection of the data reveals that, for the 55H sample, the anodes are not only more intense, but display greater lifetimes as compared with those for the 100H samples. Indeed twelve anodes are persistent (with lifetimes 18–24 h) throughout the exposure compared with only seven for the 100H sample. Hence, the larger primary zinc dendrites in the 55H sample are more prone to localised corrosive attack and reduce the overall corrosion resistance of the galvanising coating towards cut edge corrosion.

The difference between individual anode zinc losses for the 55H and 100H samples is shown in Fig. 4.10. Whilst the number of anodes is broadly similar, the larger dendrites present in the lower cooling rate (55H) samples lead to elevated levels of zinc loss from the coating. One point of interest is that the SVET measurement of individual anode zinc losses allows the number of dendrites removed per anodic event to be calculated. For the 55H sample, the average zinc loss per anode from Fig. 4.10 is 6.7 μg and the dendrite weight is 20 ng which means that each anodic event consumes some 335 dendrites. For the 100H, this falls to 155 dendrites (since the

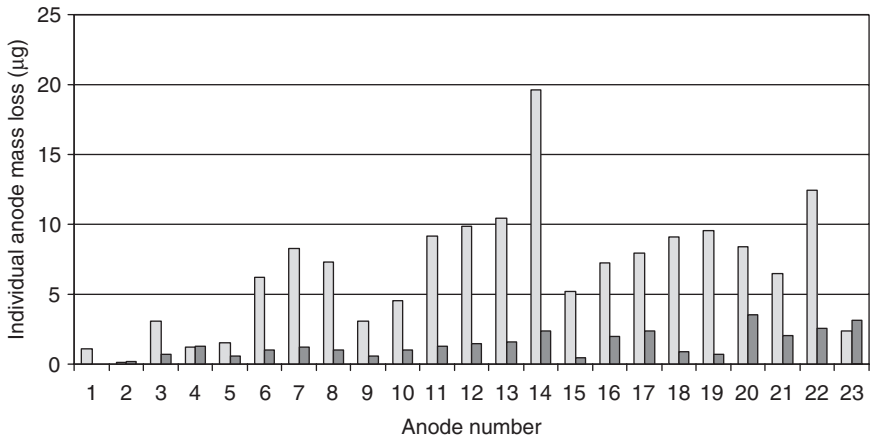

4.10 Individual anode zinc losses for 55H (light bars) and 100H (dark bars) from an exposed cut edge over 24 h of immersion freely corroding in 5% aerated NaCl.

anodic events are on average responsible for 1.4 µg zinc loss and the dendrites weigh 9 ng).

Surface corrosion: location and intensity of anodic sites

Typical SVET iso-current contour maps are shown in Fig. 4.11 for the 55H and 100H samples. These SVET maps were recorded after a 12-h immersion in 5% NaCl and show two key features. Firstly, the intensity of the corrosion activity is approximately two fold higher in the most rapidly cooled (100H) sample and, secondly, the number of active anodes in any single scan on the sample surface is actually higher for the 55H sample. The increase in corrosion activity is in marked contrast to the decreasing corrosion intensity as a function of cooling rate displayed in Figs. 4.7 and 4.8 for cut edge corrosion. In all samples exposed to surface corrosion, anodes appeared in the depressed regions, i.e. the eutectic cell grain boundaries. The same trend was also observed for the light gauge panels and further quantification of the SVET data was undertaken as detailed below.

Surface corrosion: effect of metallic coating cooling rate and gauge on total zinc loss and anodic lifetimes

As previously stated, it is possible to calculate the zinc loss (*tzl*) occurring upon the surface from the SVET iso-current contour maps using Faraday's law. Figure 4.12 is an illustration of the effect that cooling rate and gauge

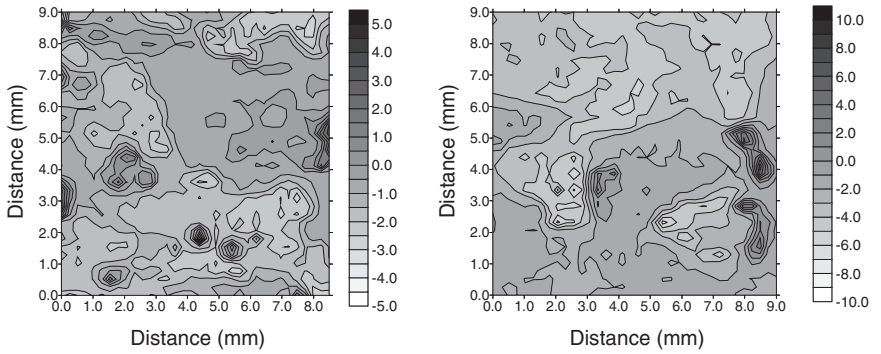

4.11 SVET iso-current contour plots showing the anodic (dark) and cathodic (light) current density distribution over: *a* 55H and *b* 100H corroding surface samples after 12 h immersion in 5% aqueous NaCl.

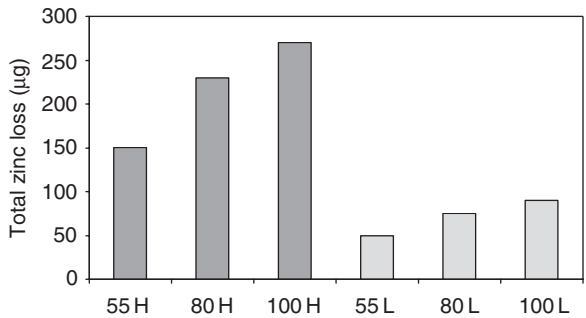

4.12 SVET-measured total zinc loss from 10 × 10 mm surfaces of zinc aluminium alloy galvanised steel samples after 24-h immersion in 5% aerated NaCl as a function of the cooling rate (55 H/L, 80 H/L and 100 H/L) applied to the solidifying metallic coating. Data are presented as an average of five 24-h experiments.

have on the *tzl* values measured from the surfaces of the galvanised materials as a function of the cooling rate. Within the cooling rate subsets, there is a reduction in zinc loss as the cooling rate is decreased. This result holds for both of the steel gauges. The results in Fig. 4.12 also show a reduced amount of zinc loss occurring upon surfaces of the light gauge samples. Interestingly, this compares with increased zinc loss for the cut edge samples on the light gauge substrate, again re-enforcing the link between microstructure and corrosion resistance. Once again, it is difficult to provide a direct reasoning for the change in microstructure between the two gauges since little is know about the surface characteristics of the two coils.

Repeated scanning using the SVET showed that the anodes active throughout the exposure period were located at triple points and eutectic

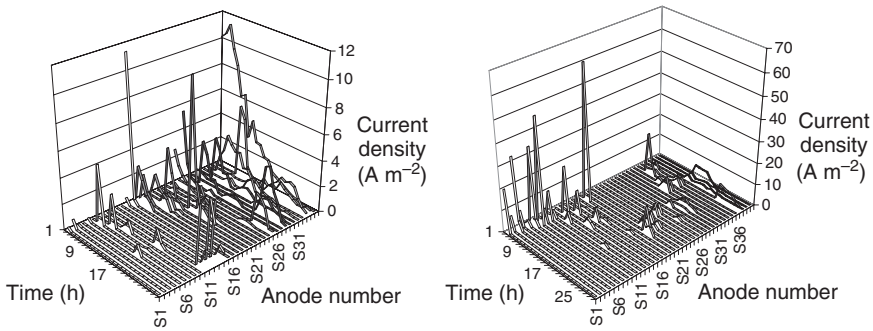

4.13 Plot of SVET-measured anodic activity against anode number for the surface corrosion over 24 h of immersion freely corroding in 5% aerated NaCl for: *a* 55H and *b* 100H. Ribbon colour indicates anode lifetime: less that 6 h (white, left-hand side), 6 to 12 h (mid grey), 12 to 20 h (dark grey), 20+ h (light grey, right-hand side).

cell grain boundaries. The increase in corrosive attack upon the more rapidly cooled samples also indicates that the differing corrosion performance is a result of the changes in solidification at the surface. As described earlier, the increase in cooling rate leads to a reduction in the eutectic cell size (and consequently a change in the visual appearance). The reduction in cell size corresponds with an increase in the unit length of the depressed grain boundaries. The depressed region is a site for dendrite arms to penetrate the surface and act as sites for the initiation of corrosion. Hence the increasing corrosion activity in the more rapidly cooled samples (100L and 100H) is due to the increasing eutectic cell boundary length and the potential for initiation of corrosion at surface zinc dendrite arms in these locations.

Upon examining the temporal evolution of anodic activity at specific sites some interesting observations can be made using the SVET data. In terms of the number of active anodes present over the 24-h exposure period, the more rapidly cooled samples display a greater total number of active anodes. In addition, the more rapidly cooled materials display higher anode intensities, but, in general, anodic lifetimes are short. By contrast, the more slowly cooled samples show anodes that are much more persistent but less intense. This is summarised in Fig. 4.13, where anode lifetimes for surface corrosion of the 55H and 100H samples are compared.

Individual anode zinc losses are compared in Fig. 4.14. These values are obtained by summation of the current emerging from anodes shown in Fig. 4.13. These results highlight not only the increasing anode numbers in the more rapidly cooled samples, but also that individual anode zinc losses are, on average, higher for the 100H sample (0.92 µg as compared with 0.51 µg

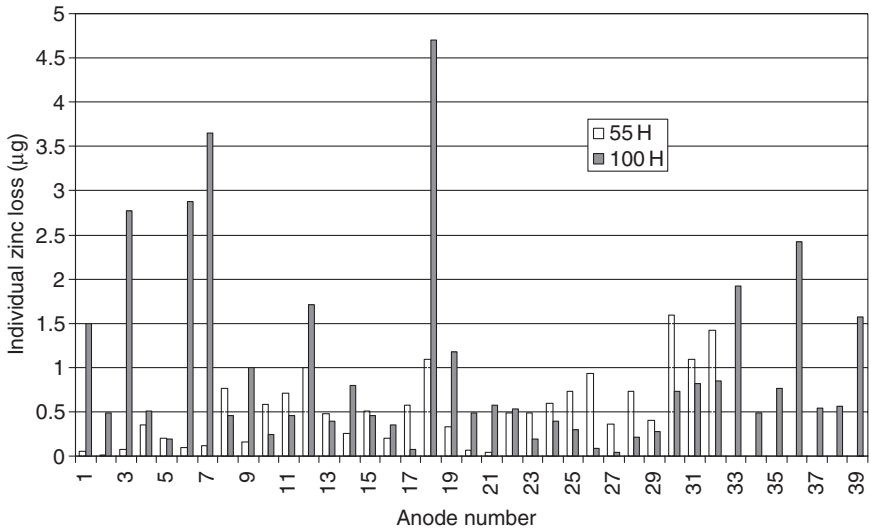

4.14 Individual anode zinc losses for 55H (light bars) and 100H (dark bars) from an exposed surface over 24 h of immersion freely corroding in 5% aerated NaCl.

for 55H). Comparison with the dendritic weights (0.01 µg for 100H and 0.02 µg for 55H) allows the estimation of the numbers of dendrites completely removed per anodic event. For surface corrosion, this is therefore 92 and 25, respectively, for 100H and 55H. The fact that each anodic event consumes more than one dendrite is not surprising since there is dendritic interconnection in the coating. This is even greater in the case of the cut edge corrosion. The individual anode mass losses from the cut edge corrosion data shown in Fig. 4.8 show that each anode in the case of cut edge corrosion removes on average 1.3 µg and 6.7 µg, respectively, for the 100H and 55H samples.

The link between the surface and edge corrosion resistance, as determined using SVET, and eutectic cell size alterations, indicative of microstructural changes, is shown in Fig. 4.15. For both the gauges, there is a good correlation between surface and edge corrosion resistance and the sizes of eutectic cells. This is important since it potentially enables the coating line operator to be able to fine tune the production parameters for maximum corrosion resistance on the basis of an on-line visual inspection.

4.4 Conclusions

The combined use of microstructural analysis and advanced localised corrosion measurements using SVET has highlighted the link between coating

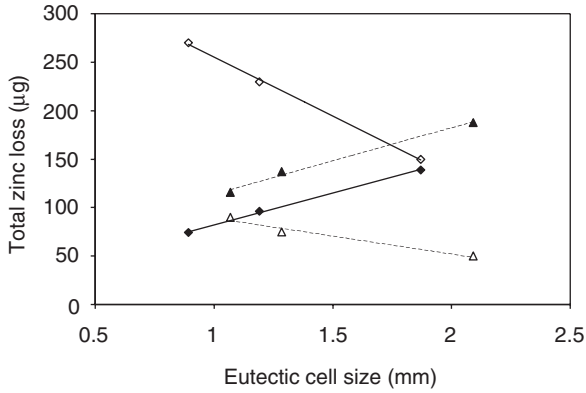

4.15 SVET-measured total zinc loss from 2 mm × 20 mm cut edges (open symbols) or 10 × 10 mm surfaces (closed symbols) for zinc aluminium alloy galvanised steel samples after 24-h immersion in 5% aerated NaCl as a function of the eutectic cell size for two steel gauges (diamonds light gauge and triangles heavy gauge).

composition and corrosion resistance and also the critical difference between corrosion measurements made on the surfaces of OCS and at their cut edges. The trends for cut edge and surface corrosion resistances determined are different, but both are a result of changes born from processing parameters altering the microstructure. Increasing the cooling rate leads to a large number of smaller primary zinc dendrites as a result of greater nucleation. However, the volume percentage of this dendritic phase remains constant, within experimental error. The increased cooling rate also produces a finer eutectic lamella, again as a result of rapid nucleation, which, at very high cooling rates, forces a change in eutectic morphology to include some rod structures. The increasing nucleation also leads to a reduction in the surface eutectic cell size upon more rapid cooling, leading to an increased length of cell boundary per unit area of coating.

The smaller number of large dendrites in the more slowly cooled samples directly influences cut edge corrosion. The dendrites are preferentially corroded and the lifetime and intensity of the anodes are greater, consequently resulting in a greater amount of zinc loss.

The increase in unit length of depressed boundaries per unit area due to the reduced eutectic cell size at higher cooling rates leads to a greater amount of surface corrosion. The combinations of increasing eutectic cell boundary and increasing dendritic penetration in the boundary region contribute to elevated surface corrosion. This microstructural change in the surface of the material leads to the formation of larger numbers of short-lived high-intensity anodes.

In summary, in the evaluation of new zinc aluminium alloy galvanising chemistries and processing conditions, it is important to consider both surface and edge corrosion and the precise way in which the localisation and intensity of corrosion is influenced by microstructual changes. The combination of SVET with conventional microscopic techniques is a powerful development tool in this regard.

4.5 Acknowledgements

The authors would like to thank Corus Colors, Shotton, for their help in the performance of this research, and acknowledge the support of EPSRC for funding this research under the Engineering Doctorate Scheme and the Materials for Better Construction Initiative.

4.6 References

1 D. Christian, 'Performance of prepainted and unpainted Galfan test panels in corrosive environments', in *Proc. of Eighth Galfan Licencees Meeting, International Lead and Zinc Research Organisation* (ILZRO), April 21 (1986).
2 F. Goodwin, *Galfan galvanising alloy technology*, 2nd Edition, ILZRO, 1984.
3 I. Suzuki, *Corrosion-resistant Coatings Technology*, Marcel Dekker Monticello, NY, 1989.
4 M. Lamberights, V. Leroy and F. Goodwin, *Proceedings of the Third International Zinc Coated Sheet Steel Conference (INTERGALVA)*, Barcelona, Spain, 1991, SID/7–13.
5 T. Hada, *Proceedings of the 4th International Conference on Zinc and Zinc Alloy Coated Steel Sheet, Galvatech 98*, Chiba, Japan, Keynote Lecture, 1998, 108–114.
6 F. Goodwin, A. F. Skerazi and R. Lynch, 25th Annual Conference of Metallurgists, The Canadian Institute of Mining and Metallurgy, Toronto, Canada 17–20 August 1986.
7 J. Hostler, 'Galfan Technical Resource Centre', ILZRO, 1992.
8 A. F. Skerazi, *Proceedings of the 14th International Galvanising Conference*, Munich Germany, Zinc Development Association, 1985, 51.
9 T. Tano and H. Higuchi, 'Development and properties of Zn-Al alloy coated steel sheet with high corrosion resistance', *Nippon Steel Tech. Rep.*, No 25, April 1985.
10 D. A. Worsley and M. Challis, *Br. Corros. J.*, 2001, **36**, 297–303.
11 M. Challis, T. Heatley and D. A. Worsley, *Corrosion and Corrosion Protection – Proceedings of the International Symposium*, J. D. Sinclair, R. P. Frankenthal, E. Kalman and W. Plieth (eds.), The Electrochemical Society, Pennington New Jersey 2001, Vol. 2001-22, 264–272.
12 P. A. Ryan, R. P. Wolstenholme and D. M. Howell, *Durability of Cladding, A State of the Art Report*, Thomas Telford, London, 1994.
13 D. A. Worsley, A. Belghazi and S. M. Powell, *Ironmaking Steelmaking*, 1999, **26**, 387–392.
14 H. S. Isaacs, *Corrosion*, 1987, **43**, 594–598.
15 I. Sekine, M. Yuasa, K. Tanaka, M. Fuke and L. Silao, *J. Japan. Soc. Col. Mater.*, 1992, **65**, 684.

16 D. Thierry and F. Zou, *Proceedings of the 4th International Conference on Zinc and Zinc Alloy Coated Steel Sheet (GALVATECH '98)*, Chiba, Japan, 1998, 376.
17 H. S. Isaacs, A. J. Aldykiewicz, D. Thierry and T. C. Simpson, *Corrosion*, 1996, **52**, 163–168.
18 F. Zou, C. Barreau, R. Hellouin, D. Quantin and D. Thierry, *Mater. Sci. Forum*, 1998, **289–292**, 83–92.
19 D. Worsley, H. N. McMurray and A. Belghazi, *J. Chem. Soc., Chem. Commun.*, 1997, 2369.
20 S. M. Powell and D. A. Worsley, *Br. Corros. J.*, 2001, **36**, 42–48.
21 S. Bohm, H. N. McMurray, S. M. Powell and D. A. Worsley, *Electrochim. Acta*, 2000, **45**, 2165–2174.
22 H. S. Isaacs and B. Vyas, *Electrochemical Corrosion Testing*, F. Mansfeld and U. Bertocci (eds.), 3 (1981).
23 H. N. McMurray and D. Worsley, *Advances in Chemical Kinetics*, (ed. R. G. Compton and G. Hancock), 1997, **4**, 149–202.
24 A. Bonnel, F. Dabosi, C. Delouis, M. Dupart, M. Kedam and B. Tribollet, *J. Electrochem. Soc.*, 1983, **130**, 753–761.
25 H. Y. Liu and H. Jones, *Acta Metall. Mater.*, 1992, **40**, 2003–2009.
26 H. S. Isaacs, *Advances in Localised Corrosion*, (H. S. Isaacs, U. Bertocci, J. Kruger and S. Smialouzka ed.), p. 221, NACE, 1988.
27 D. A. Worsley, H. N. McMurray, J. H. Sullivan and I. P. Williams, *Corrosion*, 2004, **60**, 437–448.

5

Local analysis by SVET of the involvement of biological systems in aerobic biocorrosion

R. BASSÉGUY, J. IDRAC, C. JACQUES, A. BERGEL, M. L. DÉLIA and L. ETCHEVERRY,
Laboratoire de Génie Chimique, France

5.1 Introduction

When a material is immersed in a non-sterile medium, a biofilm forms on its surface by microorganisms that attach and grow on it. The local conditions under the biofilm may induce severe biodeterioration and biocorrosion phenomena. Many industrial domains are concerned, such as harbour structures, marine transportation, cooling units using natural waters and pipelines. It has been observed that the free corrosion potential of stainless steel in a passive state is slightly more anodic when the material is immersed in natural sea water than in synthetic medium.[1,2] The risk and the severity of localised corrosion onset are consequently increased by the adhesion of marine biofilms: pits were found larger in natural than in synthetic sea water.[3] To understand this phenomenon Mollica and Trevis[4] have carried out numerous experiments and have confirmed that the free corrosion potential of stainless steel in synthetic or sterile sea water does not exceed +100 mV/SCE although in natural sea water it may be up to +400 mV/SCE. When crevice corrosion takes place, the corrosion rate is higher in natural than in sterile sea water. The passive current was the same in the two media proving that no modification of the anodic phenomena occurred. On the other hand, when a constant potential was imposed to stainless steel, the cathodic current increased at the same time as the biofilm grew. Using this current increase through a galvanic coupling, Mollica[5] has developed a sensor, called BIOX, able to detect the biofilm formation, in order to monitor biocorrosion in industrial equipments.

Concerning the aerobic MIC (microbially influenced corrosion), it is now commonly agreed that the biofilm catalyses the reduction of oxygen,[4,6] although the mechanisms are still a controversial topic. Several hypotheses have been proposed to explain this catalysis: the formation of hydrogen peroxide,[7] the modification of the oxides on the material surface[8] and the presence of biological molecules (enzymes as peroxidase, catalase . . .) that contribute to the different steps of oxygen reduction.[9] In our laboratory,

this last hypothesis has been investigated[10,11] because superoxide dismutase, peroxidase and catalase activities have been detected in some marine biofilms.[12] It has been observed that when catalase was adsorbed on a glassy carbon surface, catalase efficiently catalysed oxygen reduction via direct electron transfer from the electrode.[9,13] The results have been discussed with respect to the electrode surface properties (hydrophilic/hydrophobic forces) and the enzyme structure: to be efficient, the heme group of the catalase must be connected on the electrode surface.

This last study has shown that the measurement of global parameters, such as free corrosion potential, current under polarisation, are useful to detect the catalysis of oxygen reduction by the biofilm, but are not sufficient to determine the elementary mechanisms of the biofilm action in aerobic MIC. A local approach is needed to analyse coupling between physico-chemical conditions, surface state and electrochemical properties of the material. Although scanning vibrating electrode technique (SVET) has been commonly used in the field of corrosion to map cathodic/anodic sites on metallic surfaces, the technique has been rarely applied to biocatalysis studies. A previous local study applied to MIC has demonstrated that the sea-water biofilm has a great influence on the current (the global parameter) which increased two orders of magnitude, although only 2% of the surface had been occupied by cathodic sites where oxygen reduction was catalysed.[14] Progress in this local analysis should lead to a greater understanding of biofilm adhesion, growth and reactivity.

The purpose of the work described in this chapter was firstly to propose a configuration to model the electrochemical behaviour of the biofilm. Secondly, the goal was to show the ability of SVET to probe the biofilm activity.

The system consisted of molecules able to catalyse oxygen reduction, hemin or myoglobin, immobilised on the metallic surface. Myoglobin is a protein that was proved to catalyse oxygen reduction on a carbon electrode.[15] With its iron protoporphyrin centre (called heme group), myoglobin (Mb) is very close to enzymes like peroxydase and catalase and the electron transfer between Mb and an electrode is easier than between an enzyme and an electrode. Hemin is the heme group alone without the protein shell; it is a simple protoporphyrin with FeII/FeIII as a redox active centre for oxygen link.

Two immobilisation systems were tested:

- Adsorption of hemin from dimethylsulfoxide (DMSO) on a stainless-steel surface: this technique gave good results for the oxygen reduction catalysis on other materials[13] but has never been tested on stainless steel.
- Cast polyion technique, which consists of depositing successive layers of polyion and protein of opposite charges. The strong electrostatic

attraction between the successive polyion and protein layers would result in a stable assembly. In this study, the protein myoglobin (Mb negatively charged at pH 7.5) and the polyion poly(ethyleneimine) (positively charged) were deposited on a graphite surface.

This paper presents results from both the macro and micro analyses: the efficiency of the catalysis was demonstrated by measuring global parameters, and SVET analysis gave information on the sites where the catalysis took place. The micro analysis should give information on the area ratio of the surface responsible for the global behaviour.

5.2 Experimental methods

5.2.1 Chemicals

Horse heart myoglobin (Mb) and hemin were purchased from Sigma and Fluka, respectively. Poly(ethyleneimine) (PEI) average mol. wt. 1200 and dimethylsulfoxide (DMSO) were purchased from Aldrich.

Solutions of NaCl (0.50 or 0.01M) were used for experiments with stainless steel and tris(hydroxymethyl) aminomethane (Tris, HCl buffer, 0.01M, pH 7.5) for experiments with graphite.

5.2.2 Electrode preparation

The stainless-steel electrodes were made of URB 66 (weight percent composition: 23.92 Cr, 21.90 Ni, 5.44 Mo, 2.99 Mn 1.86 W, 1.54 Cu, 0.47 N, 0.014 N, 0.001 S, bulk iron) provided by INDUSTEEL Creusot (Le Creusot, France). Electrodes were 3 mm × 5 mm sections embedded in epoxy resin (Stuers, Epofix Kit) polished successively with P120, P180, P400, P800, P1200, P2400 abrasive papers (Lam Plan), immersed during 15 min in a HF (2%) / HNO_3 (20%) solution to be stripped and rinsed with the NaCl solution. To obtain reproducible oxidation states, polarisation during 18 h at constant potential (–0.50 V/SCE) in 0.50M NaCl solution was performed, before each experiment. The electrodes were then immersed in a DMSO solution with (1 mg mL^{-1}) or without hemin for 15 min. For SVET analysis, galvanic coupling was performed by deposing hemin only on a part of the stainless-steel surface, masking the rest under a Teflon rubber.

Pyrolytic graphite rods (6.15 mm diameter), purchased from Le Carbone Lorraine (France) were embedded in epoxy resin. The electrodes were polished successively with P240, P400, P1200 abrasive papers. The cast polyion technique presented elsewhere[16] was a modification of the classic layer-by-layer procedure.[17] Films were grown on graphite by repeated alternate deposition of PEI and Mb. 20 µL of PEI aqueous solution (7 mg mL^{-1} PEI, 0.5M NaCl) were deposited on the surface and air dried until complete

water evaporation (about 1 h). Then 20 µL MB solution (2 mg mL^{-1} in Tris, HCl buffer) were deposited on the surface and dried in air (about 1 h).

5.2.3 Electrochemical set-up

A multichannel potentiostat VMP2 (Princeton Applied Research) able to test individually four samples in the same time was used to follow the free corrosion potential evolution *versus* time and to record current–potential curves on stainless steel URB 66 electrodes. An EG&G 363A electrochemical set-up was used for cyclic voltammetry with the graphite electrode. A Solartron electrochemical interface 1286 was used to impose a constant potential during SVET analysis of the graphite surface. In each case, the saturated calomel electrode (SCE) was used and the auxiliary electrode was made of platinum.

5.2.4 SVET

Local current measurements were performed using an Applicable Electronics SVET (USA). Pt–Ir microelectrodes (Micro Probe Inc., USA) were black platinised before being used as probes. The diameter of the sphere of the black platinum deposit was about 15 µm with a corresponding capacitance of around 10 nF. The amplitude of vibration was typically 15–20 µm. The ASET Software (Science Wares Inc., USA) converted the potential drop measured by the microprobe with Ohm's law into a current density value. The calibration was made with a stainless-steel microelectrode used as a point current source. The displacement of the microprobe was performed using a motorised and computer controlled XYZ micromanipulator allowing 0.5-µm steps. A video camera was used for imaging and to control the distance between the microprobe and the sample surface. This distance was 150 and 100 µm for stainless steel and graphite samples, respectively. The results were then treated with Matlab software. For stainless steel, the local analysis was performed at open potential at the interface between areas without and with immobilised protein. For graphite samples, the surface was polarised in floating mode at –0.30 V/ECS with a 1286 Solartron Interface. The experimental set-up is illustrated in Fig. 5.1.

5.3 Results

5.3.1 Catalysis of oxygen reduction by hemin on stainless-steel surface

Sixteen samples were tested with and without immobilised haemin in 0.50 M NaCl solution. The free corrosion potential (E_{corr}) was recorded *versus* time

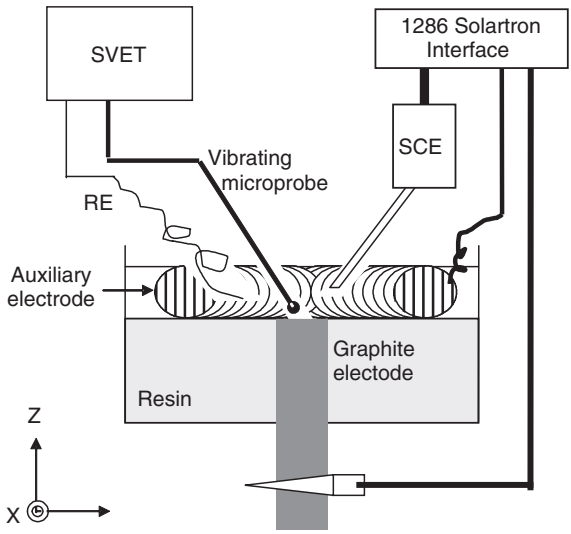

5.1 Schematic representation of the experimental setup for SVET analysis of a graphite electrode under polarisation.

Table 5.1 Influence of hemin on the free corrosion potential of stainless steel electrodes immersed in 0.50 M NaCl. 16 samples were tested in the two cases

	Samples without hemin Average potential/standard deviation V(SCE)/V	Samples with hemin Average potential/standard deviation V(SCE)/V
At $t = 0$	–0.210 / 0.066	–0.088 / 0.138
At $t = 30$ min	–0.183 / 0.083	–0.075 / 0.139
At $t = 60$ min	–0.178 / 0.082	–0.060 / 0.126

during one hour and a current–potential curve was then plotted in the cathodic direction from E_{corr} to –0.90 V/SCE with a potential scan rate of 0.005 V s^{-1}. As reported in Table 5.1, the average E_{corr} of electrodes with adsorbed hemin was higher than for electrodes without hemin. The standard deviation was also more important in the presence of hemin showing a random distribution as it is commonly encountered in biocorrosion phenomena. In one case, a sample recovered with hemin presented a E_{corr} value around +0.20 V/ECS; this potential was close to those found in natural sea water when a biofilm has grown on the surface. These results show that the immobilisation of hemin clearly shifted the potential toward anodic values. Current–potential curves like those of Fig. 5.2 proved that the poten-

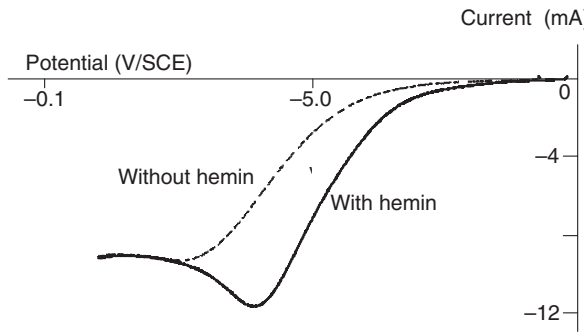

5.2 Current–potential curves obtained in 0.50M NaCl on stainless-steel electrodes with or without hemin adsorbed from DMSO. Potential scan rate: 0.005 V s^{-1}.

tial displacement of E_{corr} was linked to the increase of the cathodic current of oxygen reduction. Consequently, adsorbing haemin permitted catalysis of the oxygen reduction on stainless steel and can be considered as a modelling system for the action of aerobic biofilm. It was demonstrated for the first time to our knowledge that a very simple biological compound, which may be present in biofilm, was able to give the same results in terms of E_{corr} as a natural biofilm.

A galvanic coupling was performed on the surface of stainless-steel specimens by depositing hemin only on a part of the surface, the left side of sample as shown in Fig. 5.3a. SVET observations were carried out at open potential at the boundary between the two areas with and without hemin: three domains were observed (Fig. 5.3b):

- On the surface with hemin the local current was negative proving a cathodic behaviour.
- On the surface without hemin the local current was positive as an anodic surface
- At the boundary the current randomly varied from anodic to cathodic values.

Consequently, SVET permitted observation of the catalysis of oxygen reduction on the area where hemin was immobilised. At open potential, the catalysis was proved to be efficient enough to create a galvanic coupling between hemin (cathodic) and no hemin (anodic) zones on the surface.

5.3.2 Catalysis of oxygen reduction by myoglobin on graphite surface

To simulate the biofilm behaviour, another immobilisation technique was used, which consisted in alternatively depositing polyion and protein layers.

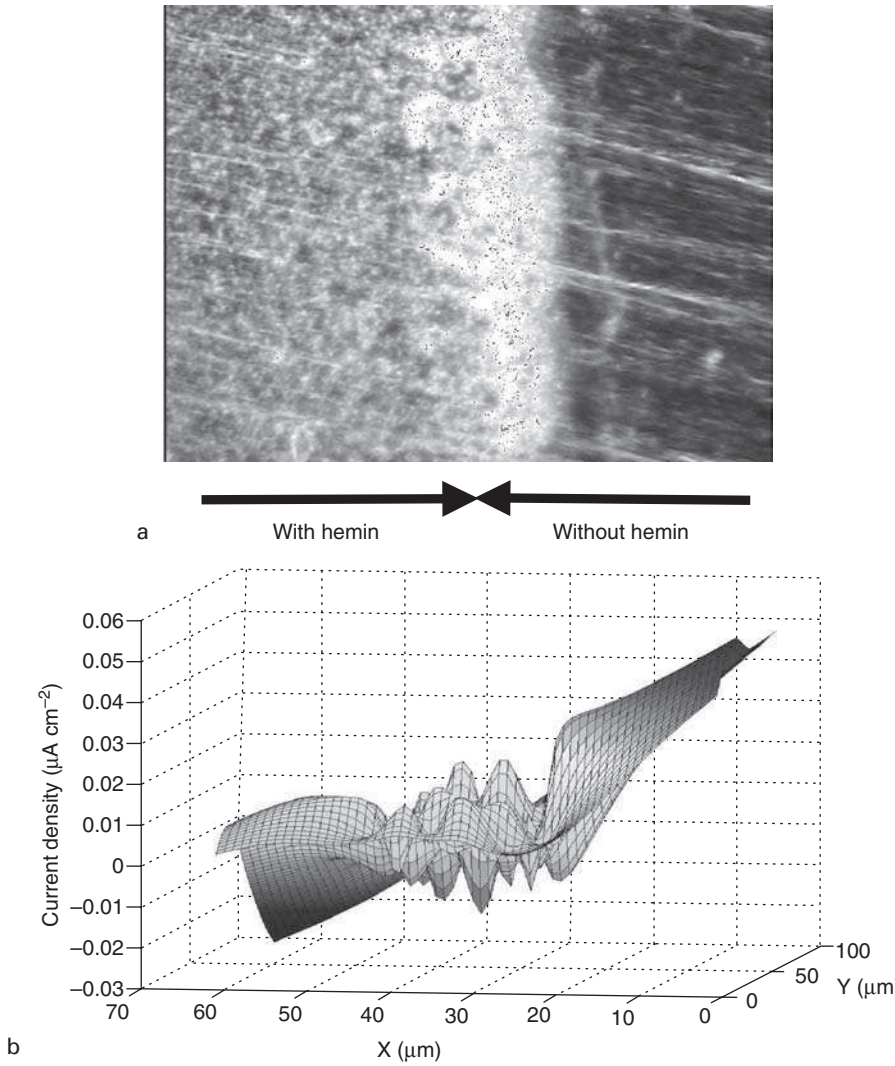

5.3 Interface between hemin and no hemin zones on stainless steel: *a* optical image of the boundary, *b* local current map (3D) obtained by SVET in 0.01M NaCl.

The protein used, myoglobin (Mb), was able to catalyse oxygen reduction on graphite carbon as observed in previous works[16] and reported in Fig. 5.4. The cathodic current was higher in the presence of Mb than in its absence in the domain of the electrochemical reduction of oxygen.

As in the case of hemin on stainless steel, mixed surfaces with and without Mb deposited on graphite were prepared and scanned with SVET

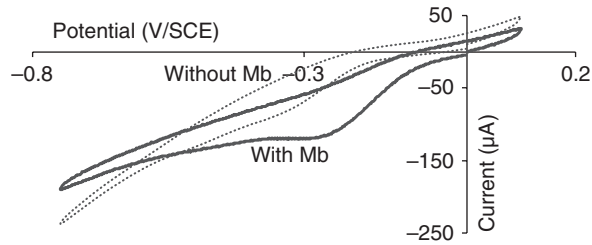

5.4 Cyclic voltammograms obtained in Tris–HCl (0.01M, pH 7.5) on graphite electrodes with or without myoglobin deposited by cast polyion technique. Potential scan rate: $0.01\,V\Delta^{-1}$.[16]

(Fig. 5.5): on the optical image, the boundary between the two areas was well observed (Fig. 5.5a). SVET analysis was performed when the sample was cathodically polarised at –0.30 V/SCE (Fig. 5.5b). Despite the cathodic polarisation of the whole surface, negative local currents were found on the right part of the electrode surface only, where Mb was deposited and catalysed the reduction of oxygen. Nevertheless, this cathodic right side remained rather heterogeneous: only around one-half of the surface area was efficient proving the distribution of the catalyst Mb was non-uniform. This demonstrates that SVET is perfectly adapted for observing sites of biocatalysis.

5.4 Conclusions

Hemin, adsorbed from DMSO, was able to catalyse oxygen reduction on a stainless-steel electrode. To our knowledge, it was the first time that this electrocatalysis was demonstrated on stainless steel.

Moreover, to compare macro and micro scales for understanding MIC, the immobilisation of hemin or myoglobin was a first step, simpler than growing a biofilm. By accessing the sites where biocatalysis took place, SVET was shown to be a powerful technique for evaluating the ratio of the surface responsible of the global behaviour. Work is now in progress to study the adhesion of micro-organisms on a surface, modelling the first stage of biofilm formation.

5.5 Acknowledgements

We gratefully acknowledge Maria Elena Lai who had the innovative idea to immobilise enzyme on stainless steel using adsorption from DMSO.

These works were supported by the French Research Minister with the program ACI 2000 ‘Surfaces, Interfaces et Nouveaux Matériaux’, project

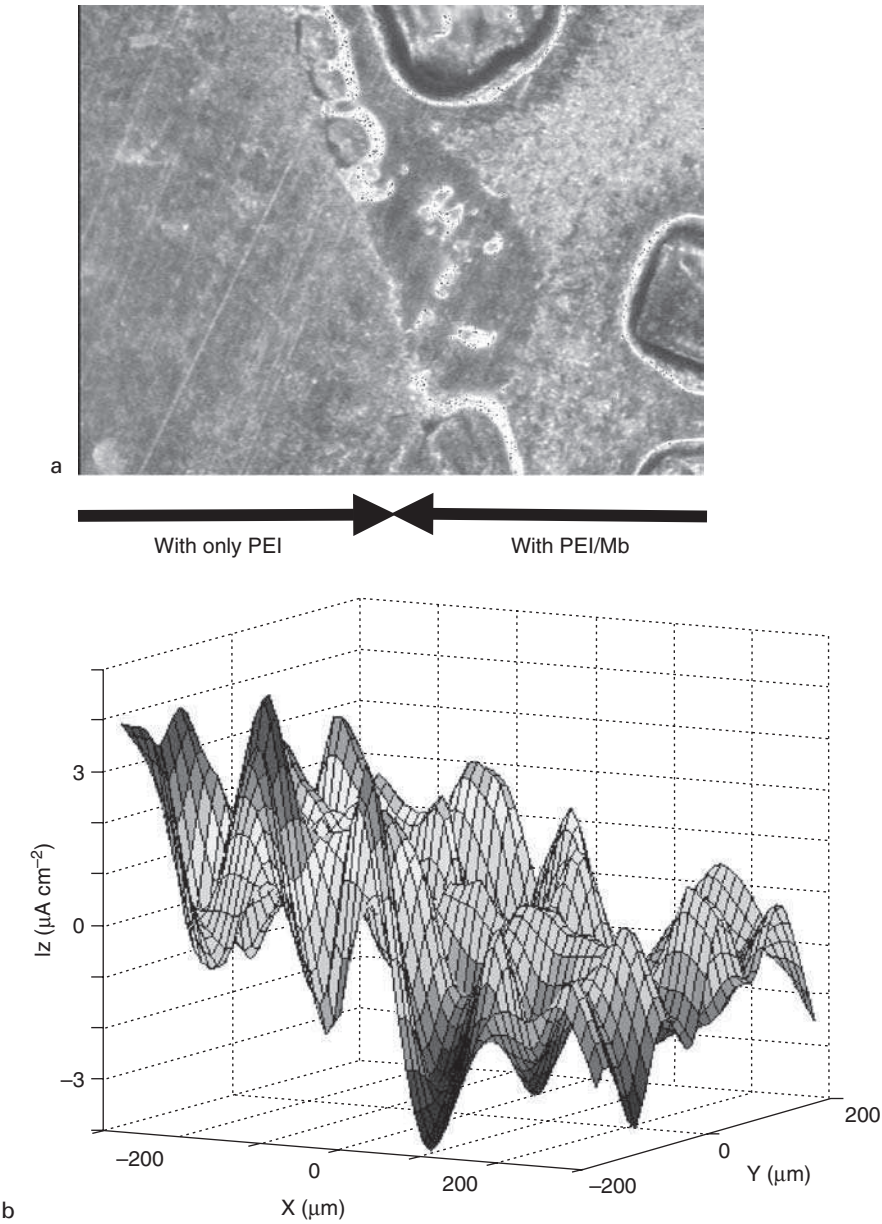

5.5 Interface between PEI/Mb (right) and only PEI (left) zones on graphite carbon: *a* optical image of the boundary between the two areas, *b* local current map (3D) obtained by SVET in 0.01M Tris–HCl (pH = 7.5).

'SVET et Biocorrosion' and the European Community in the framework of the program 'Quality of Life and Management of Living Resources', project 'Electro-Chemical Enzymes' (no. QLK CT 2000-00725) coordinated by BASF (Ludwigshafen).

5.6 References

1 F. L. LaQue, *J. Amer. Naval Eng.*, 1941, **53**, 29–64.
2 N. S. Nikitina and T. B. Ulanovski, *Trudy*, 1957, **3**, 190–199.
3 A. G. Lagutina, K. P. Danil'Chenko, O. F. Shevenko and V. P. Barannik, *Zashchita Metallov*, 1970, **6**, 48–51.
4 A. Mollica and A. Trevis. Corrélation entre la formation de la pellicule primaire et la modification de la branche cathodique sur des aciers inoxydables expérimentés en eau de mer aux vitesses de 0,3 à 5,2 m/s, *Proceedings of the 4th Int Congress on Marine Corrosion and Fouling*, 351–365, Antibes, France, 1976.
5 A. Mollica and P. Cristiani, *Water Sci. Technol.*, 2003, **47**, 45–49.
6 V. Scotto, R. Di Cintio and G. Marcenaro, *Corros. Sci.*, 1985, **25**, 185–194.
7 I. Dupont, D. Féron and G. Novel, *Int. Biodetior. Biodegrad.*, 1998, **41**, 13–18.
8 N. Le Bozec, C. Compère, M. L'Her, A. Laouenan, D. Costa and P. Marcus, *Corrros. Sci.*, 2001, **43**, 765–786.
9 V. Scotto and M. E. Lai, *Corros. Sci.*, 1998, **40**, 1007–1018.
10 M. E. Lai and A. Bergel, J. *Electroanal. Chem.*, 2000, **494**, 30–40.
11 M. E. Lai, Catalyse enzymatique de la réduction électrochimique de l'oxygène: application à la corrosion des aciers inoxydables en milieu marin, 29/09/2000, thesis of the University Paul Sabatier-Toulouse III, 118 route de Narbonne, 31062 TOULOUSE CEDEX 4.
12 M. E Lai, V. Scotto and A. Bergel, Analytical characterization of natural marine biofilm: a tool for understanding biocorrosion of stainless steel in seawater, *Proceedings of the 10th International Congress on Marine Corrosion and Fouling*, 38–41, Melbourne, Australia, 1999.
13 M. E. Lai and A. Bergel, *Bioelectrochem.*, 2002, **53**, 157–160.
14 A. Mollica, E. Traverso, D. Thierry, *EFC Working Party report on 'Aspect of Microbially Induced Corrosion'*, Publication No **22**, European Federation of Corrosion Series, Institute of Materials, London, 1997, 51–63.
15 J. F. Rusling, *Acc. Chem. Res.*, 1998, **31**, 363–369.
16 A. Pardo, Conception de réacteurs electro-enzymatiques pour la mise en oeuvre de mono-oxygénases, 09/06/2004, thesis of the University Paul Sabatier-Toulouse III, 118 route de Narbonne, 31062 TOULOUSE CEDEX 4.
17 J. F. Rusling, L. Zhou, B. Munge, J. Yang, C. Estavillo and J. B. Schenkman, *Faraday Discuss.*, 2000, **116**, 77–87.

6

Study of delamination of organic coatings by local electrochemical impedance spectroscopy

E. ARAGON and C. MERLATTI, Université du Sud Toulon Var, J.-B. JORCIN, and N. PÉBÈRE, ENSIACET, France

6.1 Introduction

Organic coatings are widely used to prevent corrosion of metallic structures because they can easily be applied for a reasonable cost. It is generally accepted that the coating efficiency is dependent on the intrinsic properties of the organic film, on the substrate/coatings interface in terms of adherence, on the inhibitive pigments included in the film and on the degree of environmental aggressiveness.

In marine corrosion, one of the main objectives is to increase the durability of organic coatings to fifteen years and more. Thus, the long-range forecast of organic coatings and the characterisation of the ageing state in service constitute key technological goals. Moreover, for environmental and human health considerations, the development of low toxicity paints (water-based paints) has become a priority. As yet, no correlation has been established between the resistance in service and results obtained in laboratories, which could allow coating durability to be reliably predicted. As a matter of fact, for these new systems, there is a lack of feedback on their behaviour in actual use. Faced with this challenge, the strategy developed in different industries is the same:

(i) To perform correlation studies between accelerated ageing and natural ageing of a whole range of paint systems.
(ii) To develop fundamental research on the structures of polymers and on the mechanisms of ageing of the organic films by using techniques such as electrochemical impedance spectroscopy (EIS), scanning vibrating electrode technique (SVET), scanning Kelvin probe (SKP), Fourier transform infrared spectroscopy (FTIS), differential scanning calorimetry (DSC) or dynamic mechanical analysis (DMA) to measure the glass transition temperature, adherence testing, etc.

Starting from these considerations, a study has been performed on a large scale to develop an accelerated procedure of ageing to obtain a good esti-

mation of the paint durability in a natural environment. In parallel, it is necessary to obtain a better knowledge of the degradation mechanisms as a function of exposure time. The present work constitutes part of this extensive project on the study of natural or artificial ageing of paints. The aim of the study is to characterise the processes involved in the degradation of an organic coating from artificial defects and to assess the extent of delamination underneath the coating by a non-conventional method: the local electrochemical impedance spectroscopy (LEIS). During the last decade, it has been demonstrated that LEIS is a powerful tool to investigate localised corrosion on bare metal surfaces and on coated alloys.[1–10]

6.2 Experimental methods

6.2.1 Samples

Substrate consisted of carbon steel sheets (150 mm × 150 mm × 2 mm). The coating was an epoxy vinyl primer with calcium ferrite, iron oxide and talc as additives. It was applied on degreased and sand-blasted (Sa 2.5) steel as defined in ISO 8501. Liquid paint was applied by air spraying and, after drying, the coating was about 80 µm thick. The corrosive medium was a 0.1 M NaCl solution for conventional impedance and 0.001 M NaCl solution for LEIS. In this case, the experiments were carried out in a low conductivity medium ($9.4\ 10^{-5}$ S cm^{-1} for 0.001 M NaCl) to optimise resolution.

6.2.2 Ageing procedure

The delamination occurred from two types of artificial defects (Fig. 6.1). The first one was done manually with a cutting knife. The defect had a V-shaped profile. The second one was performed with a scribing machine and a 2 mm width is specified for the drill.

The ageing was performed in a salt spray chamber from which the samples were removed after 20, 30 and 50 days of exposure. A reference sample (0 day) was tested for comparison. Independently of the exposure time, two corrosion product layers were observed: an outer layer, which was brown, rusty and poorly adherent, and an inner layer which was black and strongly adherent. The thickness of the layers increased with the exposure time. For global impedance, the samples were tested with the corrosion product layers. For localised impedance, it was necessary to remove the corrosion product by a cathodic polarisation at –1.5 V/SCE for 4 h because the impedance of the corrosion products was high, masking the delamination. It was assumed that the duration of the cathodic polarisation was short enough to avoid coating delamination, which is due to the exposure to the salt spray.

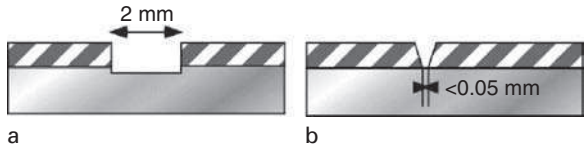

6.1 Schematic representation of the two artificial defects: *a* machine scribing, *b* cutter scribing.

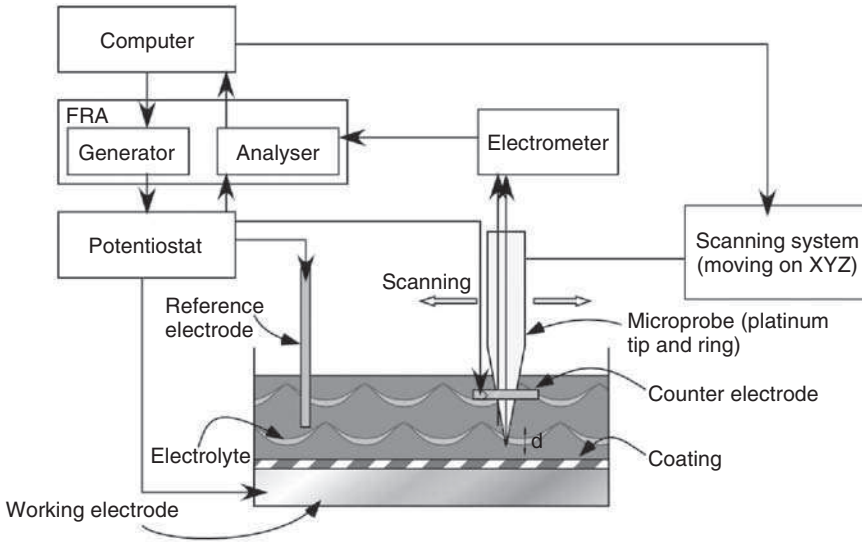

6.2 Schematic representation of the LEIS apparatus.

6.2.3 Electrochemical measurements

For the classical EIS measurements, a three-electrode cell was used: the working electrode with an exposed area of 24 cm^2, the saturated calomel reference electrode (SCE) and a platinum auxiliary electrode. Electrochemical impedance measurements were performed using a Solartron 1287 electrochemical interface and a Solartron 1250 frequency response analyser in a frequency range of 65 kHz to several mHz with eight points per decade using 10 mV peak-to-peak sinusoidal voltage.

Localised electrochemical impedance spectroscopy (LEIS) was carried out with a Solartron 1275. This method used a five-electrode configuration (Fig. 6.2). LEIS measurements were made from the ratio of the applied ac voltage to the local ac current density. The applied voltage ($\Delta V_{applied}$) was the potential difference between the working electrode and the reference electrode. The local ac current density (i_{local}) was calculated using Ohm's law:

$$i_{\text{local}} = \frac{\Delta V_{\text{local}}}{d} \times \kappa \qquad [6.1]$$

where κ is the conductivity of the electrolyte and d the distance between the two probes positioned on and in a conical plastic holder: one protrudes from the tip of the cone and the other is a ring placed around the cone 3 mm from the tip.

The local impedance Z_{local} is calculated by the relationship:

$$Z_{\text{local}} = \frac{\Delta V_{\text{applied}}}{i_{\text{local}}} \qquad [6.2]$$

For local electrochemical impedance mapping (LEIM) the probe was stepped across a designated area of the sample. In the present case, the analysed area was 32000 µm × 24000 µm above the active zone. The step size was 500 µm in the x and y directions. The extremity of the probe was positioned as close as possible to the surface; the resolution was less good when it was held 100 µm above the surface. The measurement parameters were optimised: amplitude: 0.1 V, integration time: 1 s, delay: 2 s. Admittance was plotted rather than impedance to improve the space resolution of the mapping.

To study delamination, two excitation frequencies were chosen: 5 kHz and 10 Hz. The value of 5 kHz was chosen to take into account the organic coating. The value of 10 Hz was chosen as a trade-off between quick scanning and the fact that the contribution of localised corrosion to the overall impedance is generally found in the low-frequency range. Here, only the plots at 5 kHz are reported because delamination was more visible at this frequency.

6.3 Results and discussion

6.3.1 Conventional impedance

Figure 6.3 shows the conventional impedance diagram obtained for the coating in the absence of defects. This diagram is typical of a coated system. It can be recalled that the impedance spectrum was divided into two different parts: the high frequency part (HF) is assumed to represent the properties of the coating and the low frequency part (LF) to represent the reaction occurring at the bottom of the pores of the coating.[11] The impedance values are relatively high ($1.2 \times 10^8\,\Omega\,\text{cm}^2$) and it can be considered that good protection is obtained.

Then, global impedance spectra were recorded for the coated systems with the artificial defects and for different ageing times in the salt spray chamber (0, 20, 30 and 50 days). The results are reported in Fig. 6.4 for the

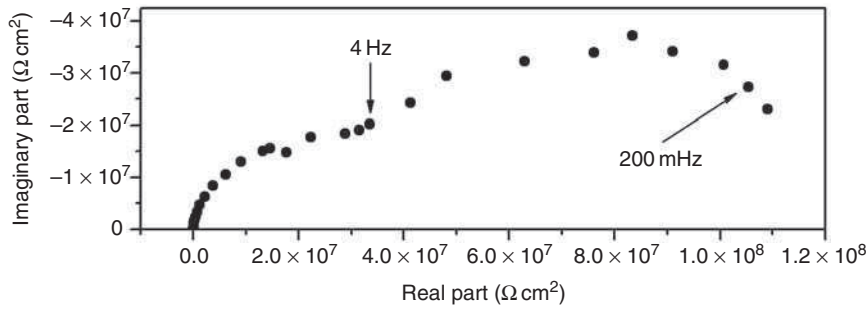

6.3 Conventional impedance diagram for the coating without defects after 24 h of immersion in 0.1M NaCl solution.

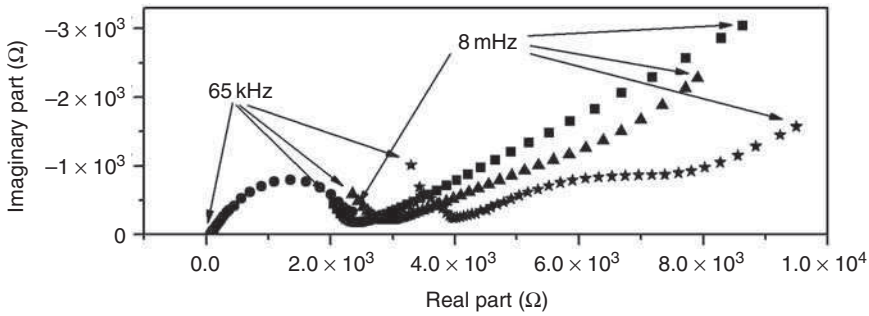

6.4 Conventional impedance diagrams obtained for the epoxyvinyl primer with an artificial defect (cutter scribing) after different durations of exposure in the salt spray chamber: (●) 0 day, (■) 20 days, (▲) 30 days, (★) 50 days.

cutter scribe mark and in Fig. 6.5 for machine scribing. The area of unprotected steel was large and thus the diagrams are only representative of the processes occurring in the defect. For the reference (without exposure to the salt spray chamber), a single distorted capacitive loop is observed. The diagram characterises the corrosion of bare metal.

During exposure to the salt spray, the corrosion spread out and the corrosion products sealed the scribes. As a consequence, the diagrams were strongly modified when the exposure time increased: a linear part can be seen in the low frequency range of the diagrams which can be attributed to diffusion processes through the corrosion product layers. Comparison of Fig. 6.4 and Fig. 6.5 shows that the impedance is lower in Fig. 6.5 due to the fact that the scribe mark was larger. The evolution of the diagrams as a function of the exposure to the salt spray was not identical for the two scribes. This could be due to a difference in the development of the corrosion product layers during the exposure to the salt spray. As a matter of fact, the two scribe marks do not have the same morphology, the cutter scribe mark being narrower. It can be assumed that the corrosion products led to a more confined environment in the narrower mark. According to Funke,[12] due to

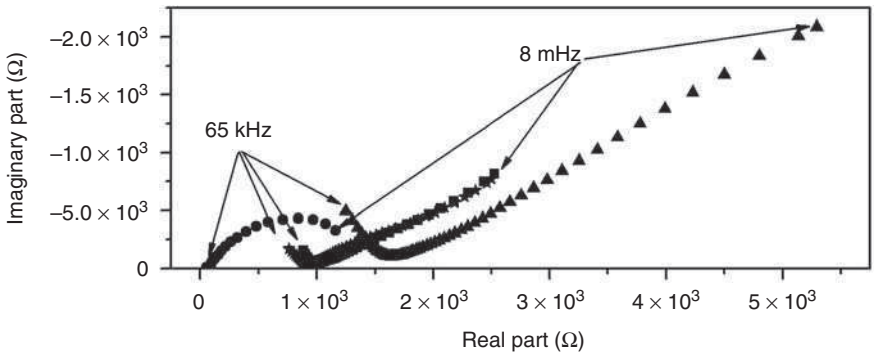

6.5 Conventional impedance diagrams obtained for the epoxyvinyl primer with an artificial defect (machine scribing) after different durations of exposure in the salt spray chamber: (●) 0 day, (■) 20 days, (★) 30 days, (▲) 50 days.

the large unprotected steel area, rust formation is dynamic: the corrosion products formed are subjected to continuous rupture and healing.

Looking at Fig. 6.4 and Fig. 6.5, it can be concluded that, from the global diagrams it is not easy to analyse the delamination process to determine the delaminated area. Thus, local impedance spectroscopy was used.

6.3.2 Localised electrochemical impedance mapping (LEIM)

Figure 6.6 presents LEIM obtained for the coating with an artificial defect (cutter scribing) after different durations of ageing in the salt spray chamber. After 20 days of exposure, a step is clearly observed on the edge of the scribe which increased with the ageing time. After 50 days of exposure, the step is no longer observed, but baseline admittance is higher. This indicates that the studied zone is not large enough to visualise the step. Thus, delamination is significant.

Figure 6.7 concerns machine scribing. After 20 days of exposure, the mapping is relatively close to that obtained for the reference. However, a modification of the admittance can be noted near the scribe, but the width of the scribe masks the phenomenon. After 30 and 50 days of exposure, delamination is clearly visible and is more significant than for cutter scribing. This could be due to the greater width of the scratch. Some blisters were observed beside the scratch.

To analyse the results, the coating was removed after the electrochemical tests. Independently of the shape of the defect, corrosion products were only observed around the scribes. This observation corresponds, on the LEIM, to the low values of admittance (high values of impedance). Around the corrosion products and particularly after 30 and 50 days of exposure in the salt

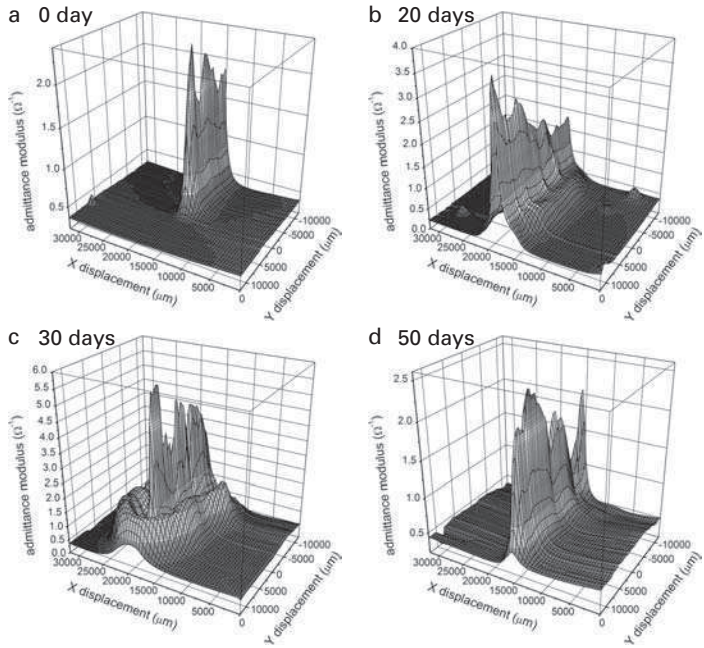

6.6 Cutter scribing. LEIM carried out at 5 kHz (a) before exposure in the salt spray chamber, (b), (c) and (d) after different durations of exposure to the salt spray.

spray chamber, the coating was easily removed revealing the delaminated zone. On the LEIM, this corresponds to high values of admittance (low impedance). The low values of impedance correspond to loss of adherence of the organic coating. Finally, it can be concluded that LEIM allowed the delamination process to be observed. A relatively good agreement was obtained between the delaminated areas measured by visual observations, after the removal of the coating, and localised electrochemical measurements.

For the studied systems, the delamination mechanism can be described by reference to the works of Funke:[12]

(i) the corrosion products are formed at the scribes and spread out around the scribes. According to Barton *et al.*,[13] in the presence of chloride, fairly soluble ferrous chloride hydrate or hydroxychlorides are formed (rusty layer). The transformation of these corrosion products to insoluble oxides, e.g. Fe_2O_3, by hydrolysis and oxidation (black layer) leads to the release of chloride anions which can again participate in producing soluble primary corrosion products, thus enhancing the action of the local corrosion elements autocatalytically.

(ii) The region located under the corrosion products becomes anodic whereas the region under the coating becomes cathodic. Oxygen, which

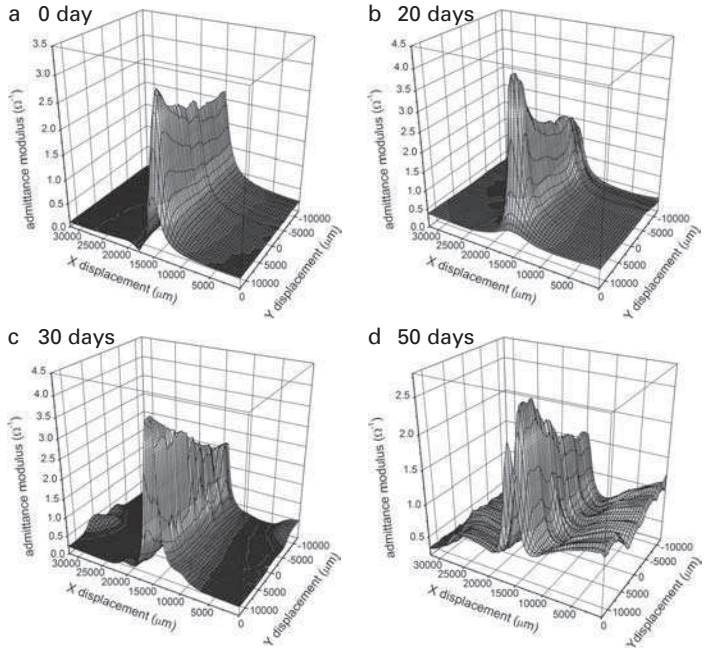

6.7 Machine scribing. LEIM carried out at 35 kHz (a) before exposure in the salt spray chamber, (b), (c) and (d) after different durations of exposure to the salt spray.

diffuses through the coating, can then be reduced to OH^-. Locally, the pH is significantly increased and the delamination is propagated.

(iii) The anodic zones advance due to the formation of corrosion products, increasing the area of the oxygen reduction and thus propagating delamination under the coating.

A schematic description of the mechanism discussed above is presented in Fig. 6.8.

According to Funke,[12] the basic principle of blister development is always the different availability of oxygen at various locations in the coated system, and this is subjected to change during exposure due to the formation of corrosion products.

6.4 Conclusions

LEIS was used to investigate delamination at the steel/organic coating interface. Initiation and propagation of delamination were clearly observed on industrial samples. This point is important because localised measurements usually are performed on small samples specially prepared for the particular technique used.[14] LEIM revealed the presence of the corrosion

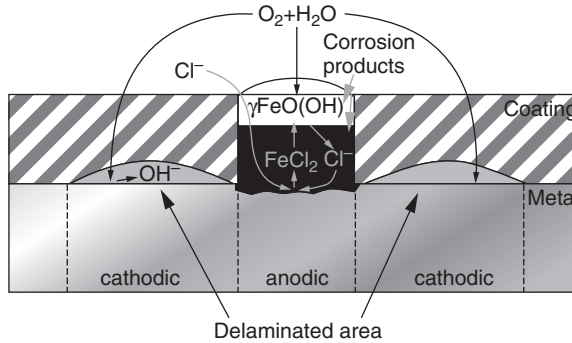

6.8 Schematic view of a section through a film showing the delamination process in the presence of a scribe mark.

products in and beside the scratches and delaminated areas around the scribe marks.

The propagation of delamination is in agreement with different studies reported in the literature. The development of the corrosion products in the scratch and diffusion of oxygen through the coating play important roles.

In the future, it will be necessary to obtain more information from local impedance spectra and also to establish the correlation between the results obtained with conventional impedance and localised impedance.

6.5 References

1 R. S. Lillard, P. J. Moran and H. S. Isaacs, *J. Electrochem. Soc.*, 1992, **139**, 1007–1012.
2 R. S. Lillard, J. Kruger, W. S. Tait and P. J. Moran, *Corrosion*, 1995, **51**, 251–259.
3 I. Annergren, D. Thierry and F. Zou, *J. Electrochem. Soc.*, 1997, **144**, 1208–1215.
4 F. Zou and D. Thierry, *Electrochim. Acta*, 1997, **42**, 3293–3301.
5 E. Bayet, F. Huet, M. Keddam, K. Ogle and H. Takenouti, *J. Electrochem. Soc.*, 1997, **144**, L87–L90.
6 E. Bayet, F. Huet, M. Keddam, K. Ogle and H. Takenouti, *Electrochim. Acta*, 1999, **44**, 4117–4127.
7 A. M. Mierisch, J. Yuan, R. G. Kelly and S. R. Taylor, *J. Electrochem. Soc.*, 1999, **146**, 4449–4454.
8 L. V. S. Philippe, G. W. Walter and S. B. Lyon, *J. Electrochem. Soc.*, 2003, **150**, B111–B119.
9 A. M. Mierisch and S. R. Taylor, *J. Electrochem. Soc.*, 2003, **150**, B303–B308.
10 G. Baril, C. Blanc, M. Keddam and N. Pébère, *J. Electrochem. Soc.*, 2003, **150**, B488-B493.
11 L. Beaunier, I. Epelboin, J. C. Lestrade and H. Takenouti, *Surf. Technol.*, 1976, **4**, 237–254.
12 W. Funke, *Prog. Org. Coat.*, 1981, **9**, 29–46.
13 K. Barton, S. Bartonova and E. Beranek, *Werkst. Korros.*, 1974, **25**, 659–663.
14 M. Rohwerder, E. Hornung and M. Stratmann, *Electrochim. Acta*, 2003, **48**, 1235–1243.

7

Initial stages of localised corrosion by pitting of passivated nickel surfaces studied by scanning tunnelling microscopy (STM) and atomic force microscopy (AFM)

V. MAURICE, T. NAKAMURA, L. H. KLEIN and P. MARCUS, ENSCP, France

7.1 Introduction

Despite a considerable amount of published data,[1,2] some fundamental aspects of the mechanisms operating in the early stages of pitting of passivated metal surfaces in chloride-containing solutions remain to be investigated in detail. In particular, nanometer and sub-nanometer scale data on the modifications of the structure of the passivated surface associated with the stages of passivity breakdown and metastable pitting are necessary to elucidate the relationship between the structure of the passivated surface and its reactivity in chloride-containing electrolytes. In this paper, recent results obtained on nickel single-crystal model surfaces are reported to illustrate the application of Scanning Tunnelling Microscopy (STM) and Atomic Force Microscopy (AFM) to the study of passivity breakdown and pitting.

A prerequisite of such studies is a good control of the passivated surface. The chemical composition[3–20] and structure[21–31] of the passive film formed on nickel are well documented. A Ni(II) hydroxylated oxide is formed. It is well described by a bilayer model with the inner part consisting of nickel oxide (NiO) and with the outer part consisting of surface hydroxylated NiO or bulk nickel hydroxide, $Ni(OH)_2$.[7–19,27,28,30] In acid electrolytes, the thickness of the passive film has been found to range between 0.9 and 1.2 nm,[4,5,7–9,10,17,19] some authors reporting a small gradual increase up to 2 nm with increasing potential.[15,18,27,28,30] The structure is crystalline with NiO growing along the (111) direction stabilised by surface hydroxylation. The surface of the inner NiO(111) crystalline structure, observed *ex situ* and *in situ*, is facetted as a result of a tilt of the oxide lattice with respect to the substrate lattice.[23,24,26–30] A non-crystalline structure, observed *in situ*,[22,27,28,30] has been assigned to a thicker and likely porous layer of hydrated hydroxide [possibly α-$Ni(OH_2)$] covering the inner NiO(111) crystalline structure.[27,28]

Recent studies have shown that the initial stages of pitting of Ni can be followed by scanning tunnelling microscopy (STM).[32,33] The measurements, performed by *ex situ* STM on Ni(111) single-crystal surfaces pre-passivated in a chloride-free sulfuric acid solution and subsequently exposed to chloride above the pitting potential, revealed localised attacks of the metal surface with a lateral size of 43 ± 13 nm at the surface, a depth of 3 ± 1 nm and a density of $\sim 3 \times 10^8$ cm^{-2}, not observable by usual current transient measurements. Their assignment to metastable (i.e. repassivated) pits was confirmed by the observation, inside the pits, of a crystalline atomic structure having the same symmetry and parameters as the structure of the passivated surface before exposure to chloride. This structure was also observed by *in situ* measurements in the non-pitted areas exposed to chloride.[34] The location of the pits at the grain boundaries of the crystalline structure of the passive film and their preferential elongation in the direction of the substrate steps show the deterministic role of the structure of the passive film and substrate in passivity breakdown.

7.2 Experimental methods

The samples used in this work were 10 and 12 mm diameter single-crystalline disks of nickel, oriented (111) within ±1° by x-ray Laüe back diffraction. Surface preparation is quite critical for the (sub-)nanometer scale identification of topographic features related to the initiation of pitting. The treatment included successively mechanical polishing with a diamond suspension (down to a grain size of 0.25 μm), electrochemical polishing in a 55% vol. solution of H_2SO_4 (at 0.5 A cm^{-2} for 10–15 min) and annealing at 1275 K for 15 h in a flow of purified hydrogen (6N purity) at atmospheric pressure. The sample was then transferred in air to the electrochemical cell of the STM/AFM where the surface (0.78 or 1.13 cm^2) was exposed to the electrolyte. The electrolytes (pH 2.8) were 0.05 M H_2SO_4 + 0.095 M NaOH without and with 0.05 M NaCl, prepared from high-purity chemicals and Millipore water (resistivity >18 MΩ cm).

The STM/AFM observations were performed with a Molecular Imaging instrument. A modified electrochemical cell was used. It consists of a Au ring counter electrode, a Pt reference electrode, the Ni(111) surface and the electrolyte (Fig. 7.1). The electrolyte (300–400 μl) is maintained by surface tension between the working electrode and the ring counter electrode. Such a configuration allows a good control of the cleanliness of the experiment and prevents the occurrence of crevice corrosion that was observed at occluded areas in the presence of chloride when a cell with a Viton O-ring sealing was used. This design also allows *in situ* STM (Fig. 7.1b) and AFM measurements. The potential of the Pt reference electrode was calibrated using the characteristic features of the polarization curve ($E_{SHE} = E_{Pt} +$

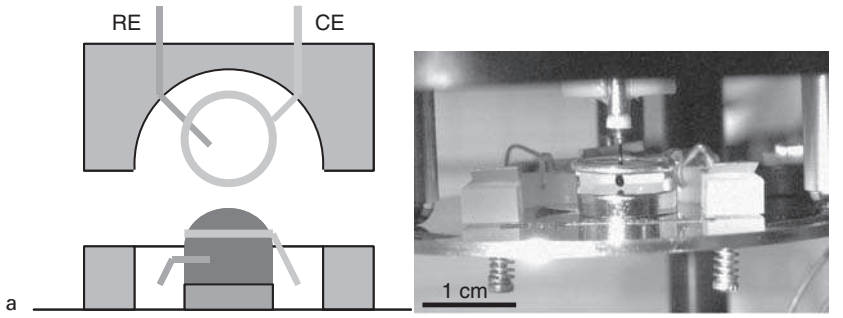

7.1 *a* Schematic views of the modified electrochemical cell, top shows the reference and counter electrodes and the electrode holder, bottom shows the cell mounted with the electrolyte above the sample surface; *b* side view of the assembled EC-STM set up showing the tip covered with Apiezon wax ready to engage.

0.75 V) and proved to be sufficiently reproducible and stable. Before each measurement, the two Pt electrodes were cleaned first in a 2:1 mixture of concentrated H_2SO_4 and H_2O_2, then in concentrated HNO_3, and finally thoroughly rinsed with Millipore water.

For STM, the tips were produced from W wire etched in KOH and isolated with Apiezon wax. The setpoint currents (I_t) used were in the range of 0.7 to 3 nA and the images of the passivated surface were empty-states images (electrons tunnelling from the tip to the surface). For AFM, Si tips (radius of curvature of 10 nm) were used. Images were acquired in the intermittent contact ('Tapping') mode at the resonance frequency of the cantilever (~68 kHz). STM and AFM images were acquired in the topographic mode.

After mounting, the electrochemical cell was connected at $-0.05\,V_{SHE}$. The natural oxide formed by exposure to air of the Ni surface was reduced cathodically at $-0.25\,V_{SHE}$, i.e. below the corrosion potential of $\sim 0\,V_{SHE}$. Then, the surface was passivated (in the chloride-free solution) by stepping the potential to $+0.55\,V_{SHE}$. Afterwards, the potential was increased stepwise by increments of 0.1 V up to $+1.05\,V_{SHE}$ in the absence or presence of chloride (0.05 M).The upper value is above the pitting potential in the Cl^--containing solution. The values of the pitting potential ($+0.9\,V_{SHE}$) and repassivation potential ($+0.45\,V_{SHE}$) were measured from polarisation curves recorded at $1\,mV\,s^{-1}$ in the presence of chloride (0.05 M) in a classical electrochemical cell (Fig. 7.2).

In the *in situ* STM experiments, the topography of the metallic surface before passivation was first checked at $-0.25\,V_{SHE}$. The passivated surface was monitored by recording sequences of images at potentials ranging from

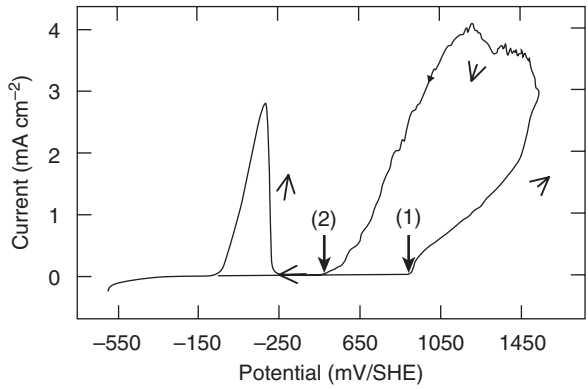

7.2 Polarisation curve of the Ni(111) surface in 0.05 M H_2SO_4 + 0.095 M NaOH + 0.05 M NaCl (pH 2.9) at a scan rate of 1 mV s^{-1}. Stable pitting (1) and repassivation (2) are observed at 0.9 and 0.45 V_{SHE}, respectively.

0.85 to 1.05 V_{SHE}. In the *ex situ* AFM experiments, the topography was observed after annealing, after passivation at 0.55 V_{SHE} for 30 min and after increasing the potential stepwise (0.1 V per step) every 30 min up to 1.05 V_{SHE}.

7.3 Results and discussion

In situ STM measurements have been used to study the effect of chloride and potential on the dissolution of the passivated surface. Figure 7.3 shows a sequence of EC-STM images of the passivated surface recorded at +0.85 V_{SHE} in the absence of chloride.

The topography is characteristic of the crystalline passivated surface. It is assigned to the growth along the (111) direction of a passive film consisting of NiO and having a hydroxylated surface. The formation of facets is due to a tilt between the oxide and substrate lattices (values ranging from 3 to 13° have been reported[24,28,29]). Their triangular shape results from the stabilisation of the facet edges along the close-packed ⟨1–10⟩ directions of the oxide lattice growing in anti-parallel epitaxy on Ni(111).[29] A similar facetted surface is observed in the presence of chlorides.[34]

The observed dissolution of the passivated surface is a 2D process localised at step edges. It is marked in one site in Fig. 7.3. The dissolution leads to a progressively decreasing size of the facets by a step flow process. No 3D dissolution of the oxide lattice (i.e. pitting) is observed in these conditions. The process is similar to that observed for the active dissolution of non-passivated metal surfaces at moderate potential on Ni[26] and Cu[35]. It

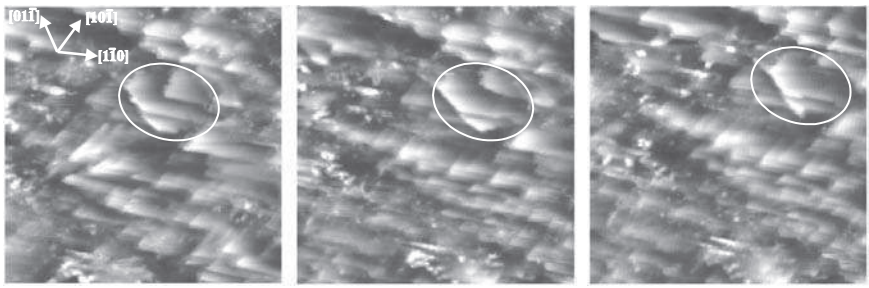

a b c

7.3 Sequence of topographic EC-STM images (75 nm × 75 nm, 63 s per image, $E_{tip} = -0.6$ V, $I_{tip} = 0.85$ nA, Z range = 1.14 nm) showing the dissolution of the passivated Ni(111) surface at +0.85 V_{SHE} in 0.05 M H_2SO_4 + 0.095 M NaOH (pH 2.9). The crystallographic directions of the oxide are indicated. The open circles show a localised area of dissolution.

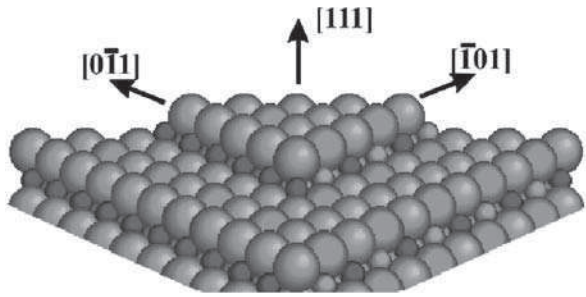

7.4 Atomic model of a (111) oriented facet delimited by edges oriented along the close-packed directions of the NiO lattice. Oxygen (or surface hydroxyls) and Ni are represented by large and small spheres, respectively.

demonstrates the role of the step edges as preferential reactivity sites of the surface of the passive film. A major observation is that the dissolution of the oxide film strongly depends on the local structure of the surface and, in particular, on the crystallographic orientation of the facet edges. It can be observed that the facets having edges oriented along the close-packed ⟨1–10⟩ directions of the oxide lattice dissolve much less rapidly, due to the higher coordination of the surface atoms at these edges, than the facets being delimited by edges having higher index directions. A resulting phenomenon is that the passivated surface slowly changes with time towards a topography constituted of more stable oxide facets, delimited by the close-packed directions of the NiO lattice. The atomic model of such a stable facet is illustrated in Fig. 7.4. The orientation of the facet edges along the

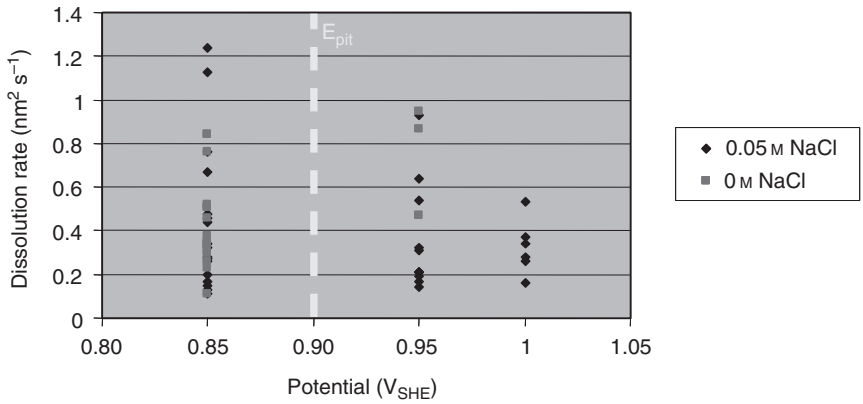

7.5 Dissolution rate of the passivated Ni(111) surface in 0.05 M H_2SO_4 + 0.095 M NaOH (pH 2.9) measured by EC-STM in the absence or presence of chlorides (0.05 M NaCl) at the potentials of 0.85, 0.95 and 1 V_{SHE}.

close-packed directions of the NiO lattice produces steps that are oriented along the {100} planes, the most stable orientations of the NiO structure.[36]

The dissolution rate of the facets can be obtained by measuring the decrease in size for a known elapsed time between two STM images. Values have been extracted from corrosion tests performed on different surfaces polarised at potentials below and above the pitting potential and in the presence (0.05 M NaCl) or absence of chlorides. They are compiled in Fig. 7.5. The values obtained at +0.85 V_{SHE} range from 0.11 to 0.95 $nm^2 s^{-1}$ with an average of 0.44 ± 0.17 in the absence of chloride. Values measured at the same potential in the presence of chloride range from 0.11 to 1.24 with an average of $0.44 \pm 0.25\,nm^2 s^{-1}$. A large dispersion is observed in both cases. It is assigned to the local structure of the facet edges that can slow down and even stop the dissolution depending on its orientation. Given that there are 13.3 Ni(II) cations per nm^2 on a NiO(111) surface, this average value amounts to 6 ± 3 Ni^{2+} cations dissolving per second. At higher potentials, similar average values of the dissolution rate are obtained ($0.35 \pm 0.19\,nm^2 s^{-1}$ at 0.95 V_{SHE} and $0.32 \pm 0.09\,nm^2 s^{-1}$ at 1 V_{SHE}). No significant effect of the presence of chlorides is observed at a potential of 0.95 V_{SHE} (i.e above the pitting potential value).

These results show that no significant increase of the average dissolution rate of the oxide lattice is measured when the potential increases from below to above the pitting value. This shows that the potential drop at the passive film electrolyte interface, which is associated with the surface reaction leading to the dissolution of the oxide, remains constant. The results also show no significant influence of the presence of chloride on the average

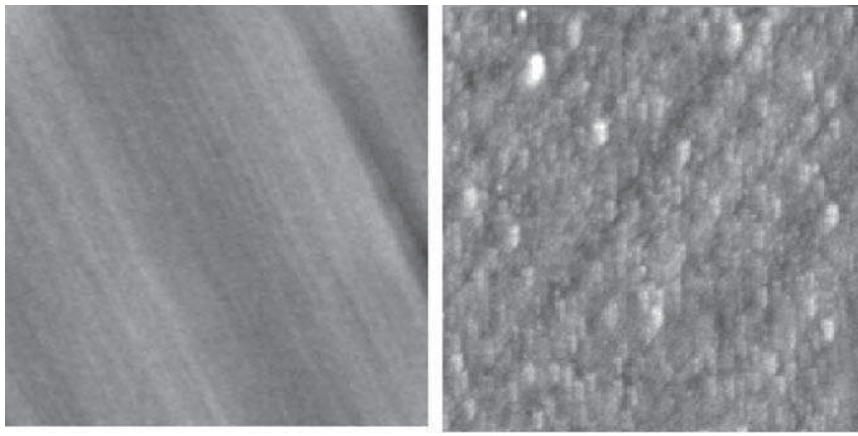

7.6 Topographic AFM images (1000 nm × 1000 nm, *Z* range = 3 nm) of the Ni[111] surface after *a* annealing and *b* passivation for 30 min in 0.05 M H_2SO_4 + 0.095 M NaOH (pH 2.9) at +0.55 V_{SHE}.

dissolution rate of the oxide lattice of the passive film. This indicates that the surface reaction of dissolution of the oxide at regular step edges of a well-passivated surface is not enhanced by the presence of chloride in the electrolyte in steady-state conditions. This result seems to be in contrast with the mechanism of passivity breakdown based on an enhanced dissolution of the barrier oxide layer in the presence of chlorides.[1] However, the chloride may have a significant role in specific sites where the dissolution of the oxide is expected to be fast on the basis of the mechanism revealed by the STM results. Such sites likely correspond to grain boundaries of the oxide film, as shown by the previous observations of pit initiation at these sites,[32,33] and confirmed by the AFM results reported below. Grain boundaries can be described by a high density of step edges forming a line defect propagating through the oxide layer. If they are not oriented along the close-packed directions of the oxide lattice, the dissolution of the step edges forming the grain boundary will be initiated and will 'open' the grain boundary. A possible role of the chloride, at this stage, could be to retard the reorientation of the dissolving step edges along the more stable close-packed directions of the oxide lattice, which is necessary to stop the dissolution of the oxide, as shown by the results presented above.

Ex situ AFM measurements were used to further investigate passivity breakdown and the effects of chlorides on the initiation of localised corrosion.

Figure 7.6 shows two AFM images showing the modifications of the topography of the Ni(111) surface induced by its passivation at +0.55 V_{SHE} (in the absence of chloride). Before passivation, the terrace and step

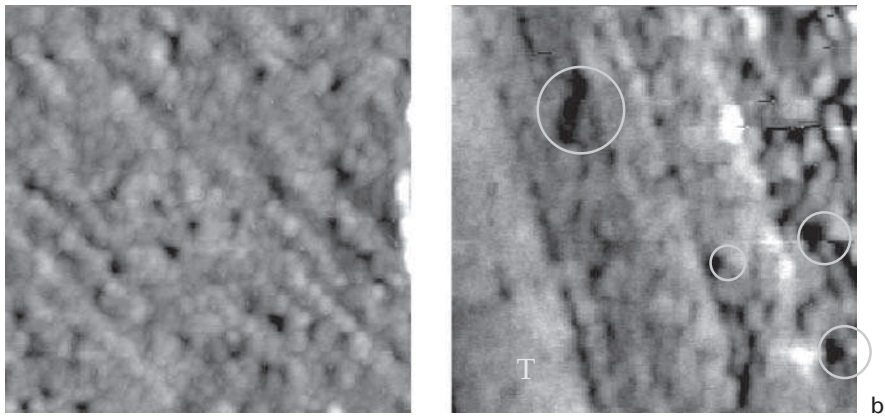

7.7 Topographic AFM images (500 nm × 500 nm, *Z* range = 3 nm) of the Ni(111) surface after pre-passivation for 30 min in 0.05 M H_2SO_4 + 0.095 M NaOH (pH 2.9) at +0.55 V_{SHE}, and subsequent increase of the potential stepwise (steps of 0.1 V) every 30 min up to +1.05 V_{SHE} in: *a* the absence or *b* the presence of chloride.

topography of the annealed surface is clearly observed (Fig. 7.6a). The steps are monoatomic (height of 1.9 ± 0.2 nm, in excellent agreement with the reticular distance of 0.203 nm for Ni(111)). After passivation at +0.55 V_{SHE}, the surface is roughened as previously observed by STM.[24,28,30] In Fig. 7.6b, the orientation of the steps of the substrate can still be identified, but the surface is covered with platelets assigned to the grains of the passive film. It was the facetted surface of these grains that was revealed by the typical higher magnification STM images shown in Fig. 7.3. The platelets completely cover the surface. Their lateral size, varying from 50 to 230 nm, suggests a varying degree of advancement of the coalescence of the oxide grains.

Between the platelets, depressions with a depth varying from 0.4 to 1.4 nm are measured. Their formation is assigned to the dissolution occurring on the not-yet passivated (or less protected) sites that are formed in the transient process of growth of the oxide film, before complete passivation of the surface. This phenomenon of localised corrosion of the partially passivated surface has been previously observed by *in situ* STM.[30] These AFM measurements confirm the topographic nature of these sites resulting from a more prolonged dissolution of the surface before passivation.

Figure 7.7 shows the modifications observed after increasing the potential up to +1.05 V_{SHE} and the effect of the presence of chloride in the solution (0.05 M). In the absence of chloride (Fig. 7.7a), the surface still appears to be covered by platelets. A major difference with the surface passivated at +0.55 V_{SHE} is the depth of the depressions observed between the platelets.

It ranges from 2.2 to 3.8 nm which is significantly larger than the depth of the depressions measured after passivation at +0.55 V_{SHE}. It is also significantly larger than the thickness of the passive film formed in these conditions (<2 nm). The lateral size of these depressions ranges from 20 to 30 nm at the surface and their density is $(3 \pm 2) \times 10^{10}\,cm^{-2}$. They are similar to the depressions previously observed by STM after exposing to chlorides the Ni(111) surface pre-passivated at +0.85 V_{SHE}.[32] These AFM measurements confirm their topographic nature. These depressions can therefore be assigned to local sites of the passivated surface where enhanced corrosion was produced by the increase of the potential in the passive range, in the absence of chloride. This implies that the surface, pre-passivated at +0.55 V_{SHE}, has been locally modified (i.e. depassivated), with a local enhancement of the corrosion of the substrate, and subsequently repaired (i.e. repassivated). It cannot be concluded, however, whether these events correspond to the exposition of the bare metal surface to the electrolyte (complete passivity breakdown) or only results from a temporary enhancement of dissolution without complete removal of the passive film. The genuine topographic nature of the observed depressions indicates nevertheless that the original passive film has been totally renewed to match the topography of a locally corroded substrate surface. One essential new result reported here is that such local modifications of the passive film occur in the absence of chloride, showing that the key role of the chloride in pitting is not related to the initiation of these modifications.

In the presence of chlorides (Fig. 7.7b), the surface also appears covered by platelets corresponding to the oxide grains. Their facetted surface is not resolved in this measurement, but is confirmed by the EC-STM results presented in Fig. 7.3. Between the grains, depressions are observed, most of them having the dimensions of the depressions observed previously. However, significantly larger depressions are also observed (marked by circles in Fig. 7.7b). Their lateral dimension ranges between 40 and 50 nm at the surface and their depth between 5 to 6 nm. Their density is $(2 \pm 1) \times 10^{9}\,cm^{-2}$ range. The values are in agreement with those of the localised attacks of the passivated surface observed by STM after exposing to chlorides the Ni(111) surface pre-passivated at +0.85 V_{SHE}.[32,33] Such attacks were assigned to metastable pits based on the absence of variations of the current characteristic of stable pitting during the corrosion test and on the measurement of the lattice of the passivated surface inside the pits.[32,33] It can also be seen in Fig. 7.7b that an area, marked *T*, corresponding to an extended terrace of the substrate, exhibits many fewer depressions than the rest of the imaged surface where narrower terraces are observed due to a higher density of substrate step edges. This confirms the role of the defects of the substrate (monoatomic step edges) in passivity breakdown previously evidenced by STM.[32]

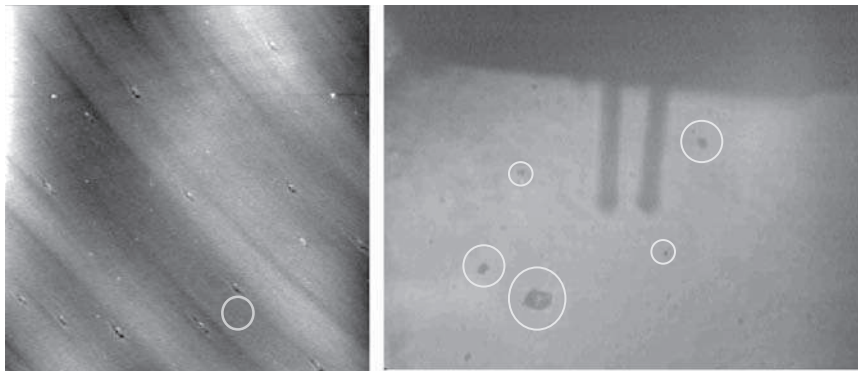

7.8 *a* AFM image (15 μm × 15 μm, *Z* range = 6 nm) and *b* optical micrograph of the Ni(111) surface after increasing the potential from 0.55 to 1.05 V_{SHE} stepwise (steps of 0.1 V) every 30 min in 0.05 M H_2SO_4 + 0.095 M NaOH + 0.05 M NaCl (pH 2.9).

The AFM results presented here confirm the formation of such metastable pits at the nanometer scale in the presence of chlorides. The measured depth clearly demonstrates that pits have been initiated. These measurements indicate that the chlorides have a marked effect in the repair stage following the modifications of passivity initiating an enhanced corrosion of the substrate. The increased size of the metastable pits observed in the presence of chloride suggests that the role of the chloride is to modify and/or retard the stabilisation of the oxide dissolving in the more defective grain boundary sites of the passive film and, thus, to sustain the transient localised corrosion of the substrate initiated by the dissolution of the oxide.

The occurrence of stable pitting was observed in the corrosion tests performed in the presence of chlorides. It was characterised by a steady increase of the current generally observed after the potential step to +1.05 V_{SHE} and could be stopped by stepping the potential down to +0.55 V_{SHE}. The AFM examination of areas of 25 μm × 25 μm or less, chosen randomly on the surface, did not reveal any pits of micrometre or submicrometre dimensions. Figure 7.8a shows one image as an example.

The local defects (one example is circled) observed in this image were already present after the surface preparation and did not result from the corrosion test. Pits of micrometre size could, however, be localised by optical microscopy as shown in Fig. 7.8b. Their lateral size ranges from 10 to 50 μm. Their density, estimated to be $5 \times 10^2\,cm^{-2}$, is low, which explains why they could not be localised when the AFM tip was positioned randomly on the sample surface. These observations show the extreme difficulty of using AFM to study the transition between metastable and stable pitting on well-prepared surfaces due to the low density of the pits. The combina-

tion of optical microscopy and AFM observation can only allow the location of pits already having a size of a few microns or more (i.e. stable pits) but not their initial stages of growth.[37] Samples with a high density of heterogeneities (i.e. inclusions) generating a high density of stable pits can be used.[38] However, their surface preparation is quite critical in order to allow nanometre scale observation at and near the inclusions. One possibility to resolve this difficulty could be to use the scanning tip of the AFM instrument during the corrosion test in order to generate a local modification of the passivated surface that could lead to stable pitting.

7.4 Conclusions

In situ EC-STM and *ex situ* AFM measurements have been combined to investigate the effects of chlorides and potential in the initial stages of localised corrosion by pitting of a Ni(111) surface pre-passivated in 0.05 M H_2SO_4 + 0.095 M NaOH (pH 2.8). The STM measurements show the deterministic role of the structure of the surface of the passive film on its dissolution, independently of the subsequent addition of chloride (0.05 M) in the electrolyte. The passive film dissolves at the edges of the facets resulting from the tilted epitaxy between the NiO(111) oxide and the Ni(111) substrate lattice. This leads to a 2D step flow process stabilising the facets with edges oriented along the close-packed directions of the oxide lattice. The average dissolution rate, measured to be $0.44 \pm 0.25\,nm^2\,s^{-1}$, does not vary significantly with applied potential below or above the pitting value (~0.9 V_{SHE}), or with the presence or not of chlorides in the electrolyte. This indicates that the potential drop at the passive film/electrolyte interface, associated with the surface reaction of dissolution of the oxide film, remains constant. This reaction is not accelerated by the presence of chloride at the regular step edges of the well-passivated surface. The chlorides may, however, prevent the stabilisation of the dissolving oxide film in the more disoriented steps forming the grain boundaries of the passive film.

The AFM measurements show that increasing the potential in the passive range by successive potential steps up to 1.05 V_{SHE} in the absence of chlorides causes the roughening of the pre-passivated surface with the formation of local depressions of nanometer dimensions (20 to 30 nm at the surface) and a density of $(3 \pm 2) \times 10^{10}\,cm^{-2}$. The depth of 2.2 to 3.8 nm is indicative of the corrosion of the substrate, locally enhanced following dissolution of the passive film, but not necessarily resulting from passivity breakdown and exposure of the bare metal surface to the electrolyte. In the presence of chloride, larger (40 to 50 nm at the surface and 5 to 6 nm deep) localised attacks of the substrate surface with a density of $(2 \pm 1) \times 10^9\,cm^{-2}$ were observed. These sites of corrosion are assigned to metastable pits. Their growth was observed in the presence of chloride whereas their

initiation was observed in the absence of chloride suggesting a predominant effect of the chlorides which is to prevent the stabilisation of the oxide dissolving at the grain boundaries of the passive film, thus sustaining the transient localised corrosion of the substrate initiated by the local dissolution of the oxide and, finally, blocking the repassivation.

7.5 References

1 H.-H. Strehblow, *Mechanisms of Pitting Corrosion in Corrosion Mechanisms in Theory and Practice*, 2nd ed, Chapter 7, (Ed. P. Marcus), M. Dekker Inc., New York, USA, 2002, and references therein.
2 G. S. Frankel, *J. Electrochem. Soc.*, 1998, **145**, 2186–2198.
3 B. MacDougall and M. Cohen, *J. Electrochem. Soc.*, 1975, **122**, 383–385.
4 B. MacDougall and M. Cohen, *J. Electrochem. Soc.*, 1976, **123**, 191–197.
5 B. MacDougall and M. Cohen, *J. Electrochem. Soc.*, 1976, **123,** 1783–1789.
6 A. Jouanneau, M. Keddam and M. C. Petit, *Electrochim. Acta*, 1976, **21**, 287–292.
7 T. Dickinson, A. F. Povey and P. M. A. Sherwood, *J. Chem. Soc. Faraday Trans.*, 1977, **73**, 327–343.
8 P. Marcus, J. Oudar and I. Olefjord, *J. Microsc. Spectrosc. Electron.*, 1979, **4**, 63–72.
9 B. P. Lochel and H.-H. Strehblow, *J. Electrochem. Soc.*, 1984, **131**, 713–723.
10 D. F. Mitchell, G. I. Sproule and M. J. Graham, *Appl. Surf. Sci.*, 1985, **21**, 199–209.
11 F. Hahn, B. Beden, M. J. Croissant and C. Lamy, *Electrochim. Acta*, 1986, **31**, 335–342.
12 P. Delichere, A. Hugot-LeGoff and N. Yu, *J. Electrochem. Soc.,* 1986, **133**, 2106–2108.
13 R. E. Hummel, R. J. Smith and E. D. Verink, *Corros. Sci.*, 1987, **27**, 803–813.
14 B. Beden and A. Bewick, *Electrochim. Acta*, 1988, **33**, 1695–1699.
15 H.-W. Hoppe and H.-H. Strehblow, *Surf. Interf. Anal.*, 1989, **14**, 121–131.
16 B. M. Biwer, M. J. Pellin, M. W. Schauer and D. M. Gruen, *Surf. Interface Anal.*, 1989, **14**, 635–646.
17 F. T. Wagner and T. E. Moylan, *J. Electrochem. Soc.*, 1989, **136**, 2498–2506.
18 H.-W. Hoppe and H.-H. Strehblow, *Corros. Sci.*, 1990, **31**, 167–177.
19 P. Marcus, *Electrochemistry at Well-Defined Surfaces*, J. Oudar, P. Marcus and J. Clavilier (Eds.) Special Volume of *J. Chim. Phys.*, 1991, **88**, 1697–1711.
20 P. Marcus and J.-M. Herbelin, *Corros. Sci.*, 1993, **34**, 1123–1145.
21 J. Oudar and P. Marcus, *Appl. Surf. Sci.*, 1979, **3**, 48–67.
22 R. Cortes, M. Froment, A. Hugot-LeGoff and S. Joiret, *Corros. Sci.*, 1990, **31**, 121–127.
23 V. Maurice, H. Talah and P. Marcus, *Surf. Sci.*, 1993, **284**, L431–L436.
24 V. Maurice, H. Talah and P. Marcus, *Surf. Sci.*, 1994, **304**, 98–106.
25 S.-L. Yau, F.-R. F. Fan, T. P. Moffat and A. J. Bard, *J. Phys. Chem.*, 1994, **98**, 5493–5499.
26 T. Suzuki, T. Yamada and K. Itaya, *J. Phys. Chem.*, 1996, **100**, 8954–8961.
27 D. Zuili, V. Maurice and P. Marcus, *Passivity and Its Breakdown* P. Natishan, H. S. Isaacs, M. Janik-Czachor, V. A. Macagno, P. Marcus and M. Seo (Eds.), PV 97–26, The Electrochemical Society Proceedings Series, Pennington, NJ, 1997, p. 1013–1024.

28 D. Zuili, V. Maurice and P. Marcus, *J. Electrochem. Soc.*, 2000, **147**, 1393–1400.
29 O. M. Magnussen, J. Scherer, B. M. Ocko and R. J. Behm, *J. Phys. Chem. B*, 2000, **104**, 1222–1226.
30 J. Scherer, B. M. Ocko and O. M. Magnussen, *Electrochim. Acta*, 2003, **48**, 1169–1191.
31 N. Hirai, H. Okada and S. Hara, *Trans. JIM*, 2003, **44**, 727–730.
32 V. Maurice, V. Inard and P. Marcus, *Critical Factors in Localized Corrosion III*, P. M. Natishan, R. G. Kelly, G. S. Frankel and R. C. Newman (Eds.), The Electrochemical Society Proceedings Series, PV 98–17, Pennington, NJ, 1999, p. 552–562.
33 V. Maurice, L. H. Klein and P. Marcus, *Electrochem. Solid-State Lett.*, 2001, **4**, B1–B3.
34 V. Maurice, L. H. Klein and P. Marcus, *Surf. Interf. Anal.*, 2002, **34**,139–143.
35 M. R. Vogt, A. Lachenwitzer, O. M. Magnussen and R. J. Behm, *Surf. Sci.*, 1998, **399**, 49–69.
36 D. Wolf, *Phys. Rev. Lett.*, 1992, **68**, 3315–3318.
37 J. Li and D. Lampner, *Colloids Surfaces A*, 1999, **154**, 227–237.
38 J. O. Park, C.-H. Paik, Y. H. Huang and R. C. Alkire, *J. Electrochem. Soc.*, 1999, **146**, 517–523.

8

In situ atomic force microscopy (AFM) study of pitting corrosion and corrosion under strain in a 304L stainless steel

F. A. MARTIN, J. COUSTY, J.-L. MASSON and C. BATAILLON, CEA, France

8.1 Introduction

For evident economic reasons, the study of localised corrosion of steels in aggressive media is crucial. It has been investigated for over 50 years so that now the kinetics of pitting and stress-induced corrosion have become more closely defined.

Corrosion as well as metallurgy and mechanical characterisation of stainless steels have been intensely studied by electronic microscopy (SEM, TEM) and classical electrochemical ways. These investigation techniques do not give an accurate picture of the very first steps in the mechanism of localised corrosion because they do not allow the instrument to closely map the surface while being in a corrosive liquid medium.

With the advent of local probe microscopy like scanning tunnelling microscopy (STM) and atomic force microscopy (AFM) 20 years ago,[1] *in situ* studies of corrosion have become possible. In metallurgy indeed, STM and AFM have proved to be very useful tools to study steels. The morphology of phases like martensite or of precipitates have been investigated by air STM. The atomic structure of passive films on austenitic steel,[2] pure iron[3] or pure chromium[4] have been imaged by STM. Surface effects of plastic deformation on steels have also been analysed by these local probe microscopies.[5] *In situ* AFM studies have been carried out on pitting corrosion of stainless steels and show the relationship between pits and precipitates on the surface.[6,7,8] To our knowledge, *in situ* stress-induced corrosion of stainless steels has never been studied by AFM. This article will relate the first attempts to fill this gap.

This paper reports the first results of an *in situ* AFM study of localised corrosion (pitting and stress-induced corrosion) of a 304L stainless steel. Therefore an original set-up including an AFM, a traction device and an electrochemical cell has been developed.

8.2 Experimental method

The original set-up developed in the laboratory needed to take into account many constraints; the sample itself had to be shaped to answer the drastic criteria of the study and the system had to be designed with respect to the congestion due to each component, which was not compressible. The set-up comprises an atomic force microscope, a traction device and an electrochemical cell.

8.2.1 Sample

The 304 L stainless steel used has the chemical composition given in Table 8.1 (wt%). The shape of the test pieces is determined by three main points: 1) the room given to the sample in the set-up, 2) the fact that the strains must be localised under the scanning area (max $100\,\mu m \times 100\,\mu m$), 3) the possibility of adapting an electrochemical cell to the sample. Therefore, the strains in samples with different shapes have been simulated with CATIA V.5[9] and the definitive design of the test pieces are shown in Fig. 8.1. The test pieces are rectangular ($57\,mm \times 19\,mm \times 0.8\,mm$) with two holes in

Table 8.1 Chemical composition of the 304L (wt%)

Composition (wt%)								
C	Mn	S	Ni	Cr	Mo	N	Cu	Fe
0.018	1.72	0.0005	10.14	18.68	0.35	0.072	0.15	balance

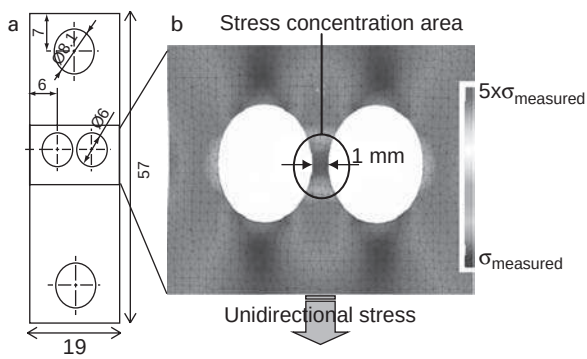

8.1 *a* Test piece shape and dimensions (mm) and *b* strain simulation with CATIA V.5. showing the concentration of stress in a very small area for this conformation of the sample. The force applied is 350 N. The figure shows the final state of the test piece.

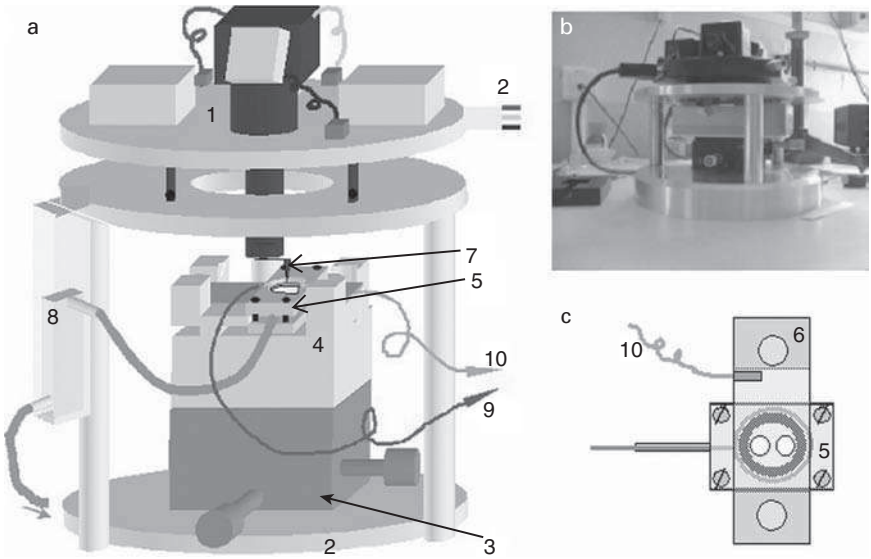

8.2 *a* General scheme of the set-up: 1 AFM head from Molecular Imaging in 'stand-alone' configuration, 2 base isolated from high-frequency vibrations, 3 *x–y* stage, 4 traction plate, 5 electrochemical cell, 6 sample, 7 AFM tip, 8 aqueous solution reservoir, 9 silver wire (CE) and 10 copper wire connected to the test piece; *b* picture of the experimental apparatus (scale 1 : 10); *c* upper view of the electrochemical cell mounted on the sample.

order to concentrate the stress in a small area. After machining, they were polished mechanically by SiC grains and diamond paste to a 3-μm grain size, then polished chemical-mechanically with colloidal silica from STRUERS (40 nm particle size) for 20 h. They were washed in distilled water, then in ethyl alcohol with ultrasonic stirring and dried with N_2. The austenitic (fcc) grain structure was completely revealed by the chemical-mechanical polishing. The typical corrugation (RMS) of the surface was about 1 Å for areas of at least 1 μm^2.

8.2.2 Description of the set-up

The atomic force microscope (AFM) used is a Picoscan II from Molecular Imaging. It is used in contact mode. It is placed in a 'stand-alone' configuration above a 'line-hole-plane' disc to ensure a good stability and reproducibility of the position of the scanner. The traction device is fixed to the base of the set-up via a vernier *x–y* translation platform to position the sample under the AFM tip. The electrochemical cell is fixed to the test piece, which is attached to the jaws of the traction device. A general scheme of the set-up is presented in Fig. 8.2.

Concerning the electrochemical cell, notice that the working electrode (WE) is the sample and that the counter electrode (CE) is a silver wire, which is also used as a pseudo reference. The potential is applied and controlled by a GAMRY interface. The solution used is a borate buffer ($[H_3BO_3] = 0.1\,mol\,L^{-1}$, $[borax] = 0.002\,mol\,L^{-1}$) with various concentrations of NaCl, pH buffered at 7.5. The whole experiment was made at room temperature (20°C).

The traction device (Deben 5000N) stretches the sample at constant speed (0.02 mm min) while the total force is measured. The scanning area is localised with a CDD camera focused on the AFM tip and the sample (i.e. the whole system: sample + electrochemical cell + traction device) is moved until the tip is pointed to the area between the two holes, in the strain-concentrating zone of the test piece.

8.3 Results and discussion

This study is divided into three parts to validate two by two the techniques associated in the set-up. The first part comprises the evaluation of the ability of the system to scan and map the surface during a traction test. The second part is dedicated to the electrochemical behaviour of the 304L test pieces in corrosive solution and, in the last part, results obtained *in situ* with AFM in solution during traction will be presented.

8.3.1 *In situ* AFM scanning during traction in air

The experiment was carried out in air at room temperature. Because of the configuration of the system (test piece fixed at one end and stress applied to the other end), the scanned area moves during traction. As a consequence, a step-by-step traction is necessary to avoid losing it. The traction speed is $0.02\,mm\,min^{-1}$. After each step, the tip is approached and the same area as before is scanned. The result of this traction observed by AFM is shown in Fig. 8.3. It should be noticed that the force value on the curve is the measured value, which corresponds to a fifth of the strain applied to the sample in the area observed. Furthermore, the spikes observed on the traction curve (see arrows) are due to relaxation of the jaws of the traction system while scanning with the AFM and depend on the scanning duration.

First of all, Fig. 8.3 shows clearly that the grain structure has been revealed by the mechanical-chemical polishing, which may have dissolved preferentially certain orientations of grains. At least six different grains can be enumerated on the images (dashed lines). When the sample is stretched, lines appear inside grains. These lines are all parallel to each other within a grain. This happens when the elastic limit of the test piece is exceeded in the scanning zone. These lines are actually steps with a typical height of

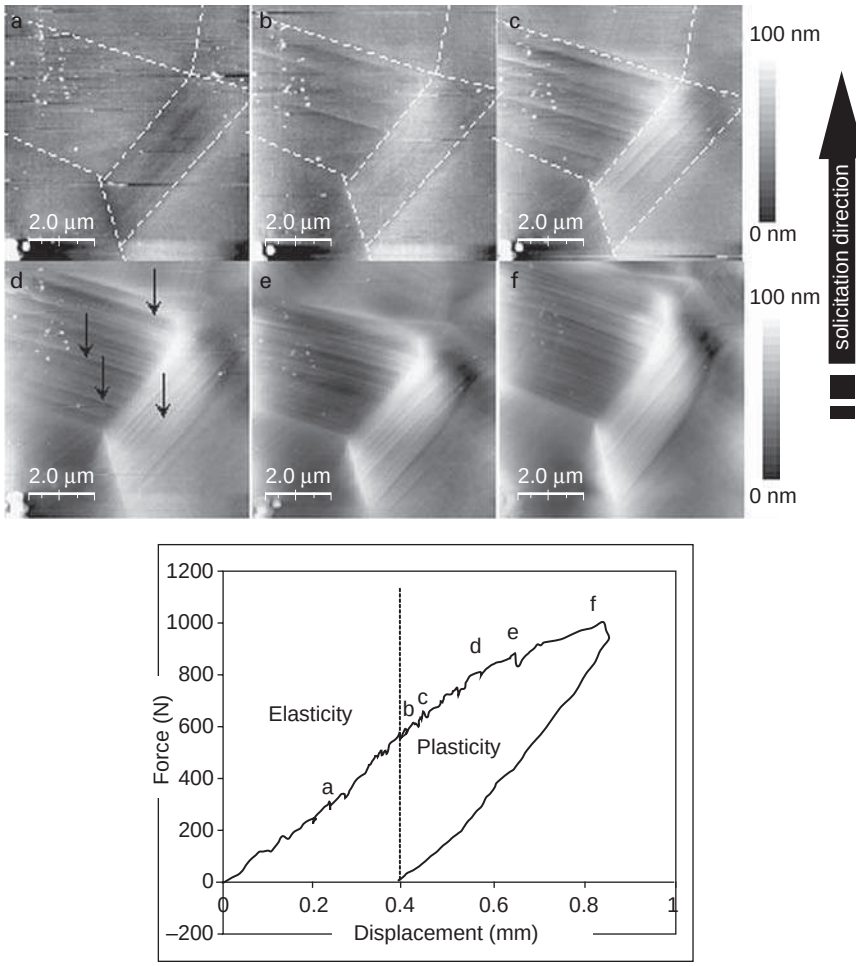

8.3 Topographic images of the same area during traction obtained in contact mode AFM and corresponding traction curve; *a, b, c, d, e, f* correspond to different deformations in the traction curve. While *a* is still in the elastic domain, *b, c, d, e,* and *f* belong to the plastic domain. At least six grains can be seen on the images, delimited here by dashed white lines. The arrows in *d* indicate the slip lines.

2 nm and correspond to slip planes emerging at the surface of the grains. When the deformation rate increases, the density of such slip lines also increases. It is assumed that, the sample being made of an austenitic stainless steel with a fcc crystallographic structure, the slip planes are the dense planes [111].[10,11] This explains why the slip lines are parallel to each other within a grain but have different orientation from grain to grain.

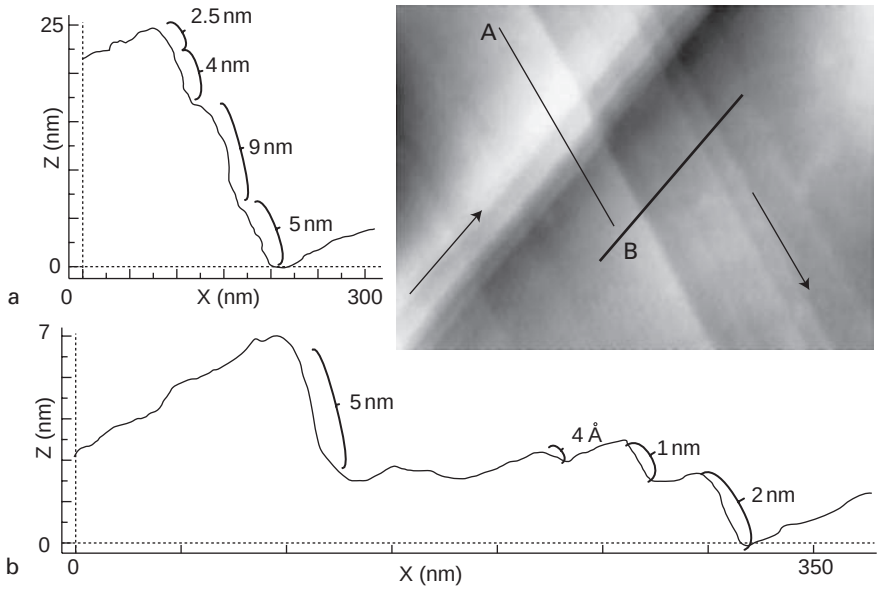

8.4 Topographic contact AFM image of the surface inside a grain. The arrows indicate the trace of the slip planes: 2 different orientations. The profiles A and B taken along the lines A and B, respectively, show steps, the height of which can vary between 4 Å and 9 nm.

Above a certain stress applied to the sample, which is around 800 N as measured on Fig. 8.3, the emerging of another slip plane system occurs inside grains (Fig. 8.4). It is then supposed that the stress at this moment is strong enough to liberate a new and tighter slip system instead of carrying on developing the first one. It is assumed that this secondary slip plane system should belong to the [111] plane type (another one with a direction hardly solicited considering the general stress direction) or to the [110] plane type. At this deformation rate, two slip plane systems are active to ensure the plastic deformation.

Figure 8.4 shows also the high vertical resolution of the set-up: a step 4 Å high can be imaged, which corresponds to few (2 or 3) Bürgers vectors translations. At the very best, it would be possible to make the system able to image a step formed by one Bürgers vector translation. This confirms the choices made during the set-up conception.

If the sample is brought to a higher stress (Fig. 8.5), the strain fields are strong enough to rotate the grains and the step emergence almost stops in favour of this grain loosening.

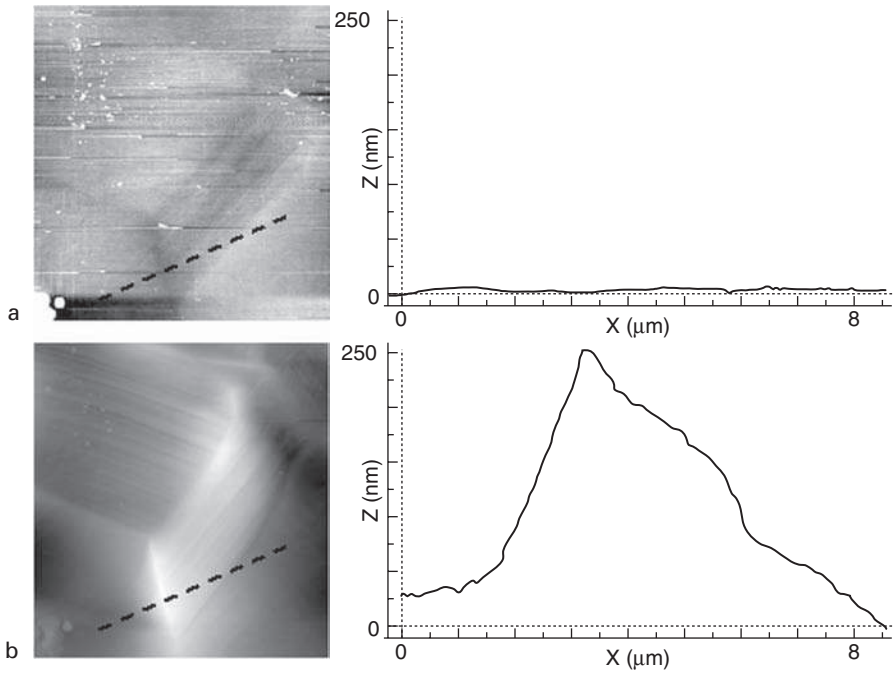

8.5 Topographic contact AFM images of the surface *a* before and *b* after high deformation rate (40% for *b*) and profiles drawn along the dashed lines. After the high deformation, grain loosening occurred, showing as different slopes from grain to grain.

All these observations are consistent with results obtained with an AFM in air after nano-indentation.[12] For the following studies, the traction was stopped before the grain loosening.

8.3.2 304L Stainless steel immersed in chloride solution

In this experiment, a sample was simply immersed in the borate buffer solution with differing concentrations of chloride, waiting for free pitting corrosion to initiate. The free corrosion potential of the stainless steel was measured and then applied to it for hours or days. At the same time, the same area of the sample was scanned with the AFM at different times and the intensity of the current between the sample and the CE was recorded. Pitting corrosion is a well known stochastic phenomenon.[13–16] On the macroscopic scale, pitting occurs after weeks in those conditions and seems not to be accelerated by the Cl^- concentration at room temperature. In order to avoid degradation of the AFM head, which is immersed in the corrosive solution too, *in situ* investigations cannot be pursued beyond three

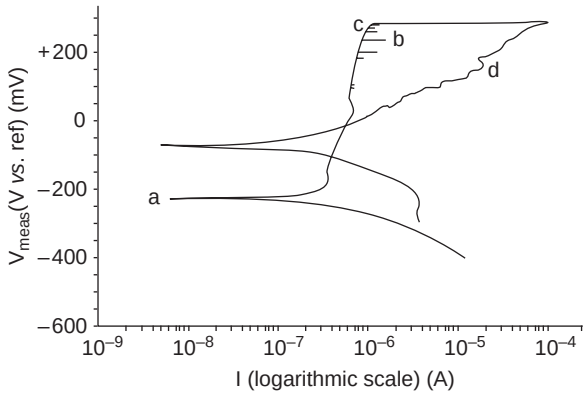

8.6 Cyclic polarisation scan of the 304L polished sample in aqueous borate buffer solution containing 9 g L^{-1} of NaCl, at room temperature: *a* corrosion potential, *b* electrochemical noise before pitting (depassivation / passivation cycles), *c* pitting potential, and *d* return.

full days. The concentrations of NaCl used were 9, 20, 30, 50, 70 and 100 g L^{-1}. In any case, there was no sign of a change at the nanometric level in the outer structure of the stainless steel on ten different areas (100 mm × 100 μm) of the sample. It is due to the fact that, at free corrosion potential, the 304 L stainless steel holds itself at about 300–400 mV under the pitting potential evaluated from cyclic polarisations (this recording is in good agreement with results previously published[17,18]). The cyclic polarisation curve (Fig. 8.6) obtained in borate buffer solution, [NaCl] = 9 g L^{-1}, confirms it. Speed scan was 0.1 mV s^{-1}.

Now, the objective is to hold the potential close to the electrochemical noise and observe what happens with or without traction of the test piece in solution. First, experiments made without stress have revealed difficulties: for potential applied to the sample too close to the pitting potential, unexpected pitting appears and chromium oxides create bichromates. These compounds precipitate and strongly perturb the measurements of the AFM cantilever position.

8.3.3 *In situ* AFM scanning during traction in chloride solution

Since the difficulties encountered for AFM-scanning and controlling the potential at the same time by an electrochemical way have not yet been dismissed, the experiments have been carried out at open circuit potential; that is, at the corrosion potential of the system (sample + CE/Reference electrode). The solution was an aqueous borate buffer, pH = 7.5, with [NaCl] =

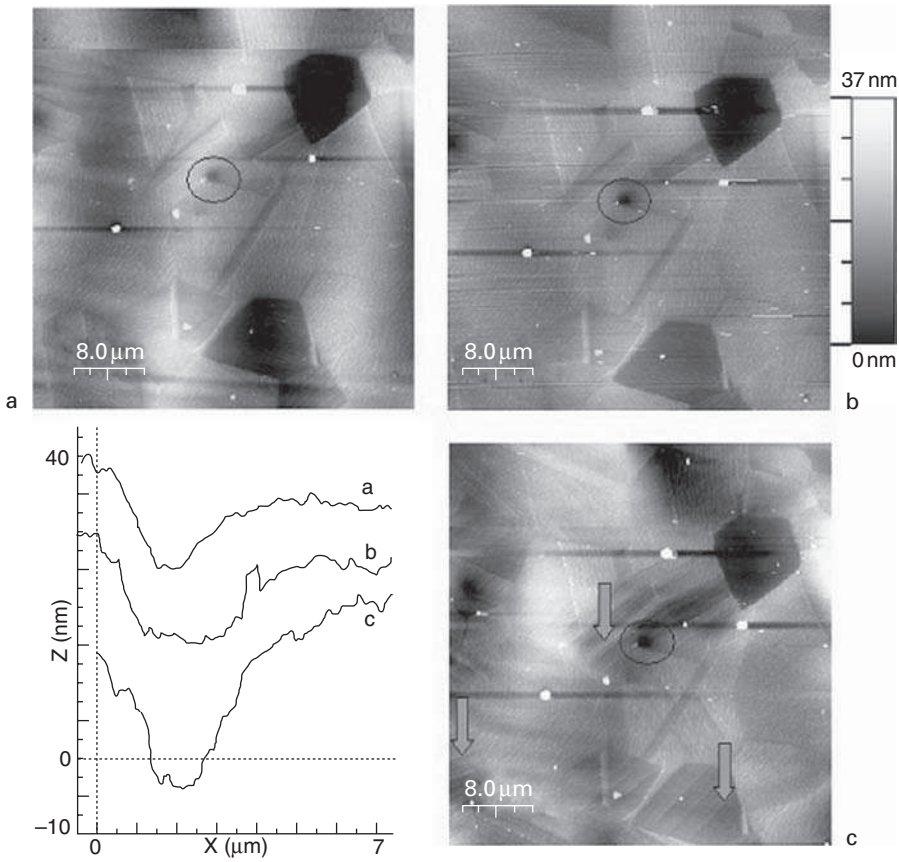

8.7 Evolution of the topography of the surface during traction (same traction curve as in air) at each step *a, b* and *c; a* and *b* are still in the elastic domain whereas *c* is in the plastic one. Time elapsed between *a* and *c*: 48 h. The rings and the horizontal profiles corresponding show the pitting propagation of a pre-existent pit and the arrows show the slip lines in the grains. The *z*-scale is the same in all three images.

1 mol L^{-1}. During AFM scanning, the solution was left open to air at ambient temperature.

A three-step traction was carried out, until the plastic domain was reached, with about 1 h left in between each step in order to scan the whole area and to allow the electrochemical system to stabilise. The traction curves were very similar to the one obtained in air and the quality of the AFM imaging in solution was preserved. Figure 8.7 sums up the experiment.

This experiment shows mainly three features: the limit of elasticity is the same even with the electrochemical cell, which could harden the system,

and the set-up is valuable for such an *in situ* study. Because of the nature of the materials (the AFM is made from stainless steel as well), the complete experiment must not exceed 72 h. Because of the time needed for imaging and for traction, the total duration of the experiment presented here was at least 48 h.

Once the plastic domain is reached, slip lines are clearly visible and are not preferentially attacked by the chloride medium. This is essentially due to the very low duration of the experiment: the stochastic phenomenon of pitting or stress corrosion had not enough time to incubate before the scan was made.

Nonetheless, the chloride solution is corrosive enough to enable pitting propagation on a pre-existing pit. The deepness of the pit indeed increases with time exposure to the solution. Measurements shown on Fig. 8.7 give a good estimation of the deepening rate of the pit, *viz.* at least 5 nm in 48 h, which corresponds to a speed of 1 Å h^{-1}. This result also illustrates the accuracy of the set-up. This pit, initiated during the mechanical-chemical polishing, is probably located around an impurity on the surface or some inclusion.

8.4 Conclusions

These first observations show that AFM allows the study of local corrosion phenomena in detail. The set-up presented here comprises all the requirements for an *in situ* investigation of stress-induced corrosion.

The set-up is now operational and presents a very good resolution at the nanoscale. It has proved its efficiency for the observation of the nanometric surface modifications during traction in chloride solutions: 4 Å high slip planes are visible, pitting can clearly be observed *in situ* and the potential of the sample controlled.

The resolution of the set-up is sufficient to get a good estimation of the growth of a pit with time in a chloride solution. Actually, pit deepening has been measured at a speed of approximately 1 Å h^{-1}.

A complementary *in situ* study of corrosion induced by stress in chloride solution is in progress and involves adjusting the potential of the sample.

8.5 References

1 G. Binnig, H. Rohrer, C. Gerber and E. Weibel, *Phys. Rev. Lett.*, 1982, **49**, 57–61.
2 J. M. Olive and V. Vignal, *Microsc. Microanal. Microstruct.*, 1994, **5**, 301–311.
3 M. P. Ryan, R. C. Newman and G. E. Thomson, *J. Electrochem. Soc.*, 1995, **142**, L177.
4 V. Maurice, S. Cadot and P. Marcus, *Surf. Sci.*, 2000, **458**, 195–215.
5 C.-O. A. Olsson and D. Landolt, *Electrochim. Acta*, 2003, **48**, 1093–1104.

6 I. Reynaud-Laporte, M. Vayer, J. P. Kauffmann and R. Erre, *Microsc. Microanal. Microstruct.*, 1997, **8**, 175–185.
7 J. H. W. De Wit, *Electrochim. Acta*, 2001, **46**, 3641–3650.
8 P. Leblanc and G. S. Frankel, *J. Electrochem. Soc.*, 2002, **149** (6), B239–B247.
9 CATIA V5 is a property of Dassault Systemes.
10 P. Villechaise, L. Sabatier and J. C. Girard, *Mater. Sci. Eng.*, 2002, **A323**, 377–385.
11 J. Man, K. Obrtlík and J. Polák, *Mater. Sci. Eng.*, 2003, **A351**, 123–132.
12 G. H. Koch, A. K. Agrawal, M. P. H. Brongers and A. W. Phelps, *Corrosion (99)*, Paper 450, NACE, San Antonio, TX, 1999.
13 T. Shibata and T. Takeyama, *Corrosion*, 1997, **33**, 243–251.
14 D. D. Macdonald and M. Urquidi-Macdonald, *Electrochim. Acta*, 1986, **31**, 1079–1086.
15 R. P. Vera Cruz., A. Nishikata and T. Tsuru, *Corros. Sc.*, 1998, **40**, 125–139.
16 J.-J. Park and S.-I. Pyun, *Corros. Sc.*, 2004, **46**, 285–296.
17 J. M. Bastidas C. L. Torres, E. Cano and J. L. Polo, *Corros. Sci.*, 2002, **44**, 625–633.
18 S. V. Phadnis, A. K. Satpati, K. P. Muthe, J. C. Vyas and R. I. Sudaresan, *Corros. Sci.*, 2003, **45**, 2467–2483.

9

Etching processes of ZnO[0001] surface in solution

J. INUKAI and K. ITAYA, Tohoku University, Japan

9.1 Introduction

In situ electrochemical scanning tunnelling microscopy (EC-STM) has quickly become an important tool for surface characterisation of electrodes with atomic resolution in electrolyte solutions.[1–3] High-resolution STM imaging has been achieved in solution for various metal electrode surfaces, deposited metal layers, adsorbed anions, and organic molecules.[2,3] STM is capable of characterising surfaces of not only metal electrodes, but also semiconductors such as Si, GaAs, and InP.[2,3] Details of etching processes of semiconductor electrodes were revealed through the observation of surface structures.[3]

The ZnO electrode is one of the most intensively investigated semiconductors for various applications such as short wavelength lasers,[4] high-sensitivity gas sensors,[5] electrodes for solar batteries,[6] and catalysts.[7] Exposure in solution of atomically well-ordered single-crystal surfaces of ZnO has long been desired for understanding electrochemical reactions taking place at the ZnO electrode on an atomic scale. However, surface topographic images of ZnO in aqueous solutions have only been acquired without atomic resolution mainly because of the difficulty in the preparation of a well-defined semiconductor surface as described in our previous paper.[8] It was reported that ZnO surfaces etched in a concentrated HCl solution showed a rolling hill topography, and atomically flat terraces were rarely observed.[8]

Figure 9.1 shows an illustrative depiction of the surface structure of ZnO[0001]. To obtain atomically flat surfaces of ZnO[0001]-Zn, surface structures were systematically investigated after etching using various acid and alkaline solutions. In a previous study, it was found that alkaline solutions such as 3M NaOH produce atomically flat surfaces with wide terraces on ZnO[0001]-Zn.[9] Each atom was resolved by STM, showing a $[1 \times 1]$ structure in solution. In this study, the etching processes of ZnO[0001]-Zn surface in solution is reported.

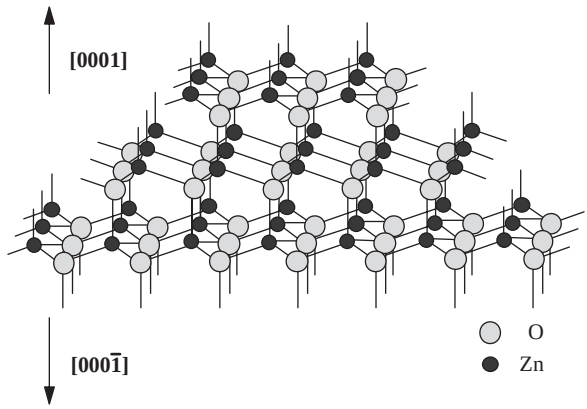

9.1 Schematic view of ZnO[0001] surface.

9.2 Experimental methods

ZnO[0001] single crystals (5 mm × 5 mm × 1 mm, undoped) were obtained from Atomergic Chem. Corp. USA. The surface of the crystals was polished and metallographically finished with 0.25 μm diamond paste, and sonicated in acetone, ethanol, and pure water. They were further etched in the dark at the rest potential either in 6M HCl for 30 s or in 3M NaOH for 5 min. After the chemical etching, the surface was repeatedly rinsed in pure water.

Current–potential curves were obtained in the dark in a 0.1M $KClO_4$ solution previously deoxygenated with N_2. *In situ* STM measurements were carried out in 0.1M $KClO_4$ or 0.1M NaOH near respective rest potentials in the dark using a NanoScope-E (Digital Instruments, Inc.). Two Pt wires as the reference and the counter electrodes were fixed in the electrochemical cell for STM. Tungsten wires electrochemically polished and insulated with nail polish were used as the scanning tips.

Solutions were prepared from ultrapure grade reagents, obtained from Kanto Chemical Co., of HCl, NaOH, and $KClO_4$, and ultrapure water (Millipore-Q). All potentials were reported with respect to a saturated calomel electrode (SCE).

9.3 Results and discussion

Figure 9.2 shows a current–potential curve in 0.1M $KClO_4$ (pH = 5.3) for a ZnO[0001]-Zn previously etched in NaOH as described above. Practically no current was seen in the potential range between –0.3 and 1 V in the dark. The cathodic current commencing at ca. –0.4 V is due to the hydrogen evolution reaction. The reduction of ZnO might also be expected to occur at

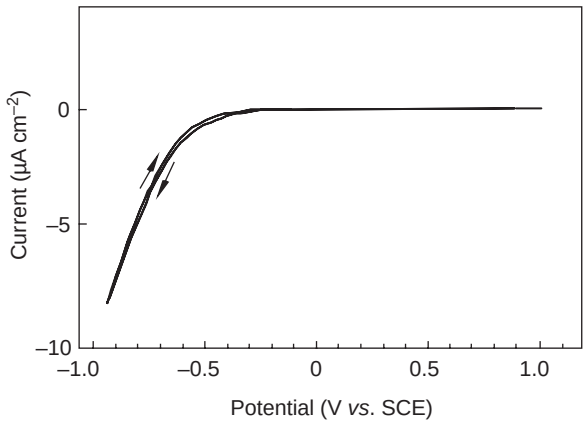

9.2 Current–potential curve recorded in 0.1M $KClO_4$ (pH = 5.3) in the dark with a ZnO[0001]-Zn etched in 3M NaOH. Scan rate = 0.02 V s^{-1}. The arrows indicate the direction of potential scan.

cathodic potentials. The flat-band potential of ca. –0.7 V was measured from Mott-Schotky plots, and was significantly more negative than that of –0.3 V *vs*. Ag/AgCl found in 0.1M KCl (pH = 4.0).[8] This result strongly suggests that the surface structure is an important factor determining the flat band potential.

STM measurements were first made for surfaces pretreated with 6M HCl. The tip electrode potential was set at a value more negative than the flat band potential. Under this condition, stable electron tunnelling from the tip electrode to the semiconductor was observed, allowing an accurate determination of surface topography based on the energy diagram for a semiconductor/liquid/metal junction discussed in our previous paper.[8] STM images were subsequently observed at –0.2 V. The surface etched in 6M HCl was atomically rough, characterised by a 'rolling-hill' structure. Many pits and large steps were consistently observed for the sample prepared in acidic solutions. No clear atomic steps were observed on the surfaces. This result was almost the same as that reported previously.[8]

The appearance of wide atomically flat terraces on a large scale STM image of the ZnO[0001]-Zn surface in 0.1M $KClO_4$ after etching in 3M NaOH clearly shows that the etching procedure using 3M NaOH produces well-defined surfaces.[9] Wider terraces extend over 100 nm. All steps are of the bilayer type with a height of 0.26 nm. On the ZnO[0001]-Zn surface, pits are rarely observed on terraces. The steps are composed of straight lines, which are located in the direction forming an angle of 60° as expected for a surface with threefold symmetry. Etching in 3M NaOH even for a prolonged period of 1 h produced atomically flat Zn-terminated surfaces.

It is clearly seen on a top view of a high-resolution STM image of an area of 4.7 nm × 4.7 nm on the ZnO[0001]-Zn in 0.1M NaOH that the atomic structure has a threefold symmetry. The interatomic distance was measured to be 0.33 nm. No sign of contamination was seen in the STM images. This result shows that the Zn-terminated ZnO[0001]-[1 × 1] structure can be exposed by chemical etching using NaOH.[9] We also succeeded in imaging atoms on the terraces of the O-terminated ZnO[000$\bar{1}$] surface in solution, and obtained atomic images of a [1 × 1] structure. Our study demonstrates that the known etching processes[10,11] of ZnO[0001]-Zn as well as ZnO[000$\bar{1}$]-O can now be elucidated on an atomic level by *in situ* STM.

An etching process of ZnO[0001]-Zn in 0.1M NaOH was recorded in 4 min. It is notable that straight and zigzag steps are alternately aligned on the ZnO[0001]-Zn surface. Etching was observed at steps, and the etching rate was higher at zigzag steps than at straight steps. The etching processes can be explained by the arrangement of Zn and O atoms on ZnO[0001]-Zn (Fig. 9.1).

9.4 Acknowledgements

The authors thank Mr Katsuya Ito who carried out experiments. This work was supported partially by the COE project, 'Giant Molecules and Complex Systems, 2004', from the Ministry of Education, Culture, Sports, Science and Technology, Japan, and by Core Research for Evolutional Science and Technology organised by the Japan Science and Technology Agency.

9.5 References

1 H. Siegenthaler, *Scanning Tunneling Microscopy II*, R. Wiesendanger and H.-J. Guntherodt (eds.), Springer–Verlag, Berlin, 1992, p. 7.
2 A. A. Gewirth and B. K. Niece, *Chem. Rev.*, 1997, **97**, 1129–1162.
3 K. Itaya, *Prog. Surf. Sci.*, 1998, **58**, 121–248.
4 D. C. Reynolds, D. C. Look and B. Jogai, *Solid State Commun.*, 1996, **99**, 873–875.
5 W. Gopel, *Prog. Surf. Sci.*, 1985, **20**, 96–103.
6 M. Matsumura, Y. Nomura and H. Tsubomura, *Bull. Chem. Soc. Jpn.*, 1977, **50**, 2533–2537.
7 M. Watanabe, *Surf. Sci.*, 1992, **279**, L236–L242.
8 K. Itaya and E. Tomita, *Surf. Sci.*, 1989, **219**, L515–L520.
9 J. Inukai, K. Ito and K. Itaya, *Electrochemistry*, 1999, **67**, 1126–1128.
10 A. Fujishima and K. Honda, *Denki Kagaku* 1972, **40**, 33–38.
11 H. Gerischer, M. Lübke and N. Sorg, *Z. Phys. Chem. N. F.*, 1986, **148**, 11–19.

10

Scanning Kelvin probe force microscopy (SKPFM) applied to various conversion coated aluminium surfaces

B. S. TANEM, O. LUNDER and O. Ø. KNUDSEN,
SINTEF, Norway

10.1 Introduction

The formation and properties of conversion coatings on aluminium may be rather complex due to the heterogeneous microstructure inherent with commercial alloys. In particular, corrosion as well as surface treatment processes are significantly influenced by the presence of intermetallic particles exhibiting electrochemical properties different from the aluminium matrix. The influence of alloy metallurgy in the formation of chromate conversion coating (CCC) on AA2024-T3 alloy has been extensively addressed.[1–5] The CCC films have been found to significantly reduce the activity of both cathodic and anodic sites on the alloy surface.[6–8] Among the chromate-free pre-treatments, Ti–Zr based processes appear to have gained the most widespread acceptance. It has been shown that Ti–Zr based conversion layers deposit preferentially at cathodic particles on the aluminium surface due to locally high pH in these areas during immersion treatment.[9,10]

Scanning Kelvin probe force microscopy (SKPFM) allows mapping of topography and Volta potential distribution on passive surfaces in air.[11] It combines the classical Kelvin probe technique[12] with atomic force microscopy.[13–15] Since the SKPFM probes are much smaller than probes used in the classical Kelvin probe technique and operate at much smaller distances from the surface, an improved lateral resolution is obtained. The lateral resolution of SKPFM is reported to be better than 0.1 μm,[16–18] compared with ~100 μm for the standard Kelvin probe technique.[19] SEM has frequently been used in combination with SKPFM to relate local Volta potential maps with local microstructure and chemistry of aluminium alloys.[20–31] The ability to map the potential on a sub-micron scale is very useful in electrochemical studies of commercial aluminium alloys, which contain intermetallic particles on that scale and larger.

Several factors are believed to influence the Volta potential measurements, e.g. composition and structure of the oxide film covering the aluminium surface and intermetallics, tip–sample distance and adsorption of

material at the surface.[20] A linear relation between the Volta potential measured in air and the open circuit potential in different corrosive aqueous environments has been established.[21–24] Even though the surface state in air is different from that in solution, this linear relation gives first-hand indications of the expected electrochemical properties at sub-μm scale of different phases on dry surfaces.

Conventional polishing methods have generally been employed to obtain surfaces suitable for SKPFM mapping. However, mechanical polishing is known to produce a deformed fragmented surface layer which distorts local chemistry and microstructure and adds chemical substances (lubricants) to the surface. Recent works have therefore introduced ultramicrotomy (UM) as a suitable sample preparation technique for AFM[4,32] and SKPFM[33,34] studies of aluminium. In addition to preserving the bulk chemistry of the samples at the surface[35] extremely smooth surfaces are obtained.[4] Furthermore, the ultramicrotomed thin foils can be utilised to combine SKPFM and transmission electron microscopy (TEM) from the same area.[33]

In the present work, SKPFM was used to study how conventional chromating and Ti–Zr based pre-treatment, respectively, affect the Volta potential of intermetallic particles relative to the matrix of an extruded EN AW-6082 aluminium alloy. UM was employed to obtain clean and microscopically smooth surfaces and the SKPFM measurements were combined with field emission SEM and electron probe microanalysis (EPMA) to identify the intermetallic phases present at the surface. The significance of the results is briefly discussed in the light of previous filiform corrosion (FFC) test results obtained for painted specimens subjected to similar pre-treatments.[36,37]

10.2 Experimental methods

10.2.1 Materials and specimen preparation

The test material was commercially produced EN AW-6082-T6 aluminium (composition by weight as determined from spectrographic analysis: 0.63%Mg, 1.0%Si, 0.53%Mn, 0.17%Fe, 0.0034%Cu, 0.016%Zn, 0.013%Ti, Al balance) which was cut from 150 × 4 mm extrusions. Clean and smooth surfaces of the alloy, suitable for SKPFM examination, were prepared by use of a Reichert-Jung ultramicrotome. The mounted specimen block was trimmed with fresh glass knives to obtain rectangular 35 μm × 2 mm section surfaces. Final sectioning was performed with a MicroStar diamond knife. The specimen was oriented such that the ultramicrotomed surfaces were parallel and close to (within a few μm of) the original as-extruded surface.

The freshly generated surfaces were treated according to the following conversion coating procedures, respectively:

(i) *Ti–Zr based pre-treatment*: Deoxidation in 4% Alfideox 73 (Candor Sweden AB) for 30 s, tap water rinsing, immersion in 4% Gardobond® X4707 (Chemetall GmbH) (pH 2.9, 20°C) for 1 min, rinsing in distilled water and air drying.
(ii) *Chromating*: Deoxidation in 4% Alfideox™ 73 for 30 s, tap water rinsing, immersion in 15 mL^{-1} Alodine® C6100 (Henkel Surface Technologies) for 3 min, rinsing in distilled water and air drying.

10.2.2 Surface characterisation

Topography and Volta potentials of the ultramicrotomed surfaces before and after the chemical treatments were mapped using a Nanoscope IIIa Multimode™ AFM, equipped with an Extender™ Electronics Module. All potential mapping was performed in air with commercially available metal-coated cantilevers from MicroMasch. The lift scan height employed was 100 nm, where effects of dipole charges close to the surface are believed to be small. The areas mapped with SKPFM were identified and imaged by a Hitachi S-4300SE field emission SEM equipped with an energy dispersive x-ray analysis system (EDS). Before conversion coating, selected intermetallic particles exposed at the freshly sectioned surface were identified and their composition determined by use of a JXA-8900 Superprobe electron probe microanalyzer (EPMA) operated at 15 kV.

10.3 Results

10.3.1 Intermetallic particles in the alloy

Optical microscopy showed that the extruded EN AW-6082-T6 alloy exhibited a fibrous microstructure with a recrystallised surface layer, about 500 µm in thickness. SEM examination of the as-extruded surface (Fig. 10.1a) showed the presence of intermetallic particles typically a few micrometres in size. According to EPMA of the ultramicrotomed surface (Fig. 10.1b) these particles were a) Al–Mn–Fe–Si particles consisting of 63–73% Al, 11–13% Mn, 10–16% Fe and 7–9% Si, corresponding to the cubic α-Al(Fe,Mn)Si phase[38] and b) Mg–Si particles with a Mg/Si ratio similar to the binary Mg_2Si phase. In addition, precipitation hardening Mg–Si phase particles will obviously be present in the artificially aged alloy; however, these can only be resolved in TEM and are not considered in the present study.

10.3.2 Effect of Ti–Zr based pre-treatment

SKPFM Volta potential maps were recorded at different Mg_2Si particles before and after Ti–Zr based treatment. On the freshly ultramicrotomed

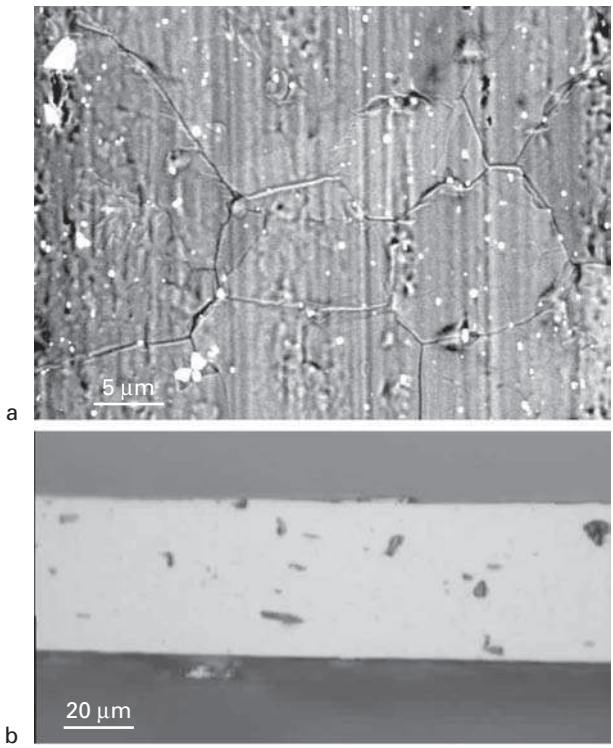

10.1 *a* SEM image of as-extruded EN AW-6082 surface, *b* optical micrograph of ultramicrotomed specimen surface.

surface a Volta potential difference of about 300 mV was typically recorded between the Mg_2Si particles and the aluminium matrix. An example is shown in Fig. 10.2a, where part of a relatively large Mg_2Si particle (appears bright) was mapped. According to earlier observations[10,38,39] the Mg_2Si phase is electrochemically more active than the aluminium matrix. However, after Ti–Zr treatment (Fig. 10.2b), no significant Volta potential difference was observed between the same particle and the aluminium matrix. Subsequent SEM/EDS analysis at an accelerating voltage of 10 kV, corresponding to an analysis depth of about 1 μm, showed that this particle was depleted in Mg during the chemical treatment, leaving a Si-rich oxide particle on the surface (Fig. 10.3).

Contrary to the behaviour of the Mg_2Si phase, SKPFM measurements showed that the Volta potential difference between the α-Al(Fe,Mn)Si phase and the aluminium matrix was generally little affected by the Ti–Zr treatment. The Volta potential difference measured on the ultramicrotomed

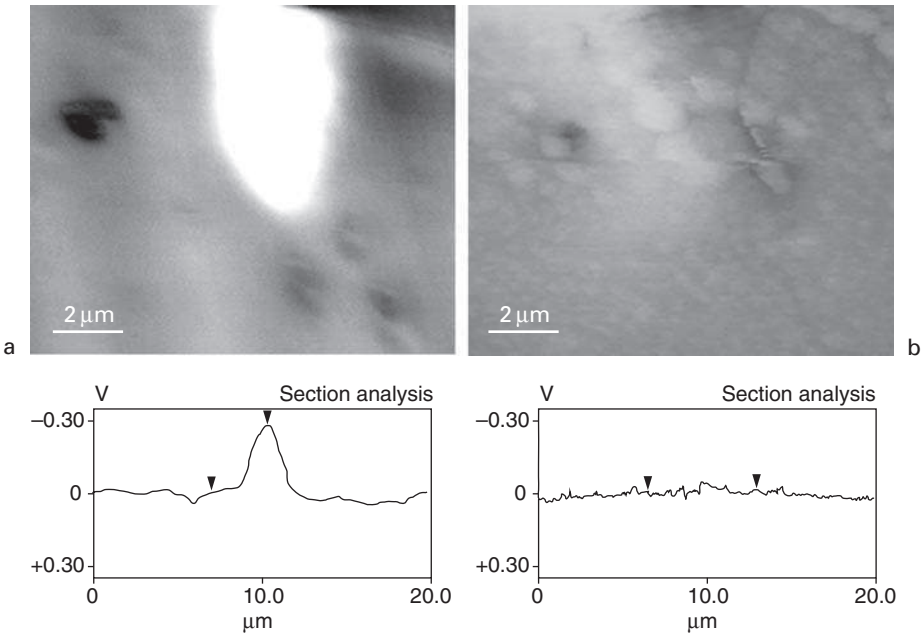

10.2 SKPFM Volta potential maps with line scans across an Mg_2Si particle *a* before and *b* after Ti–Zr based treatment.

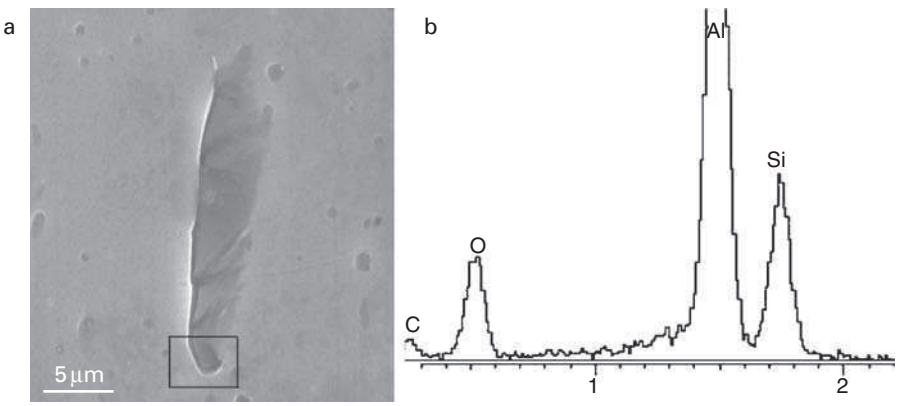

10.3 *a* SEM image of transformed Mg_2Si particle and *b* x-ray EDS spectrum, indicating that all Mg is selectively dissolved during treatment (no MgKα peak observed at 1.25 keV). Framed area in *a* corresponds to area mapped in Fig. 10.2b.

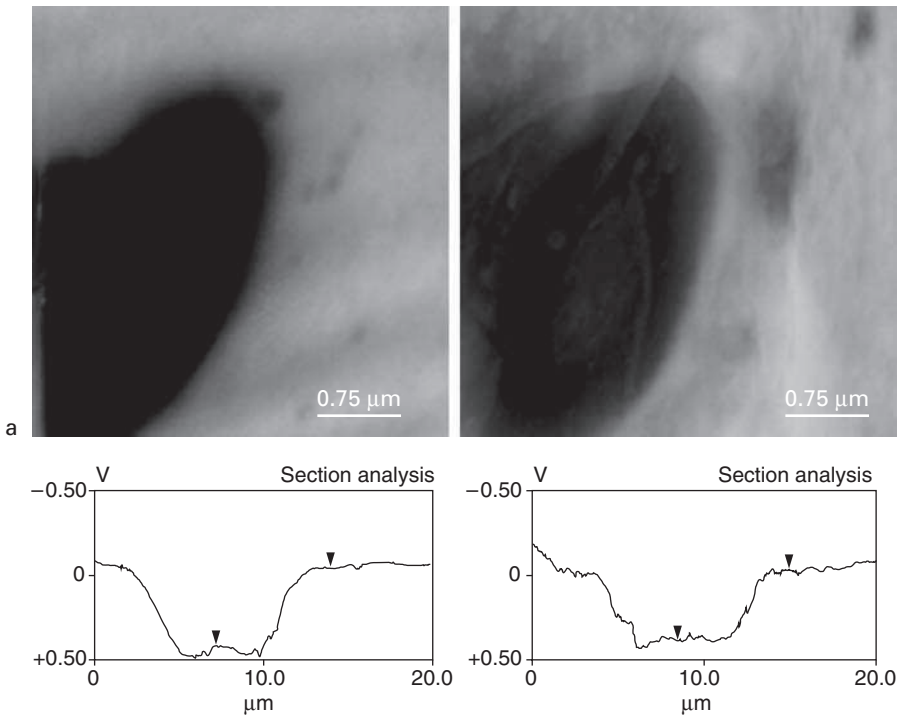

10.4 SKPFM Volta potential maps with line scans across α-Al(Fe,Mn)Si particle *a* before and *b* after Ti–Zr based treatment.

surface was typically about 500 mV (Fig. 10.4a). The contrast from the α-Al(Fe,Mn)Si phase (appears dark in Fig. 10.4) was reversed relative to the Mg_2Si phase, indicating that the α-Al(Fe,Mn)Si particle is nobler than the surrounding matrix, as expected.[8,10,38] After Ti–Zr treatment, the Volta potential difference was reduced by 50–100 mV (Fig. 10.4b), i.e. only a reduction of 10–20% compared with the untreated surface.

SEM/EDS analyses of α-Al(Fe,Mn)Si particles showed no significant change in the composition of this phase as a result of the Ti–Zr treatment. The conversion layers formed by Ti–Zr based pre-treatment are generally too thin (typically 10–50 nm) to be detected by EDS analysis. However, since these layers deposit preferentially at cathodic sites on the aluminium surface,[9,10] significant variations in thickness occur. Thus, the presence of a thin Ti–Zr oxide film deposited on the α-Al(Fe,Mn)Si particles could generally be confirmed by SEM/EDS analysis.

10.3.3 Effect of chromate conversion coating

SKPFM results obtained before and after chromate conversion coating are summarised in Fig. 10.5. As shown in Figs. 10.2 and 10.4, the cathodic α-Al(Fe,Mn)Si phase appeared dark while the anodic Mg_2Si phase appeared bright relative to the aluminium matrix on the ultramicrotomed surface. The Volta potential difference of the α-Al(Fe,Mn)Si particle on the as-ultramicrotomed surface in Fig. 10.5a was about 500 mV, as seen from the potential line scan across the particle. Shortly after chromating (2 h) the measured Volta potential difference was less than 100 mV (Fig. 10.5b), i.e. a reduction of more than 80% relative to the as-ultramicrotomed surface. However, another SKPFM measurement performed 24 h after the chromate treatment showed that the Volta potential difference between the α-Al(Fe,Mn)Si particle and matrix was increased significantly by storage under ambient conditions (Fig. 10.5c).

After chromate conversion treatment, the Mg_2Si phase exhibited no Volta potential contrast relative to the surrounding matrix, similar to the result obtained for the Ti–Zr treated surface.

Examination of the chromated surface in SEM showed that the aluminium matrix was coated with a cracked CCC (Fig. 10.6a). A significantly thinner film, not detectable by x-ray EDS analysis (Fig. 10.6b), was formed on the α-Al(Fe,Mn)Si particles. This is in good agreement with earlier observations.[3,5,8]

10.4 Discussion

The SKPFM results showed that the Volta potential difference of the α-Al(Fe,Mn)Si particles relative to the matrix in EN AW-6082 aluminium was little affected by the Ti–Zr based treatment, whereas a significant reduction in the Volta potential difference occurred as a result of chromate conversion treatment. Although questions exist regarding the nature of the potential measured by SKPFM in air, these observations are consistent with recent results which showed that chromating effectively inhibited cathodic activity of the α-Al(Fe,Mn)Si phase in chloride solution, while the Ti-Zr based process provided little or no cathodic inhibition.[40]

Furthermore, the present SKPFM results showed an increasing Volta potential difference for the α-Al(Fe,Mn)Si particles with time after chromate treatment. In other words, the effect of chromate treatment appeared to be gradually reduced with time. CCCs are known to age during storage in air, generally leading to a loss in the corrosion protection provided by the coating. While the improvement in corrosion resistance due to the CCC is lost gradually during ambient temperature exposure, corrosion resistance is lost in a matter of minutes at temperatures above 60°C. The ageing

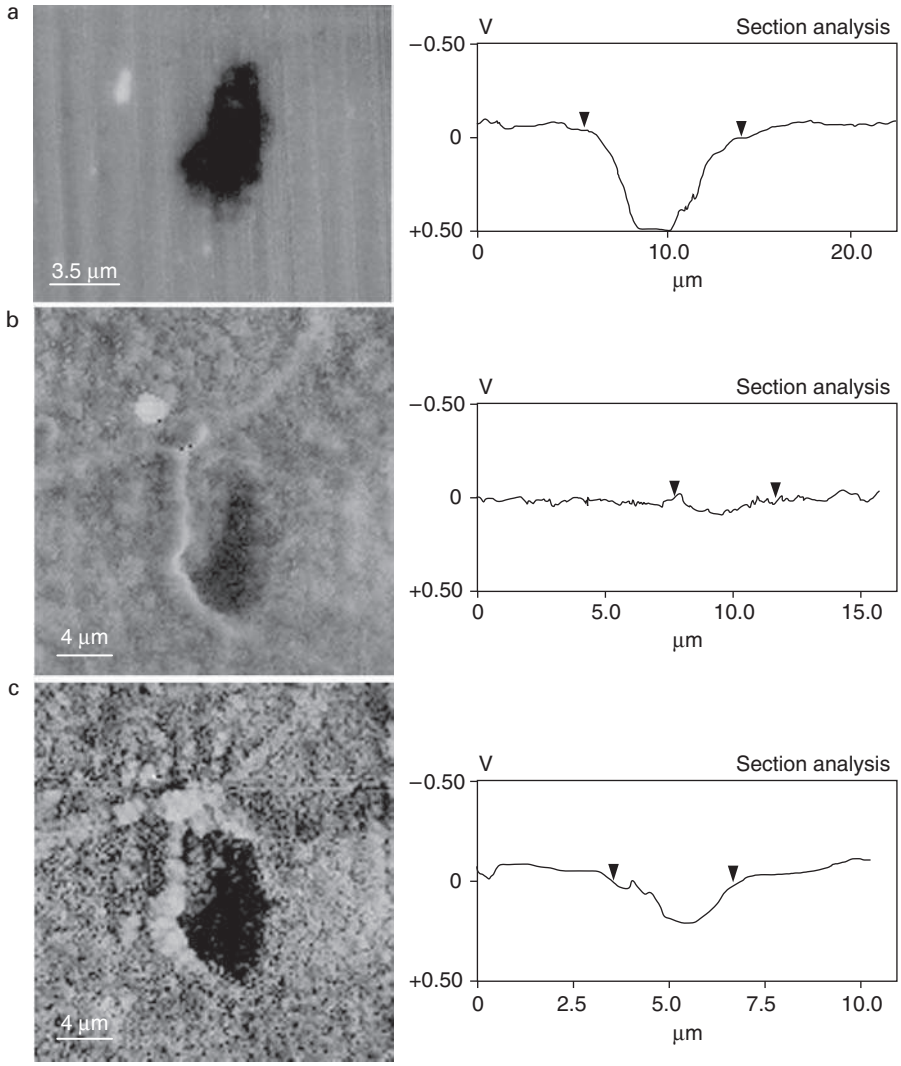

10.5 SKPFM Volta potential maps with line scans across an α-Al(Fe,Mn)Si particle on EN AW-6082, *a* as ultramicrotomed, *b* 2 h after chromating and *c* 24 h after chromating.

process is attributed to various phenomena, including immobilisation of the Cr^{6+}, dehydration and structural changes in the conversion coatings.[41–45] Dehydration of the CCC leads to the development of shrinkage cracking in the conversion coating and this was suggested as the main cause of a gradual loss in the oxygen reduction inhibition by CCC on AA2024 alu-

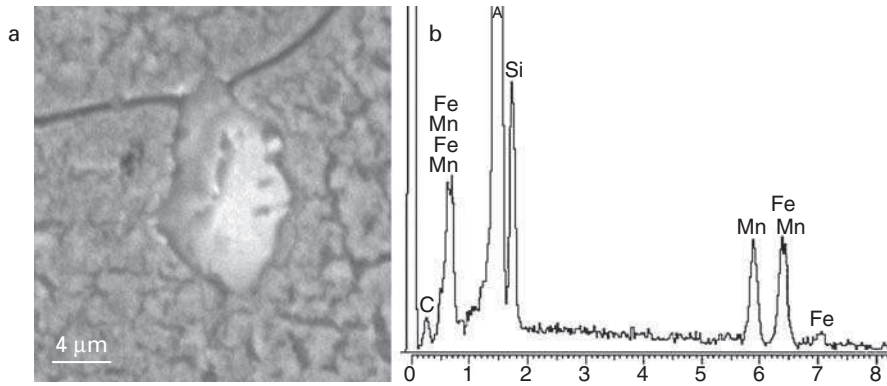

10.6 *a* SEM image of chromated surface with α-Al(Fe,Mn)Si particle mapped in Fig. 10.5 *b* x-ray EDS analysis of particle. The CCC on the α-Al(Fe,Mn)Si particle was too thin to be detected.

minium.[45] Apparently, shrinkage cracking facilitated the oxygen reduction reaction by exposing the underlying Cu-rich substrate.

SKPFM results shown in Fig. 10.5 indicate that ageing of the thin CCC on the α-Al(Fe,Mn)Si particles also occurred, apparently leading to increased ennoblement (increased Volta potential difference) of the particles relative to the surrounding matrix. More detailed analysis of the structural and compositional changes occurring on the intermetallic particles is required in order to better understand the nature of this ageing process.

The relatively large Mg_2Si particles observed in EN AW-6082 are probably not crucial with respect to the corrosion properties of this alloy after pre-treatment. The acidic deoxidation and conversion coating solutions apparently cause Mg to dissolve selectively from the Mg_2Si phase, resulting in the formation of electrochemically inert Si-rich oxide particles on the alloy surface.

The presence of cathodic particles has previously been shown to have a crucial effect on the susceptibility of aluminium alloys to FFC[46,47] and other types of localised corrosion.[48,49] In fact, corrosion tests have demonstrated that the presence of electrochemically noble second-phase particles is a necessity for FFC to occur.[37,47] Thus, inhibition of the cathodic activity on the iron-containing phases is clearly a desirable feature, which should be considered in searches for CCC replacements.

Application of the presently studied conversion coatings on EN AW-6060 aluminium in earlier work[36,37] showed that the chromate treatment was superior to the Ti–Zr based alternative in terms of FFC resistance of epoxy-coated surfaces. This was partly attributed to a more effective inhibition of the oxygen reduction reaction on the α-Al(Fe,Mn)Si particles by the CCC

during corrosion. The SKPFM results presently obtained for alloy EN AW-6082 indicate that the cathodic inhibition of such particles by the CCC becomes less important with time due to ageing of the conversion coating, a process which seems to occur also in the thin CCC film on the α-Al(Fe,Mn)Si particles. However, in order to obtain a high FFC resistance, good adhesion between the organic coating and the substrate is another important factor. Previous adhesion tests [37] showed that the CCC was superior to the Ti–Zr based alternative also in this respect.

10.5 Conclusions

Local potential measurements with SKPFM on ultramicrotomed EN AW-6082 surfaces before and after application of a conversion coating showed that:

- The Volta potential difference of cathodic α-Al(Fe,Mn)Si particles present in the alloy surface was reduced from about 500 mV to <100 mV as a result of chromate treatment. However, the Volta potential difference increased again during exposure to ambient atmosphere, indicating an ageing effect of the thin CCC present on the α-Al(Fe,Mn)Si particles.
- Application of a chromate-free Ti–Zr based treatment, which caused preferential deposition of a thin Ti–Zr oxide film on the α-Al(Fe,Mn)Si particles, reduced the Volta potential difference of the particles only to a very limited extent.
- Anodic Mg_2Si particles exhibited a Volta potential difference of about 300 mV (reversed polarity relative to the α-Al(Fe,Mn)Si phase) on the as-ultramicrotomed surface. During chemical treatments, these particles were transformed by selective dissolution of Mg to form Si-rich oxide particles with no significant Volta potential difference relative to the surrounding matrix.
- The SKPFM results indicate that the CCC inhibits the cathodic activity of the α-Al(Fe,Mn)Si phase considerably while the Ti–Zr based process provides little or no cathodic inhibition, in line with previous electrochemical studies performed for these conversion coatings.

10.6 Acknowledgements

This work has been done as part of the '*Light Metal Surface Science*' joint project between SINTEF and NTNU, financed by the Norwegian Research Council, Hydro Aluminium, Profil-Lakkering AS, Norsk Industrilakkering AS, Fundo Wheels AS, Jotun Powder Coatings and DuPont Powder Coatings Scandinavia. The authors acknowledge M. Raanes, Norwegian University of Science and Technology, for performing the EPMA analyses.

10.7 References

1 G. M. Brown, K. Shimizu, K. Kobayashi, G. E. Thompson and G. C. Wood, *Corros. Sci.*, 1992, **33**, 1371.
2 G. M. Brown, K. Shimizu, K. Kobayashi, G. E. Thompson and G. C. Wood, *Corros. Sci.*, 1993, **34**, 1045.
3 P. L. Hagans and C. M. Haas, *Surface Interface Anal.*, 1994, **21**, 65.
4 G. M. Brown and K. Kobayashi, *J. Electrochem. Soc*., 2001, **148**, B457.
5 L. Juffs, A. E. Hughes, S. Furman and P. J. K. Paterson, *Corros. Sci.*, 2002, **44**, 1755.
6 G. S. Frankel and R. L. McCreery, *Interface*, 2001, **10**, 34.
7 G. O. Ilevbare and J. R. Scully, *J. Electrochem. Soc*., 2001, **148**, B196.
8 O. Lunder, J. Walmsley, P. Mack and K. Nisancioglu, 'Formation and characterisation of a chromate conversion coating on AA6060 Aluminium', EuroCorr 2003, Budapest, Hungary, 27 Sept–2 Oct 2003.
9 J. H. Nordlien, J. C. Walmsley, H. Østerberg and K. Nisancioglu, *Surf. Coatings Technol.*, 2002, **153**, 72.
10 O. Lunder, C. Simensen, Y. Yu and K. Nisancioglu, *Surf. Coatings Technol.*, 2004, **184**, 278.
11 F. M. Ferry, K. Kjoller, J. T. Thornton, R. J. Tench and D. Cook, *Electric Force Microscopy, Surface Potential Imaging, and Surface Electrical Modification With the Atomic Force Microscopy (AFM)*, Digital Instrument, Veeco Metrology Group, Application note 27, 1999.
12 M. Stratmann and H. Streckel, *Corros. Sci.*, 1990, **30**, 681.
13 G. Binnig, C. F. Quate and C. Gerber, *Phys. Rev. Lett*., 1986, **56**, 930.
14 Q. Zhong, D. Inniss, K. Kjoller and V. B. Elings, *Surf. Sci*., 1993, **290**, L688.
15 A. P. Quist, J. Ahlbom, C. T. Reimann and B. U. R. Sundqvist, *Nucl. Instr. Meth*., 1994, **B88**, 164.
16 P. Schmutz and G. Frankel, *J. Electrochem. Soc*., 1998, **145**, 2285.
17 H. O. Jacobs, H. F. Knapp, S. Müller and A. Stemmer, *Ultramicroscopy*, 1997, **69**, 39.
18 M. Nonnenmacher, M. P. O'Boyle, H. K. Wickramasinghe, *Appl. Phys. Lett*., 1991, **58**, 2921.
19 S. Yee, A. Oriani and M. Stratmann, *J. Electrochem. Soc*., 1991, **138**, 55.
20 V. Guillaumin, P. Schmutz and G. S. Frankel, *J. Electrochem. Soc*., 2001, **148**, B163–173.
21 P. Schmutz and G. Frankel, *J. Electrochem. Soc*., 1998, **145**, 2285.
22 P. Schmutz and G. Frankel, *J. Electrochem. Soc*., 1998, **145**, 2295.
23 P. Schmutz and G. Frankel, *J. Electrochem. Soc*., 1999, **146**, 4461.
24 P. Leblanc and G. S. Frankel, *J. Electrochem. Soc*., 2002, **149**, B239.
25 P. Campestrini, E. P. M. van Westing, H. W. van Rooijen and J. H. W. de Wit, *Corros. Sci.*, 2000, **41**, 1853.
26 P. Campestrini, E. P. M. van Westing, J. H. W. de Wit, *Electrochim. Acta*, 2001, **46**, 2553.
27 P. Campestrini, 'Microstructure-related Quality of Conversion Coatings on Aluminium Alloys', PhD Thesis, Delft University Press, ISBN 90-407-2342-7, The Netherlands 2002.
28 F. Andreatta, H. Terryn and J. H. W. de Wit, *Corros. Sci.*, 2003, **45**, 1733.
29 F. Andreatta, M. H. Lohrengel, H. Terryn and J. H. W. de Wit, *Electrochim. Acta*, 2003, **48**, 3239.

30 P. Campestrini, H. Terryn, A. Hovestad and J. H. W. de Wit, *Surf. Coatings Technol.*, 2004, **176**, 365.
31 F. Andreatta, 'Local Electrochemical Behaviour of 7xxx Aluminium Alloys', PhD Thesis, Netherlands Institute for Metals Research, TUDelft, Pasmans Offsetdrukkerij, Den Haag, ISBN 90-407-2342-7, The Netherlands 2004.
32 K. Shimizu, K. Kobayashi, P. Skeldon, G. E. Thompson and G. C. Wood, *Corros. Sci.*, 1997, **39**, 701.
33 B. S. Tanem, J. H. Nordlien, J. Mårdalen and B. Holme, *ATB Metallurgie*, 2003, **43**, 346.
34 B. S. Tanem, G. Svenningsen, J. E. Lein, J. Mårdalen and J. H. Nordlien, *ATB Metall.*, 2003, **43**, 228.
35 T. F. Malis and D. Steele, 'Workshop on Specimen Preparation for TEM of Materials II'; ed. R. Anderson, Vol 199, *Materials Research Symposium Proceedings*, Materials Research Society, Pittsburgh 1990.
36 O. Lunder, K. F. Heen and K. Nisancioglu, *Corrosion*, 2004, **60**, 622–631.
37 O. Lunder, F. Lapique, B. Johnsen and K. Nisancioglu, *Int. J. Adhesion Adhesives*, 2004, **24**, 107.
38 L. F. Mondolfo, *Aluminium Alloys: Their Structure and Properties*, Butterworths, London, 1976.
39 E. H. Hollingsworth and H. Y. Hunsicker, *ASM Handbook, Vol 13: Corrosion*, ASM International, 1987.
40 O. Lunder, Dissertation, Norwegian University of Science and Technology, ISBN 82-471-5610-5, Trondheim, Norway, 2003.
41 J. Zhao, L. Xia, A. Sehgal, D. Lu, R. L. McCreery and G. S. Frankel, *Surf. Coatings Technol.*, 2001, **140**, 51.
42 M. Jaime Vasquez, G. P. Halada and C. R. Clayton, *Electrochim. Acta*, 2002, **47**, 3105.
43 A. E. Hughes, R. J. Taylor and B. R. W. Hinton, *Surf. Interface Anal.*, 1997, **25**, 223.
44 V. Laget, C. S. Jeffcoate, H. S. Isaacs and R. G. Buchheit, *J. Electrochem. Soc.*, 2003, **150**, B425.
45 W. Zhang and R. G. Buchheit, *Corros. Sci*, 2003, **59**, 356.
46 A. Afseth, J. H. Nordlien, G. M. Scamans and K. Nisancioglu, *Corros. Sci.*, 2002, **44**, 2491.
47 A. Afseth, J. H. Nordlien, G. M. Scamans and K. Nisancioglu, *Corros. Sci.*, 2002, **44**, 2529.
48 K. Nisancioglu, J. H. Nordlien, A. Afseth and S. Scamans, 'Significance of Thermomechanical Processing in Determining Corrosion Behaviour and Surface Quality of Aluminum Alloys', *Proc. of ICAA7: Aluminium Alloys: Their Physical and Mechanical Properties*, Charlottesville, Virginia, USA, 9–14 April 2000. Trans Tech Publications Ltd, Trans Tech House, Aedermannsdorf, 4711, Switzerland (2000).
49 K. Nisancioglu, 'Corrosion of Aluminium', *Proceedings of the 3rd International Conference on Aluminium Alloys: Their Physical and Mechanical Properties*, Trondheim, Norway, 1992, **3**, 239.

11

Scanning Kelvin probe force microscopy and scanning Kelvin probe in investigation of effect of microstructure on corrosion behaviour of magnesium alloys

M. JÖNSSON, Swedish Corrosion Institute, Sweden,
D. THIERRY and N. LEBOZEC,
Institut de la Corrosion, France

11.1 Introduction

Magnesium has gained much interest as a structural material for automotive and aerospace applications due to its low density and high specific strength. However, the use of magnesium alloys in engineering applications is mainly limited by their unsatisfying surface properties and their poor corrosion resistance. In recent years, significant improvements have been made in achieving a better corrosion resistance, in particular by reducing impurities such as Fe, Cu, and Ni. Intermetallic phases, a result of the casting process, play an important role in the corrosion process. The role of these intermetallic phases has been addressed in a number of papers.[1–10] Lunder *et al.*[2,5,9] have studied the detrimental effect of intermetallic phases found in AZ91D magnesium alloy (i.e. Al_8Mn_5, Al_6Mn), by performing electrochemical studies on synthesised phases in solution. The same authors have also studied the beneficial role of Mn additions[6] and the influence of β-$Mg_{17}Al_{12}$ phase,[4] suggesting that this phase acts as a corrosion barrier and, thereby, reduces the corrosion rate of AZ91D alloy. However, despite the fact that magnesium alloys as structural materials are mostly used in atmospheric environments, the literature on the effect of intermetallics on the corrosion behaviour of magnesium alloys is exclusively dealing with an electrochemical approach in solution. It is well known that the corrosion processes in aqueous solutions are different from that of atmospheric environments. Therefore, a better knowledge of the corrosion properties of magnesium alloys under atmospheric conditions is crucial for the understanding of the corrosion mechanisms of magnesium alloys.

Recently, new techniques, such as the scanning Kelvin probe (SKP) and the scanning Kelvin probe force microscopy (SKPFM), have been developed making possible the investigation of the corrosion processes under

atmospheric weathering conditions at the micro- or even at the nano-scale. SKP is a non destructive technique for measuring the surface distribution of the Volta potential. Stratmann *et al*.[11–13] have shown that the open-circuit potential is linearly dependent on the Volta potential measured under a thin electrolyte layer. This has been confirmed by others authors.[14,15] Since the beginning of the 90s, SKPFM was mainly used by physicists for investigating the behaviour of thin films.[16–19] However, a few studies have been conducted using SKPFM in the field of corrosion science. Schmutz and Frankel[15,20,21] have studied the localised corrosion of AA2024 T3 using SKPFM. The Volta potential of intermetallic particles on AA 2024 T3 was determined at the submicron scale. It has been shown that the lateral resolution was at least 0.1 μm.[15] This gives unique information on the local nobility of inhomogeneities on surfaces at the submicron scale. More recently, the mechanisms of filiform corrosion of coated carbon steel have been investigated by SKPFM.[22]

In the present study, SKP and SKPFM techniques have been used together with topographic atomic force microscopy (AFM) and field emission gun scanning electron microscopy (FEG-SEM) in order to obtain a better understanding on the influence of the microstructure on the corrosion behaviour of AZ91D magnesium alloy.

11.2 Experimental methods

11.2.1 Materials

Die cast commercial AZ91D magnesium alloy was used. The composition of the alloy is given in Table 11.1. Pure magnesium (99.9%) and pure aluminum (99.999%) were also used.

Bulk material β-$Mg_{17}Al_{12}$ phase, Al_8Mn_5 intermetallic particles and homogenised magnesium phase (2.7 Al, 0.3 Mn, 97 Mg in wt%) were synthesised in a similar way to that described in references 2, 5 and 9, e.g. by a controlled solidification procedure from pure components.[4] The β-$Mg_{17}Al_{12}$ phase was prepared by melting pure magnesium together with 44 wt% of pure aluminum in a boronitride crucible. To protect the melt from

Table 11.1 Nominal composition (weight %) of AZ91D magnesium alloy

Composition (wt%)							
Al	Zn	Mn	Ni	Cu	Si	Fe	Mg
8.9	0.75	0.26	0.0008	0.0019	0.009	0.0027	remainder

oxidation, the melt was covered by a salt solution (NaCl–KCl–$MgCl_2$) and kept in a protective atmosphere (CO_2–4%SF_6). The Mg–Al melt was homogenised at 700–720°C and cooled to 650°C. The salt solution was then removed and the melt was subsequently slowly cooled to 460°C. Then, the furnace was turned off and the temperature was recorded. The melt slowly solidified between 455 and 450°C. When the cast reached 430°C, it was rapidly cooled to room temperature in order to avoid the formation of other phases. Homogenised Mg 3wt% Al was prepared in a similar way as β-$Mg_{17}Al_{12}$ phase. The homogeneity was then evaluated by slicing the cast in two and examining the sections with an optical microscope.

The η-Al_8Mn_5 phase was prepared by mixing aluminium and 52 wt% of manganese in an alumina crucible. The metals were then introduced in an infrared oven and heated at 1140°C. The melt was also protected by a liquid salt and a CO_2–4%SF_6 atmosphere. After approximately 30 min, the melt was slowly cooled to 800°C, homogenised in order to get a large grain size, and finally quickly cooled to room temperature. The phase was then identified using x-ray diffraction and a microprobe technique using a Cameca SX 100.

11.2.2 Electrochemical methods

Electrochemical measurements were performed using an EG & G potentiostat / galvanostat 283. All potentials were measured *versus* a saturated calomel electrode (SCE) and expressed *versus* the standard hydrogen electrode (SHE) in the text. The cathodic polarisation curves were recorded at the rate of 20 mV min^{-1} from the rest potential towards –1.75 V *vs.* SCE. Solutions were prepared from reagent grade chemicals and de-ionised water. The electrochemical measurements were performed in different NaCl solutions of 1, 0.85, 0.1, 0.01 and 0.001 mol L^{-1}. NaCl solution 0.85 mol L^{-1} was saturated with $Mg(OH)_2$. The solutions were de-aerated by purging with nitrogen. The pH was 6.7 for all solutions except for 0.85 mol L^{-1} NaCl where a pH of 10.3 was measured.

11.2.3 Scanning Kelvin probe

SKP is a non-destructive technique that can measure the Volta potential of a metal or a polymer-coated metal. The principle of SKP has been given in the literature.[14,22] The Volta potentials were measured using a commercial scanning Kelvin probe from 'UBM Messtechnik'. The equipment can be used for measuring the change in Volta potential *versus* time at a single point above the surface or mapping the Volta potential on a part of the sample. The reference electrode was made of a Ni–Cr alloy with a tip diameter of about 50 μm. The distance between the needle and the sample was

kept constant at 50 µm during all measurements. This arrangement gives a lateral resolution of the probe in the range of 80–100 µm. The probe was calibrated in humid air (95% rh) above a $Cu/CuSO_4$ saturated electrode and potentials are given *versus* SHE. The sample were polished down to 1200 grit, and cleaned ultrasonically in an acetone–ethanol bath. The samples were thereafter exposed to air at a controlled relative humidity between 10 and 95%. The relative humidity was controlled using a sensor located inside the exposure chamber. All measurements were performed at room temperature, e.g. 20°C.

11.2.4 Scanning Kelvin probe force microscopy

A commercial atomic force microscope (Thermomicroscope) was used in this work. The tip was made of silicon nitride coated with silver and supplied by Veeco Thermomicroscopes. All measurements were conducted at room temperature (20°C) and at a controlled relative humidity (40% rh). The samples were prepared in a similar way as described above for SKP measurements. The grinding of the surface of AZ91D causes a smear out of the soft magnesium. Therefore, in order to reveal the microstructure of the AZ91D alloy, the sample was etched for 2 s in 1 ml HNO_3, 20 ml glacial acetic acid, 50 ml ethylene glycol and 17 ml distilled H_2O.[23] The samples were then cleaned ultrasonically in an ethanol bath. The measurements were performed at the height of 100 nm.

11.2.5 Field emission gun scanning microscopy

Compositional analysis of the AZ91D surface was performed using a field emission gun scanning electron microscopy (FEG-SEM) model LEO 1530 equipped with energy dispersive spectrometry (EDS) model INCA-Energy from LINK. The acceleration voltage was 15 kV.

11.3 Results and discussion

11.3.1 Microstructure of AZ91D magnesium alloy

In agreement with the literature,[6,24] the intermetallic particles observed in the microstructure of AZ91D alloy, have a size ranging from 0.5 to 15 µm. In order to identify the intermetallic phases, electron probe microanalysis (EPMA) was performed. The results are presented in Table 11.2. It should be noticed that for intermetallics of small size (e.g. less than 5 µm), several particles were analysed to get a representative value. The analysis showed that the phase surrounding the grains consisted of approximately 71 at% Mg and 27 at% Al, and that the intermetallic particles consisted of approx-

Table 11.2 Typical EPMA analysis of the matrix and intermetallic particles in AZ91D

Element	Concentration (at%)		
	Matrix	$Al_8(Mn,Fe)_5$	β-$Mg_{17}Al_{12}$
Mg	97	(1)	71.5
Al	2.95	61.1	26.8
Si	0	0.15	0.046
Mn	0.025	37.7	0.041
Fe	0.004	(2)	0
Cu	0.007	0.022	0.004
Zn	0.04	0.11	1.6
Ca	0	0.02	0
La	≤0.003	≤0.003	0.002
Ce	≤0.003	≤0.001	0

(1) Mg varied from 0 to 41 at% in the analysis of Al_8Mn_5-particles due to the surrounding magnesium-matrix that influences the EDAX signal. (2) The content of iron in Al_8Mn_5 varied from 0.2 to 2.8 at%.

imately 61 at% Al and 38 at% Mn. By comparing the results from the microprobe analysis with existing phase diagrams, it was possible to conclude that the phase that precipitated around the grains was β-$Mg_{17}Al_{12}$ and that the intermetallic particles were made of η-Al_8Mn_5. As further inferred from Table 11.2, and in agreement with the literature, zinc was mainly dissolved in the β phase (1.6 at% in the β-phase compared with 0.04 at% in the matrix). The phases detected in AZ91D alloy are consistent with the literature on the subject.[5,9] It was also observed that Al_8Mn_5 intermetallic particles also contained a small percentage of iron. It should be mentioned that the content of iron varied from about 0.2 to 2.8 at%. It is well known that manganese has a high tendency to bind to iron to form different intermetallic particles.[6,25] Iron is often a result from impurities during the casting process.[3] It should be noted that even other particles such as Mg_2Si can be found in AZ91. However, these particles are harmless with respect to corrosion and consequently these particles were not included in this work.

11.3.2 Electrochemical measurements

The open-circuit potential of the different phases, pure magnesium and AZ91D alloy was measured in different electrolytes containing various concentrations of chloride ions. The results are summarised in Table 11.3. The open-circuit potential of the different phases increased in the following order: η-Al_8Mn_5 > β-$Mg_{17}Al_{12}$ > homogenised magnesium ~ pure

Table 11.3 Corrosion potential in different NaCl solutions. The solution at 0.85 mol L^{-1} was saturated with $Mg(OH)_2$

Phase/Alloy	NaCl, mol L^{-1}			
	0.01	0.1	0.85	1
Homogenised magnesium	−1.30	−1.33	−1.36	−1.36
β-$Mg_{17}Al_{12}$	−0.90	−0.93	−0.98	−0.96
η-Al_8Mn_5	−0.42	−0.49	−0.97	−0.53
AZ91D	−1.26	−1.28	−1.33	−1.33
Pure magnesium	−1.24	−1.30	−1.35	−1.36

magnesium ~ AZ91D. This indicates that η-Al_8Mn_5 is the noblest phase. As further inferred from Table 11.3, the open-circuit potential decreased with increasing NaCl concentration in the electrolyte independently of the composition of the phase or the alloy. This is due to an increase of the active surface areas. The surface was covered with a protective oxide layer. In the case of pure magnesium and homogenised magnesium, the layer probably consisted of $Mg(OH)_2$,[26] whereas in the case of aluminium containing phases, the oxide layer is formed by Al_2O_3.[27] In the presence of NaCl, the protective oxide layer is weakened due to the adsorption of chloride ions, and $Mg(OH)_2$ is thus transformed into soluble $MgCl_2$.[28] Consequently, an increase in chloride concentration resulted in the formation of larger active areas. This could also be observed visually, as the number of pits formed on the surface increased with increasing NaCl concentration. The potential values obtained in the presence of 0.85 mol L^{-1} NaCl electrolyte saturated with $Mg(OH)_2$ are in agreement with the literature.[9] The low open circuit potential observed for η-Al_8Mn_5 in 0.85 mol L^{-1} NaCl saturated with $Mg(OH)_2$ may be explained by the high pH of this electrolyte leading to a depassivation of the surface of η-Al_8Mn_5 phase at this pH. It should be noted that the open-circuit potential of the β-phase remained unchanged even at alkaline pH. This may be due to a better corrosion resistance of the β-phase compared with the η-Al_8Mn_5 phase at alkaline pH.

Figure 11.1 shows the cathodic polarisation curves for AZ91D alloy, pure magnesium, β-$Mg_{17}Al_{12}$ phase, homogenised magnesium, and η-Al_8Mn_5 phase. The measurements were performed in 0.85 mol L^{-1} NaCl saturated with $Mg(OH)_2$. It can be seen that AZ91D alloy, pure magnesium and homogenised magnesium phase have approximately the same cathodic behaviour. The cathodic current densities of the samples increased in the following order: AZ91D alloy ~ homogenised magnesium ~ pure magnesium < β-$Mg_{17}Al_{12}$ < η-Al_8Mn_5. Hence, the β-$Mg_{17}Al_{12}$ and η-Al_8Mn_5 showed the highest cathodic current densities. The cathodic reaction is

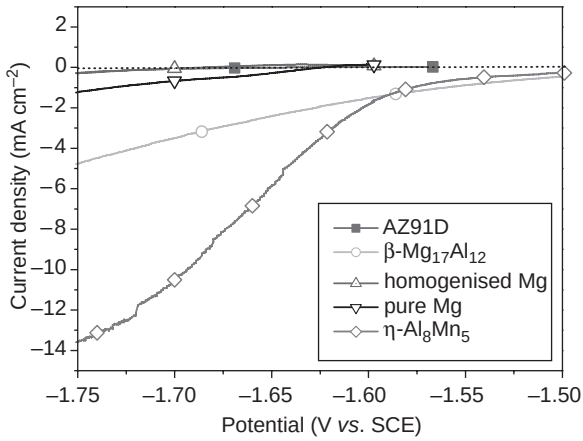

11.1 Cathodic polarisation curves obtained in 0.85 mol L^{-1} NaCl saturated with $Mg(OH)_2$ for AZ91D, β-$Mg_{17}Al_{12}$, homogenised magnesium, pure magnesium and η-Al_8Mn_5.

almost exclusively due to water reduction.[29] This could be seen visually since gas bubbles were formed at the surface. The number of gas bubbles increased when decreasing the potential. Hence, from Fig. 11.1, it can be concluded that in 0.85 mol L^{-1} NaCl solution saturated with $Mg(OH)_2$, both β-$Mg_{17}Al_{12}$ and η-Al_8Mn_5 will work as a cathode when coupled with the homogenised magnesium phase. The cathodic activity of the η-Al_8Mn_5 was, however, much higher than β-$Mg_{17}Al_{12}$ phase. This is in agreement with the literature on the subject.[5,30]

11.3.3 Scanning Kelvin probe measurements

It has been shown by Stratmann and co-workers that the corrosion potential of a bare metal covered with a layer of electrolyte is related linearly to the Volta potential measured in air according to the following equation:[11–13]

$$E_{\text{corr}} = \frac{W_{\text{e}}^{\text{ref}}}{F} - \chi_{\text{gas}}^{\text{sol}} + E_{1/2} + \Delta\Psi_{\text{sol}}^{\text{ref}} \qquad [11.1]$$

where $W_{\text{e}}^{\text{ref}}$ is the electronic work function of the probe material, F is the Faraday constant, $\chi_{\text{gas}}^{\text{sol}}$ is the dipole potential of the solution gas interface, $E_{1/2}$ is the half cell potential of the reference electrode, and $\Psi_{\text{sol}}^{\text{ref}}$ is the Volta potential difference.

In agreement with previous works, a linear relationship with a slope close to unity has been measured between the Volta potential and the open-circuit potential of pure metals. This is clearly shown in Fig. 11.2, for 6

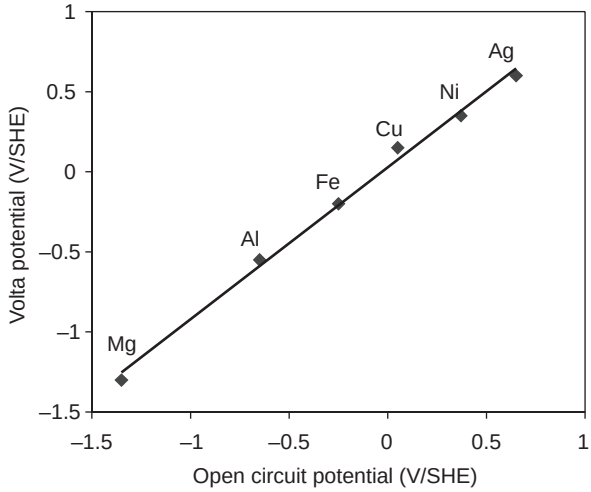

11.2 Calibration of scanning Kelvin probe with six pure metals.

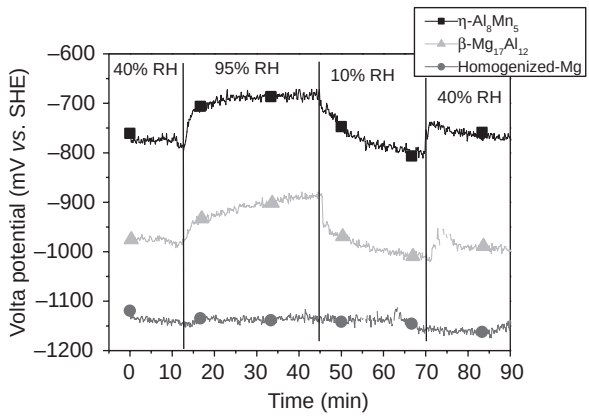

11.3 Volta potential *vs.* relative humidity for different phases.

different pure metals. The Volta potential was measured in air at 40% rh whereas the open-circuit potential was measured in deaerated water. From Fig. 11.2, it is clear that, over a broad potential range, the Volta potential of pure metals is a linear function of the open-circuit potential with a slope close to unity. This is in agreement with the literature on the subject.[13–22]

Volta potential measurements have also been performed on various magnesium-containing phases and at three different relative humidities, i.e. 10, 40 and 95% rh. The results are shown in Fig. 11.3. From the results, it is obvious that the Volta potential for the different phases decreased in the following order: η-Al_8Mn_5 > β-$Mg_{17}Al_{12}$ > homogenised Mg. It is well

known that the Volta potential is highly influenced by the surface state of the samples.[31] A freshly polished surface resulted in a higher Volta potential. In the case of the homogenised magnesium, the Volta potential was at around –1300 mV for a freshly polished surface, but the potential increased as the oxide/hydroxide layer formed and finally stabilised at about –1140 mV. The η-Al_8Mn_5 and β-$Mg_{17}Al_{12}$ phases exhibited a similar behaviour. A Volta potential of –780 mV and –980 mV was measured for η-Al_8Mn_5 and β-$Mg_{17}Al_{12}$, respectively, at 40% rh. As shown in Fig. 11.3, the Volta potential of η-Al_8Mn_5 and β-$Mg_{17}Al_{12}$ phases was influenced by the relative humidity in the exposure chamber. The Volta potential increased by about 80 mV for η-Al_8Mn_5 when changing the relative humidity from 40 to 95% rh. The Volta potential decreased again when decreasing the relative humidity. On the other hand, the Volta potential of the homogenised magnesium phase seems to be rather independent of the changes in the relative humidity in the exposure chamber. This is related to the aluminium content in the different phases (e.g. 54.7 and 44 wt% for η-Al_8Mn_5 and β-$Mg_{17}Al_{12}$, respectively, compared with 2.7 wt% for the homogenised magnesium phase). The high aluminium content in η-Al_8Mn_5 and β-$Mg_{17}Al_{12}$ phases will favour the oxygen reduction as the cathodic process, while hydrogen evolution will govern the cathodic reaction on the homogenised magnesium phase.

11.3.4 AFM/SKPM measurements

In order to measure the potential of the different phases at the nano- and micro-scale, it is important to calibrate the scanning Kelvin probe force microscope. Figure 11.4 shows a plot of the Volta potential measured by SKPFM *versus* the Volta potential measured by SKP. Care was taken to measure exactly over the same area with both techniques. As inferred from Fig. 11.4, the Volta potentials measured by SKPFM show a linear dependency with those measured by SKP. As observed in Fig. 11.2, the correlation in Volta potential observed by the two techniques remained valid for different metals and alloys over a wide potential range. This indicates that the Volta potential was more or less independent of the distance between the tip and the sample (e.g. the operating distance), which was ranging from about 100 nm for SKPFM to about 50 μm for SKP. However, the lateral resolution of SKPFM will largely be dependent upon the operating distance (e.g. the distance between the probe and the metal surface). Thus, the results shown in Figs. 11.2 and 11.4 justify the use of SKPFM to measure a difference in local nobility at the sub-micron scale.

The structure of a grain in AZ91D alloy was studied. The relative compositions of magnesium, aluminium and manganese were measured at four different locations. The results are given in Table 11.4. The grain consists of homogenised magnesium, with a composition of about 6 at% aluminium

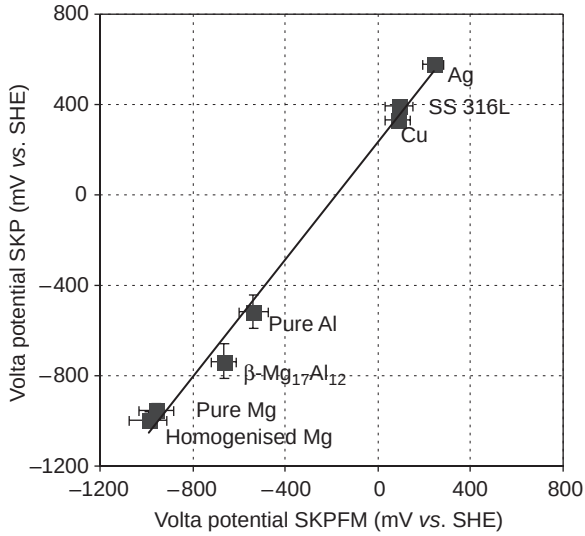

11.4 Comparison of Volta potentials measured with the SKPFM and the SKP.

Table 11.4 Composition and Volta potential measured by SKPFM (at 40% rh and 20°C) at locations 1–4

Location	Concentration (at%)			Phase	Volta potential (mV *vs.* SHE)
	Mg	Al	Mn		
1	15.8	53.8	30.4	Al_8Mn_5	–640
2	93.8	6.1	0.1	Homogenised Mg	–1025
3	89.2	10.6	0.2	β-$Mg_{17}Al_{12}$	–805
4	71.2	28.7	0.1	β-$Mg_{17}Al_{12}$	–760

and 94 at% magnesium (location 2). At the grain boundaries, around the homogenised grain (locations 3 and 4), β-$Mg_{17}Al_{12}$ phase was observed. The concentration of aluminium in β-$Mg_{17}Al_{12}$ varied from 6 at% in the homogenised magnesium grain to about 30 at% at the grain boundaries (location 1), in agreement with the literature.[28] In the middle of the grain, an Al–Mn intermetallic particle can be clearly seen. Comparing the composition determined using FEG-SEM coupled to EDS technique with the analysis performed by microprobe and existing phase diagrams, it can be concluded that the Al–Mn intermetallic particle is of type Al_8Mn_5. It should be noted that, although EDS analysis of this particle shows a content of magnesium, this is an artefact due to interference of the EDS signal with

Table 11.5 Corrosion potential of homogenised magnesium, β-$Mg_{17}Al_{12}$ and η-Al_8Mn_5 phases measured in NaCl solutions and under atmospheric conditions using SKP and SKPFM

Phases	NaCl solution			Atmosphere		
	Corrosion potential (mV *vs.* SHE)			Volta potential (mV *vs.* SHE)		
	0.01 M	0.1 M	1 M	SKP		SKPFM 40% rh
				40% rh	95% rh	
Homogenised magnesium	–1300	–1330	–1360	–1140	–1140	–980
β-$Mg_{17}Al_{12}$	–900	–930	–960	–980	–900	–800
η-Al_8Mn_5	–420	–490	–530	–780	–690	–690

the magnesium matrix surroundings. Most of the intermetallic particles found in AZ91D had a circular form and were found in the middle of the homogenised magnesium grain, in full agreement with the solidifying process.

Measurements of Volta potential distribution for AZ91D were performed using SKPFM at 40% rh and at 20°C. Brighter areas indicate higher Volta potentials and the darker locations correspond to lower Volta potentials, which in this case corresponds to the homogenised magnesium phase. The average Volta potentials at the four different locations studied by FEG-SEM are shown in Table 11.4. As inferred from Table 11.4, the Volta potential of the homogenised magnesium phase was about –1025 mV. Both Al_8Mn_5 intermetallic and β-$Mg_{17}Al_{12}$ phase showed nobler potentials of about –640 and –760 mV, respectively. Again, the high Volta potential of β-$Mg_{17}Al_{12}$ phase compared with the magnesium matrix is linked to the aluminium content of 30 at% for β-$Mg_{17}Al_{12}$ phase. It should also be noted that the locations between homogenised magnesium and β-$Mg_{17}Al_{12}$ where the aluminium content was lower (e.g. around 10 at%) showed a lower Volta potential at –800 mV.

It should be pointed out that, since the Thermoscope instrument lacks the lift mode capability, the Volta potential was mapped at the same time as the topographic image, which gave rise to a so called 'etching-effect' that might generate a noisy signal. Therefore, an area analysis should be preferred to a single-point analysis when analysing the Volta potential image. The area analysis has been used to average the Volta potential in a number of SKPFM images of the homogenised magnesium, β-$Mg_{17}Al_{12}$ and the Al_8Mn_5 particle. The results are given in Table 11.5. The potential within a single phase was not uniform. Relatively large variations of up 80 mV could

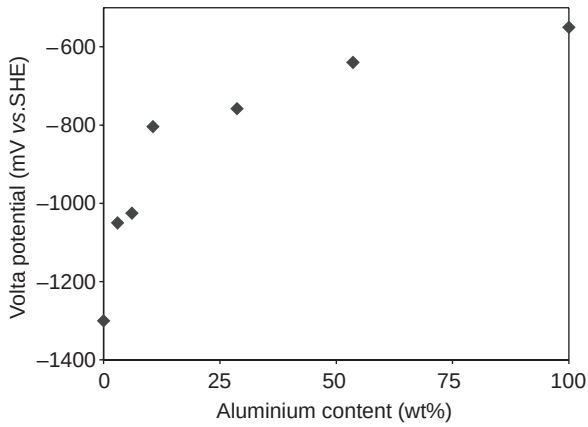

11.5 Volta potential as a function of aluminium content in Mg–Al phases.

be found within the homogenised magnesium phase. For Al_8Mn_5 intermetallic particles, variations within different particles were in the range of 120 mV. This is due to variation in the aluminium content of the intermetallic particles from 58 to 67%.

The difference in Volta potential between the homogenised magnesium and β-$Mg_{17}Al_{12}$ was around 200 mV while a higher potential difference around 300–350 mV was observed between the homogenised magnesium and Al_8Mn_5 intermetallic particle. Analyses of other locations in AZ91D alloy indicated that a similar relative difference could be found between the homogenised magnesium, β-$Mg_{17}Al_{12}$ and Al_8Mn_5 intermetallic. The relative differences between β-$Mg_{17}Al_{12}$ phase and Al_8Mn_5 intermetallic measured using SKPFM correspond well to the Volta potential values obtained using SKP and measured over bulk made phases (see Figure 11.4). One should, however, note that minor deviations can be expected due to differences in composition between the synthesised phases and the phases found in the actual alloy.

A closer examination of a large number of SKPFM images on AZ91D indicates that the surface coverage of areas with a Volta potential higher than 100 mV above that of the homogenised magnesium phase can be estimated to approximately 45% of the total area. The areas with higher Volta potential correspond mainly to areas with β-$Mg_{17}Al_{12}$ phase and areas with a higher aluminum content (see Table 11.5).

The influence of the aluminium content on the Volta potential of Mg–Al phases is given in Fig. 11.5. It is clear that a high aluminium content results in an increase in the Volta potential as expected. Thus, it is more likely that the areas of high Volta potential in Fig. 11.5 are closely linked to areas with increasing aluminium content. Therefore, the formation of a zone at higher

Volta potential along the grain boundary corresponds probably to the formation of an Al-rich coring. It has also been reported that the aluminium content is higher at the surface layer than in the bulk of Mg–Al alloys.[27,32] This can be an explanation of the relatively large areas with a higher Volta potential.

As reported elsewhere, manganese content in the Al_8Mn_5 phase also decreases from the centre of the particle to the edges.[23] This effect may explain the decrease in the Volta potential observed at the edges of intermetallics of Al_8Mn_5 type. The remaining area in AZ91D alloy corresponds to homogenised magnesium. It should be noted that the intermetallic phase Al_8Mn_5 covered less than 1% of the surface area.

From SKPFM results, it is clear that β-$Mg_{17}Al_{12}$ phase and Al_8Mn_5 intermetallic work as local cathodes when coupled to the homogenised magnesium phase. The surface coverage of β-$Mg_{17}Al_{12}$ phase is much higher than that of the intermetallic phases (e.g. about 40% compared with 1%) and consequently, this first phase should play an important role in the initiation of the corrosion on AZ91D. However, it is well known that β-$Mg_{17}Al_{12}$ phase itself is resistant to corrosion, forming a corrosion resistant barrier with the precipitation of an Al-rich coring along the grain boundary. Thus, more work is needed in order to fully understand the exact role of the β-$Mg_{17}Al_{12}$ phase.

It is well known from the literature that the intermetallic particles play an important role in the initiation process of localised corrosion attacks on passive surfaces.[1,8] The effect of Al_8Mn_5 particles is linked to the fact that these particles will act as efficient cathodes with respect to the homogenised magnesium phase (see Fig. 11.2). Although these particles are only covering about 1% of the surface, an important effect may be expected as the cathodic efficiency of Al_8Mn_5 particles is much higher than that of β-phase. An examination of AZ91D samples after exposure to NaCl solutions confirmed these results. The amount of pits increased together with the amount of NaCl. The pitting started at locations where the passivity of the AZ91D alloy was weaker, e.g. around the intermetallic particles.

11.4 Conclusions

The following conclusions may be drawn from this work:

- SKPFM is a powerful tool to measure difference in local nobility induced by the microstructure.
- A linear relationship was observed between the Volta potential measured by SKPFM and that measured by SKP.
- The Volta potential of Mg-Al phases was dependent on the aluminium content.

- A good relationship was observed between the precipitation of Al-rich phases and the Volta potential.
- β-$Mg_{17}Al_{12}$ phase and Al_8Mn_5 intermetallic particles work as local cathodes when coupled to the homogenised magnesium phase under atmospheric weathering conditions.
- Corrosion on AZ91D magnesium alloy was initiated as pits starting at locations around the intermetallic particle Al_8Mn_5, probably due to the combined effect of high local nobility and high cathodic efficiency.

11.5 Acknowledgements

The authors would like to thank Dr. Christian J. Simensen, from SINTEF (Materials Technology, Norway) for help with microprobe investigations of AZ91D alloy and manufacturing of intermetallic phases, and Stanislaw Zajac from the Swedish Institute for Metals Research, for the help with FEG-SEM investigations.

11.6 References

1 O. Lunder, J. E. Lein, S. M. Hesjevik, T. K. Aune and K. Nisancioglu, *Werkstoffe und Korrosion*, 1994, **45**, 331–340.
2 O. Lunder and K. Nisancioglu, Electrochemical Behaviour of Intermetallic Phases in mg–Al Cast Alloys, in *The Understanding and Prevention of Corrosion (Conf.)*, 1993, Barcelona, Spain.
3 O. Lunder, M. Videm and K. Nisancioglu, *J SAE Tech. Paper*, 1995, 950428, 57–62.
4 O. Lunder, J. E. Lein, T. K. Aune and K. Nisancioglu, *Corrosion*, 1989, **45**(9), 741–748.
5 O. Lunder, J. H. Nordlien and K. Nisancioglu, *Corros. Rev.*, 1997, **15**(3–4), 439–469.
6 O. Lunder, T. K. Aune and K. Nisancioglu, *Corrosion*, 1987, **43**(5), 291–295.
7 G. Song, A. Atrens and M. Dargusch, *Corros. Sci.*, 1999, **41**, 249–273.
8 L.-Y. Wei, H. Westengen, T. K. Aune and D. Albright, *Magnesium Technology 2000*, The Minerals, Metals & Materials Society, 2000.
9 O. Lunder, K. Nisancioglu and R. S. Hansen, *SAE Technical Paper Series*, 1993, 930755.
10 S. Mathieu, C. Rapin, J. Steinmetz and P. Steinmetz, *Corros. Sci.*, 2003, **45**, 2741–2755.
11 M. Stratmann and H. Streckel, *Corros. Sci.*, 1990, **30**(6/7), 681–696.
12 M. Stratmann, H. Streckel, K. T. Kim and S. Crockett, *Corros. Sci.*, 1990, **30**(6/7), 715–734.
13 M. Stratmann, H. Streckel, K. T. Kim and S. Crockett, *Corros. Sci.*, 1990, **30**(6/7), 697–714.
14 Y. Shelgon, R. A. Oriani and M. Stratmann, *J. Electrochem. Soc.*, 1991, **138**(1), 55–61.
15 P. Schmutz and G. S. Frankel, *J. Electrochem. Soc.*, 1998, **145**(7), 2285–2294.

16 Y. Martin, D. Abraham and K. Wickramasinghe, *Appl. Phys. Lett.*, 1988, **52**(13), 1103.
17 H. O. Jacobs, H. F. Knapp and A. Stemmer, *Rev. Sci. Instrum.*, 1999, **70**(3), 1756–1760.
18 H-Y. Nie, K. Horiuchi, H. Yamauchi and J. Masai, *Nanotechnology*, 1997, **8**, A24–A31.
19 L. F. Chi, S. Jacobi and H. Fuchs, *Thin Solid Films*, 1996, **284–285**, 403–407.
20 P. Schmutz and G. S. Frankel, *J. Electrochem. Soc.*, 1998, **145**(7), 2295–2306.
21 V. Guillaumin, P. Schmutz and G. S. Frankel, *J. Electrochem. Soc.*, 2001, **148**(5), B163–B173.
22 R. Aveyard and D. A. Haydon, *An Introduction to the Principles of Surface Chemistry*. University Press, Cambridge, 1973.
23 'Metallography and microstructures', in *Metals Handbook*, 1985, American Society for Metals, p. 425.
24 G. Song, A. Atrens, X. Wu and B. Zhang, *Corros. Sci.*, 1998, **40**(10), 1769–1791.
25 I. J. Polmear, *Light Alloys: Metallurgy of the Light Metals, Metallurgy and Materials Science Series*. 1995, 362.
26 J. H. Nordlien, O. Sachiko, M. Noburo and K. Nisancioglu, *J. Electrochem. Soc.*, 1995, **142**(10), 3320–3322.
27 J. H. Nordlien, O. Sachiko, M. Noburo and K. Nisancioglu, *J. Electrochem. Soc.*, 1996, **143**(8), 2564–2572.
28 R. Ambat, N. N. Aung and W. Zhou, *J. Appl. Electrochem.*, 2000, **30**(7), 865–874.
29 I. L. Rozenfeld, *Atmospheric Corrosion of Metals*, 1972, Houston, 221.
30 S. Mathieu, C. Rapin, J. Steinmetz and P. Steinmetz, *Corros. Sci.*, 2003, **45**, 2737–2756.
31 H. H. Uhlig, *J. Appl. Phys.*, 1951, **22**(12), 1399–1403.
32 J. H. Nordlien, K. Nisancioglu, S. Ono and N. Masuko, *J. Electrochem. Soc.*, 1997, **144**(2), 461–466.

12

Use of scanning Kelvin probe force microscopy and microcapillary cell to investigate local corrosion behaviour of 7xxx aluminium alloys

F. ANDREATTA and H. TERRYN,
Netherlands Institute for Metals Research, The Netherlands,
M. M. LOHRENGEL, Heinrich Heine University, Germany,
J. H. W. DE WIT, Netherlands Institute for Metals Research,
The Netherlands

12.1 Introduction

The 7xxx aluminium alloys, such as AA7075, are susceptible to severe localised corrosion, like pitting, intergranular corrosion and exfoliation corrosion.[1–3] The susceptibility of these alloys is strongly affected by heat treatments, which change the microstructure of the alloy in order to give optimum mechanical properties.[4–6] The low resistance to localised corrosion of particular microstructures represents a problem for the application of 7xxx alloys in the aerospace industry.

The microstructure of AA7075 exhibits intermetallics and strengthening particles.[7] The intermetallics are formed during casting and ingot homogenisation due to interaction between alloying elements and impurities present in the alloy.[8] In AA7075, the Al_7Cu_2Fe and $(Al,Cu)_6(Fe,Cu)$ are the most abundant intermetallics, while Mg_2Si intermetallics are present in smaller quantities.[7,9] The strengthening particles have the composition $MgZn_2$ (η phase). Their precipitation in the matrix during aging provides strength to the alloy.[4,5] In addition, the strengthening particles precipitate at the grain boundaries strongly affecting the resistance to intergranular corrosion of the alloy. Solution heat treatment and aging both change the size, the composition and the distribution of the strengthening particles in AA7075.[6,10]

The electrochemical behaviour of 7xxx alloys has been investigated by means of open circuit potential (OCP) and potentiodynamic polarisation measurements. The potentiodynamic polarisation curves for AA7075 exhibit one breakdown potential for the peak-strength T6 temper and two breakdown potentials for the solution heat treated and the overaged (T76) tempers.[11–13] The Al_7Cu_2Fe and $(Al,Cu)_6(Fe,Cu)$ intermetallics are the initi-

ation sites for pitting in Al–ZN–Mg–Cu alloys.[1–3] The pitting is due to local dissolution of the matrix or to dissolution of the intermetallics because there is galvanic coupling between intermetallics and matrix.[3] The intermetallics containing Cu and Fe are cathodic with respect to the matrix and promote dissolution of the matrix, while Mg-rich intermetallics are anodic with respect to the matrix and dissolve preferentially.[1,14] Scanning Kelvin probe force microscopy (SKPFM) is used to measure the Volta potential difference between intermetallics and matrix in air.[15–20] In AA7075, the Volta potential difference between intermetallics and matrix depends on the composition of the intermetallics and on the heat treatments performed on the alloy.[21,22] The microcapillary cell technique[23–26] is used to measure local breakdown potentials for areas of aluminium alloys containing one or a few intermetallics.[27,28] The Volta potentials measured with the SKPFM are related to the local breakdown potentials measured with the microcapillary cell.[28–30]

12.2 Results and discussion

Table 12.1 reports the wt% composition for two intermetallics in AA7349, which was measured by means of SEM-EDS. Both intermetallics contain Cu and Fe. The intermetallic 1 exhibits a higher Cu content and a lower Fe content than the intermetallic 2. Moreover, both intermetallics contain Mn with the Mn content of intermetallic 2 significantly higher as compared with intermetallic 1.

After characterisation of a large number of intermetallics (about 50), the intermetallic 1 is identified as a Al_7Cu_2Fe+Mn intermetallic and intermetallic 2 as a $(Al,Cu)_6(Fe,Cu)$+Mn intermetallic. Mg_2Si intermetallics are also present in the microstructure of AA7349. Fig. 12.1 shows the intermetallics 1 and 2 in AA7349.

AA7349 exhibits the same types of intermetallics found in AA7075 and in the experimental alloy (indicated as EA1) with composition in the range of AA7449.[28–30] In contrast with AA7075, the Cu- and Fe-rich intermetallics in AA7349 and EA1 contain small amounts of Mn (and Si for EA1). This is indicated by '+Mn' in the composition of the intermetallics (Fig. 12.1).

Table 12.1 Wt% composition for two intermetallics in AA7349

Intermetallic	Al	Zn	Mg	Cu	Fe	Si	Cr	Mn
1	61.6	3.5	0.7	23.6	9.6	0	0.2	0.8
2	65.4	4.1	0.1	6.3	20.9	0	0.5	2.7

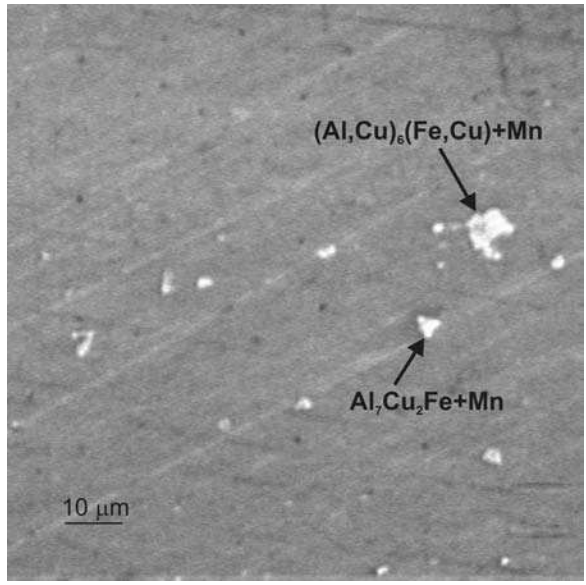

12.1 Example of intermetallics in AA7349.

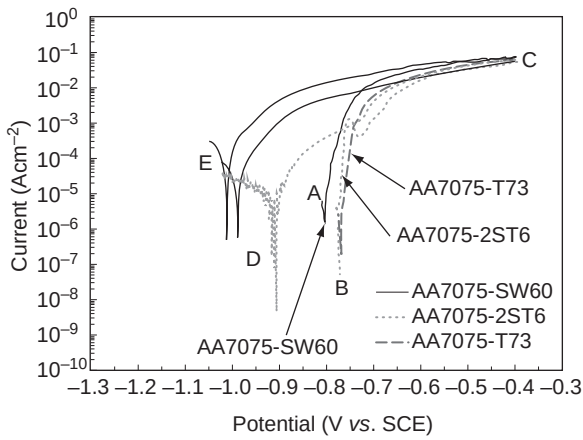

12.2 Potentiodynamic polarisation curves for AA7075-SW60, AA7075-2ST6 and AA7075-T73 in 3.5% NaCl solution at pH 4.

This is attributed to the different chemical composition of the alloys investigated.

Figure 12.2 shows the potentiodynamic polarisation curves for different tempers of AA7075 (macro-electrochemical behaviour). This topic is discussed in detail in another paper.[29] The temper that underwent solution heat treatment at 470°C for 1 h (AA7075-SW60) exhibits a breakdown at

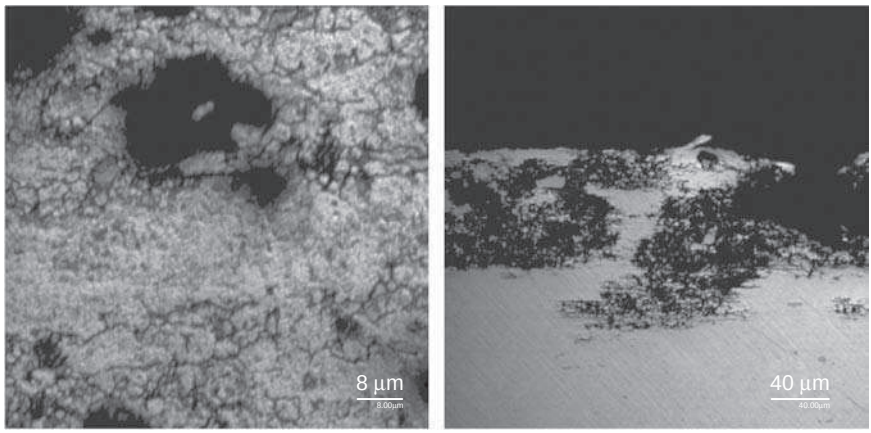

12.3 Micrographs of *a* the exposed surface and *b* the cross-section for AA7349-T76511 after potentiodynamic polarisation in 3.5% NaCl solution at pH 4.

–0.799 V *vs.* SCE, while the peak-strength T6 temper (AA7075-2ST6) and the overaged temper (AA7075-T76) show the breakdown respectively at –0.770 V *vs.* SCE and at –0.762 V *vs.* SCE. The existence of a more negative breakdown for AA7075-SW60 than for AA7075-2ST6 and AA7075-T76 demonstrates that solution heat treatment increases the susceptibility to localised corrosion, while aging to the peak-strength and overaging improves the resistance to localised attack.

Figure 12.3 shows that the localised attack takes place in the form of pitting at the periphery of the intermetallics and as intergranular and exfoliation corrosion in AA7349-T76511. This was also observed for AA7075 and EA1, as reported elsewhere.[28–30] In particular, it was shown that the intermetallics are the initiation sites for the localised corrosion.

Figure 12.4 shows a topographic map (a), a Volta potential map (b), a topographic line scan (c), and a Volta potential line scan (d) measured with the SKPFM for AA7075. The intermetallics 1, 2 and 3 are brighter than the matrix (Fig. 12.4b) meaning that a positive Volta potential difference exists between these intermetallics and the surrounding matrix. The intermetallic 3 exhibits a Volta potential difference of +437 mV relative to the matrix in the Volta potential line scan in Fig. 12.4d. The intermetallics 4 and 5 are darker than the matrix (Fig. 12.4b) indicating that a negative Volta potential difference exists between these intermetallics and the surrounding matrix. In Fig. 12.4d, the intermetallic 4 exhibits a potential difference of about –95 mV relative to the matrix.

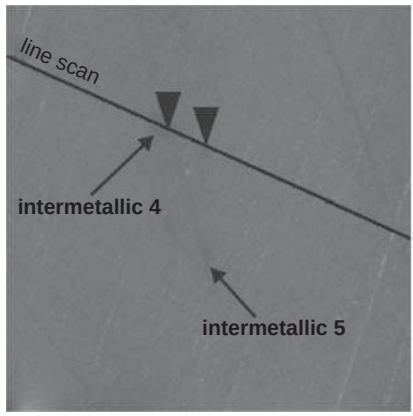

a

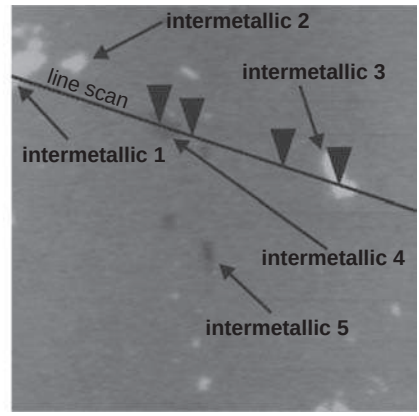

b

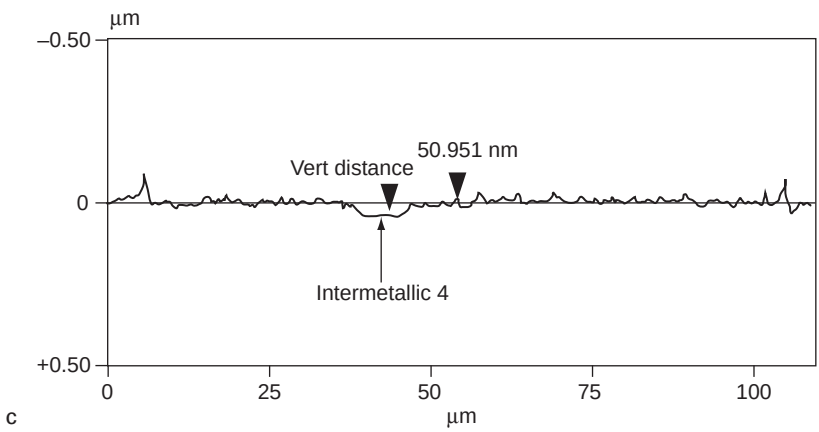

c

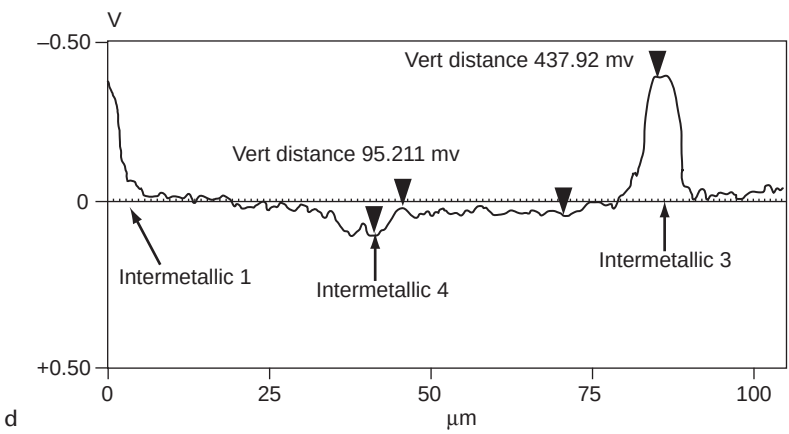

d

12.4 *a* Topographic map, *b* Volta potential map, *c* topographic line scan along the line shown in *a* and *d* Volta potential line scan along the line shown in *b*.

Table 12.2 Volta potential differences relative to the matrix for different types of intermetallics in as received AA7075-T6 (ART6) (number of intermetallics, maximum and minimum, average and standard deviation)

Temper	Number		Volta potential difference (mV)		
			Al_7Cu_2Fe	$(Al,Cu)_6(Fe,Cu)$	Mg_2Si
ART6	36	max.	+475	+402	−112
		min.	+281	+257	−181
		av.	+396	+341	−141
		st. dev	64	38	34

Table 12.2 reports the Volta potential differences measured for as received AA7075-T6. The existence of positive Volta potential differences between the intermetallics and the matrix indicates that the intermetallics have cathodic behaviour relative to the matrix, while the existence of negative Volta potential differences implies that the intermetallics have anodic behaviour relative to the matrix.

The Volta potential differences in Table 12.2 exhibit a rather large standard deviation for all types of intermetallics. This is associated with a rather large range of variation, as shown by the values of the maximum and minimum Volta potential differences.

Figure 12.5 shows an SEM micrograph (a), a Volta potential map (b), a Volta potential line scan (c) and EDS elemental maps (d and e) for a Cu- and Fe-rich intermetallic in AA7075. Figure 12.5c shows a Volta potential difference of 102 mV between point 1 and point 2 in Fig. 12.5a and b. The EDS elemental maps in Fig. 12.5d and e indicate that the existence of this potential difference is associated with a higher Cu content at point 2 than at point 1. Therefore, it is concluded that the existence of a range for the Volta potential difference (Table 12.2) is due to small changes in the composition of the intermetallics (content of Cu, Fe, Si and Mg).

Previous work[29] shows that solution heat treatment strongly increases the Volta potential differences relative to the matrix for all types of intermetallics in AA7075, while aging and overaging decreases the potential differences. This is related to the change in Mg and Zn content of the matrix caused by either dissolution or precipitation of $MgZn_2$ strengthening during heat treatment.

Figure 12.6 shows the areas characterised with the microcapillary cell for solution heat treated AA7075-SW60 (Fig. 12.6a) and for over-aged AA7075-T73 (Fig. 12.6b) and the potentiodynamic polarisation curves (Fig. 12.6c) for these tempers (micro-electrochemical behaviour). The

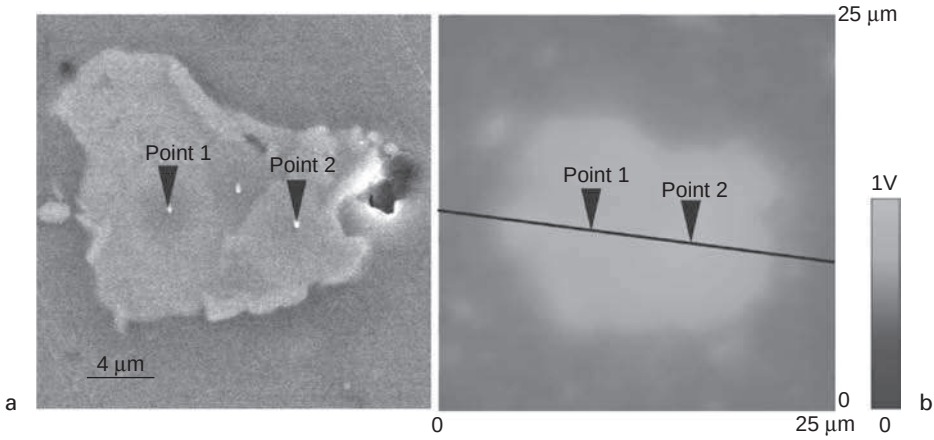

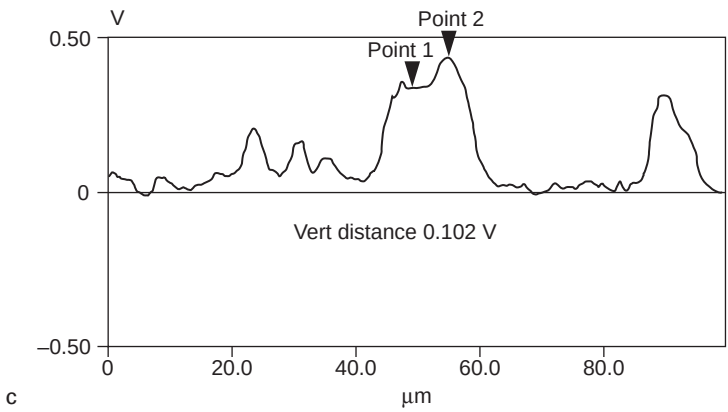

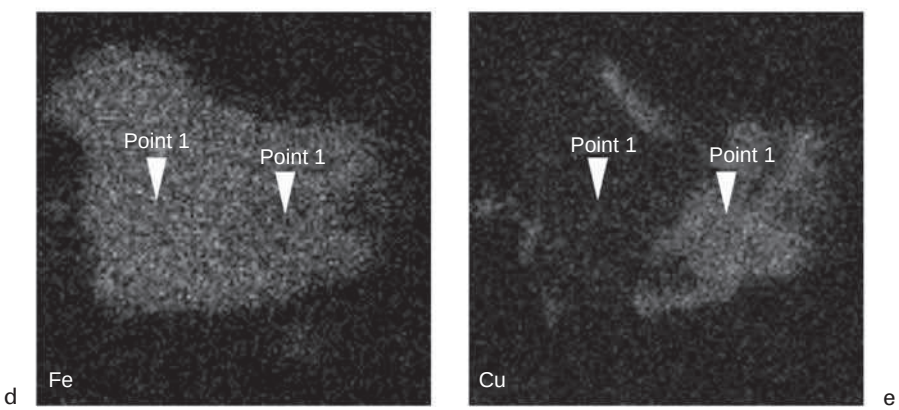

12.5 *a* SEM micrograph, *b* Volta potential map, *c* Volta potential line scan along the line in *b*, and *d* EDS elemental map for Fe in an intermetallic in AA7075, and *e* EDS elemental map for Cu for an intermetallic in AA7075.

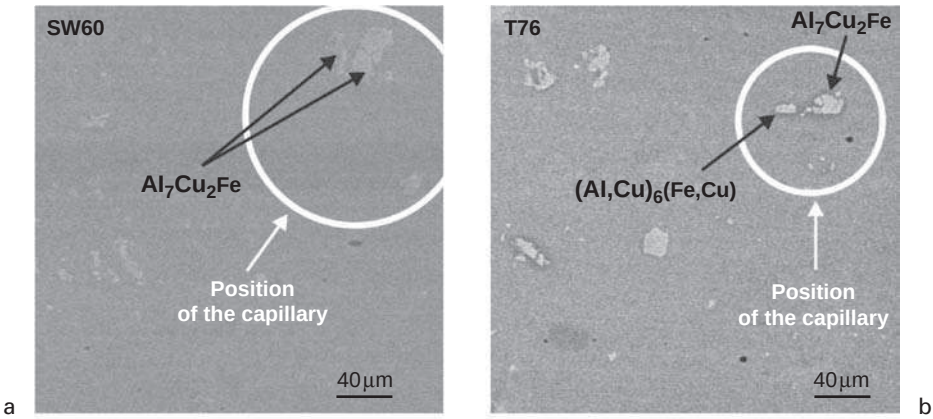

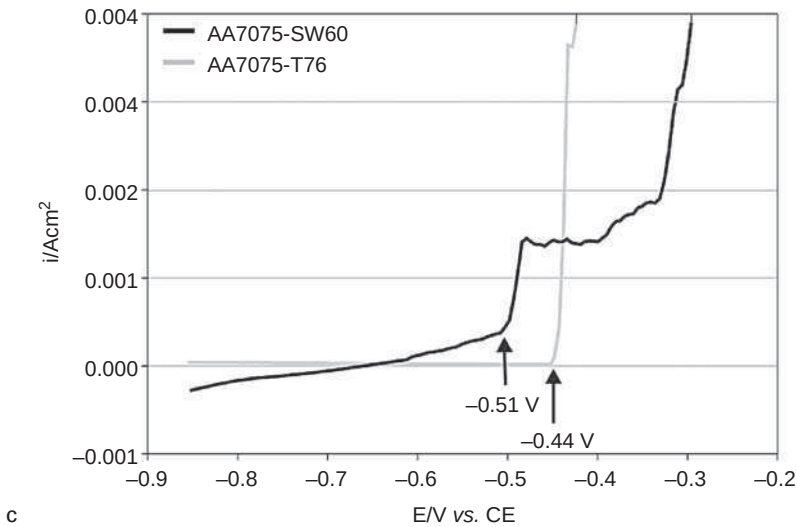

12.6 SEM micrographs showing the areas characterised with the microcapillary cell for *a* AA7075-SW60 and *b* AA7075-T76; and *c* first 0.05 V of the potentiodynamic polarization curves for these two tempers. The scan rate was 0.1 V s^{-1}.

micro-electrochemical behaviour of AA7075 is considered in detail in another paper.[29] The potentiodynamic polarisation curve for AA7075-SW60 exhibits a breakdown at –0.51 V *vs.* CE (1 M calomel electrode), while AA7075-T73 shows a breakdown at –0.44 V *vs.* CE. This is associated with a higher Volta potential difference for the intermetallics visible in Fig. 12.6a for AA7075-SW60 (about 700 mV) than for those in Fig. 12.6b (about 500 mV).[29] The existence of a more negative local breakdown potential for

AA7075-SW60 than for AA7075-T73 (similar temper to AA7075-T76) is in accordance with the macro-electrochemical behaviour shown in Fig. 12.2. This confirms that the solution heat treatment of AA7075 increases the susceptibility to localised corrosion, while aging and overaging decrease it.

Furthermore, the areas containing Al_7Cu_2Fe intermetallics exhibit more negative local breakdown potentials than the areas containing $(Al,Cu)_6(Fe,Cu)$ intermetallics.[28–30] This is in accordance with the existence of higher Volta potential difference for the former type of intermetallics (Table 12.2). The local breakdown potentials measured for AA7349 are more negative than those for AA7075 when similar tempers are compared (not shown here). This is associated with a higher susceptibility to localised corrosion for the former alloy in the macro-electrochemical behaviour.[30] The effect of heat treatment is less strong for EA1 than for AA7075.[30]

The results of the characterisation by means of the SKPFM and micro-capillary cell validate the interpretation of the Volta potential between the intermetallics and the matrix as a driving force for the initiation of localised corrosion. The areas of the sample surface showing high Volta potential differences between the intermetallics and the matrix exhibit higher susceptibility to localised corrosion (more negative breakdown potentials) than areas with low Volta potential differences. This is observed both when the effect of the composition of the intermetallics is considered and when the effect of the heat treatment is investigated.[28–30]

12.3 Conclusions

From the measurements of Volta potential difference with the SKPFM for AA7075, AA7349 and EA1, it can be concluded that:

- Rather high Volta potential differences (in the order of a few hundred mV) exist between the intermetallics and the matrix for the alloys investigated. The Al_7Cu_2Fe and $(Al,Cu)_6(Fe,Cu)$ have cathodic behaviour relative to the matrix, while the Mg_2Si intermetallics have anodic behaviour. Furthermore, the Al_7Cu_2Fe intermetallics have stronger cathodic behaviour than the $(Al,Cu)_6(Fe,Cu)$ intermetallics.
- The Volta potential difference between the intermetallics and the matrix is strongly affected by heat treatment of AA7075.
- The existence of Volta potential differences between the intermetallics and the matrix is interpreted as the driving force for the initiation of localised corrosion at the location of the intermetallics.

From the measurements of local breakdown potential with the micro-capillary cell, it can be concluded that:

- The existence of intermetallics in the matrix of the alloys causes a breakdown in the potentiodynamic polarisation curves measured with the microcapillary cell. The areas containing intermetallics exhibit a more negative local breakdown potential than the matrix.
- The areas containing the Al_7Cu_2Fe intermetallics are more susceptible to localised corrosion than the areas containing the $(Al,Cu)_6(Fe,Cu)$ intermetallics.
- The local breakdown potentials measured with the microcapillary cell are strongly affected by heat treatments performed on AA7075. The solution heat treatment increases the susceptibility of AA7075 to the initiation of localised corrosion. The aging and overaging decrease the susceptibility of AA7075 to the initiation of localised corrosion.
- The local breakdown potentials measured for AA7349 are more negative than for AA7075. This indicates a higher susceptibility to localised corrosion for the former alloys than for AA7075. The effect of the heat treatment on the measurements of Volta potential difference is less strong for EA1 than for AA7075.

The complementary use of SKPFM, SEM-EDS and microcapillary cell gives access to complementary information about the micro-electrochemical behaviour of the alloys investigated. The SKPFM technique is very useful for measuring the Volta potential differences between the intermetallics and the matrix (in air), while the microcapillary cell technique makes it possible to study of the local breakdown potentials of areas containing the intermetallics (in solution). The measurements of Volta potential difference and of local breakdown potential exhibit the same trend. This indicates that a high driving force for the initiation of the localised corrosion (Volta potential difference) corresponds to a high susceptibility to the initiation of the attack (local breakdown potential).

12.4 References

1 R. P. Wei, C. M. Liao and M. Gao, *Metall. Mater. Trans. A*, 1998, **29A**, 1153–1160.
2 T. G. Dunford and B. E. Wilde, 'The use of quantitative microscopy in studying the localised corrosion of aluminium 7075', in *Microstructural Science*, 263–272, (M. E. Blum, P. M. French, R. M. Middleton and G. F. Vander Voort), American Society for Metals and International Metallographic Society, USA, 1987.
3 P. S. Pao, C. R. Feng and S. J. Gill, *Corrosion*, 2000, **56**, 1022–1031.
4 J. K. Park and A. J. Ardell, *Metall. Trans. A*, 1983, **14A**, 1957–1965.
5 J. K. Park and A. J. Ardell, *Scr. Metall.*, 1988, **22**, 1115–1119.
6 C. W. Bartges, *J. Mater. Sci. Lett.*, 1994, **13**, 776–778.
7 R. Ayer, J. Y. Koo, J. W. Steeds and B. K. Park, *Metall. Trans. A*, 1985, **16A**, 1925–1936.
8 R. G. Hamerton, H. Cama and M. W. Meredith, *Mater. Sci. Forum*, 2000, **331–337**, 143–154.

9 M. Gao, C. R. Feng and R. P. Wei, *Metall. Mater. Trans. A*, 1998, **29A**, 1145–1151.
10 P. Guyot and L. Cottignies, *Acta Mater.*, 1996, **44**, 4161–4167.
11 S. Maitra and G. C. English, *Metall. Trans. A*, 1981, **12A**, 535–541.
12 S. Maitra and G. C. English, *Metall. Trans. A*, 1982, **13A**, 161–166.
13 T. Ramgopal, G. S. Frankel, 'Role of alloying elements and intermetallic particles in the intergranular corrosion of AA7150', in *Corrosion and corrosion prevention of low density metals and alloys*, 411–421, R. G. Buchheit, B. A. Shaw and J. P. Moran (eds.), Electrochemical Society, Phoenix, Arizona, USA, 2000.
14 C. M. Liao and R. P. Wei, *Electrochim. Acta*, 1999, **45**, 881–888.
15 P. Schmutz and G. S. Frankel, *J. Electrochem. Soc.*, 1998, **145**, 2285–2295.
16 P. Schmutz and G. S. Frankel, *J. Electrochem. Soc.*, 1998, **145**, 2295–2306.
17 P. Schmutz and G. S. Frankel, *J. Electrochem. Soc.*, 1999, **146**, 4461–4472.
18 P. Campestrini, E. P. M. van Westing, H. W. van Rooijen and J. H. W. de Wit, *Corros. Sci.*, 2000, **42**, 1853–1861.
19 P. Campestrini, E. P. M. van Westing, H. W. van Rooijen and J. H. W. de Wit, *Mater. Corros.*, 2000, **51**, 616–627.
20 V. Guillaumin, P. Schmutz and G. S. Frankel, *J. Electrochem. Soc.*, 2001, **148**, B163–B173.
21 F. Andreatta, J. R. Flores, E. P. M. van Westing and J. H. W. de Wit, 'AFM and SEM characterisation of the microstructure of AA7075-T6', in *Corrosion and corrosion protection*, 1009–1017, J. D. Sinclair, R. P. Frankenthal, E. Kalman and W. Plieth (eds.), Electrochemical Society, San Francisco, California, USA, 2001.
22 F. Andreatta, H. Terryn and J. H. W. de Wit, *Corros. Sci.*, 2003, **45**, 1733–1746.
23 M. M. Lohrengel, A. Moehring and M. Pilanski, *Electrochim. Acta*, 2001, **47**, 137–141.
24 M. M. Lohrengel, A. Moehring and M. Pilanski, *Fresenius J. Anal. Chem.*, 2000, **367**, 334–339.
25 A. W. Hassel and M. M. Lohrengel, *Electrochim. Acta*, 1997, **42**, 3327–3333.
26 H. Böhni, T. Suter and F. Assi, *Surf. Coat. Technol.*, 2000, **130**, 80–86.
27 T. Suter and R. C. Alkire, *J. Electrochem. Soc.*, 2001, **148**, B36–B42.
28 F. Andreatta, M. M. Lohrengel, H. Terryn, J. H. W. de Wit, *Electrochim. Acta.*, 2003, **48**, 3239–3247.
29 F. Andreatta, H. Terryn, J. H. W. de Wit, *Electrochim. Acta.*, 2004, **49**, 2851–2862.
30 F. Andreatta, PhD thesis, Local electrochemical behaviour of 7xxx aluminium alloys, 2004, Delft University of Technology.

13

Atmospheric corrosion of low alloy steels in a high-humidity seashore environment

H. MASUDA, NIMS, Japan

13.1 Introduction

Atmospheric corrosion of steels is a commonly observed phenomena. It is well known that the atmospheric corrosion of steel is accelerated by sea salt particles in a seashore environment. However, the mechanism of atmospheric corrosion of steel has not been clarified because of the difficulty of experimental work. We have developed a new atmospheric corrosion test device that can control the amount of attached sea salt particles. By using this device, a certain concentration of sea salt particles was attached to a low alloy steel and the initiation of atmospheric corrosion was observed by the super Kelvin force microscope (SKFM).[1]

13.2 Experimental method

The Kelvin force method used in SKFM was originally developed by Yasutake *et al.*[2] In this method, topography and surface potential can be obtained at the same time in the non-contact mode. The scanning device for x–y direction involves an accurate x–y stage. The accuracy of the x–y stage is less than 0.1 μm for repeated positioning. The x–y stage can move up to 10 cm × 10 cm, but the maximum scanning area is limited to 1 cm × 1 cm. The minimum step of the x–y stage is 0.1 μm, so the scan area of 25.6 μm × 25.6 μm is the minimum scan area for the stage scan mode when the acquired data points are 256 × 256. The specimen size of 20 cm × 20 cm × 2.5 cm can be observed. Two types of piezo scanner can be used. One is 100 μm × 100 μm × 15 μm of working distance and another is 0 × 0 × 40 μm of working distance. After setting the observing position, the scan mode can be chosen as either the stage scan mode or the piezo scan mode. If we use the scanner of 100 × 100 × 15 μm, the scan range can be chosen from 10 nm to 1 cm. The tip used for SKFM measurement was a conductive gold-coated Si tip with a resonant frequency of around 25 kHz. The SKFM image was taken every hour with data points of 256 × 256.

Test specimens were two types of low alloy steels, SM50B and 3%Ni steel, mechanically polished up to 1 μm roughness. For SKFM observation, sea salt particles of 0.012 mg cm^{-2} were attached by using a new atmospheric corrosion test device under low relative humidity conditions (30% rh) for preventing the corrosion. An accumulation rate of sea salt particles of 0.2 to 1 mdd was used for the corrosion test at a constant humidity of 90% rh. The number of attached sea salt particles is estimated by using 30 MHz of gold-coated quartz crystals. The initiation of atmospheric corrosion was observed by SKFM under humidity control conditions. A relative humidity range of between 48 and 85% rh was used to study the initiation of atmospheric corrosion. In this case, relative humidity was controlled by controlling the specimen surface temperature with a cooler. A Kelvin force microscope and a colour laser microscope were also used to observe the detail of corrosion. The nucleation of a thin liquid film was observed by KFM and SKFM at rh of 35 to 40% after keeping the specimen at 85% rh for 1 h and attaching a sea salt particle concentration of 0.01 mg cm^{-2}.

13.3 Results and discussion

13.3.1 SKFM observation of initiation of corrosion

Figure 13.1 shows the SKFM images of SM50B tested in a humidity of 48 to 85% rh. The concentration of attached sea salt particles was 12 μg cm^{-2}. As the relative humidity increased, the area of the part where the potential was more negative than that of usual sea salt particles attached increased rapidly, as shown in Fig. 13.1b to d, and the potential of the most observed area moved in a negative direction as seen in Fig. 13.1e. Filiform corrosion with widths much bigger than the diameter of the sea salt particle attached progressed rapidly. The increase in the area of the negative potential part is considered to be due to the increase of the formation of $FeCl_3$, resulting from an increase in the amount of liquid, due to the NaCl which is the main component of the sea salt particle becoming liquid above 73% rh. The size of sea salt particle also increased due to the increase in volume from the state change of NaCl from solid to liquid. The potential of the corroding part was more negative than the other part. After the relative humidity was decreased to 48% again, the area of the negative potential part still remained as seen in Fig. 13.1f. Figure 13.2 shows the optical microscope image immediately after the corrosion test. A transparent green liquid was observed at the corroding part. The former FT IR microscope analysis showed[3] that this liquid was $FeCl_2$. The volume of this liquid was over 100 times bigger than that of a sea salt particle. The mechanism of the formation of the big liquid droplet is considered as follows: after the

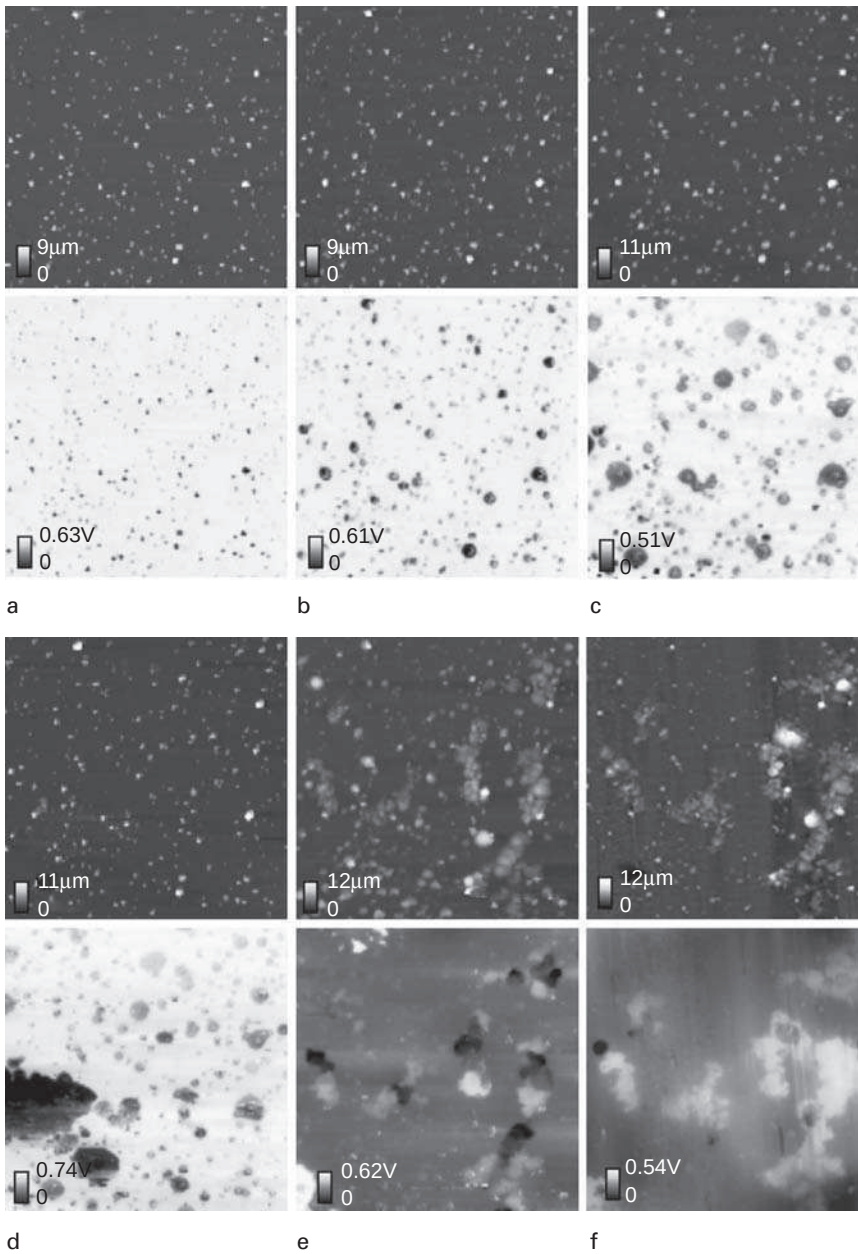

13.1 SKFM observation of atmospheric corrosion of SM50B at rh of 48 to 85%: *a* at the start (48% rh), *b* after 3 h (67% rh), *c* after 9 h (83% rh), *d* after 11 h (85% rh), *e* after 15 h (85% rh), *f* after 17 h (48% rh).

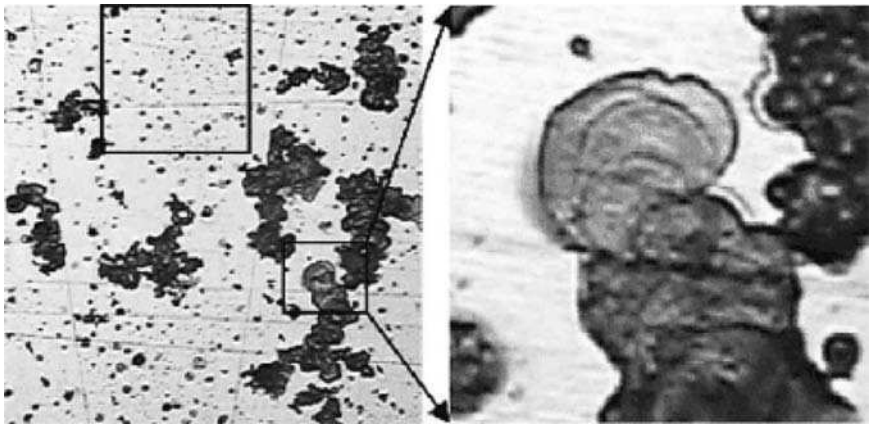

13.2 Optical microscope image immediately after corrosion test.

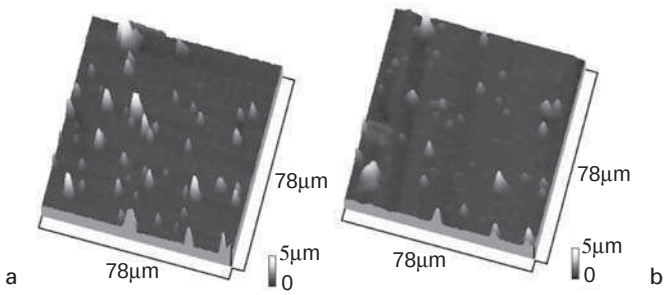

13.3 Distribution of sea salt particles at *a* the beginning and *b* 17 h after test started.

specimen surface is covered with thin liquid film, the Cl^- ion can move to the corroding part to keep electrical neutrality. Cl^- ion is supplied by the sea salt particles near the corrosion part. Figure 13.3 shows the distribution of sea salt particles in the square area indicated in Fig. 13.2 at the start as shown in Fig. 13.3a and 17 h after test started as seen in Fig. 13.3b. The decrease in the height of sea salt particles shows evidence of Cl^- ion movement. Thus, the existence of a very thin liquid film plays an important role in the mechanism of atmospheric corrosion in a seashore environment.

13.3.2 Observation of nucleation of thin liquid film

Figure 13.4 shows the SKFM image of SM50B (left image) and 3%Ni steel. The existence of a negative potential part indicates the existence of a thin

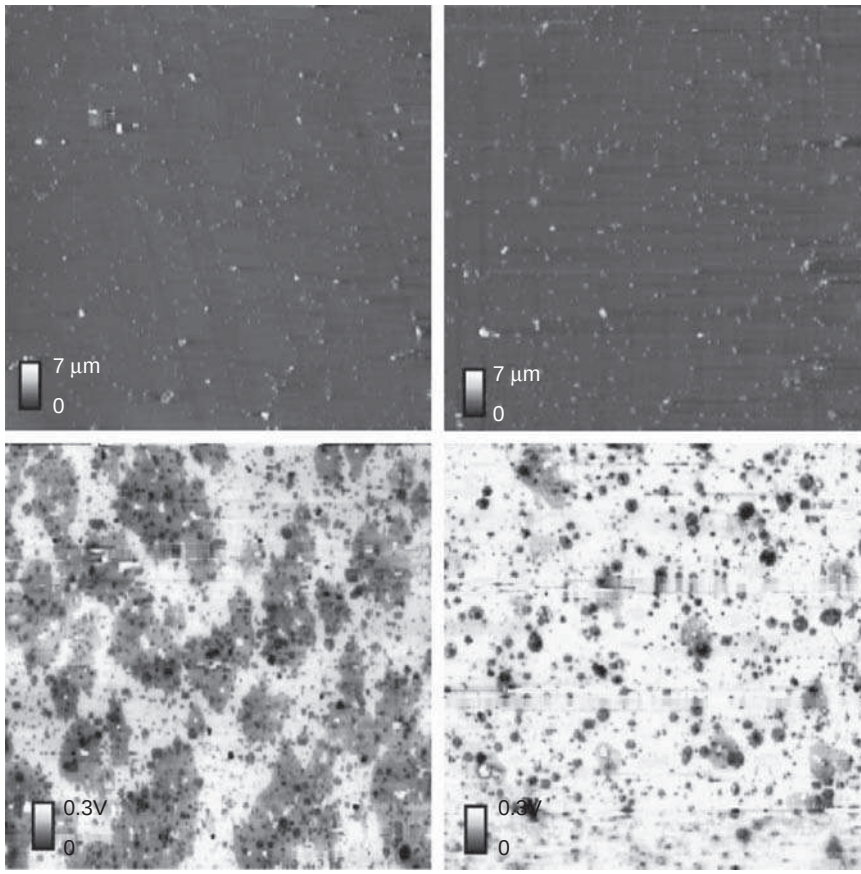

a b

13.4 SKFM image of low alloy steels after keeping at 85% rh for 1 h (1.2 mm × 1.2 mm): *a* SM50B, *b* 3%Ni.

liquid film. The coverage ratio of thin liquid film on SM50B was bigger than that on 3%Ni steel, because 3%Ni steel is more resistant than SM50B to corrosion. The corrosion product in which the potential is noble was observed within the negative potential part (Fig. 13.5). This also shows the thin liquid film was produced by corrosion. Fig. 13.6 shows the KFM image of the part where the potential was changed. No evidence of the existence of a thin liquid film was observed on the surface profile image of SM 50B in spite of the maximum height difference in the surface profile being about 20 nm, while small particles of 10 nm in maximum height were observed at the negative potential part on 3%Ni steel.

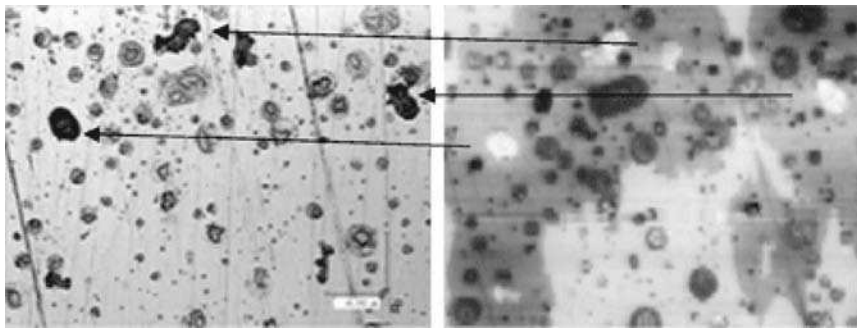

13.5 Relation between corrosion product and thin liquid film (SM50B).

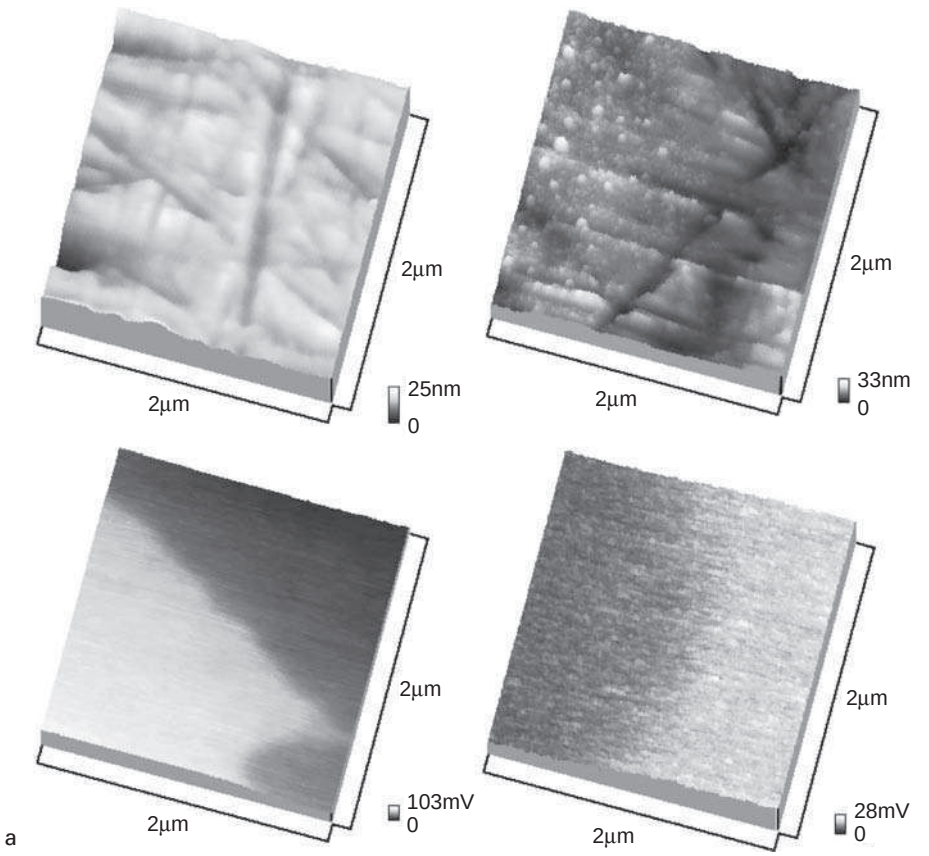

13.6 KFM image of low alloy steels near the potential boundary: *a* SM50B, *b* 3%Ni.

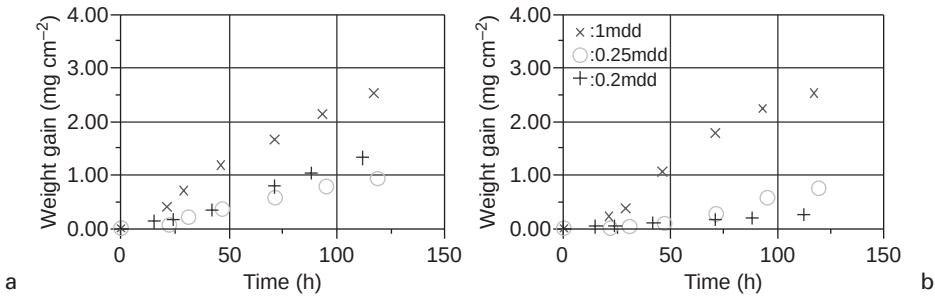

13.7 Effect of accumulation rate of sea salt on corrosion rate for low alloy steels: *a* SM50B, *b* 3%Ni steel.

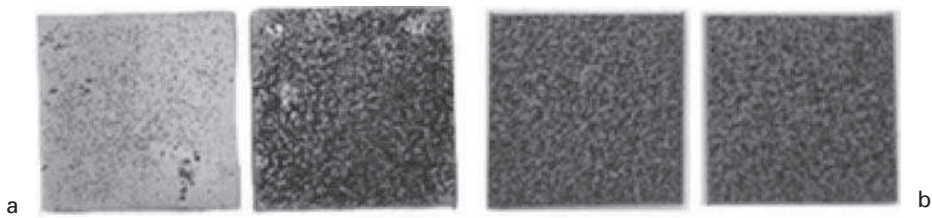

13.8 Optical microscope image of low alloy steels after constant humidity test: *a* 0.2 mdd, left 3%Ni steel, right SM50B; *b* 1 mdd, left 3%Ni steel, right SM50B.

13.3.3 Constant relative humidity test

Figure 13.7 shows the results of a constant relative humidity test for low alloy steels with a sea salt accumulation rate of 0.2 to 1 mdd (mg dm^{-2} day^{-1}). When the sea salt accumulation rate was low, the corrosion rate of 3%Ni steel was much lower than SM50B, whereas the corrosion rate became similar as the sea salt accumulation rate increased. Figure 13.8 shows the optical microscope image of low alloy steels after testing. The corrosion morphology was the same at the sea salt accumulation rate of 1 mdd. Thus, the main difference between 3Ni steel and SM50B was the initiation time of atmospheric corrosion.

13.4 Conclusions

Atmospheric corrosion tests were carried out under high relative humidity conditions. The results show that a very thin liquid film was formed around the corrosion products once corrosion started. After the specimen surface was covered with a thin liquid film, Cl^- ion could move to the corroding

part to increase the corrosion rate. The mechanism of atmospheric corrosion by sea salt particles under high relative humidity condition was similar on both SM50B and 3%Ni steel. The main difference was the initiation time of corrosion.

13.5 References

1 H. Masuda, *Corros.*, 2001, **57**, 99–109.
2 M. Yasutake, D. Aoki and M. Fujihira, *Thin Solid films*, 1996, **273**, 279–283.
3 H. Masuda and K. Noda, *J. Electrochemical Society*, Proc. Vol (The 196th Meeting of ECS), 2000, **99-28**, 351.

14

Effect of surface microcracks on pitting susceptibility of manganese sulfide containing stainless steels

V. VIGNAL and R. OLTRA,
Université de Bourgogne, France

14.1 Introduction

Numerous studies have shown that MnS inclusions in stainless steels are good precursor sites for pitting corrosion.[1–3] The dissolution of MnS inclusions which produces sulfur species in the solution (HS^- ions during the chemical dissolution[4] and $S_2O_3^{2-}$ ions during the electrochemical dissolution[5–7]) is generally accompanied with a local drop of the pH. It has been suggested that once a critical value of pH is reached, pits initiate. Other workers[8–9] have proposed that pit initiation is induced by the precipitation of a $MnCl_2$ salt film which prevents repassivation of the metal and maintains a local acidity due to hydrolysis reactions. However, heterogeneous surface stress distributions are developed at the interface between the matrix and such heterogeneities[10–18] and these stress gradients may significantly affect the mechanisms of dissolution and pitting corrosion.

For applied stresses close to the apparent yield strength, surface microcracks may initiate either along the matrix–inclusion interface or through some inclusions. Local electrochemical experiments performed in chloride-based media using microcapillary-based techniques[19] have revealed that the presence of such microcracks shifts the onset potential for MnS dissolution to more negative values and that stable pitting is observed after a period of MnS dissolution. In the absence of microcracks, only current transients occur during dissolution of the inclusion. To explore whether such microcracks might serve to generate locally high concentrations of aggressive species, the chemistry inside a crack along the interface was simulated using a finite element difference model.[19] For experimental conditions where stable pitting was observed, simulations predict that the pH is about 2 and the chloride concentration is around 6M in a 3μm deep crack. Although stainless steels are ductile, other mechanisms of cracking were identified above the apparent yield strength, including surface microcracks in the metallic matrix close to the inclusions.[20] It should be mentioned that surface microcracks can nucleate on stainless steels under various modes of

deformation (such as cyclic loading on sites of plastic strain localisation[21] and cyclic bending[22]) and during the outgassed cycle after hydrogenation.[23–24] To our knowledge, no local electrochemical measurements have been carried out to determine the influence of such surface microcracks on the pitting susceptibility of stainless steels.

Therefore, the objective of this paper is to determine the influence of surface microcracks initiated in the matrix on the electrochemical behaviour and the pitting susceptibility of stainless steels. The location where microcracks initiated was predicted by calculating the surface stress field around inclusions considering the real microstructure of materials[20–25] and by analysing the local electrochemical measurements performed using the electrochemical microcell technique on the bases of these mechanical data.

14.2 Experimental method

Experiments were performed on a resulfurised 316L stainless steel (chemical composition: Ni 11.04, Cr 16.67, Mn 1.529, S 0.0251, Si 0.424, P 0.025, Mo 2.26, C 0.018 and N 0.069 wt%). The yield and ultimate strength of tensile specimens are 258 and 590 MPa, respectively. Specimens were mechanically polished with emery papers and smoothed with diamond pastes (down to 1 μm). It should be noticed that the polishing operations were systematically carried out along the x_1-axis (rolling direction). Spheroidised inclusions (depth below 5 μm and size ranging from 5 to 40 μm) were found to be heterogeneously distributed on the surface, as shown in Fig. 14.1. A set of specimens was then subjected to an uniaxial tensile loading at 10% plastic strain along the x_1-axis. The morphology of microcracks near MnS inclusions was investigated after unloading using a field-emission type

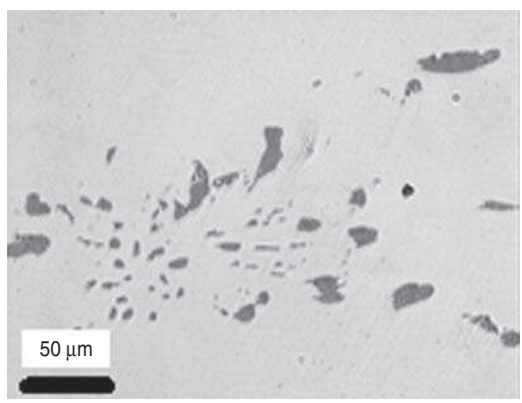

14.1 Morphology of MnS inclusions observed using optical microscopy.

scanning electron microsope (FE-SEM, JEOL 6400F) with an integrated electron dispersion spectrometer (SEM-EDS).

Local electrochemical measurements were carried out on the unstrained specimens and on the strained specimens after unloading using the electrochemical microcell technique.[26] This technique consists of a glass microcapillary which is filled with electrolyte. The tip of the capillary (100 µm in diameter) is sealed to the specimen surface with a layer of silicon rubber. The entire setup is mounted on a microscope for precise positioning of the capillary on the surface. After positioning the microcapillary, a cathodic potential of –600 mV/SCE was applied for 2 min after which potentiodynamic polarisation curves were determined in 1.5M NaCl, pH 3 at a scan rate of 1 mV s^{-1}. A modified high resolution potentiostat having a current detection limit of 20 fA (Jaissle 1002T-NC-3) was used. The counter electrode was a platinum wire and the reference electrode was a saturated calomel electrode (SCE).

14.3 Results and discussion

14.3.1 Local electrochemical behaviour of matrix in absence of surface microcracks

In order to have reference plots and to determine some key parameters such as the onset potential for MnS dissolution and the pitting potential, local electrochemical measurements were first performed on the unstrained specimen (Fig. 14.2). In the absence of inclusions, it can be seen that the

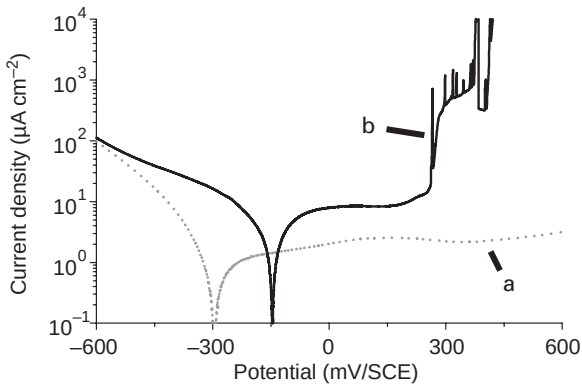

14.2 Local polarisation curves determined in 1.5M NaCl, pH 3 at 24°C on 316L SS with 0.025% S. The sites on the unstrained specimen contain *a* the matrix without inclusions and *b* the matrix with a large MnS inclusion.

current remains low and more-or-less constant in the passive range. On the other hand, the polarisation curves determined on sites containing the matrix and a large inclusion show a current peak in the passive range starting between 160 and 280 mV/SCE which was attributed to the electrochemical dissolution of the inclusion,[19] as shown in Fig. 14.2(b). Numerous current transients were observed at the top of the current peak, indicating that metastable pitting occurred frequently. In 80% of these experiments, stable pitting was observed between 320 and 500 mV/SCE.

14.3.2 Local electrochemical behaviour of matrix in presence of surface microcracks

Particular attention was then paid to the role of microcracks initiated in the matrix above the apparent yield strength on pit initiation. Three microcrack morphologies were identified at 10% plastic strain and the electrochemical behaviour of sites containing these different microcracks was determined after unloading using the electrochemical microcell technique.

Microcracks in the inclusion or along the interface

In the presence of microcracks along the interface and in the inclusion, the current peak associated with the dissolution of the inclusion was detected at a lower potential than on the unstrained specimens (from a potential between 50 and 100 mV/SCE), as shown in Fig. 14.3(b and c). This confirms previous results conducted at low plastic strains indicating that such micro-

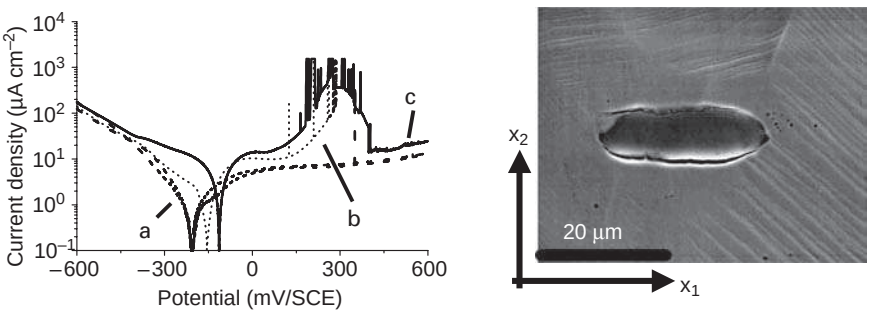

14.3 Local polarisation curves determined on sites containing the matrix without inclusions (a), the matrix with a large MnS inclusion and numerous microcracks both through the inclusion and along the interface (b) and the matrix with a large MnS inclusion and some microcracks at the interface (c) as shown in the SEM image. Plastic strain was applied along the x_2-axis.

cracks promote the dissolution of MnS inclusions.[19] Numerous large metastable events were detected during MnS dissolution and in the presence of numerous microcracks both through the inclusion and along the interface, stable pitting was detected during this process (between 240 and 350 mV/SCE), as shown in Fig. 14.3(b). The experiments where pits repassivate were encountered on sites where microcracks propagated along the interface, as shown in Fig. 14.3(c) and the SEM image. One may assume that these microcracks are not deep enough to reach the chemical conditions necessary for stable pitting.[19]

Microcracks in the matrix close to the inclusions

Above the apparent yield strength, microcracks with a length between 2 and 5 μm were observed in the metallic matrix in the close vicinity of some MnS inclusions, as shown in Fig. 14.4a. In the absence of emerging slip

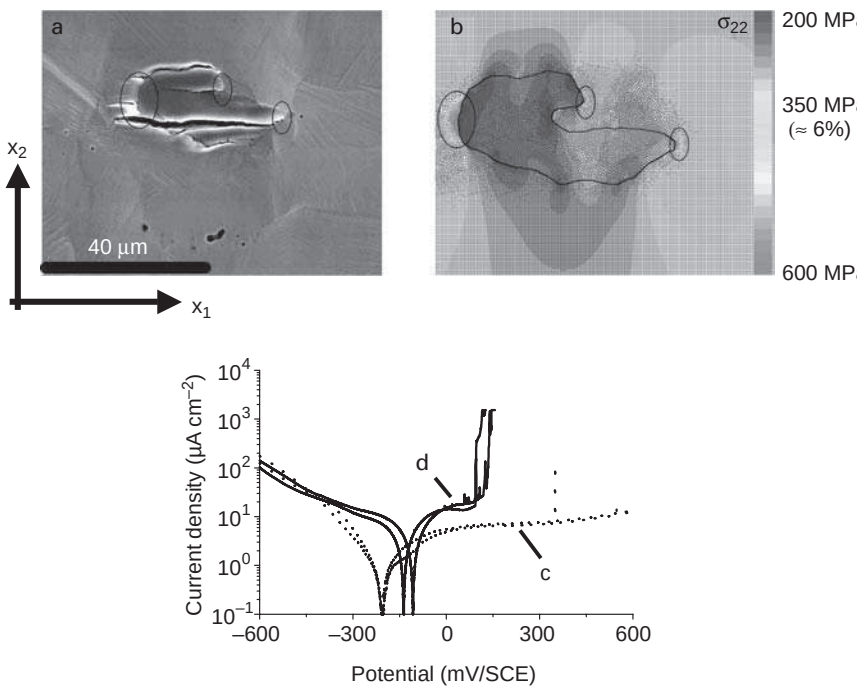

14.4 *a* SEM image on the elongated specimen of microcracks in the matrix and through a large MnS inclusion and *b* stress field deduced from numerical simulation around this inclusion for an applied stress of 350 MPa. Local polarisation curves determined on sites containing the matrix without inclusions (c) and the matrix with a large MnS inclusion and numerous microcracks (d). Plastic strain was applied along the x_2-axis.

bands, the driving factor for crack initiation is the ratio of the elastic modulus of the inclusion to that of the matrix. This ratio has a strong influence on the stress amplitudes inside and around the inclusion whereas the morphology of the inclusion controls the location where the stress gradients are observed. The surface stress field was calculated under straining conditions (applied stress of 350 MPa corresponding roughly to 6% plastic strain) around the inclusion shown in Fig. 14.4a using the numerical method described above[20] and a two-dimensional meshing composed of 122 023 elements. The stress calculation involves the development of new image analysis processing and implementation in the finite element (FE) code of a new operator for meshing the real microstructure and material models capable of describing the complex behaviour of real materials (anisotropic mechanical and crystallographic properties).

Three stress gradients reaching the ultimate strength of the matrix were found in the matrix close to the inclusion, as shown in Fig. 14.4b. Comparing the surface stress distribution derived from simulation and the SEM micrograph, it is demonstrated that microcracks initiate where stress gradients are developed. Therefore, it is possible to predict where microcracks initiate during straining and consequently such an investigation combined with the electrochemical microcell technique would be possible to follow the corrosion sensitivity of such micro-cracked areas.

Figure 14.4 shows two typical polarisation curves (d) measured on sites containing an inclusion with numerous microcracks both in the matrix and through the inclusion. A few small current transients were visible in the passive range (between 0 and 80 mV/SCE) before the current increase related to the electrochemical dissolution of the inclusion. This indicates that pits first initiated and repassivated at microcracks located in the matrix. Stable pitting was then systematically observed between 90 and 130 mV/SCE. Within this potential range, a small amount of MnS was dissolved, suggesting that sulfur species did not play a major role in pit initiation and that microcracks in the matrix were the weakest zones.

Microcracks in the matrix generated by sub-surface inclusions

At higher plastic strains, microcracks were detected in the matrix whereas no inclusions were visible on the surface, as shown in Fig. 14.5a. However, EDS experiments revealed the presence of a sub-surface inclusion. This situation which was often observed on the specimen surface at 10% plastic strain was reproduced using numerical simulation. A 3-D meshing composed of $28\,755 \times 13$ elements was considered and the inclusion was embedded 0.4 μm below the surface. It was found that the stress concentration in the thin metallic layer between the surface and the inclusion reaches the

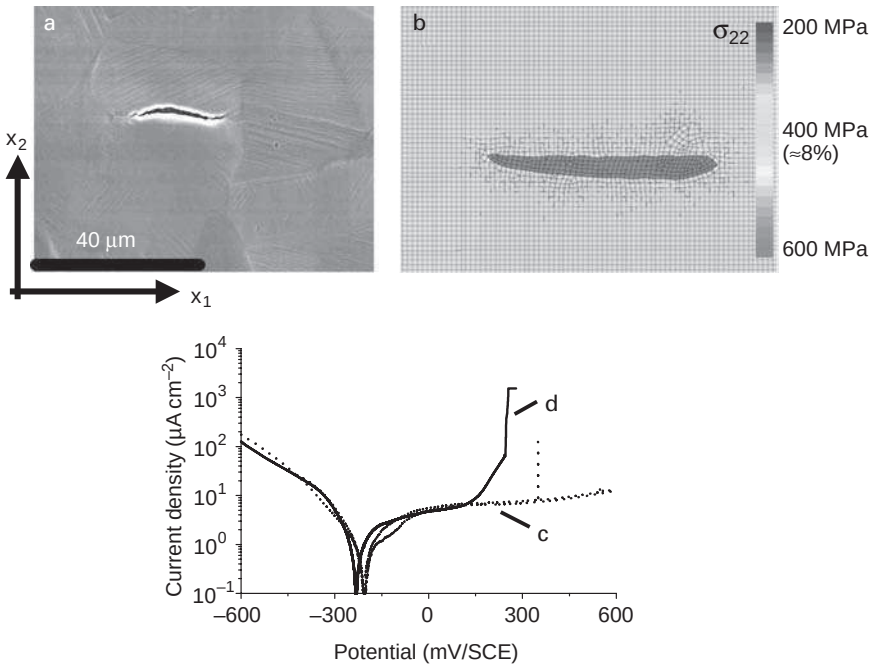

14.5 *a* SEM image on the elongated specimen of microcracks initiated in the matrix by a MnS inclusion just beneath the surface and *b* stress field deduced from numerical simulation for an applied stress of 400 MPa. Local polarisation curves determined on sites containing the matrix without inclusions (c) and a microcrack initiated in the matrix by an inclusion just beneath the surface (d). Plastic strain was applied along the x_2-axis.

ultimate strength of the matrix from about 8% plastic strain, as shown in Fig. 14.5b.

The local polarisation curve determined on these sites is shown in Fig. 14.5(d). Roughly the same polarisation curve as that obtained on sites containing the pure matrix (d) was found until the dissolution of the inclusion. No microcracks were formed in this inclusion that is embedded in a closed volume. Therefore, regarding the conditions of dissolution of this inclusion and stability of pits, an intermediary behaviour between that found for the inclusions with microcracks and that found for the inclusions on the unstrained specimens was obtained. Dissolution of the inclusion started at around 120 mV/SCE (instead of between 160 and 280 mV/SCE on the unstrained specimen and between 50 and 100 mV/SCE in the presence of microcracks through the inclusion and along the interface). Stable pitting was systematically detected at lower potentials, between 200 and 300 mV/SCE.

14.3.3 Local electrochemical measurements in low concentration solutions

The deleterious effect of microcracks on the corrosion resistance of stainless steels was also observed in low concentration solutions. In order to estimate the iR ohmic drop in the electrochemical cell, the resistance of the microcapillary was calculated considering that it is composed of two parts, the body with a cylinder-like shape (length 2.5 cm and inner diameter 0.84 cm) and the head with a trapezoid-like shape designed during the pulling process (length 0.675 cm and inner diameter at the tip 0.1 cm). A cell resistance of about 1 MΩ was obtained for a microcapillary filled with 0.02M NaCl, pH 3. As the current measured in these experiments was in the range of pA and nA, the ohmic drop was neglected. Fig. 14.6 shows the local polarisation curves determined in 0.02M NaCl, pH 3 at 25°C on the pure matrix, the matrix with a small inclusion and the matrix with a large inclusion. It can be seen that nearly no current transients were detected on the unstrained specimens during the dissolution of MnS inclusions (even for the large inclusions). On the other hand, a large number of current transients were systematically observed on sites containing a small inclusion and a microcrack either along the MnS/matrix interface and through the inclusion, indicating that initiation of metastable pits is promoted at microcracks. The presence of numerous microcracks at large MnS inclusions induces stable pitting at around 750 mV/SCE, as shown in Fig. 14.6.

14.4 Conclusions

The results obtained from local electrochemical measurements show that the presence of microcracks in the metallic matrix affects significantly the electrochemical behaviour of the material in 1.5M NaCl, pH 3. In the pres-

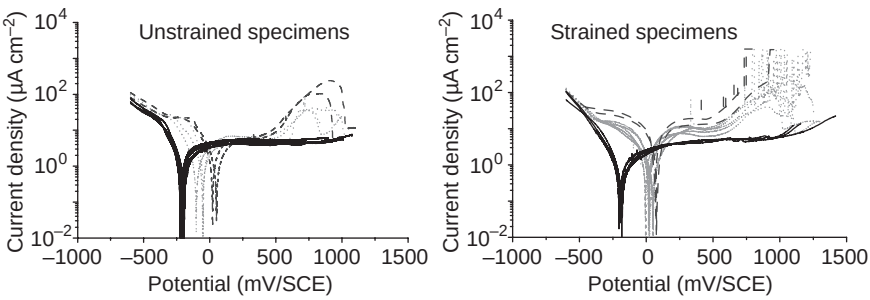

14.6 Local polarisation curves determined in 0.02M NaCl, pH 3 at 25°C on 316L SS with 0.25% S. The sites contain the matrix (black lines), the matrix with a small MnS inclusion (dotted lines) and the matrix with a large MnS inclusion (dashed lines).

ence of such microcracks, the pitting potential was found to decrease significantly with respect to those found on the unstrained specimens (between 320 and 500 mV/SCE) and on the strained specimens with microcracks along the interface or though the inclusion (between 240 and 350 mV/SCE). Two morphologies of microcracks were observed in the matrix:

(i) in the presence of microcracks in the matrix generated by an inclusion embedded close to the surface, stable pitting was detected between 200 and 300 mV/SCE.
(ii) in the presence of microcracks in the matrix close the inclusions, stable pitting was found to drop to between 90 and 130 mV/SCE. It was also concluded that microcracks in the matrix were the weakest zones and that MnS plays no role in pitting.

14.5 Acknowledgements

The authors are grateful to CEA-DRN/DMT/SEMT (Saclay, France) which has designed and developed the FE code Cast3M.

14.6 References

1 G. Wranglen, *Corros. Sci.*, 1974, **14**, 331.
2 G. S. Eklund, *J. Electrochem. Soc.*, 1974, **121**, 467–473.
3 Z. Szklarska-Smialowska, *Corros. NACE*, 1972, **28**, 388–396.
4 E. G. Webb, C. H. Paik and R. C. Alkire, *Electrochem. Solid-State Lett.*, 2001, **4**, B15–B18.
5 C. H. Paik, H. S. White and R. C. Alkire, *J. Electrochem. Soc.*, 2000, **147**, 4120–4124.
6 S. E. Lott and R. C. Alkire, *J. Electrochem. Soc.*, 1989, **136**, 973–978.
7 S. E. Lott and R. C. Alkire, *J. Electrochem. Soc.*, 1989, **136**, 3256–3261.
8 D. E. Williams, T. F. Mohiuddin, Y. Y. Zhu, *J. Electrochem. Soc.*, 1998, **145**, 2664–2672.
9 M. A. Baker and J. E. Castle, *Corros. Sci.*, 1993, **34**, 667–682.
10 K. K. Chawla and M. Metzger, *Metall. Trans. A: Phys. Metall. Mater. Sci.*, 1977, **8A**, 1681–1687.
11 K. K. Chawla and M. Metzger, *J. Mater. Sci.*, 1972, **7**, 34–39.
12 T. A. Kuntz, H. N. Wadley and D. R. Black, *Metall. Trans. A: Phys. Metall. Mater. Sci.*, 1993, **24A**, 1117–1124.
13 K. L. Kendig, W. O. Soboyejo and D. B. Miracle, *Scr. Metall. Mater.*, 1995, **32**, 669–674.
14 D. L. Davidson, *Metall. Mater. Trans. A: Phys. Metall. Mater. Sci.*, 1997, **28A**, 1297–1314.
15 D. L. Davidson and R. C. McClung, *Int. J. Fracture*, 1997, **84**, 81–98.
16 L. Allais, M. Bornert, T. Bretheau and D. Caldemaison, *Acta Metall. Mater.*, 1994, **42**, 3865–3880.
17 Y. L. Liu and G. Fischer, *Scr. Mater.*, 1997, **36**, 1187–1194.

18 E. E. Nugent, R. B. Calhoun and A. Mortensen. *Acta Mater.*, 2000, **48**, 1451–1467.
19 T. Suter, E. G. Webb, H. Böhni and R. C. Alkire, *J. Electrochem. Soc.*, 2001, **148**, B174–B185.
20 V. Vignal, R. Oltra and C. Josse, *Scr. Mater.*, 2003, **49**, 779–784.
21 T. Kruml, J. Polak, K. Obrtlik and S. Degallaix, *Acta Mater.*, 1997, **45**, 5145–5151.
22 C. S. Oh and J. H. Song, *Int. J. Fatigue*, 2001, **23**, 251–258.
23 Q. Yang and J. L. Luo, *Mater. Sci. Eng., A: Struct. Mater.: Prop., Microstruct. Process.*, 2000, **A288**, 75–83.
24 W. Godoi, N. K. Kuromoto, A. S. Guimaraes and C. Lepienski, *Mater. Sci. Eng., A: Struct. Mater.: Prop., Microstruct. Process.*, 2003, **354A**, 251–256.
25 N. Mary, V. Vignal, R. Oltra and L. Coudreuse, *Philosoph. Mag.*, 2005, **85**, 1227–1242.
26 H. Böhni, T. Suter and F. Assi, *Surf. Coat. Technol.*, 2000, **130**, 80–86.

15

Effect of applied stress on localised corrosion measurements on aluminium alloy friction stir welds

B. J. CONNOLLY,
The University of Birmingham, UK

15.1 Introduction

Welding in the aerospace industry is currently experiencing renewed interest and expanding application due to new developments, innovations, and technology. Welds are currently replacing conventional joining methods such as rivets and fasteners in numerous applications in military aircraft, commercial aircraft, and space vehicles.[1] Improvements in welding techniques result in significant reduction of distortion, lower residual stress, and smaller regions of metallurgical / microstructural heterogeneity compared with conventional fusion based welds.

Friction stir welding (FSW)[2–4] has been shown to be an effective method for joining high strength 7xxx and 2xxx series aluminium alloys, which were previously considered unweldable in aircraft and automotive structures.[5] The ability to produce high-quality welds in high-strength aluminium alloys sets FSW apart from fusion welding techniques. The strength of friction stir welds is 30–50% greater than that of conventional arc welding while the fatigue life is similar to that of riveted components.[1] Subsequent widespread use of FSW aluminium aircraft and aerospace components will effectively reduce the cost of manufacture and maintenance whilst increasing the performance and reliability of civilian as well as military platforms.

FSW is carried out by plunging a rotating tool piece into the junction between two metal plates. The resulting frictional heat allows plastic flow of the metal, stirring together the metal from the two plates to form a seamless join. The process generates three microstructural regions: the nugget, where the material has undergone severe stirring and heating; the thermomechanically affected zone (TMAZ), which is subjected to both deformation and heating; and the HAZ, where the material experiences only a thermal cycle. Microscopically, these regions are significantly different, especially in heat-treatable aluminum alloys such as 2xxx series.

Although knowledge of the localised corrosion behaviour as well as the environmental fracture behaviour of each of the micro-zones that make up

the FSW weldment will be helpful in developing models for life prediction of friction stir welded aerospace components exposed to high loading and aggressive (corrosive) environments, limited studies[6–11] have been performed. It has been shown that welded regions are more susceptible to localised corrosion than the parent metal in FSW 2024 and 7075 alloys.

Electrochemical measurements utilising microelectrochemical cells to determine local anodic and cathodic behaviour have previously been performed.[12–14] Moreover, the varied microstructure provides an excellent platform to investigate the effects of applied stress on electrochemical reactivity of each region of the weld. Previous investigators have shown deleterious effects of applied stress on localised corrosion behaviour of structural metals. Effects on the dissolution rate,[15] passivity[16,17] and localised corrosion initiation and propagation[18–21] have been reported. One investigator reported that a possible controlling factor in localised corrosion initiation in steel was due to the presence of micro-cracks near inclusions resulting from an applied remote load.[22]

In the present work, the anodic reactivity of the parent and of the various regions of friction stir welded AA2024 is characterised as a function of remote applied stress state in chloride-containing environments.

15.2 Experimental method

The material used in this work was AA2024-T351 plate (Al, 4.43% Cu, 1.42% Mg, 0.06% Si, 0.61% Mn, 0.08% Fe, 0.06% Zn). Testing was performed on the as-received parent plate material and on friction stir welded plate. The FSW was performed using a spindle speed of 350 rpm and a travel speed of 120 mm min^{-1}.

Local electrochemical measurements were performed on the parent plate and in each distinct region of the FSW weldment utilising a 'droplet cell' microelectrochemical method (Fig. 15.1a). The droplet cell method involves placing the tip of a 1 mm diameter micropipette above the specimen surface and making contact with a droplet of solution. Detailed description of the set-up is located elsewhere.[11,12] The electrochemical testing consisted of anodic potentiodynamic scans at 1 mV s^{-1} and potentiostatic holds at –0.6 $V_{Ag/AgCl}$ for 60 min in 0.1M NaCl solution. All electrochemical measurements were performed on polished surfaces parallel to the crown of the weld at a thickness of *T*/4. Remote tensile loads were applied via a 3-point bend stressing frame.

The effect of applied remote stresses on the microstructure of parent 2024-T351 was analysed at high resolution utilising an *in situ* field emission gun scanning electron microscope (FEG-SEM) equipped with a 10 kN servo-electric loading stage (Fig. 15.1b). Stresses (i.e. 1, 50, 90 and 110% of yield stress) were applied via a 4-point bend stressing frame. Specific

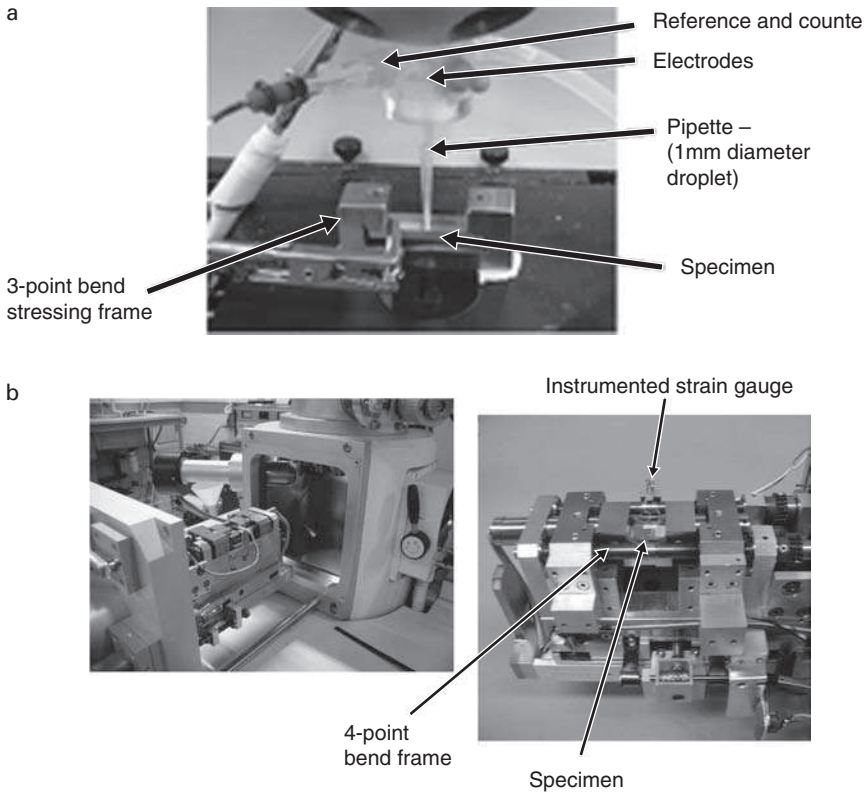

15.1 *a* The microelectrochemical test setup (*i.e.* droplet cell) consists of a three electrode cell within a fine pipette mounted on an optical microscope body. Local measurements were performed using pipettes with diameters from 5–10 μm up to 1 mm. *b* FEG-SEM with *in situ* tensile / 4-point bend stressing stage.

interest was given to the morphology of the constituent particle/matrix interfaces as a function of remote applied load.

15.3 Results and discussion

Preliminary results indicate a reduction of pitting potential of AA2024-T351 parent metal when subjected to a remote load (Fig. 15.2). This result was observed when the applied stress was oriented parallel to the rolling direction as well as when the applied stress was oriented perpendicular to the rolling direction. The increase in the anodic activity of the alloy is a result of the formation of preferential localised corrosion sites and

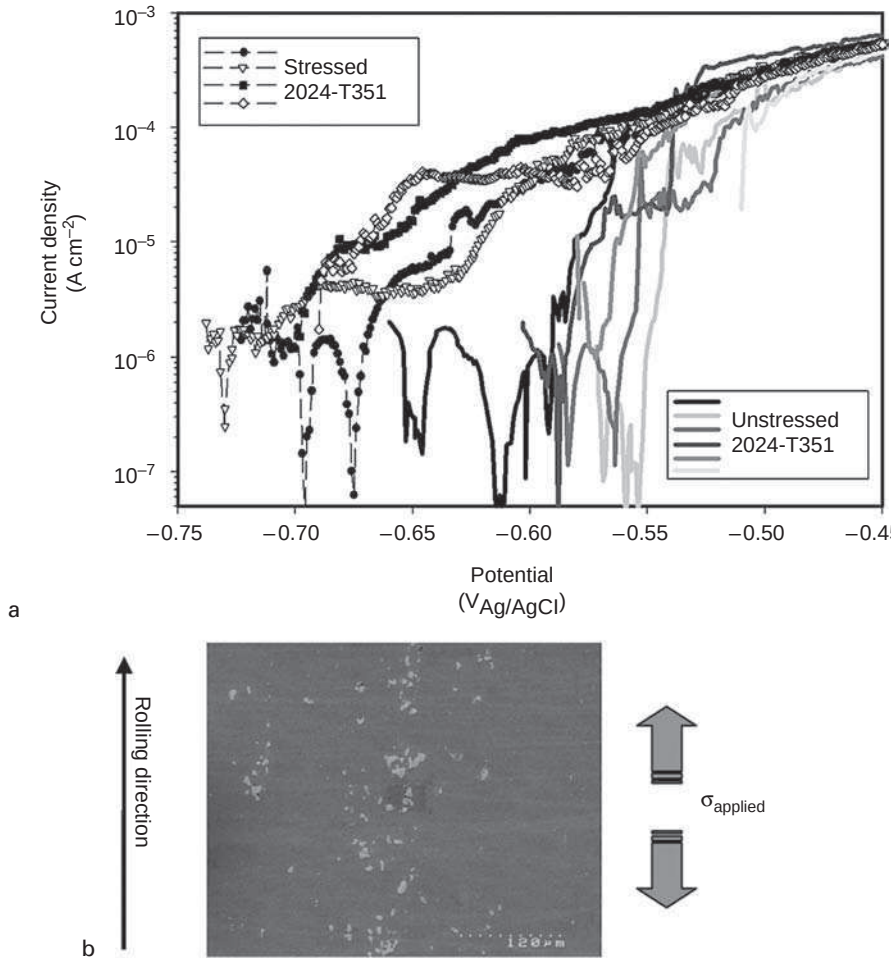

15.2 *a* Anodic potentiodynamic scans characterising the effect of applied stress on the pitting potentials of AA2024-T351. *b* The remote applied stress was oriented parallel to the rolling direction. Note the characteristic band of constituent particles parallel to the rolling directions.

subsequent aggressive environments at crevices or micro-crevices formed at constituent particle–matrix interfaces when subjected to a remote load.

In situ FEG-SEM analysis (Fig. 15.3) as a function of applied strain shows that as the material is stressed above 90% of the yield strength, delamination occurs between the particle and the matrix. Figure 15.3b and c clearly shows the formation of a sub-micron crevice along the edge of the constituent particle. Delaminations were never observed at previously cracked particles or at flawed/damaged particles such as that seen at the left-centre in Fig. 15.3a. EDX analysis of the delaminated particles confirmed that this

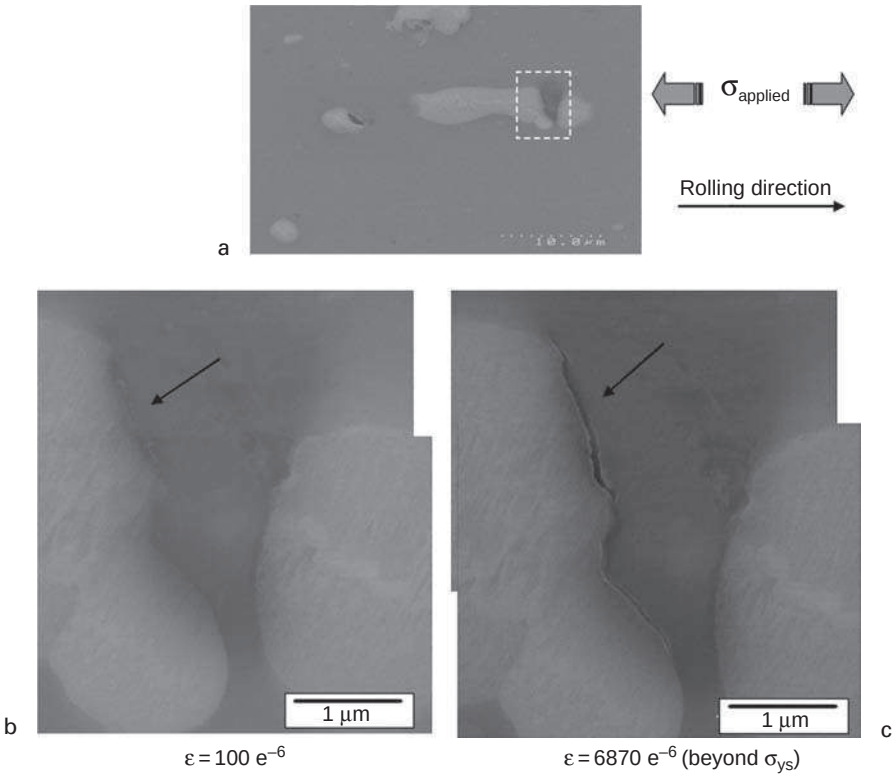

15.3 In situ FEG-SEM documentation of a constituent particle–matrix interface upon application of plastic strain. A distinct delamination occurs along the interface perpendicular to the applied stress. The remote stress in this case was applied parallel to the rolling direction of the 2024-T351.

phenomenon occurs to both the Fe–Mn–Cu rich particles and the Cu–Mg rich particles.

Microelectrochemical testing as a function of applied remote stress was also performed on the HAZ and nugget regions of friction stir welded 2024-T351. Figure 15.4 shows the etched microstructure of the various FSW regions. The elongated pancake grains are clearly visible in the parent and HAZ regions while the nugget displays fine equiaxed grains characteristic of a recrystallisation process. The most interesting microstructure occurs in the TMAZ and at the HAZ/TMAZ boundary. The grain structure at the HAZ/TMAZ boundary has been dramatically changed due to the friction stir process. The grains are aligned perpendicularly to the original rolling

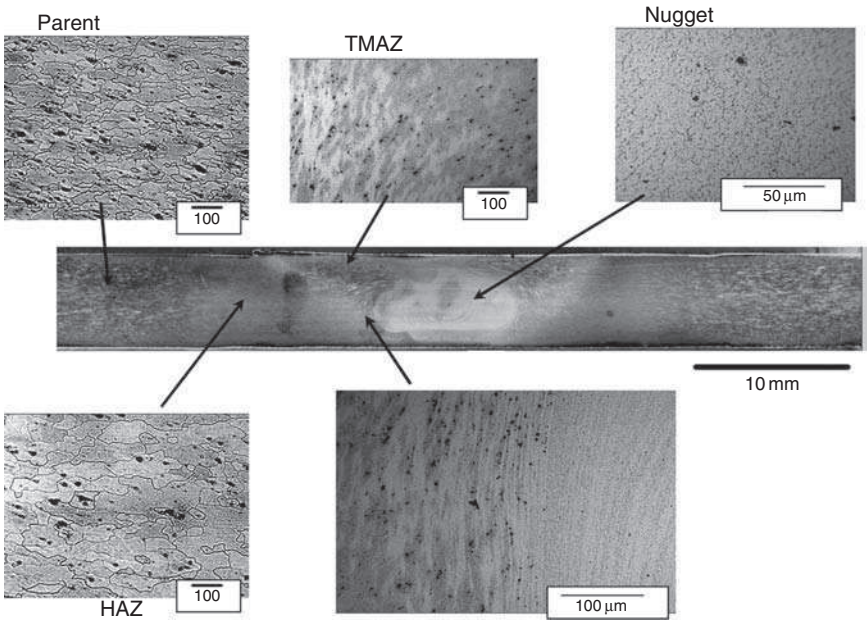

15.4 Etched microstructure (Keller's reagent) of the cross section of friction stir welded 2024-T351. The varied microstructure is evident across the four regions (i.e. parent material, HAZ, TMAZ and the weld nugget) of the weld.

direction. As seen later, this structure is key to the subsequent enhanced dissolution rates observed during potentiostatic testing while subjected to applied loads.

Results from the microelectrochemical potentiodynamic testing of the HAZ as a function of applied stress are presented in Fig. 15.5. No difference is observed between the breakdown potentials in the unstressed condition compared will the stressed condition. In each case, the scatter of the breakdown potentials lay between $-0.610\,V_{Ag/AgCl}$ and $-0.640\,V_{Ag/AgCl}$. It is reasonable to conclude from these observations that applied remote stress state has no effect on the initiation of localised corrosion sites in the HAZ. It should be noted that the breakdown potentials recorded for the HAZ were significantly more active than those of the unstressed parent material.

Examination of the localised corrosion morphology of the different regions of the weld revealed that, whereas the parent metal displayed classic pitting associated with constituent particles, the predominant form of corrosion in the HAZ and the nugget was intergranular in nature. From this observation, the question was posed as to whether applied stressed could

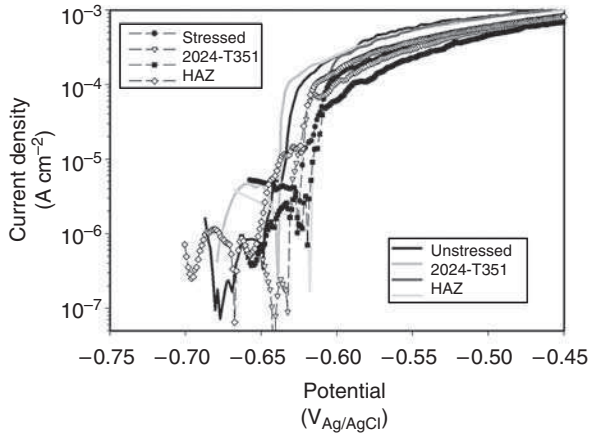

15.5 Anodic potentiodynamic scans characterising the effect of applied stress on the breakdown potentials of the HAZ region in friction stir welded 2024.

effect the propagation rate of intergranular corrosion sites. With this in mind, potentiostatic experiments were performed on stressed and unstressed specimens as a function of location within the HAZ and nugget regions of the weld.

Results from the potentiostatic testing as a function of position within the HAZ region are presented in Figures 15.6 and 15.7. Figure 15.6 displays current–time data from tests performed in the middle of the HAZ region. The current produced by the unstressed specimens is higher than that produced by the stressed specimens. Moreover, the total charge passed of the stressed specimens during the 60-min test is consistently lower than that of the unstressed specimens. It is reasonable to conclude from these results that applied stress does not enhance the intergranular corrosion dissolution rate of the HAZ region. In contrast, Figure 15.7 displays the results from tests performed at the HAZ/TMAZ boundary (see Fig. 15.4 for microstructure) and reveals that the current observed for the stressed specimens after the 60-min potentiostatic test is twice that of the unstressed specimens. It is unclear as to what the applied stress is doing to the local microstructure at the HAZ/TMAZ boundary, but it can be assumed that the elongated grains aligned perpendicularly to the rolling direction play a significant role. It can be speculated that the applied stress enhances the rate of intergranular corrosion along these boundaries whereas no such enhancement is observed along similar boundaries within the HAZ that are aligned parallel to the rolling direction.

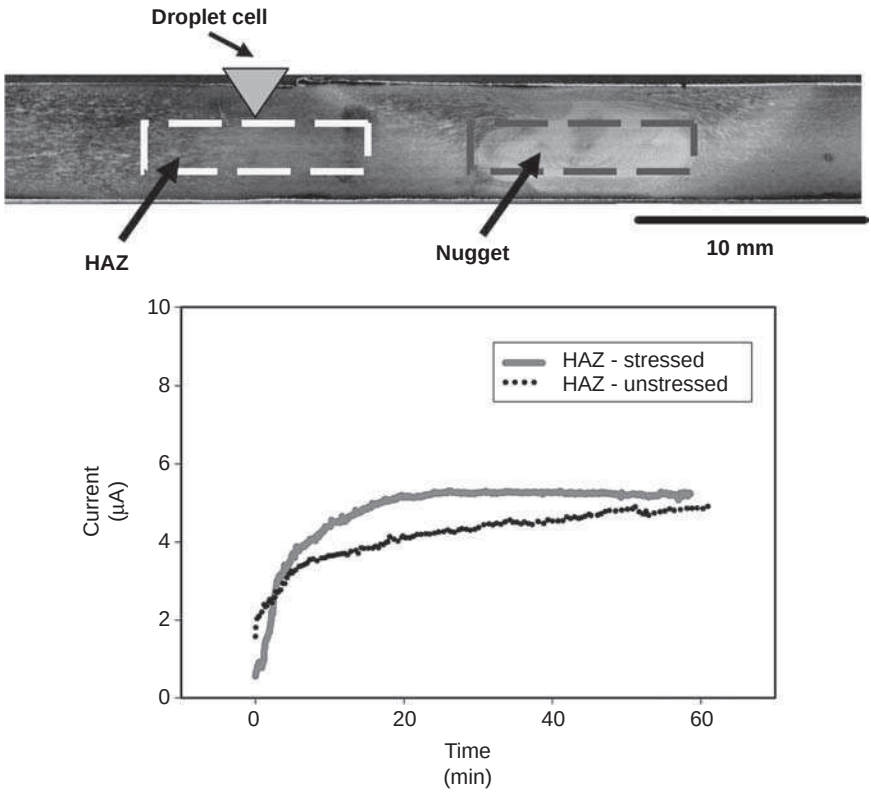

15.6 Current–time relationship (potentiostatic hold at $-0.6\,V_{Ag/AgCl}$) as a function of applied stress of the HAZ region in a 2024-T351 friction stir weld. The remote stress was applied parallel to the rolling direction and the welding direction.

Results from the microelectrochemical potentiodynamic testing of the nugget as a function of applied stress are presented in Fig. 15.8. As in the case of the HAZ, no difference is observed between the breakdown potentials in the unstressed condition compared with the stressed condition. In each case, the scatter of the breakdown potentials lay between $-0.640\,V_{Ag/AgCl}$ and $-0.660\,V_{Ag/AgCl}$.

Results from the potentiostatic testing as a function of position within the nugget region are presented in Fig. 15.9. Similar to the results from tests performed on the HAZ region, the stressed specimens display lower currents (dissolution rates) than the unstressed specimens. Again, as concluded for the HAZ region, it is reasonable to conclude from these results that applied stress does not enhance the intergranular corrosion dissolution rate of the nugget region. Reasons as to why the currents measured in the

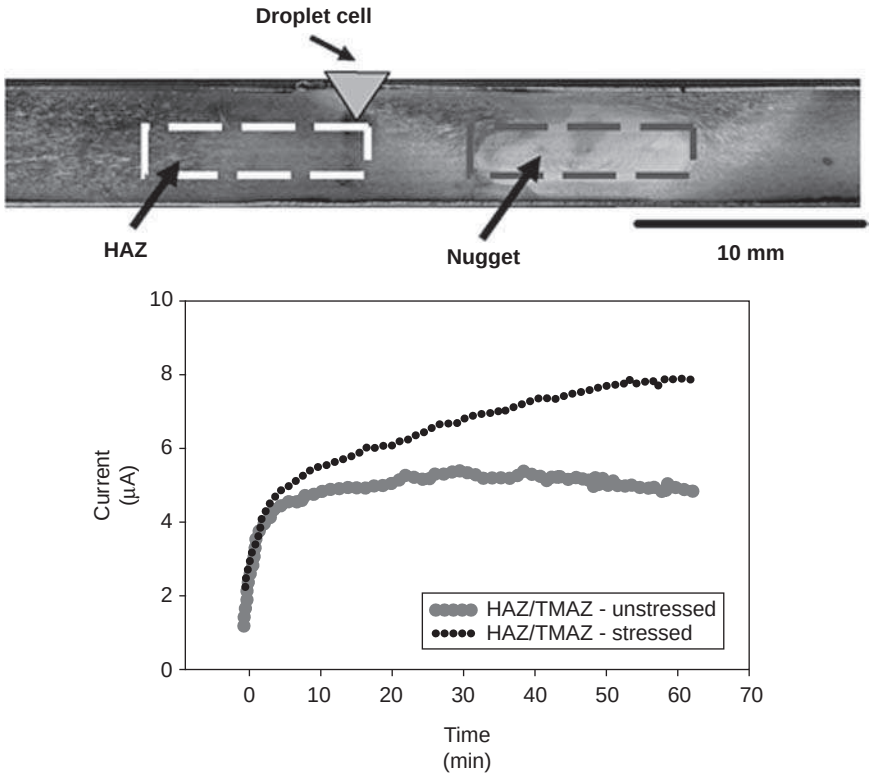

15.7 Current–time relationship (potentiostatic hold at –0.6 $V_{Ag/AgCl}$) as a function of applied stress of the HAZ/TMAZ boundary region in a 2024-T351 friction stir weld. The remote stress was applied parallel to the rolling direction and the welding direction.

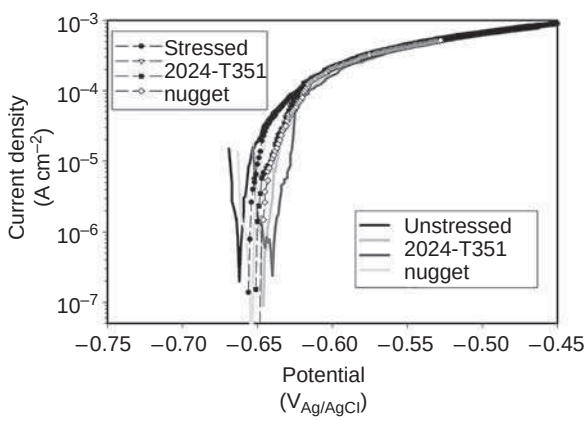

15.8 Anodic potentiodynamic scans characterising the effect of applied stress on the breakdown potentials of the nugget region in friction stir welded 2024-T351.

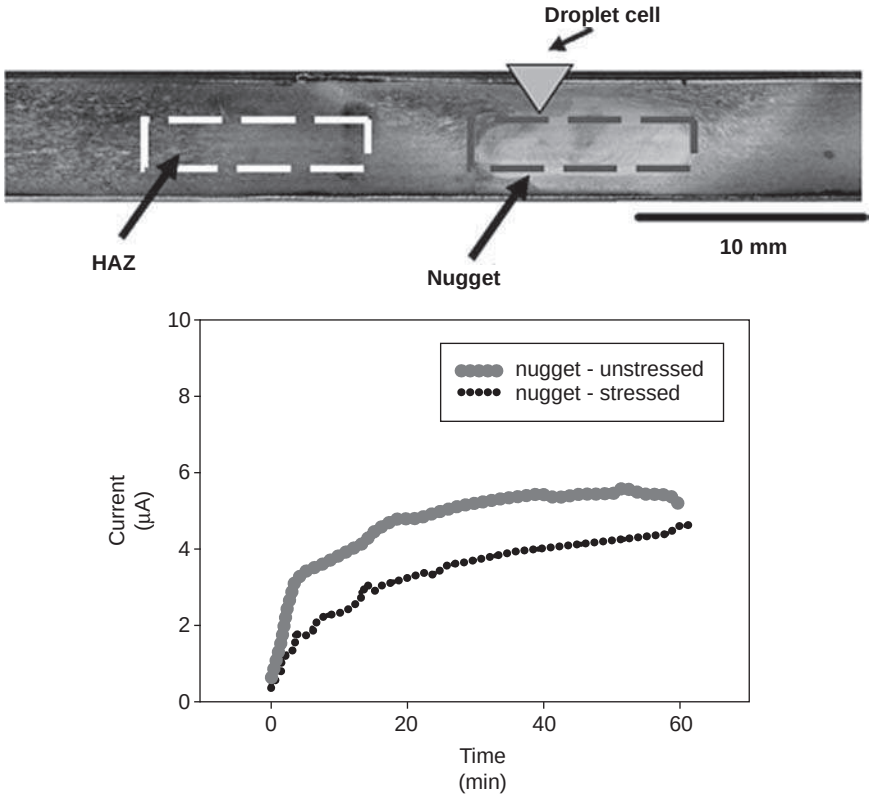

15.9 Current–time relationship (potentiostatic hold at $-0.6\,V_{Ag/AgCl}$) as a function of applied stress of the nugget region in a 2024-T351 friction stir weld. The remote stress was applied parallel to the rolling direction and the welding direction.

stressed HAZ and nugget specimens are lower and not equal to those measured in the unstressed specimens are as yet unresolved.

15.4 Conclusions

- Remote tensile stresses above 80% yield increases in the electrochemical reactivity for localised corrosion site initiation (i.e. decrease in the breakdown potential) in parent 2024-T351. This occurs both when the remote stress is applied parallel as well perpendicularly to the rolling direction.
- *In situ* FEG-SEM analysis reveals that delamination occurs at constituent particle–matrix interfaces in parent 2024-T351 when subjected to remote loads greater than 90% of the yield strength. It is reasonable

to assume that these micro-crevices readily develop aggressive environments resulting in the formation of preferential localised corrosion sites.

- No increase in the electrochemical reactivity for corrosion initiation is observed in the HAZ or nugget regions of the 2024 FSW as a function of remotely applied tensile stress.
- Applied remote stresses enhance the localised corrosion propagation at the HAZ/TMAZ boundary in FSW 2024-T351. No other area within the HAZ or nugget of the weld displays this behaviour.

15.5 Acknowledgements

Funding for this work was provided by the Royal Society via the USA Research Fellow scheme. Additional material support was provided by BAE Systems and Airbus UK.

15.6 References

1 P. F. Mendez and T. W. Eagar, *Adv. Mater. Process.*, 2001, **159**(5), 39.
2 W. M. Thomas, E. D. Nicholas, J. C. Needham, M. G. Murch, P. Templesmith and C. J. Dawes, 'Friction stir butt welding', Int. Patent Appl. No. PCT/GB92/02203 and GB Patent Appl. No. 9125978.8, Dec. 1991. US Patent No. 5,460,317, Oct. 1995.
3 M. Ellis and M. Strangwood, *TWI Bull.*, 1995, **6**, 138.
4 C. J. Dawes and W. M. Thomas, *Weld. J.*, 1996, **75**(3), 41.
5 A. P. Reynolds, W. D. Lockwood and T. U. Seidel, *Mater. Sci. Forum*, 2000, **331–337**, 1719–1724.
6 G. S. Frankel and Z. Xia, *Corrosion*, 1999, **55**, 139–150.
7 J. B. Lumsden, M. W. Mahoney, C. G. Rhodes and G. A. Pollock, *Corrosion*, 2003, **59**, 212–219.
8 J. B. Lumsden, M. W. Mahoney, G. A. Pollock and C. G. Rhodes, *Corrosion*, 1999, **55**, 1127–1135.
9 P. S. Pao, S. J. Gill, C. R. Feng and K. K. Sankaran, *Scr. Mater.*, 2001, **45**, 605–612.
10 J. Corral, E. A. Trillo, Y. Li and L. E. Murr, *J. Mat. Sci. Lett.*, 2000, **19**, 2117–2122.
11 F. Hannour, A. J. Davenport and M. Strangwood, in *Proc. 2nd Int. Symposium on Friction Stir Welding*, Gothenburg, Sweden, 2000.
12 R. Ambat, M. Jariyaboon, A. J. Davenport, S. W. Williams, D. A. Price and A. Wescott, in *Proc. 15th Int. Corrosion Congress*, Granada, Spain, Sept. 22–29, 2002.
13 T. Suter and R. C. Alkire, *J. Electrochem. Soc.*, 2001, **148**(1), B36–B42.
14 H. Böhni, T. Suter and A. Schreyer, *Electrochim. Acta*, 1995, **40**(10), 1361–1368.
15 C. M. Rangell, M. H. Simplicio and M. G. S. Ferreira, *Br. Corros. J.*, 1992, **27**, 237–240.
16 F. Navai and O. Debbouz, *J. Mater. Sci.*, 1999, **34**, 1073–1079.
17 V. Vignal, C. Valot, R. Oltra, M. Verneau and L. Condreusse, *Corr. Sci.*, 2002, **44**, 1477–1496.

18 P. Peyre, X. Scherpereel, L. Berthe, C. Carboni, R. Fabbro, G. Beranger and C. Lemaitre, *Mater. Sci. Eng.*, 2000, **A280**, 294–302.
19 F. Navai, *J. Mater. Sci.*, 2000, **35**, 5921–5925.
20 T. Suter, E. G. Webb, H. Böhni and R. C. Alkire, *J. Electrochem. Soc.*, 2001, **148**, B174–B185.
21 X. Liu, G. S. Frankel, B. Zoofan and S. I. Rokhlin, *Corr. Sci.*, 2004, **46**, 405–425.
22 V. Vignal, R. Oltra and C. Josse, *Scr. Mater.*, 2003, **49**, 779–784.

16

In situ detection of galvanic coupling during pitting by scanning vibrating electrode technique and microcapillary electrochemical cell

H. KRAWIEC, AGH University of Science and Technology, Poland, and R. OLTRA and V. VIGNAL, Université de Bourgogne, France

16.1 Introduction

Microelectrochemical methods which have been developed appear to be powerful techniques to study chemical and/or electrochemical reactions in the micro- and nano-range.[1–4] Local investigations of the electrochemistry on multi-phase materials at the scale of the microstructure can be investigated by invasive or non-invasive techniques as shown in Fig. 16.1. In the case of non-invasive ones, like the microcapillary electrochemical cell,[5] a reduced area containing a well defined ratio of the phases or a single phase can be selected and electrochemical properties can be defined easily under potentiostatic conditions. Nevertheless, the galvanic interaction cannot be studied. This can be done with invasive probes like the scanning vibrating electrode technique (SVET), which enables detection of distribution of the current lines in the bulk of electrolyte or the scanning electrochemical microscope (SECM). SVET offers the possibility of mapping variations in current densities on the microscale over a corroding system by measuring potential gradients developed in the solution due to the flow of ionic currents and of locating anodic and cathodic zones.

SVET measurements at open circuit potential (OCP) have only been performed in specific cases such as for characterising the current evolution during the initiation and growth of surface microcracks under straining conditions[6] and the deterioration of organic coatings[7,8] and for studying microbial influenced corrosion.[9] The main reason is that it is difficult to activate a single pit at OCP on a sufficiently long time scale to perform local current measurements.

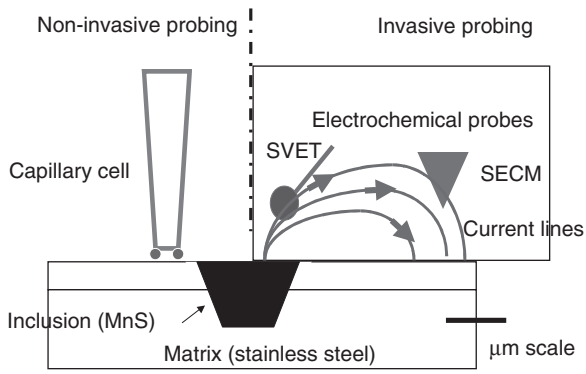

16.1 Schematic description of local electrochemical techniques to study galvanic coupling as function of the microstructure of multi-phase materials.

16.2 Experimental methods

Measurements were performed on a resulfurised 304 L type stainless steel (Ni 8.75, Cr 18.3, Mn 1.7, S 0.17, Si 0.5, P < 0.035 and C 0.05 wt%). The samples were machined from sheets along the short transverse direction. Spheroidised inclusions were observed (depth <5 μm) and their size ranged between 5 and 40 μm. These inclusions were heterogeneously distributed on the surface. The samples were mechanically polished with silicon carbide emery papers down to 4000 grit, smoothed with diamond pastes down to 1 μm and ultrasonically rinsed in ethanol. After polishing, the depth of the inclusions emerging at the surface ranged from the nano- to the microscale, depending on the quantity of MnS removed during polishing.

The local electrochemical behaviour of specimens was studied at 25°C using the microcapillary electrochemical cell (MEC).[5] This technique consists of a glass microcapillary which is filled with the electrolyte. The microcapillary tip was sealed to the specimen surface with a layer of silicone rubber. The microcell was mounted on a microscope for precise positioning of the microcapillary on the surface and the entire setup was placed in a faraday cage. The diameter of the microcapillary tip was 50 μm and the counter electrode was a platinum wire. A modified high resolution potentiostat was used in order to have a current detection limit of 20 fA (Jaissle 1002T-NC-3).

An Applicable Electronics SVET was used to perform galvanic current measurement in OCP conditions. SVET probes consist of Pt–Ir microelectrodes (MicroProbe Inc.) black platinised leading after deposition to a sphere of 20 μm in diameter. The vibration amplitude was 20 μm and the vibration frequency was 600 and 200 Hz in the direction parallel and normal

to the surface, respectively. The ASET Software (Science Wares Inc.) converted the potential drop measured by the microelectrode with Ohm's law into a current density value after amplification. The displacement of the microelectrode was performed using a motorised and computer-controlled XYZ micromanipulator allowing 0.5 µm steps. Two video cameras (140× magnification) were used for imaging and controlling the distances between the microelectrode, the microcapillary and the specimen surface. The distance between the microelectrode and the surface was fixed to 50 µm and the Y-component of the current was measured. A saturated calomel electrode (SCE), to which all the potentials in the text are referred, was used as reference.

16.3 Results and discussion

16.3.1 Non-intrusive probing of a 'weak area': MEC experiments

The first step consisted of defining the electrochemical conditions leading to a possible dissolution of the MnS inclusion which is a well-known triggering step for pitting initiation. Using the MEC, it was possible to isolate representative areas of the metallic surface containing or not an inclusion. The electrochemical response of sites containing the pure matrix and the matrix with a single MnS inclusion were performed in 1 M $NaClO_4$ buffered with a mixture of 0.1 M disodium citrate ($Na_2C_6O_7H_6$) and 0.1 M HCl at pH 3. A potential of –500 mV corresponding to the cathodic zone (the OCP values ranged between –200 and –300 mV/SCE in the different solutions) was applied for 3 min and the potentiodynamic polarisation curves were then measured at a scan rate 1 mV s^{-1}.

Polarisation curves on a site containing a small and shallow inclusion were performed between 70 and 500 mV, as shown in Fig. 16.2. Particular attention was paid to the electrochemical dissolution of the inclusion as it will be used in the SVET experiment to initiate a stable pitting in OCP condition. The current peak observed around +320 mV was ascribed to a complex combination of electrochemical reactions concerning the inclusion dissolution and the activation–repassivation of the bare metal.[10] The most important finding is that the first part of the peak current peak observed at 320 mV was associated with the electrochemical dissolution of the shallow MnS inclusion. No current peak associated with MnS dissolution was obtained when a second polarisation curve was performed on the same location, confirming that the inclusion dissolution was complete after the first curve. Following this observation it can be concluded that MnS inclusion can be dissolved at high potential in an acidic solution.

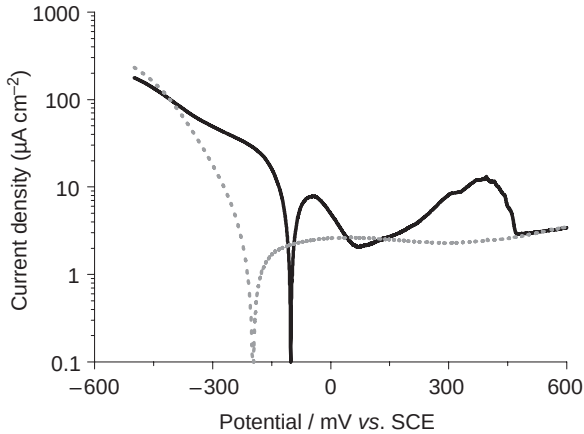

16.2 Local polarisation curves determined in a buffered solution 1M $NaClO_4$, pH 3 on sites containing the pure matrix (dotted) and the matrix with a shallow inclusion (black).

16.3.2 SVET above a pit triggered by local induced dissolution of a selected MnS inclusion

Following the MEC experiments, the local activation of a selected inclusion was carried out exactly on the same material but in free corroding conditions. The metallic electrode was immersed into a buffered solution 0.1M citric acid ($C_6H_8O_7$) + 0.2M Na_2HPO_4 (pH = 6.8 and $\kappa = 2.3\,mS\,cm^{-1}$). The microcapillary (previously used in MEC experiments) was used, but filled with a mixture of 1M HCl (80 mL) and H_2O_2 (0.3 mL) in order to promote the dissolution of the selected inclusion at high anodic potential (in the range of +100 to +300 mV *vs.* SCE). As explained previously, the sample was immersed into a citrate/citric acid buffered solution and only a small quantity (of about 1.5 μL) of activating solution was injected close to an inclusion while keeping the microcapillary in contact with the metallic surface for a few seconds. This corresponded to the time necessary for removing the microcapillary far from the surface and for starting the SVET measurements and therefore, such a current perturbation had nearly no effects on these measurements. Local current measurements were performed at OCP.

Once the inclusion was dissolved, pits initiated in the bare metal due to the low value of the pH and the high density of chloride ions in the close vicinity of the selected site. The anodic current was always detected above the site where the bare metal was exposed to the solution after complete dissolution of the shallow inclusion.[10]

These results are the first experimental evidence of the galvanic coupling between the bare metal exposed to the solution after MnS dissolution and

the passive surface on stainless steels. Nevertheless, it is a qualitative illustration of the origin of the galvanic coupling. More quantitative analysis has been tentatively performed taking into account the spatial convolution of the SVET measurement.[11]

16.4 Conclusions

In this paper, combination of two local techniques to probe the electrochemical behaviour of 'weak points' in the microstructure of a modelling stainless steel (resulfurised 304L) has been illustrated. It was demonstrated that OCP galvanic current can be detected by SVET on the basis of the locally induced dissolution of a well located MnS inclusion which is triggering the local activation in the 'weak point' of the microstructure. Triggering of metal dissolution has been validated by using the MEC.

This spatial activation has been achieved by a local microinjection of aggressive and oxidising solution with a glass microcapillary maintained in gentle contact with the metallic surface.

Quantitative studies to define the interfacial reactions (spatial location and real current densities) must take into account the convolution of the SVET measurement and must be completed by SECM measurements.

16.5 References

1 C. H. Paik, H. S. White and R. C. Alkire, *J. Electrochem. Soc.*, 2000, **147**, 4120–4124.
2 D. E. Williams and Y. Y. Zhu, *J. Electrochem. Soc.*, 2000, **147**, 1763–1766.
3 J. O. Park, C. H. Paik, Y. H. Huang and R. C. Alkire, *J. Electrochem. Soc.*, 2000, **146**, 517–523.
4 B. Vuillemin, X. Philippe, R. Oltra, V. Vignal, L. Coudreuse, L. C. Dufour and E. Finot, *Corr. Sci.*, 2003, **45**, 1143–1159.
5 T. Suter, E. G. Webb, H. Boehni and R. C. Alkire, *J. Electrochem. Soc*., 2001, **148**, B174–B185.
6 H. Uchida, M. Yamashita, S. Inoue and K. Koterazawa, *Mater. Sci. Eng.*, 2001, **A319–321**, 496–500.
7 I. Sekine, M. Yuasa, N. Hirose and T. Tanaki, *Prog. Org. Coat.*, 2002, **45**, 1–13.
8 M. Khobaib, A, Rensi, T. Matakis and M. S. Donley, *Prog. Org. Coat.*, 2001, **41**, 266–272.
9 M. J. Franklin, D. C. White and H. S. Issacs, *Corr. Sci.*, 1991, **32**, 945–952.
10 H. Krawiec, V. Vignal and R. Oltra, *Electrochem. Comm.*, 2004, **6**, 655–660.
11 H. S. Isaacs, *Corrosion*, 1990, **46**, 677–679.

17

Photoelectrochemical imaging of thermally grown oxide scales

Y. WOUTERS, L. MARCHETTI, A. GALERIE,
P. BOUVIER and J.-P. PETIT,
Institut National Polytechnique de Grenoble, France

17.1 Introduction

Thermal oxidation of titanium in pure oxygen is a relevant example of the connection between the stress development during the growth of the oxide film and the durability of the material. As known for many years,[1–4] in the range 500–1000°C, titanium oxidation in pure oxygen exhibits an initial parabolic rate law followed by a post-breakaway rapid linear period (Fig. 17.1). After breakaway (BWY), microscopic observations reveal a cracked and stratified TiO_2 scale. This phenomenon is generally interpreted as the result of the growth of an initial TiO_2 scale, followed by cracking due to a high Pilling and Bedworth ratio (PBR = 1.71) and subsequent series of growth and cracking periods.[4] The use of photoelectrochemical imaging provides information about mechanical aspects during the growth of a thermal oxide film of titanium in pure oxygen.

17.2 Experimental method

A schematic representation of the laboratory-made microphotoelectrochemistry (MPEC) device used is presented in Fig. 17.2. The photocurrent is generated using the modulated ($f = 21$ Hz) monochromatic light from an argon laser (Innova 90C-A6, coherent, $\lambda = 353$ nm). The beam is focused onto the surface of the oxidised sample studied via the objective of an inverted microscope (Olympus IX71, spot size# 1μm). The image is built by moving a high resolution XY motorised Marzhauser microscope stage (Scan IM120 × 100) ensured with a positioning system (two axes stepping motor controller: LStep, Lang Gmbh). The sample is used as the working electrode in a classical three-electrodes electrochemical cell with a flat quartz bottom. The reference electrode is an $Hg/HgSO_4$ reference electrode (MSE); the counter-electrode is a platinum plate of 1 cm^2 area. The electrolyte is de-aerated sodium sulfate aqueous solution (0.5 mol L^{-1}).

The lock-in technique is applied to separate the photocurrent from the total electrochemical current. For that purpose, the current output of the

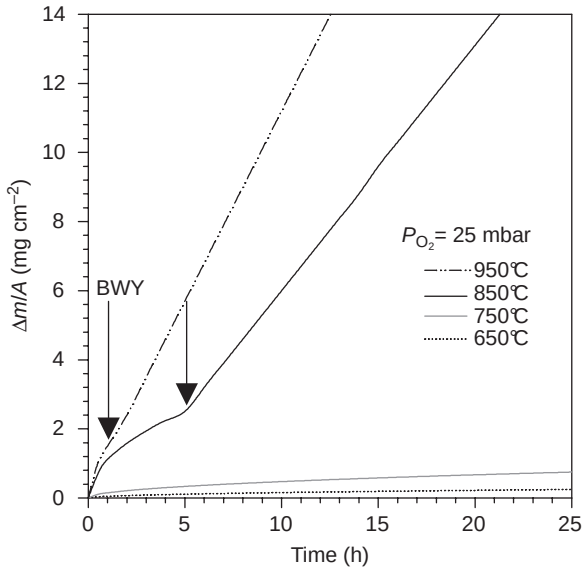

17.1 Oxidation kinetics of titanium in pure oxygen.

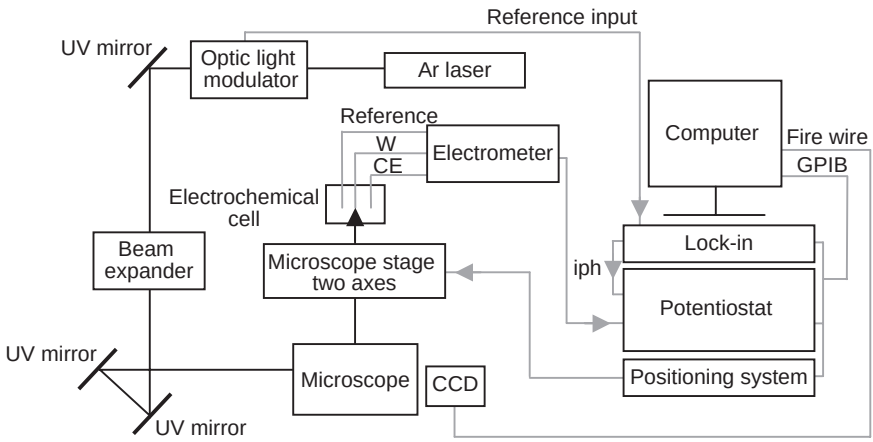

17.2 Schematic representation of the microphotoelectrochemical set-up.

potentiostat (PAR 273A, EG&G) is connected to the signal input of the lock-in amplifier (Stanford Research SR830) and the trigger signal of the optic light modulator (PAR 197, EG&G) is fed to the reference input of the lock-in amplifier. A photoelectrochemical image is built at a given applied potential, by recording for each position of the stage, the amplitude and the phase of the photocurrent. The investigated area is selected on the

optical image provided by a CCD camera. In the present experiments, the photocurrent images have a 170×170 points definition, with a step of 3 µm between each point in the x and y directions. The whole of the instrumentation is controlled by a laboratory-made software.

17.3 Results and discussion

The two samples studied here were prepared at 700°C and 850°C in a dynamic atmosphere of pure oxygen under a pressure of 150 mbar. Titanium specimens (15 mm × 15 mm × 1 mm) from Goodfellow Metals, with a purity of 99.6%, were mechanically mirror-polished (SiC papers, diamond pastes and silica finish) before they were hung in a Setaram B70 thermobalance. After experiment, the cooling rate of the sample is that of the furnace. The oxidation duration was such as to grow a 1.75 µm thick oxide film. The results of the PEC imaging of these samples are presented in Fig. 17.3 (700°C) and 17.4 (850°C).

Figures 17.3a and 17.4a show photo current images obtained using increasing potential values. Figures 17.3b and 17.4b are so-called photocurrent *vs.* potential photocharacteristics: they correspond to two different points of the images, one in a low photocurrent area and the other in a high photocurrent area. For each of the later photocharacteristic, the photocurrent value at the maximum potential was normalised to 1. Each point in Figs. 17.3c and 17.4c represents the integral of the corresponding normalised photocharacteristic. Such images will be referred to as structural quality images (SQI). The images 17.3d and 17.4d show the distribution of the phase values recorded at –550 mV/MSE.

As expected for n-type semi-conducting TiO_2, each individual photocharacteristic exhibits anodic photocurrent increasing with increasing potential. The shape and the photocurrent onset potential of these photocharacteristics are different from one point to another, ranging from 'type 1' curves in high photocurrent areas to 'type 2' curves in low photocurrent areas. Previous results have shown that the shape and photocurrent onset potential of the photocharacteristics are connected with the density of recombination centers,[5] classically associated with micropores, microcracks, voids, microspallation.[6–7] Thus, the building of the SQI is an attempt to represent the level of growth strain in the oxide films, or more precisely, via its relaxation which leads to the creation of recombination centres. Dark areas on the SQI represent a high level of growth strain, whereas bright areas represent a low level of growth strain.

For both samples, it is observed that high photocurrent areas are approximately, but not exactly, correlated with the bright zones in SQI. These areas are also correlated with the dark zones of the phase image which reveals the cartography of the photocurrent onset potential. Table 17.1 shows the

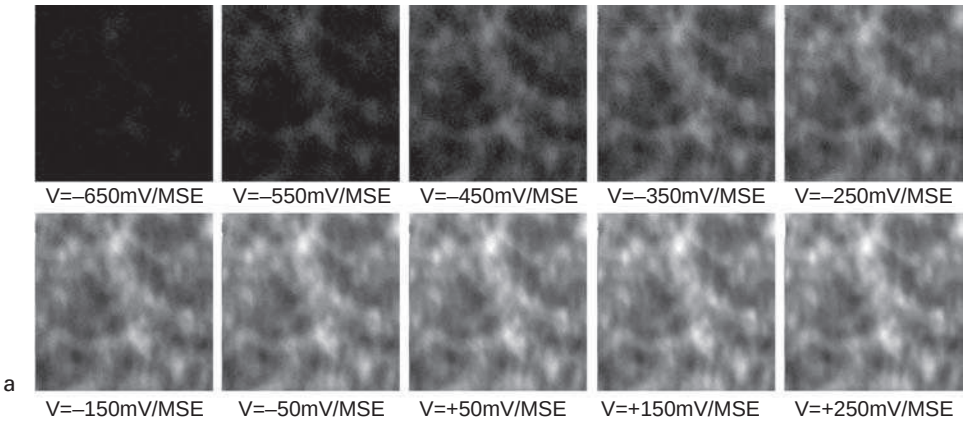

a

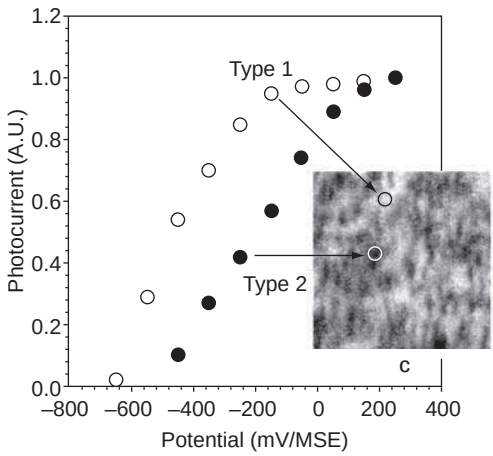

b

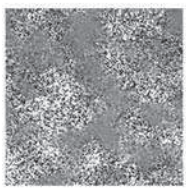

d

17.3 Sample grown at 700°C in pure oxygen: *a* photocurrent images vs. potential, *b* normalised evolution of the photocurrent as a function of the potential at low and high photocurrent areas, *c* structural quality image (SQI), *d* phase image (V = –550 mV/MSE).

Table 17.1 SQI factor at 700 and 850°C

SQI factor	Minimum	Maximum	Average
700°C	0.61	0.83	0.72
850°C	0.53	0.78	0.66

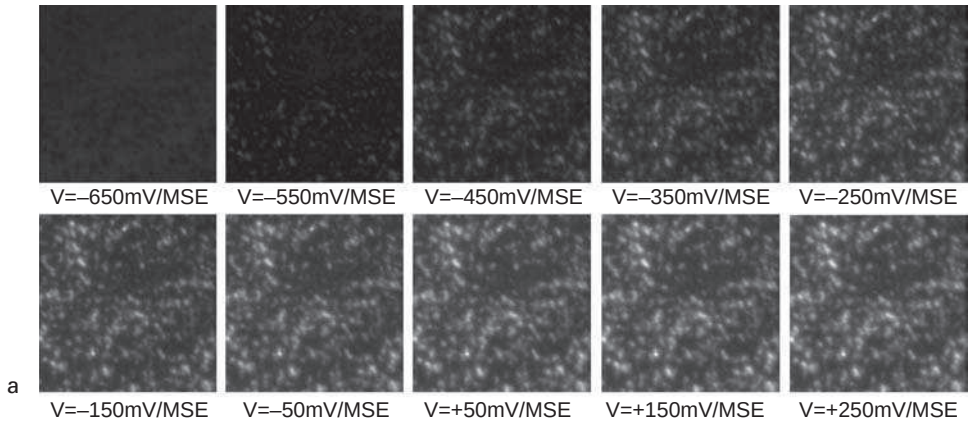

a

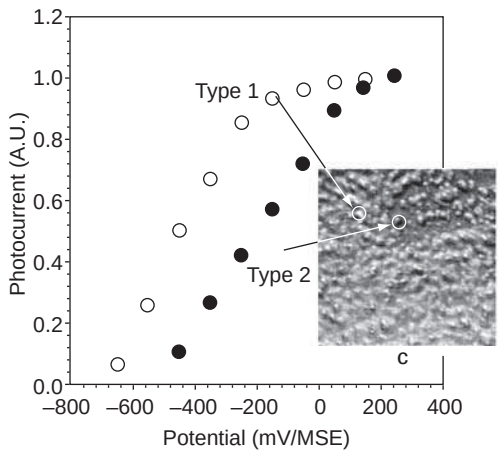

b

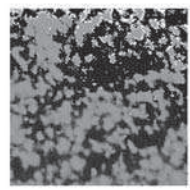

d

17.4 Sample grown at 850°C in pure oxygen: *a* photocurrent images vs. potential, *b* normalised evolution of the photocurrent as a function of the potential at low and high photocurrent areas, *c* structural quality image (SQI), *d* phase image (V = –550 mV/MSE).

minima, maxima and average of the SQI for both temperatures of oxidation. One can conclude from these results that the global growth strain of the oxide film increases with the temperature of oxidation at a fixed thickness. This observation is in good agreement with the evolution of the breakaway time typically observed during the thermal oxidation of titanium in pure oxygen as recalled in the introduction. Moreover, this statement accords with the kinetics of oxidation, the development of stress being linked with the growth rate of the thermal oxide film. It is particularly remarkable here to note that the fluctuations of the SQI are quite differ-

ent at 700°C where large areas of low growth strain are observed (high SQI factor, bright areas) and at 850°C where growth strain is more disseminated in the image. This suggests that the mechanism of decohesion changes according to the temperature.

Because of the latter observations, we expect that the SQI is related to the real cartography of growth strain. Further experimentation and modelling is underway to resolve this issue, in the case of titanium as well for other model systems (metal or alloys).

17.4 Conclusions

The MPEC technique appears to be a promising tool in the field of thermal oxidation. This paper has shown one facet of this technique: the possibility of characterising the growth strain. At the same time, more results are needed to improve our understanding of the SQI. In addition, MPEC is expected to be an efficient technique to detect the presence of minor phases in thermal oxide scales.

17.5 References

1 P. Sarrazin, F. Motte and J. Besson, *J. Less. Common Met.*, 1978, **59**(2), 111–117.
2 F. Nardou, P. Raynaud and M. Billy, *J. Chim. Phys.*, 1984, **81**(4), 271–277.
3 V. I. Dyachkov, *J. Chim. Phys.*, 1991, **88**, 37–44.
4 P. Kofstad in *High Temperature Corrosion*, Elsevier Applied Science, London, 1987, 297.
5 Y. Marfaing, *Ecole Interface Semi-conducteur/Electrolyte*, Aussois, Editions du CNRS, 1984, 35.
6 A. Galerie, Y. Wouters and J. P. Petit, *Mater. Sci. Forum*, 1997, **251–254**, 113–118.
7 Y. Wouters, A. Galerie, L. Antoni and J. P. Petit, *Microscopy of Oxidation 3*, S. B. Newcomb, M. J. Bennett (Eds.), Institute of Materials, London, 1997, 420–426.

Index